

Aus dem Zentrum für Kinder- und Jugendmedizin der Universität Heidelberg
(Geschäftsführender Direktor: Univ. - Prof. Dr. med., Prof. h. c. (RCH) Georg F. Hoffmann)
Sektion für Pädiatrische Nephrologie

**Development of An Automated High-Content Screening Platform for Identification of
Cystic Kidney Disease Modifying Substances in Zebrafish Model of Human Cystic
Kidney Disease**

Inauguraldissertation
zur Erlangung des Doctor scientiarum humanarum (Dr. sc. hum.)
an der
Medizinischen Fakultät Heidelberg
der
Ruprecht-Karls-Universität

vorgelegt von
Gunjan Pandey
aus

Sitapur, Indien
2019

Dekan: Prof. Dr. med. Andreas Draguhn

Doktorvater: Prof. Dr. med. Franz Schaefer

It is by reading what discoverers have done that we lift and maintain the sacred flame of discovery

– Louis Pasteur

Table of Contents

Abbreviations	8
1 Introduction	11
1.1 Human kidneys and Associated Cystic Nephropathies	12
1.1.1 Role of Cilia in Cystic Nephropathy	13
1.1.2 Ciliary Assembly and <i>ift172</i>	15
1.2 Zebrafish as a Model for Human Cystic Nephropathy	16
1.2.1 Cystic Nephropathy and <i>ift172</i> in Zebrafish	19
1.3 High-Content Screening and Drug Discovery	20
1.4 Zebrafish as a Model for Drug Discovery	23
1.4.1 Transgenic Kidney Models of Zebrafish	25
1.4.2 Screening Technologies in Zebrafish	25
1.4.3 Rescuing Disease Phenotypes with Chemical Screening	26
1.5 Technical Challenges in High-Content Screening	29
2 Objectives	35
3 Material and Methods	36
3.1 Ethics Statement	36
3.2 Fish Husbandary Protocols	36
3.2.1 Fish Keeping	36
3.2.2 Embryo Collection	36
3.2.3 Raising Embryos	37
3.3 High-Content Drug Screening Protocols	37
3.3.1 Injection Solution Preparation	37
3.3.2 Injection Needle Preparation	37
3.3.3 Morpholino Injections	38
3.3.4 Dose Response Optimisation Curve for <i>ift172</i> Morpholino	38
3.3.5 Time Lapse Study to Determine Cytogenesis in Cystic Nephropathic Larvae	39
3.3.6 Dose Response Optimisation Curve for Control : Rapamycin, Valproic Acid, Trichostatin A, Curcumin	39

3.3.7	Drug Treatment of Zebrafish Larvae	40
3.3.8	Dose Response Studies on Hits	40
3.3.9	Preparation of Microtitre Plate	40
3.4	High-Content Imaging Protocols	41
3.4.1	Image Acquisition	41
3.4.2	Image Pre-processing	42
3.4.3	Blurry, Blank and Wild-Type Kidney Check	42
3.4.4	Image-Based Area Quantification for Morphology Gradation	43
3.4.5	Heatmap Representation	44
3.5	Statistical Test on Screened Compound Library	44
3.6	Molecular Methods	44
3.6.1	RNA Extraction	44
3.6.2	DNase Digestion	45
3.6.3	<i>ift172</i> Morpholino Knockdown Quantification with RT-PCR	45
3.6.4	Agarose Gel Electrophoresis	45
3.6.5	Fixation of Zebrafish Embryos	46
3.6.6	HE Staining and Imaging	46
4	Results	48
4.1	Optimisations for High-Content Screening	48
4.1.1	Dose Response Optimisation Curve for <i>ift172</i> -MO	48
4.2	Morpholino Knockdown Quantification	49
4.3	Sub-cellular Phenotype Visualisation Utilising HE Stain	50
4.4	Time Lapse Study to Determine Cystogenesis in Cystic Nephropathic Larvae	51
4.4.1	Dose Response Optimisation Curve for Positive Control : Rapamycin	52
4.4.2	Dose Response Optimisation Curve for Controls : Valproic Acid and Trichostatin A	54
4.4.3	Dose Response Optimisation Curve for Control : Curcumin	56
4.5	High-Content Imaging	57
4.5.1	Image Pre-processing	57
4.5.2	Blank, Blurry and wild-type Scoring	59
4.5.3	Image Processing and Pronephric Area Quantification	62
4.5.4	Heatmaps: An Interactive Output for Compound Class Scoring	64

4.6	High-Content Screening Results	65
4.6.1	Pharmacological Cyst Modifiers Identified by High-Content Screening	65
4.6.2	Dose Response Studies on High-Content Screening Hit Compounds	71
5	Discussion	85
5.1	Choice of the Disease Model	86
5.2	Development of the High-Content Screening System	87
5.2.1	Image Acquisition	87
5.2.2	Image Pre-processing	89
5.2.3	Image Filtering	90
5.2.4	Image Quantification	91
5.2.5	Empowering High-Content Screening by Smart Imaging	91
5.3	Choice of Control Compounds	93
5.4	High-Content Screening	94
5.4.1	Pharmacological Modifiers of Cystic Nephropathy Identified from High-Content Screening	95
5.5	Concluding Remarks	105
6	ZUSAMMENFASSUNG	106
7	References	109
8	Publication and Awards	128
8.1	Original Publications	128
8.2	Abstracts	128
9	Supplement	131
9.1	Materials	131
9.1.1	High-Content Drug Screening	131
9.1.2	High-Content Imaging	131
9.1.3	RNA, cDNA Extraction and Agarose Gel Electrophoresis	132
9.1.4	HE Staining	132
9.2	Figures	134
9.3	Scripts	140

S.1	Step-by-step execution of smart-imaging workflow for organ-specific screening in a cystic kidney zebrafish disease model	140
S.2	Script codes	144
S.3	Smart Imaging	144
S.4	Multilayer TIFF Generation	147
S.5	Image Analysis	148
10	CURRICULUM VITAE	169
11	Acknowledgement	170
12	EIDESSTATTLICHE VERSICHERUNG IN DEUTSCHER SPRACHE	171

Abbreviations

°C	degree celsius
A	alimentary tract and metabolism
ADPKD	autosomal dominant polycystic kidney disease
ANP	atrial natriuretic peptide
Ap	adapalene
ARPKD	autosomal recessive polycystic kidney disease
Az	astemizole
ATC	anatomical therapeutic code
BF	bright-field
B	blood and blood forming products
BN	butconazole nitrate
bp	base pair
C	cardiovascular System
CA	cyproterone acetate
cDNA	complementary DNA
cGMP	guanosine 3',5'-cyclic monophosphate
PKD	polycystic kidney diseases
Cz	clotrimazole
CRISPR	clustered regularly interspaced short palindromic repeats
Cs	ciclesonide
Ctrl	control
Cx	cycloheximide
D	dermatologicals
DNA	deoxyribonucleic acid
ED	ethynodiol acetate
EMA	european medicines agency
FDA	food and drug administration
Fp	fluspirilen
Fq	flumequine
Fz	flubendazole
G	genito urinary systems and sex hormones
GFP	green fluorescent protein

HCS	high-content screening
HDAC	histone deacetylase inhibitors
HE	haematoxylin eosin
HEPES	4-(2-hydroxyethyl)-1-piperazineethanesulfonic acid
hPa	hectopascal
hpf	hours post fertilization
HSC	hematopoietic stem cells
ift	intra flagellar transport
IM	intermediate mesoderm
IM04	(aquifer high-content) imaging machine version 4
J	anti-infectives for Systemic Use
L	anti-neoplastic and Immunomodulating Systems
μ M	micromolar
min/s	minute/second
M	musculo-skeletal system
mm	millimetre
MO	morpholino
Mz	monobenzene
O	omeprazole
Pz	phenothiazine
N	nervous system
NA	numerical aperture
nl	nanolitre
P	anti-parasitic products, insecticides, repellents
PBS	phosphate buffered saline
PC	polycystin
PCR	polymerase chain reaction
PPI	proton pump inhibitor
PT	proximal tubules
PTU	1-phenyl-2-thiourea
Q	veterinary use
R	respiratory systems
Ra	racecadotril
RNA	ribonucleic acid
ROI	region of interest

RT	room temperature
s	second
S	sensory organs
SI	smart imaging
SD	standard deviation
SN	sertaconazole nitrate
TSA	trichostatin A
Tz	toltrazuril
UB	ureteric bud
VPA	valproic acid
wt	wilms' tumour

1 Introduction

Cystic nephropathy affects 12.5 million people across the globe. Approximately, 50% of the affected individuals inherit the disease and transmit it to their progenies (Harris and Torres, 2009). Mainly occurring due to ciliary dysfunctioning, Polycystic Kidney Diseases (PKD) are broadly divided into Autosomal Dominant Polycystic Kidney Diseases (ADPKD), Autosomal Recessive Polycystic Kidney Diseases (ARPKD), Nephronophthisis, Bardet Biedel Syndrome associated cystic kidneys and Glomerulo-cystic kidney diseases. In the quest to find a suitable treatment for this disorder some randomised clinical trials have been conducted. Most of these trials targeted the signalling pathways affected in ADPKD. For instance, the HALT-PKD trial (Halt Progression of Polycystic Kidney Disease), explored the effect of renin-angiotensin-aldosterone system antagonists and blood pressure control, the ALADIN trial (A Long-Acting somatostatin on Disease progression in Nephropathy due to ADPKD), investigated the effect of somatostatin analogue Octreotide, and other trials tested mammalian Target of Rapamycin (mTOR) inhibitors (Sirolimus, Everolimus), the sirtuin inhibitor Niacinamide, and the Vasopressin type 2 receptor antagonist Tolvaptan (Caroli et al., 2013; Chapman et al., 2010; Kenneth et al., 1997; Serra et al., 2010; Torres et al., 2017; Walz et al., 2010; Wang et al., 2008; Zhou et al., 2013). Among all these trials the TEMPO trial (Tolvaptan Efficacy and Safety in Management of Autosomal Dominant Polycystic Kidney Disease and Its Outcomes) has so far led to the approval of a single effective drug against ADPKD, i.e. Tolvaptan. Despite its efficacy in slowing ADPKD progression, Tolvaptan pertains to have lingering risk of hepatotoxicity in patients and is only approved for short term administration (Yu et al., 2015). Moreover, tolvaptan may impact negatively on the quality of life of patients due to its heavy aquaretic effect (Sans-Atxer and Joly, 2018). Pharmaceutical trials in cystic kidney diseases have been limited to ADPKD, whereas no therapeutic approaches have been made to other progressive cystic kidney diseases such as ARPKD and the other ciliopathies affecting the kidneys, Hence, there is an eminent medical need for preclinical research to identify and test novel candidate compounds that may attenuate cyst development and growth and delay disease progression in affected patients.

Preclinical analysis of candidate compounds typically takes up more than half of the drug discovery timescale and eventually leads to a small number—if any—compounds that meet the criteria for exploration in humans (Drummond and Wingert, 2016). In this work, I attempted

to address the drawbacks of preclinical compound analysis by establishing and utilising an automated High-Content Screening (HCS) platform targeting human cystic kidney disease in a zebrafish animal model, which resulted in faster and more efficient isolation of potential drug-gable candidate compounds. To gain deeper insights on cystic nephropathies and HCS, the subsequent chapters introduce the organisation of human kidneys and cystic nephropathies, the role of cilia in cystic nephropathies, the zebrafish kidney and its suitability for HCS and the current progress and challenges in the field of HCS.

1.1 Human kidneys and Associated Cystic Nephropathies

Arising from embryonic Intermediate Mesoderm (IM), all mammalian kidneys undergo a similar set of sequential events giving rise to a fully functioning pair of retroperitoneally located adult kidneys. Kidney development occurs in three major stages demarcated by the species' position in the phylogenetic tree: the first stage is marked by the presence of pronephroi, which is followed by the mesonephros stage and culminated by the appearance of metanephros (Drummond and Davidson, 2016). The complexity of each successive stage increases during development, however the structure and function of the basic filtration unit, the nephron, remains unchanged across vertebrates. In humans, pronephroi appear on the 22nd day of gestation and unlike the functional pronephroi of zebrafish are considered non-functional elementary organs. Despite lacking proper functionality and eventually progressing towards senescence, the caudal portion of the pronephric duct persists and gives rise to the Wolffian duct, which induces the development of mesonephros (Grantham, 1997; Paul and Vanden Heuvel, 2014). The second stage of mesonephros generates non-functional mesonephric nephroi, which regress. The Wolffian duct then elongates downwards to join the urogenital sinus, which differentiates into the urinary bladder. At this stage, a diverticulum off the Wolffian duct becomes the ureteric bud (UB). Branching and outgrowth of the UB in metanephric mesenchyme gives rise to the metanephric kidneys, which instigates waves of nephron formation, ensuing which, each branch of UB ends up in a nephron. Up to a million of these ultimate functional units can be found in an adult kidney. The fully branched UB eventually differentiates into the collecting ducts, renal pelvis, and ureters.

Critical functions of the nephron include filtration, reabsorption, secretion, and excretion. Each nephron is made up of a renal corpuscle and renal tubule. The renal corpuscle is comprised of a tuft of high-pressure capillaries of afferent arterioles – the glomerulus and a continuous soph-

isticated tubule, whose proximal end surrounds the glomerulus called the Bowmann's capsule. Wrapped around the glomerular capillaries the long foot processes of podocytes can be found along with the slit diaphragm. It is here in the renal corpuscle unit, where the actual blood filtration takes place. The particle size- and charge-based filtration occurs via endothelial cells of the capillary wall, the basement membrane, and between the foot processes of the podocytes lining the glomerular capillaries. The glomerulus filters one-fifth of the blood volume entering the kidneys and the reject from here enters the renal tubule. The renal tubule is made up of the proximal convoluted tubule, Loop of Henle, distal convoluted tubule and the connecting tubule. Egressing the tubules, urine enters the collecting duct system, where the final electrolyte and fluid balance check is performed via optimised reabsorption and excretion processes through the bladder (Buchser et al., 2012; OpenStax, 2016). Overall, kidney regulates the volume of various body fluid compartments, fluid osmolality, acid-base balance, various electrolyte concentrations, and toxin removal. Impeccable functioning of such an intricately orchestrated renal system is essential for the regulation of body equilibrium in living systems. Malformations causing primary molecular lesions in the cilia or its structural components could cause retention of unwanted and excretion of useful molecules, thus, creating massive setbacks in the overall ion gradient. This ion-gradient disruption is followed by desensitisation of ion-channels is accompanied by urine accumulation, which ends up forming fluid filled cystic sacs in kidneys. The occurrence of cysts goes along with numerous alterations of molecular pathways and the resultant phenotype is broadly categorised as cystic nephropathies. Cystic nephropathies comprise a group of typically monogenic anomalies involving mutations in genes that regulate the structure and function of the primary cilia, in both humans and zebrafish. These ciliary dysfunctions are often grouped together as nephronophthisis-related ciliopathies. Few important causative mutations involved in the disease are introduced here.

1.1.1 Role of Cilia in Cystic Nephropathy

Primary cilia projects as an apical outgrowth from the surface of epithelial cells, lining nephrons in mammalian kidneys (Harris and Torres, 2009; Jonassen et al., 2012). The microtubule-organising centre and mother centriole lying underneath the cell membrane give rise to the basal body of cilia. The transition fibres along with the basal body are integral for monitoring the protein content of the ciliary membrane. Ciliary core known as axoneme extends from the basal body template and is comprised of peripherally organised nine doublets of microtubules.

The presence or absence of the central doublet divides cilia into two major categories i.e. “9+2” motile or “9+0” non-motile primary cilia. The motile cilia in mammals and lower organisms such as, *Chlamydomonas* and *Tetrahymena* have been well studied and are known for their role in mucous clearance, cerebrospinal fluid movement, locomotion, and assimilation. However, the immotile nature of the primary cilia originally led to its consideration as vestigial organ for a long time. It was only during the past two decades that they were identified as facilitator of cells’ interaction with their surroundings by actively participating in mechano-sensing and critical signalling pathways, such as hedgehog and PDGF-A (Berbari et al., 2009; Yoder, 2007). Moreover, the critical role of the primary cilia for renal epithelial cells was confirmed only in 2003, when a study investigating kidney specific knockout of the Kinesin II subunit motor, an integral component of intra flagellar transport (*ift*), led to complete deletion of primary cilia accompanied by the presence of renal cysts (Lin et al., 2003).

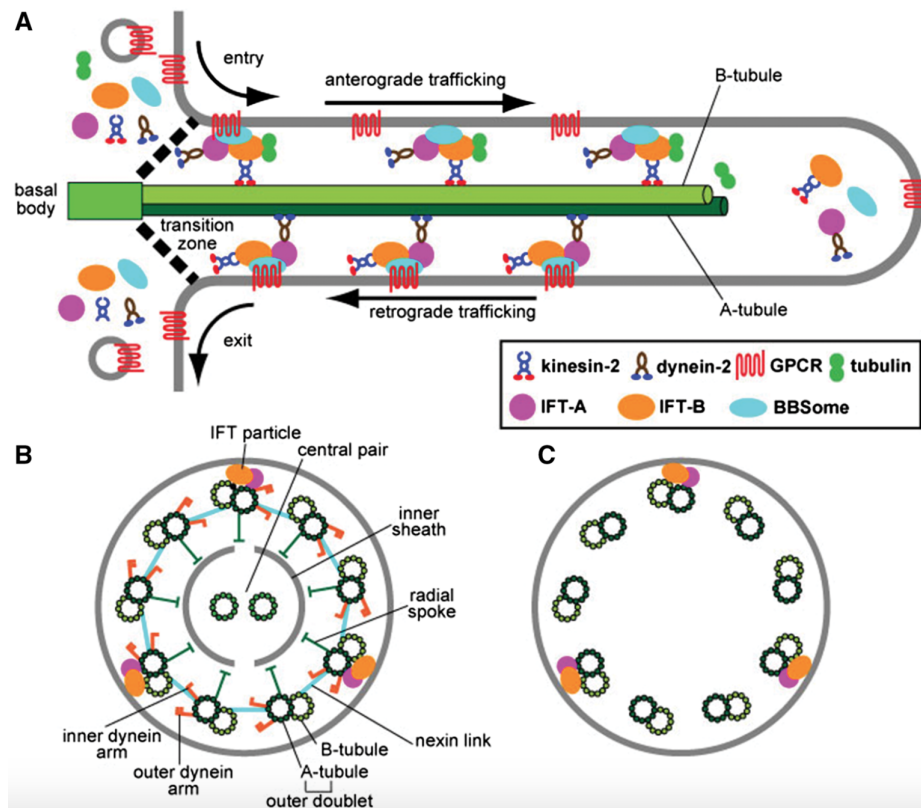


Fig. 1: **Illustration showing cilium and IFT.** (A) IFT-A and B families assemble at the base of cilia to form IFT complex, which initiates the transportation with the assistance of Kinesin-2, dynein-2 and the BBSome. IFT complex moves along the axoneme in anterograde manner fuelled by heterotrimeric kinesin-2. On reaching the tip, the complex disassembles and reassembles to perform retrograde trafficking facilitated by dynein-2. (B) shows 9+2 axoneme of a motile cilium and (C) is a 9+0 axoneme of primary cilium (figure adapted from (Kato et al., 2016)).

1.1.2 Ciliary Assembly and *ift172*

The construction, maintenance and disassembly of cilia is achieved by bi-directional *ift* complex (Berbari et al., 2009; Jonassen et al., 2012; Singla and Reiter, 2006). First discovered in chlamydomonas, *ift* was found to be conserved across eukaryotic species, providing a rationale for the translation of human cystic nephropathies to lower vertebrate models. *ift* is comprised of two protein complexes, i.e. A and B, which are involved in retrograde and anterograde transportation respectively. Kinesin-II motor fuels the anterograde transportation, while the retrograde transportation is performed by dynein 2/1b. Complex A is comprised of 6 subunits i.e. *ift144*, *140*, *139*, *122*, *121* and *43*. According to the *in silico* studies, the core domain of the complex should be comprised of *ift144*, *140*, *122* subunits and the rest should form the periphery (Taschner and Lorentzen, 2016). Similarly, in complex B, 9 out of its 14 structural subunits i.e. *ift88*, *81*, *74*, *70*, *52*, *46*, *27*, *25* and *22* form the core sub-complex. The remaining 5 subunits including *ift172*, *80*, *57*, *54* and *20* form the peripheral sub-complex (Halbritter et al., 2013; Katoh et al., 2016; Taschner and Lorentzen, 2016). Mutations in the peripheral subunits *ift80* and *ift172* have been established to cause human diseases such as Jeune asphyxiating thoracic dystrophy (JATD) and Mainzer Saldino Syndrome (MZSDS) (Beales et al., 2007; Halbritter et al., 2013). *ift172* is mainly responsible for the flagellar tip turn around during anterograde to retrograde transport switch. Based on the mutational analysis of *ift172* in the hedgehog signalling pathway, it has also been presumed to regulate Gli3 repressor (Huangfu et al., 2003; Pazour, 2004). The *ift172* gene encodes for a protein with 1,749 amino acid residues and has 9 N-terminal WD-40, 14 C-terminal TPR (tetratricopeptide repeat) and 1 LIM domain (Halbritter et al., 2013). Whole Exome Resequencing (WER) studies in patients showed that biallelic mutations in its structure lead to renal insufficiency, cystic renal degeneration followed by End Stage Renal Disease in the second decade of life (Halbritter et al., 2013). In humans, biallelic mutations in *ift172* lead to cystic renal degeneration with chronic renal insufficiency and End Stage Renal Disease in the second decade of life (Halbritter et al., 2013). The human *ift172* mutation was replicated in a zebrafish model by morpholino knocking down of splice sites exon 1-intron 1 and intron 1-exon 2. Both target sites led to a phenotype resembling human disease, including cystic kidneys, ventral body-axis curvature, hydrocephalus and otolith malformations with shortened cilia, resembling also the previously reported mouse model (Halbritter et al., 2013; Yoder, 2007). The varied range of diseases originating from cilia demand for study of molecules that target the associated pathways and assist in reviving their balanced functioning.

1.2 Zebrafish as a Model for Human Cystic Nephropathy

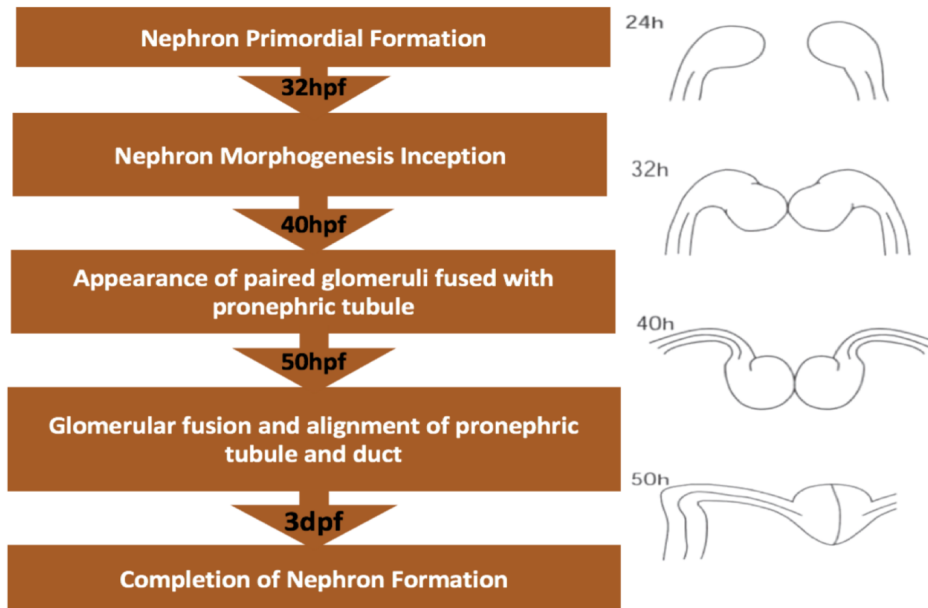


Fig. 2: **Zebrafish embryonic kidneys.** Illustration of embryonic development of zebrafish pronephroi adapted from (Drummond et al., 1998).

The zebrafish embryonic kidney has been a subject of special interest for drug and developmental studies due to its close resemblance with human kidneys and simple anatomical organisation. Despite the aquatic habitat, cell types composing nephron structures are common among all vertebrates and are functionally conserved. Zebrafish nephron primordium already appears at 24 hpf as an infold in the coelomic lining and is functional around 2 dpf, accomplishing the tasks of blood filtration and osmoregulation (Fig. 2). The connection between nephric lumen and coelom exists till 32 hpf, which is followed by the formation of a double layered sac of cells with a central lumen. At 40 hpf, nephron primordium gets partitioned into a clear medial glomerular and lateral tubular domain. Cells on the anterior side of the primordium migrate to the centre to give rise to podocytes (Drummond and Wingert, 2016). Mimicking metanephric human renal architecture at molecular level, the podocytes are entailed with slit diaphragms encompassing extensively interdigitised foot processes made up of nephrin and podocin. Podocytes recruit cells, which form the glomerulus in the centre. It is a fused blood filtration unit with fenestrated endothelial cells in capillary tufts surrounded by a distinct basement membrane under the dorsal aorta. Functional but leaky at 48 hpf, this filtration unit is shared on either sides by a pair of pronephric tubules. By 30-40 hpf, proximal tubule (PT) formation completes and one can see the paired PT posteriorly attached to the glomerulus in the

centre (Fig. 2) (Drummond, 2003). At 50 hpf, the contact of the glomerulus with the caudal pronephric ducts (PD) is facilitated by arching of the PT. The PT is divided into three main segments, which emerge as the neck followed by two proximal sections of Proximal Convolved Tubule (PCT) and Proximal Straight Tubule (PST) and two distal sections, i.e. Distal Early and Distal Late Tubule (Wingert et al., 2007). The segments have been mapped by isolating markers of renal cell types over the length of tubules and ducts. These structures presented conserved structural and physiological properties as well as spatiotemporal gene-expression patterns that are homologues to the human kidney (Nichane et al., 2006; Wingert et al., 2007). The entire proximal segment is covered with apical microvilli and possesses brush border characteristic of mammalian kidneys (Drummond, 2003; Wang et al., 2014). Cluster of endocrine glands are present in the early Distal Late region called Corpuscle of Stannius. Corpuscle of Stannius is responsible for maintenance of calcium-phosphate homeostasis. The tubules are connected to pronephric ducts, which fuse together by Bone Morphogenetic (BMP4) signalling and follow organised cell apoptosis and arrangement to form the common exit portal cloaca at posterior end (Drummond and Davidson, 2016; Pyati et al., 2006). Completion of PD formation at 24 hpf is marked by mesenchymal to epithelial transformation of IM. At 3 dpf, zebrafish nephron formation is complete with a clear connection between the Bowman's space and lumen of PNT (Fig. 2). At 4 dpf, mature podocyte foot processes and endothelial cell fenestrations provide size selectivity and refined filtration in the glomerular unit. All living systems evolve as per environmental requirements; as a water-borne creature, zebrafish does not require water conservation, therefore unlike humans they lack a collecting duct system. However, the architecture of its paired pronephron system is conserved in the vertebrate and hence serves as an excellent model for pathological studies (Drummond and Davidson, 2016; Wingert and Davidson, 2008). Most cystic nephropathies in zebrafish, just like humans are caused by mutations in commonly present ciliary components. At variance to humans, zebrafish tubular epithelial cells have motile cilia and their beating motion plays a crucial role in regulating kidney fluid drift and proper functioning (Lunt et al., 2009). Zebrafish expresses human cystic nephropathy orthologous genes i.e PKD1a/b and PKD2. Mutations in these genes lead to renal cysts, left/right asymmetry defects, strong dorsal axis curvature and hydrocephalus, similar to ADPKD and ARPKD in humans (Le Corre et al., 2014; Mangos et al., 2010). Other ciliopathic genes associated with renal cysts in zebrafish include *AH1*, *ARL13B*, *CC2D2A*, *Cdc42*, *CEP41*, *CSPP1*, *C8ORF37*, *ift221*, *ift80*, *ift81*, *ift172*, *INPP5e*, *KIAA0556*, *RP2*, *RPGRIP1*, *SDCCAG8* and *TMEM67*. A list of such genes is provided in the (Tab. 2) (Shi et al., 2017; Tobin and Beales, 2008). Ap-

proximately 70 genes known to associate with Nephronophthisis in humans have an ortholog in zebrafish and several renal ciliopathy models of zebrafish exist.

Tab. 2: Ciliopathy models of zebrafish

Phenotype	Affected gene	Disease
Cystic kidneys	<i>ift221</i>	RP (Retinitis Pigmentosa)
	<i>ift172</i>	JATD (Jeune asphyxiating thoracic dystrophy) , MSDS (Mainzer saldino syndrome) , BBS (Bardet Biedel syndrome), NPHP (Nephronophthisis)
	<i>ift81</i>	Retinal dystrophies
	<i>ift80</i>	JATD, MSDS, MKS
	<i>nphp2,3,5,6</i>	NPHP
	AH1	JBTS (Joubert syndrome)
	ARL13B	JBTS
	<i>mks1,3</i>	MKS (Meckel-Gruber syndrome)
	BBS4,5,6,8	PKD, BBS, NPHP, MKS
	CC2D2A	MKS
	Cdc42	PKD
	CEP41	JBTS
	CSPP1	JBTS
	C8ORF37	JBTS
	Exoc5	PKD
	INPP5e	JBTS
	KIAA0556	JBTS
	POC1B	JBTS, PKD, LCA (Leber's congenital amaurosis)
	RP2	Renal-retinal ciliopathies
	RPGRIP1	NPHP, RP
SDCCAG8	NPHP	
TMEM67	MKS	
Fibrocystic kidney disease	ARMC9	JBTS
Polydactylyrenal malformations	ARL6	JBTS
Renal malformations	CEP290	JBTS, LCA
Pronephric duct malformations	NBCe1	Glaucoma and cataract
Cloacal cysts and other renal malformations	PDE6D	JBTS
Pronephric tubule and duct dilation	TTC26	Renal-retinal ciliopathies

1.2.1 Cystic Nephropathy and *ift172* in Zebrafish

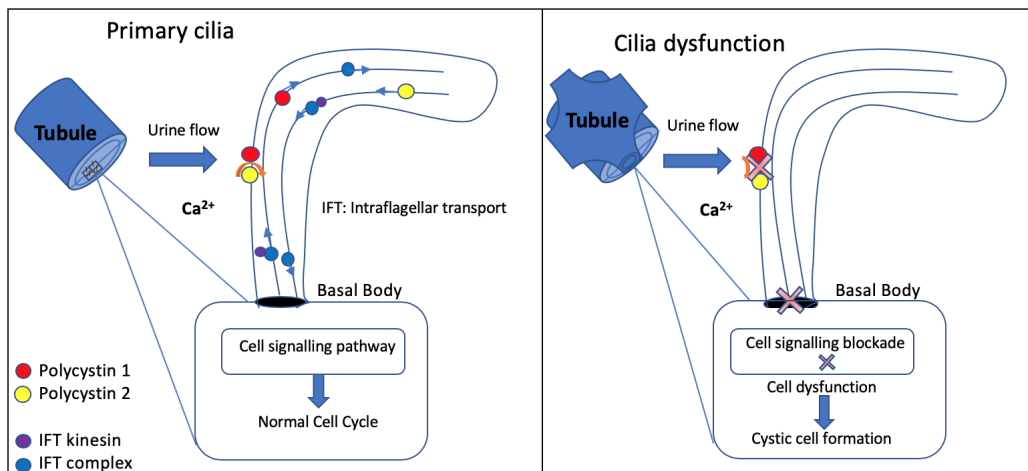


Fig. 3: **Illustration showing the normal and malformed cilia functioning.** The first panel displays the normal cilia mechano-sensing proper fluid flow and subsequently regulating ion-channels, while the latter shows disrupted ciliary behaviour leading to fluid filled cyst creation.

Analogous to human *ifts*, zebrafish *ift* proteins localise to the cilium, basal body and/or centrosome and are functional in development and maintenance of motile and sensory cilia (Fig. 3) (Halbritter et al., 2013; Sun et al., 2004). Similar to the array of symptoms displayed by mutations in human *ift80*, zebrafish *ift80* knockdown also results in strong body curvature, large cysts in pronephroi and pericardial edema. Located in the axoneme and pericentriolar regions of the cilia, 14 biallelic mutations in *ift172* were described in humans (Halbritter et al., 2013). These mutations are associated with Jeune and Mainzer Saldino syndromes and Bardet Biedel syndrome comprising of Nephronophtisis, skeletal, liver and eye malformations (Halbritter et al., 2013; Su et al., 2014). Both *ift172* and *ift57* are known to play a critical role in planar cell polarity (PCP) and are also associated with renal cyst generation. *ift* component prickle1 is a common marker for the functionality of both *ift172* and *ift57*. The marker's identification led to the understanding of PCP-signalling-based establishment of polarity among epithelial cell sheets. Alteration of this pathway could be the underlying mechanism of cystogenesis in organisms with mutated *ift172* (Cao et al., 2010). Faulty *ift172* gene leads to loss of ciliary integrity, beating and signalling in the pronephroi, leading to paired glomerular cyst formation (Graf et al., 2011). Zebrafish mutants and morphants for *ift172* recapitulate all these phenotypes including renal cysts (Fig. 4) (Cachat et al., 2011; Halbritter et al., 2013; Kenneth et al., 1997; Patton and Zon, 2001; Zhou et al., 2013).

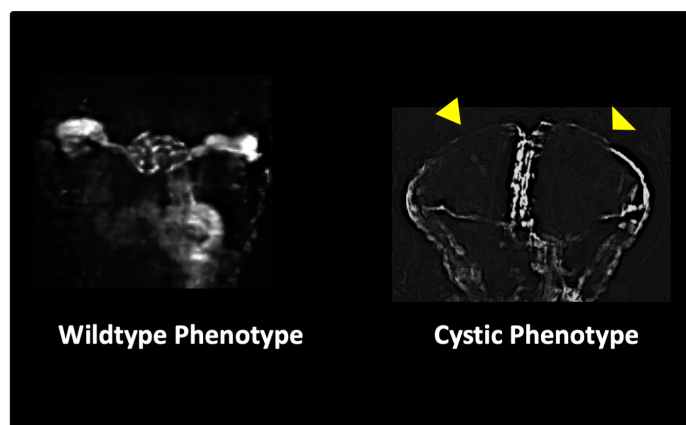


Fig. 4: **Zebrafish pronephroi.** Images of transgenic *Tg(wt1b::EGFP)* zebrafish pronephroi at 72 hpf for both wild-type and cystic pronephroi. Cystic pronephroi were created by injection of *ift172*-MO.

1.3 High-Content Screening and Drug Discovery

Large scale *in vivo* screening studies usually employ automated microscope-based technology which enables studies of living materials, ranging from single-cell activity to whole organism, exposed to chemicals or modifiers of gene expression in microtitre format. Large scale screens can be classified into subtypes such as: High-Content Analysis (HCA), High-Content Imaging (HCI), Image Cytometry (IC), High-Throughput Screening (HTS) and High-Content Screening (HCS). HCA, HCI, IC and HCS all refer to lower frequency chemical testing, whereas HTS and HCS allow more than 100,000 test compounds. HCS complements HTS by addition of multi-parametric quantification of images with improved signal to background ratio. Along with multiplexed feature analysis, HCS provides both targeted and phenotype-based analysis, which makes inter and intra-cell or organismal study possible. HCS can extract all the contained spatial and temporal information and, simultaneously allows single or a specific subset of the cell population to be studied in a heterogenous system (Giuliano et al., 2003). In cases where single sample study tends to be statistically ineffective, HCS, with its multiple feature assessment adds to the predictive power of the assay. The advent of bioinformatics and biocomputing laid the foundation of HCS encompassing pioneer studies such as, BDS chromosome painting, Oncor Videometric150 and the Meridian ACIS Ca^{2+} image tracker (Buchser et al., 2012). Among multiple applications of HCS, the most powerful is its ability to test the efficacy of chemical compounds in relevant systems such as, monolayer cell cultures, 3-D cultures, organoid systems or whole organisms (Buchser et al., 2012).

High-Content Screening is often used for drug target identification by either knocking down or

increasing RNA expression or overexpressing protein or RNAi mediated protein reduction. This screening approach can be broadly classified as forward or reverse genetic screen, depending on the chosen target for analysis. Forward genetic screen identifies genes responsible for causing a particular phenotype, whereas reverse genetic screens investigate the phenotype resulting post gene disruption. Insertional mutagenesis screen is a type of forward genetic screen. In one such screen carried out on zebrafish, 12 genes responsible for PKD were identified. Ten out of these 12 hits were cloned and found to be ciliary in nature (Sun et al., 2004). Another mutagenesis screen using N-ethyl-N-nitrosourea (ENU) led to the identification of 300 mutational loci influential in developmental defects (Geisler et al., 2007). Approaches causing locus specific mutations (such as CRISPR-Cas9 systems) are particularly useful for reverse genetic screens. An example is a study conducted to identify electric synapse formation in zebrafish across 48 loci, which led to the identification of two new genes in the process (Shah et al., 2015). In another *in vivo* glomerular permeability assessment screen, the role of Crb2b, a protein involved in the maintenance of epithelial cell apical-basal polarity was ascertained in facilitating podocyte differentiation generating functional filtration barrier (Ebarasi et al., 2009). High-Content Screening have/can also lead to discovery of novel targets and pathways for the drugs with known mechanism of actions for a phenotype.

In phenotype screens High-Content Screening is used to detect mechanism of action of an orphan compounds with unknown effects (Westwick and Lamerdin, 2011). Apart from the effect of interest, many secondary effects may also be observed. These off-target effects often remain cryptic and a topic of much discussion while conducting drug studies. Approaches to tackle these problems in HCS include assays of *in vitro* micronuclei formation, toxicity studies on whole embryos/organisms, where unrelated effects that might lead to *in vivo* DNA damage and mortality are assessed (Shi et al., 2010; Sipes et al., 2011; Truong et al., 2016; Westhoff et al., 2013). Other than that, HCS offers platforms to study cellular activities lacking a particular end-point, for instance, localisation and trafficking of proteins or vesicles, cell morphology alterations comprising neurite growth, gap-junction formation, cell differentiation (epithelial cells to mesenchymal, astrocytes and neurons, precursor cells into oligodendrocytes etc), cell movement tracking in case of wound healing, chemotaxis and migration along with cytotoxicity. Additionally, lead molecule identification HCS are used in screening of clinical/preclinical blood sample analysis for biomarker activity, ceramic formation/structure, corrosion resistance or crystallisation conditions (Buchser et al., 2012; Wickstrom et al., 2007).

In the field of **kidney studies**, High-Content Screening has been used in 3-D cyst cultures of

cystic nephropathies mimicking *in vivo* environment, where drug exposure has led to identification of key pathways such as, aurora kinase, CDK, Chk, IGF-1R, Syk, and mTOR involved in cyst swelling in Pkd1/2 PKD (Booij et al., 2017). In another *in vitro* screen, 8 out of 344 member library of Traditional Chinese Medicine compounds were found effective against renal fibrosis (Wang et al., 2018). A novel podocyte screening technology for proteinuric kidney disease detected 24 hits from a set of >2100 diverse chemicals. The secondary validation of the hits have led to the isolation of a β 1-integrin agonist, pyrintegrin, which reduces podocyte effacement (Lee et al., 2015; Reiser et al., 2017).

In summary, High-Content Screening provides the ability to assay microscopically observed phenomena at a large scale, be it *in vivo* toxicity, *in vivo* activity, effects of compounds and biological molecules (for example: plasmids carrying cDNAs, or RNAs in cell populations, sub-populations or specific subset of heterogenous culture) or tracking cellular intracellular, or intercellular movements. Microscopy forms the backbone of all High-Content Screening experiments. In principle, **High-Content Screening microscopes** can be divided into three major sectors i.e wide-field imaging, confocal imaging and laser scanning (Buchser et al., 2012). **Wide-field microscopy** is one of the most widely used HCS methodology, executed in this project on ACQUIFER High-Content Imaging Machine-IM04. It is a modified version of inverted research microscopes combined with imaging algorithms incorporating features such as, ROI capture, fast acquisition rates, high sensitivity and comparatively low sample bleaching. Wide-field microscopy, with its distinct proficiency in quick data acquisition along with specimen protection from photobleaching fulfils the two key-points of HCS, therefore making it a popular choice.

By contrast, confocal setups with a pinhole improve the resolution depth to a great extent, but at the same time increment the acquisition times and cost of the setup. Moreover, these setups work best when scanning single point in the system at a given time, hence demanding for the sample movement. Confocal setups are normally preferred in studies capturing small cells, intracellular structures, complex 3-D structures and samples with strong background fluorescence (Buchser et al., 2012).

The third sector of High-Content Screening relies on **Laser Scanning Cytometers**. These are flatbed scanner like devices, which use laser beams to scan the entire surface of the plate and detect fluorescence with PMTs. The produced image quality is equivalent to a 20x objective and considered good for medium content, high-throughput technology. With their ability to detect fluorescence signals way above threshold, they are implemented in assays requiring as-

assessment of nuclear translocation of proteins, cell detection utilising their DNA content and colonies (Buchser et al., 2012).

The optimal imaging technique and instrument to be used in a particular High-Content Screening depends on factors such as, the required imaging speed, the number of compounds to be screened and the complexity of the parameters to be analysed. The design of the chosen equipment should correspond to these basic questions. Based on which, the microscope components such as, light source (light, laser or light emitting diode); objective type (wet or dry), magnification of the objective, Numerical Aperture (NA) of the objective, detector type (digital camera or photomultiplier tube); autofocus (laser-based system detecting bottom of the plate or image-analysis-based system which enters through specimen to detect the optimal focus); environmental controls (temperature, humidity and CO₂ levels); liquid handling option (drug exposure, media renewal etc) and last but not the least image and data analysis software are incorporated.

1.4 Zebrafish as a Model for Drug Discovery

Average life-span of drug development is about 10-15 years. During this period of preclinical trials a gigantic number of compounds are discarded as they fail to meet the standard requisites of being classified as druggable agents (Huiting et al., 2015). Therefore, it is of utmost importance to speed up the process at this stage by testing huge number of compounds in reproducible, less cumbersome and whole-organism format, rather than in complex and small sample sizes of murine models. In 1981, George Streisinger's pioneering work on generating homozygous diploid clones of zebrafish brought several interesting features of this animal model to light, leading to its present day prominence in the field of drug discovery (Streisinger et al., 1981). This cyprinoid teleost, while maintaining rearing efficacy of lower animal models has an elaborate organ system constitution inclusive of cardiovascular, renal, nervous, immune and reproductive systems making studies done on it closely comparable to mammals (Briggs, 2002; Huiting et al., 2015). They also have a rather cost-effective husbandry requisites compared to contemporary animal models like rats, mouse, rabbits, primates etc. The optical transparency of zebrafish allows it to be used as *in vivo* model for compound studies, shedding light on criteria inclusive of tissue specific toxicity and bioavailability, which remain elusive in *in vitro* systems. Additionally, the straightforward uptake of aqueous compound solutions by zebrafish larvae add to its suitability for drug studies (Huiting et al., 2015). Prolific egg production rate

(100–300 eggs per clutch) coupled with its small size favour the possibility to have statistically significant sample size for testing compounds in 96–384 well microtitre format (Murphey et al., 2006). Moreover, zebrafish have more than 70% genetic conservation with humans, ex-utero body development and easily tractable genetic and phenotypic transformations; making it a reliable model for whole organism screening (Briggs, 2002; Huiting et al., 2015). Coalesced with all these properties, zebrafish can cost-effectively bridge the gap between high-throughput experimentation in cellular models deficient of physiological context and low-throughput rodent models, that are closer to human biology (Gehrig et al., 2018; MacRae and Peterson, 2003; Rennekamp and Peterson, 2015; Veldman and Lin, 2008). *In vivo* phenotypic screens on zebrafish larvae/embryos provide a significant advantage over *in vitro* assays as they have the scope for unbiased identification of druggable compounds. Due to recent advancements in genetic manipulation technologies, various zebrafish transgenic lines have been generated (www.zfin.org, www.ezrc.kit.edu, www.zebrafish.org) (Geisler et al., 2016). These transiently labelled lines with edited genome provide a rich arsenal to model and visualise elemental disease and developmental machinations. Zebrafish's 84% homology in disease causing genes with humans helps in faster translation of readouts from zebrafish-based screens (Kalueff et al., 2014). The success of zebrafish in mimicking human diseases phenotypically and genetically has led to establishment of several genetic disease models. Major fields with existing disease models include renal diseases, wound healing, behavioural, host-microbe interactions, gastrointestinal and cardiovascular diseases (Cirio et al., 2015; Drummond et al., 1998; Kalueff et al., 2014; McCampbell and Wingert, 2012; McKee and Wingert, 2015; Stainier et al., 1996). All these already established models and tools such as, Clustered Regularly Interspaced Short Palindromic Repeats (CRISPR-Cas9) system, Targeting Induced Local Lesions in Genomes (TILING), Zinc Finger Nucleases (ZFN) and Transcription activator-like effector nuclease (TALEN). facilitate and accelerate High-Content Screening in zebrafish to a great extent. Aspects including survival rates, overall morphology, physiological parameters, cell-and tissue specific phenotypes, reporter gene expression patterns and behavioural phenotypes can be easily studied (Cachat et al., 2011; Creton, 2009; Kokel et al., 2010; Mathew et al., 2007). Additionally, they also provide biodistribution, metabolism and pharmacokinetic information (MacRae and Peterson, 2003; Rennekamp and Peterson, 2015). Complemented with automated microscopy, zebrafish serves as an excellent candidate for large scale phenotypic whole organism screening assays. As the detailed discussion of all the models is out of scope for this thesis, I briefly touched upon some kidney models in the next section.

1.4.1 Transgenic Kidney Models of Zebrafish

More than 150 genes have been identified to date that lead to kidney development malformations or specific glomerular and tubular diseases in humans (Devuyst et al., 2014; Eckardt et al., 2013). In zebrafish, disruption in podocyte function, transporters and ion channels as well as primary cilia lead to flawed pronephric kidneys that can replicate human diseases (Drummond, 2005; Drummond et al., 1998). Resultantly, lines labelling pronephric structures, for instance, podocytes, or the glomerular, tubular and ductal system, are widely available to date (Ashraf et al., 2013; Drummond, 2003; Ebarasi et al., 2009; Fukuyo et al., 2014; Gbadegesin et al., 2008; Gee et al., 2013, 2015; Halbritter et al., 2013; Hinkes et al., 2006; Kramer-Zucker et al., 2005; Lee et al., 2015; Miyake et al., 2015; Niaudet and Gubler, 2006; Perner et al., 2007; Reiser et al., 2017; Schmidts et al., 2015; Su et al., 2014). Other than that transgenic zebrafish expressing GFP (green fluorescent protein)-tagged vitamin D-binding protein (VDBP), which acts as a tracer for proteinuria, serves as an important model for functional assessment of glomerular filtration and barrier integrity (Kotb et al., 2014; Rider et al., 2012). It can be achieved by microinjection of fluorescently labeled inulin or dextrans into the vascular system followed by monitoring of the reporter activity (Hanke et al., 2015; Kotb et al., 2014; Zhou and Hildebrandt, 2012). Genetic alteration toolkit enables zebrafish to mimic cystic nephropathies and larval optical transparency allows for *in vivo* fluorescence microscopy of the defective pronephroi. However, to our knowledge, large-scale screening experiments other than the one presented here assessing fluorescent pronephric phenotypes in models of genetic kidney diseases have not yet been executed.

1.4.2 Screening Technologies in Zebrafish

Zebrafish with its docile nature permitting low husbandry costs, high fecundity, *ex utero* development and imaging compatible small body form aids in large scale screen conduction. As previously mentioned, screens in zebrafish can be broadly divided into two main categories i.e genetic and chemical. Genetic screening in turn have two subtypes depending on the target of the study. If the screen involves phenotype to genotype approach, which begins by establishing and characterising a standard phenotype and is followed by comprehending its genetic cause is classified as forward genetic screen. On the other hand, if the genotype to phenotype approach is favoured, the technique is grouped in reverse genetics section. This type of screen involves selection of a gene and mutating it with one of the several known molecular techniques.

The chemical screens involve the use of small molecule chemical libraries. This screening technique has led to boosts in the genetic screens with complementary points, such as, use of known pathways of compounds to pin down the underlying mechanisms of interest, possibility of compound titration, compound contact and removal at any point during the development making way for studying dormant gene effect, if any. Similar to genetic screens, chemical screens could also be conducted in both forward and reverse pattern. In the forward approach, the chemical libraries are studied on a known phenotype to reveal the associated genetic target. These screens are helpful in understanding the developmental, behavioural issues along with devising better treatment for diseases. The reverse chemical screen, on the other hand, involves studying the libraries on a genetic target without known specific phenotypic effects. This type of screen is useful in identifying latent functionality of compounds thus, elucidating their effect in treating diseases other than their known scope, toxicity tests and finding new bioactive molecules. In the year 2000, the first chemical screen was conducted by (Peterson et al., 2000) utilising 1,100 compounds from the DIVERSet E Library (Chembridge). The screen was effective in studying developmental effects on 72 hpf zebrafish larvae in 96-well microtitre plate format. It revealed several molecules effectively regulating central nervous system, cardiovascular system, neural crest, ear, melanocyte and otolith development. Small molecule chemical screening being the main subject matter of the thesis will be elaborated upon in the upcoming sections.

1.4.3 Rescuing Disease Phenotypes with Chemical Screening

Several mutational genes have been identified in zebrafish over past decades facilitating conduction of chemical screens. Chemical screens directed towards different organ systems and pathways have been conducted in zebrafish till date. Few compounds from such screens have made it to the clinical trials and some have even made it to the bedside. An example of such a compound is PGE2 (Prostaglandin E2). Haematopoietic stem cells (HSC) formation is essential for maintenance of tissue perfusion, immunity and perennial haematopoietic homeostasis. HSC transplantation is used for treatment of several haematological aberrations like, leukaemia, lymphoma and bone marrow failure. The current HSCs availability accounts for 10% of the total demands, hence an increase in their number could directly help the treatment process (Goessling et al., 2011). (North et al., 2007) identified PGE2 (Prostaglandin E2) as a result of screening three chemical libraries: NINDS Custom Collection (1,040 compounds), SpecPlus Collection (960) and BIOMOL ICCB Known Bioactives (480) for molecules that might help

in increasing Haematopoietic stem cell count. Successful in treating lymphoma and leukaemic patients, PGE2 has now entered Clinical Trial Phase II under the name ProHema (Fate Therapeutics) (Hagedorn et al., 2014; Rennekamp and Peterson, 2015).

Another instance of disease phenotype rescue on large scale is provided by (Peterson et al., 2004), where they treated gridlock mutant embryos of zebrafish with over 5000 small molecules from the DIVERSet E library (Chembridge) till 48 hpf to identify chemical suppressors of aortic coarctation. They found two structurally related compounds that suppressed the gridlock phenotype. This screen led to identification of a novel pathway rescuing the phenotype via up-regulation of vascular endothelial growth factor (VEGF), which was followed by the escalation in blood vessel development. The discovered pathway can be used in designing new treatment plans.

One of the several unaddressed medical issues include the proper functioning of retinal vasculature network and appropriate neovascularisation for proper vision in humans. Malformations associated with the process can lead to severe forms of blindness and retinal diseases. Comprehending the retinal vasculature is much needed to alleviate retinal diseases. *fli1:egfp* transgenic line of zebrafish, expressing bright GFP in the entire vasculature under the influence of *fli* promoter allows for a detailed retinal vascular network studies (Alvarez et al., 2007). Out of 2000 screened chemicals from the bioactive Spectrum library on *fli1*-GFP embryos at 60 hpf, five displayed effects on retinal vessel morphology. Out of them, one affected both vessel diameter and number, two affected the vessel diameter but not the vessel number and two were extremely toxic causing 80% vessel damage (Alvarez et al., 2009). This study was followed by screening of known angiogenesis regulators, and an inhibitor of PI3 kinase signalling - LY294002 was found. LY294002 exposure within certain developmental time-windows inhibited intra-ocular angiogenesis without additional system effects or altering visual function (Alvarez et al., 2009). The study provides a concrete framework for identifying chemicals, which can improve sight in people around the world.

In another screen conducted by (Peterson et al., 2000), 4-(4-morpholinobutylthio)phenol (MoTP) was found effective in rapid degradation of melanocytes in zebrafish. Building up on these results, small molecule screen conducted by (Hultman et al., 2009) identified ICI-118,551, a chemical that blocks melanocyte regeneration post MoTP exposure, without any effect on ontogenetic melanocyte development. Gaining hold of chemicals controlling zebrafish melanocytes will serve as an important tool to understand mammalian melanoma progression. Among other disease related findings, a toxicity screen revealed herbicide butafenacil to cause anaemia by

completely eliminating haemoglobin in transgenic *fli1:egfp* model (Leet et al., 2014). High-Content Screening on embryonic stem cells has led to the identification of indolactam V's role in differentiation of pancreatic cells and neuropathiazol's role in neural differentiation (Chen et al., 1988); (Chen et al., 2009); (Warashina et al., 2006).

Zebrafish has also served as a model for isolation and discovery of several cell-cycle regulators. In this field, crash and burn mutant (*crb*) model of zebrafish for *bmyb* gene was used. The gene is a MYB family transcription factor involved in unregulated cell-cycle progression causing cancer, with zebrafish heterozygous mutants for *crb* having higher rates of carcinogen-induced cancer (Ebarasi et al., 2009; Stern et al., 2005). Using this transgenic line, a DIVERSet E library (Chembridge) of 16,320 potential rescuing agents of *crb* phospho-histone H3 mitotic aberration persynthamide was identified (Murphey et al., 2006; Stern et al., 2005). Persynthamide temporarily delays S-phase via an ATR dependent checkpoint with a simultaneous increase in cyclin B1 expression leading to alleviation in the *crb* mutant. Here, by targeting an alternative pathway a genetic phenotype was rescued by phenotype-based chemical screening. Six out of 14 identified hits from this study were also effective on mammalian cell lines, therefore, confirming the conservation of some pathways across species.

Among signalling pathways, instances of unregulated FGF-MAPK pathway leading to several diseases such as, Parkinson's diseases, chronic obstructive pulmonary disease risk and kidney agenesis are documented. Phosphatases are the main limiting agents of signalling in this pathway, specifically the dual-specificity phosphatase (*dusp*) 6, which dephosphorylates the extracellular signal-related kinase (ERK). The transgenic line with visible *dusp6* expression as a biosensor for FGF signalling was used in a screen to identify compounds, that increases FGF signalling. BCI was one of the agents resulting from the screen, which caused an uprise in *dusp6*-GFP expression, and is in turn dependent on FGF8 signalling. BCI was also found effective in human cells, once again supporting conservation between the human and zebrafish MAPK pathway (Molina et al., 2009). In addition to that, in a separate automated High-Content Screening, 8-hydroxyquinoline sulphate and pyrithione zinc were identified as hyperactivating compounds for FGF signalling (Saydmohammed et al., 2011). Thus, showing the utility of the model in exploring cell-cycle modifiers one more time.

Behavioural screens are integral for identification of neuroactive molecules that can assist in treating bipolar disorder, schizophrenia and chronic sleep disorders. Using a tracking device, zebrafish were behaviourally profiled after exposure to 56,000 compounds by (Rihel et al., 2010). These profiles led to identification and better characterisation of different drugs involved

in perturbing rest/wake cycles, which could be used for human arousal and sedation drug formulations. In this field, Peterson and colleagues have also discovered a novel phenotype called photomotor response (PMR) in zebrafish, when exposed to light stimulus (Kokel et al., 2010). As referred earlier, several ciliary mutations causing cystic nephropathies in zebrafish analogous to humans have already been identified (Booij et al., 2017; Lee et al., 2015; Reiser et al., 2017; Wang et al., 2018). However, other than handful of renal screens and recently released drug Tolvaptan with limited efficacy, cystic nephropathies still demands for a reliable cure (Torres et al., 2017). Few screens conducted in this discipline by (Booij et al., 2017; Cao et al., 2009; de Groh et al., 2010; Sun et al., 2004) include the attempts to screen for chemical modifiers, which affect the presence of renal cysts morphological parameters such as, body axis curvature and/or laterality defects in *pkd2/hi4166* and *ift172/hi2211* mutants with custom libraries. In one such screen conducted by (Cao et al., 2009), Histone Deacetylase Inhibitors (HDACs) TSA and VPA were found to effectively suppress these phenotypes. In addition to that, a 2,000 compound screen identified HDACs to be embryonic renal progenitor cells multiplier, which is required for regeneration after acute kidney injury (de Groh et al., 2010). Dealing with the burden of present need for new drugs and the large amounts of information provided by treating a few zebrafish larvae with thousands of compounds support the potential of high-throughput screening in zebrafish in unraveling new leads and pathways for complex behaviours and diseases.

1.5 Technical Challenges in High-Content Screening

Although, the raised number of FDA approved drugs (31/year) in present decade mark the improvement in screening efficacy, but bottlenecks of varying degrees still persist within the modules of High-Content Screening (US Food and Drug Administration). Serving as the first step in finding druggable compounds, HCS comes bundled with variety of challenges, which are multiplied severalfold on combining it with *in vivo* studies. Broadly, HCS can be divided into three major steps i.e. sample preparation, image acquisition and quantification, where each step presents its own set of challenges. Regularly encountered problems when executing these steps include animal model selection and their handling, implementation of high-throughput imaging techniques, ascertaining region of interest (ROI) acquisition, high-resolution ROI capture, resulting data management, quantification and analysis (Fig. 5). Despite the rapid progress and improvements in HCS, several issues still remain unresolved and demand further investigation.

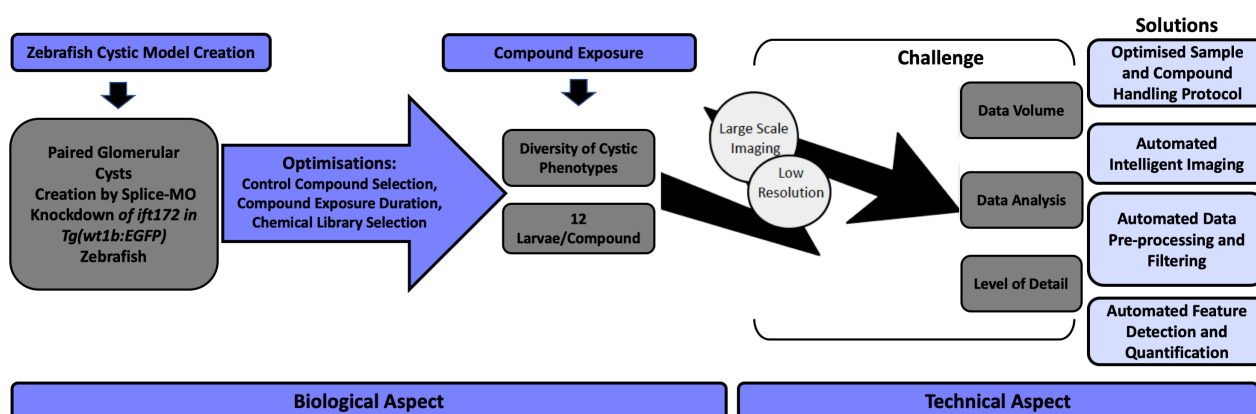


Fig. 5: **Biological and technical aspects of High-Content Screening.** Representation of modules involved in this HCS project for identifying phenotypic modifiers of cystic nephropathies in human disease mimicking zebrafish animal model. The whole workflow was grouped under two main categories i.e. 'Biological Aspect' and 'Technical Aspect' and the main technical challenges included the presence of large sample sizes and volumes of poor quality data accumulation for manual analysis. The flow further elaborates upon the steps such as, optimised sample and compound handling, automated imaging and data quantification are implemented here to upgrade the efficiency of the process by addressing the bottleneck issues.

Irrespective of the targeted objective, all High-Content Screenings begin with the generation of animal model replicating disease of interest. Although, the recent success in genetic manipulation tools has made manipulations at genetic level relatively easier. In a recent study, CRISPR/CAS9 has been used as alternative in an HCS for generating mutants for 162 varied target loci using sgRNA. Phenotypes were scrutinised by inbreeding injected founder fish, evaluations of insertions/deletions were done by multiplexed next-generation sequencing and fluorescence PCR (Varshney et al., 2015). Although, quite successful in the stated instance, the technique demands several improvements, for example, in cases of unknown phenotype, off-target artefacts could lead to jumbled results without any possibility to check for phenotype/genotype correlation by genetic linkage. Among other approaches for model generation, chemical mutations exists as a popular method (Haffter et al., 1996; Solnica-Krezel et al., 1994). The mutations in these case are induced by incubation of adults in the chemical solutions. However, the accuracy of chemical delivery in these cases must be ensured for reproducible results. In this area, Hewlett-Packard D300 Digital Dispenser facilitates automated delivery of chemicals up to 10-12 significance level. However, proper care should be taken by sealing the plates once larvae are incubated at 28°C after chemical exposure to avoid prevention of evaporation (Truong et al., 2016). Morpholino-based knockdown of the gene of interest offers another feasible alternative for disease modelling on a large scale. However, due to the presence of off-target effects by

Morpholino (MO) knockdown, its highly recommended to cross validate the observed phenotypes of the morphant with its mutant model (Stainier et al., 2017). MO injection rates can be escalated by using robotic injectors utilising 3-D datum position. The method can be successfully implemented for morpholino injections leading to gene knockdown, DNA for transgenesis induction, cancer cells for tumorigenesis and microbes for infection studies with an overall accuracy of 2,000 embryos/hour (Spaink et al., 2013).

In this project, I used morpholino knockdown approach for zebrafish cystic nephropathy model generation. In spite of the above mentioned methods, the process of model creation at a large scale remains a fundamental issue for High-Content Screening and further upgradations in the genetic manipulation field might improve it. Disease model generation is ensued by the proper orientation of sample for correct phenotype observation and faster image acquisition. For this purpose, zebrafish larvae in HCS are normally added to microtiter plates. Several formats ranging from 96–384 well plates have been used till date (Rennekamp and Peterson, 2015). However, in contrast to cellular models, zebrafish larvae are 3-D objects with complex morphology, which often leads to their chaotic orientation in microtiter plates. Therefore, new automation techniques are required to upscale the classical zebrafish mounting process. Recent advances in the field has led to the development of capillary-based orientation of larvae along all three axes for cell-specific imaging. In this system, larvae are pre-screened for the presence of debris and transferred to a capillary tube. Here, they are oriented and redirected for microsurgery and imaging; after which, they are finally discharged from the system (Early et al., 2018; Jarque et al., 2018). These microfluidic systems although fulfil the requirement, but have rather complicated setups and are often unable to document developmental and disease-associated changes seen in time-lapse experiments. In our work, I use orientation tools allowing the generation of agarose cavities within wells of microtiter plates for consistent positioning and orientation of zebrafish embryos (Westhoff et al., 2013; Wittbrodt et al., 2014). The cavities were created using moulds which were modelled out of polylactic acid filament using OpenSCAD designing software and 3-D printed on MakerBot Replicator 2 and Ultimaker 2 (Wittbrodt et al., 2014). This enables the automated acquisition of consistent views of 2-4 dpf zebrafish larvae in large scale screening scenarios. Henceforth, providing a great leap in improving the *in vivo* imaging of the larvae by quicker and more accurate orientation.

Once the sample preparation has been overcome, the limiting step in all High-Content Screenings becomes the accurate execution of image acquisition. Available screening methodologies being usually optimised for cellular assays make it difficult to perform large-scale imaging and

phenotypic scoring. Nowadays, most zebrafish screens use low magnification to capture the entire zebrafish embryo, which is subsequently analysed for phenotypic changes. Such an approach remarkably diminishes the underlying potential of utilising a live organism for *in vivo* visualisation of morphological, physiological or genetic events at tissue-specific or cell level. The unpopularity of high-resolution acquisition in High-Content Screening is mostly because it reduces the scan field significantly, making it utterly complex to accurately document the region of interest (ROI) in high-resolution. To confirm the ROI acquisition a compromise is made by increasing the field of view and thereby, decreasing the resolution of images (Peravali et al., 2011). Moreover, acquisition complexity multiplies due to the variable spatiotemporal location of ROIs within the larvae body. This lack of ROI-based automated imaging and quantification methods, data acquisition and archiving create a major bottleneck in HCS experiments. Few advances in this direction have been made, which allow the objective lenses of microscopes to focus on ROI. For instance, in the method proposed by (Peravali et al., 2011), the resolution of images was improved notably by two-step automated imaging approach. This involved an initial pre-screening of the entire microtiter plate at low resolution to find the ROI using customised algorithms. The identified co-ordinates from the initial pre-screen were used to acquire high-resolution images of the ROI in second step. Such an approach leads to documentation of only the required region at high-resolution; thus, saving space, improving accuracy and speed. While several methods are being used at the moment, but their applications are usually restricted to cell-based experiments and often demand expert knowledge in image processing, programming and hard- and software- interfacing. Therefore, its essential to simplify such toolsets in order to allow unhindered usage of these workflows by biomedical researchers.

In this study, I use robotic microscopy platform (www.acquifer.de) with a smart imaging interface built on inverted wide-field microscope that allows feedback imaging. Feedback imaging is a type of imaging technique which lets the image processing software send back human-readable script commands to the imaging device, which in turn determines the set ROI. I implemented this technique to acquire high-resolution cystic kidney datasets. Images acquired were automatically deblurred for spatial resolution improvement, maximum projected and cropped to include ROI before being scored for phenotype altering compounds. Henceforth, presenting an automated approach to overcome acquisition bottleneck with smart imaging.

Following the required image acquisition, High-Content Screening experiments generate large amounts of data over time, whose manual analysis makes it a rather slow and labor intensive task. In addition to that, zebrafish provides for several types of screening assays, which

generate complex phenotypic read-outs. Image-based datasets can be used to extract multiple potential quantitative descriptors including fluorescence intensity, tissue dynamics, morphological descriptors or dynamic parameters and ranges from simple whole embryo signal intensity to spatiotemporal activity of fluorescent reporters and beyond (Mikut et al., 2013). Automation in this module could amplify the scoring to a higher level. For instance, advanced segmentation techniques were used in the *Tg(Cdh17:EGFP)* zebrafish line to detect the fluorescent labelled tubular cells of the zebrafish kidney (Sanker et al., 2013). Other than that, fluorescence-based approaches assist in fast quantification along with visual corroboration up to certain extent. Fluorescent-plate-reader-based method called Automated Reporter Quantification in vivo (AR-Qiv), allows genetic and chemical observations in HTS format (Walker et al., 2012). In another experiment, Molecular Devices ImageXpress Ultra laser scanning confocal HCS reader was used to automate image acquisition in 96-well plate format. FGF (Fibroblast Growth Factor) dependent GFP expressing zebrafish line *Tg(dusp6:d2EGFP)* was used in this experiment. The analysis was done by automated imaging Cognition Network Technology-based algorithm to automatically identify GFP regions and quantify the effect of small molecules on FGF expression (Vogt et al., 2010). Fluorescence has also been used as an indicator to identify compounds that either suppressed neuronal stress or activated heat shock response in ZNStress assay performed on *sod1* mutant model of zebrafish for neurodegenerative disorder Amyotrophic Lateral Sclerosis (ALS) (McGown et al., 2016). The assay was quite strategically performed, however, it does not keep the fish alive for downstream experimentation. In an appetite-enhancer-suppressor-based HTS, quick quantification based on fluorescently labelled paramecia *in vivo* on exposure to appetite influencing drugs was done with the help of fluorescent microplate reader. Supplemented with analysis of *bdnf* (brain derived neurotrophic factor) pattern, the study demonstrated HTS approach for scoring compounds affecting hyperphagia and anorexia (Shimada et al., 2012). Automated quantification of data with supervised and unsupervised algorithms provide for another more advanced alternative scoring strategy. Such a machine learning approach was implemented in HTS studying light induced locomotor response. An efficiency of 80-95% was attained in isolating response-based differences in behaviour of wild-type and *pde6c* mutant models (Gao et al., 2014). However successful, all these approaches demand for core bioinformatics and computing knowledge, which might not be readily accessible to many scientists in biomedical research and might turn them back to manual analysis. Manual analysis being slow and labor intensive draws us to look for a simplified solution to automate this module and amplify the rate of compound scoring in preclinical analysis.

In this project, I applied Fiji and Python-based scripted modules to automatically score for cystic kidneys. Post-acquisition analysis strategies are integral for the success of screening assays, therefore, proper planning of scoring module should be done at early stages of experimental planning.

To summarise, cystic nephropathies especially ARPKDs, still lack a proper pharmacological modifier that can successfully suppress the disease phenotype and ameliorate the condition. Focussing on the issue, few clinical trials have taken place in the past, however the candidate compound outcome lies far behind the required clinical demands to tackle the disease. On paying close attention to the process of compound selection, it was noticed that a boost in the initial step of testing at non-mammalian level could be of assistance in reducing the overall time spent in the process. This could in turn lead us towards the clinical trials at a faster pace. The non-mammalian High-Content Screening, however comes laced with its own set of problems such as, appropriate animal model selection, proper replication of disease, HCS compatibility of the model, setting of large scale image acquisition parameters and image quantification algorithms. Improvements in these individual steps could accelerate the HCS and the ensuing compound assortment by a large extent. To put this concept in action, I developed and executed an automated HCS with the focus on cystic kidney disease.

2 Objectives

The research project described here pursued the following main objectives: With the long-term aim to find **novel pharmacotherapies for human cystic kidney diseases**,

- 1) a stable **zebrafish model of cystic nephropathy** suitable for high-content phenotype screening should be developed;
- 2) an **automated experimental and analytical pipeline** for high-content screening should be established;
- 3) a large number of known **pharmacological compounds should be screened** for cyst modifying activity.

To serve the first objective, I chose a transgenic zebrafish line with fluorescent nephron structures *Tg(wt1b:EGFP)* and applied morpholino knockdown strategy targeting the integral ciliary component *ift172*, the deficiency of which causes a cystic nephropathy in humans zebrafish model.

To meet the second objective, I established a **workflow** addressing the issues of optimised sample and compound handling and developed an **automated modules for Smart Imaging and image quantification**.

The third objective was met by screening of the **Prestwick compound library with 1,280 FDA/EMA approved compounds** on the automated high-content screening platform and further validation of the primary hits in **dose response studies**.

3 Material and Methods

3.1 Ethics Statement

All zebrafish husbandry and experimental procedures were performed in accordance with the German animal welfare standards (Tierschutzgesetz 11, Abs. 1, Nr. 1, husbandry permit number 35-9185.64/BH Wittbrodt) and European Union animal welfare guidelines. The fish facility was under the supervision of the local representative of the animal welfare agency.

3.2 Fish Husbandry Protocols

3.2.1 Fish Keeping

Tecniplast standalone ZebTec Active Blue aquarium equipped with 50 individual 3.5 l tanks was used for rearing zebrafish. Each tank contained 5-7 pairs of adult zebrafish stocks. The water conditions were: conductivity 400-500 μ S, hardness 5°dH, pH 7.0-7.5 and temperature between 26°C and 28°C. Zebrafish in the facility were kept in controlled day/night cycle of 12 hours light/12 hours dark phase as the breeding behaviour of the fish depends on the photo period. The zebrafish were fed thrice a day and water quality (ammonium, nitrate) was controlled on a monthly basis. Transgenic Wilms' tumor 1b: Enhanced Green Fluorescence Protein [*Tg(wt1b:EGFP)*] fish line with GFP expression in pronephroi was used for the experiments.

3.2.2 Embryo Collection

Tecniplast beach style polycarbonate crossing cages with 1.7 l capacity were used for embryo production from adult zebrafish. The crossing cages contained two types of inlays. One was a sloped mesh, which provided shallow end in the tank as egg laying activity of the fish tends to be higher in the shallow waters. This mesh also separated the eggs from the parents post egg laying, therefore prevented parental egg cannibalism. The other inlay was a removable divider, which allowed separation of the sexes overnight. Zebrafish male-female pairs were transferred in these tanks the evening prior to crossing, with inlayed divider separating the sexes. On the inception of light period next morning, the divider was removed to reunite the sexes. After 5-15 mins after egg laying water from the tanks was drained through a small net to collect the eggs, which were transferred to a petri dish. The eggs were raised for further experimentation at 28°C

in E3 medium.

3.2.3 Raising Embryos

Dechorionated and chorionated zebrafish embryos with or without morpholino injections were raised in E3 media 28°C until 24 hpf. After this, the medium was supplemented with 0.003% 1-phenyl-2-thiourea (PTU, Alfa Aesar, Karlsruhe, Germany) to avoid pigment formation. Enzyme assisted removal of chorion surrounding embryos was carried out using 10 mg/ml Pronase (Sigma-Aldrich, Missouri, USA) around 24 hpf. Embryos were transferred in petri dishes and maximum amount of media was removed. This was followed by addition of 0.5 ml of Pronase stock solution for approximately 15 mins. The embryos were gently swirled and observed under a stereomicroscope until the first embryos started to come out of the chorion. Then, they were transferred to a beaker and washed four times with 1:1 solution of E3 media and system water to remove residual enzyme (Gehrig et al., 2009). In case of older embryos (>24hpf), dechoriation was performed manually using forceps. Afterwards, the embryos were transferred back to petri dishes containing E3 media supplemented with PTU. As the transgenic fish population was heterozygous for pronephric GFP expression, the embryos were sorted under fluorescence microscope at 24 hpf before downstream steps.

3.3 High-Content Drug Screening Protocols

3.3.1 Injection Solution Preparation

Injections solutions were prepared by combining morpholinos (MO) (Gene Tools, LLC, Philomath, USA) with nuclease free water and phenol red (final concentration 0.1 %). Morpholino sequences: *ift172* exon-1 splice: 5'-ACGTCGTC AATATTTTACCTGAGGC-3', Standard Control: 5'-CCTCTTACCTCAGTTACAATTTATA-3'. MO of 50 µM concentration was used. Injection solutions were stored at -20°C – -80°C until needed.

3.3.2 Injection Needle Preparation

Injection needles were pulled utilising horizontal needle puller beforehand. Fire and filament polished borosilicate glass capillaries of 100 mm length; 1 / 0.58 mm OD/ID; were used. Fire polishing allowed for easy loading of the needle on the microinjector and filament polishing allowed smooth flow of injection solution down the needle. Lack of this polishing creates lag in

the solution flow and leads to bubble formation, which in turn obstruct the set flow of solution volume exiting the needle per injection round.

On the micropipette puller (P-97 Flame/Browning Micropipette Puller, Sutter Instruments, Florida, USA), capillaries were loaded horizontally over the heating filament with the following settings: Heat-510, Pull-115, Vel-240, Del-105. On switching the machine, the filament turned red hot and pulled the capillary apart laterally in both directions using the defined settings. Each capillary resulted in two injection needles. On the day of injection, injection solution was pipetted in these needles and loaded on a microinjector.

3.3.3 Morpholino Injections

Previously aliquoted injection solutions were heated at 65°C for 10 mins and spun down for a minute before use. The antisense splice blocking MO oligonucleotide was targeted against the exon1-intron1 boundary of zebrafish *ift172* gene. A standard control oligonucleotide was used as control. MO solutions were pipetted in the previously prepared injection needles and loaded on a microinjector (Eppendorf, FemtoJet, Germany) with the following settings: injection pressure - 100-200 hPa, injection time - 0.1 s, compensation pressure - 10 hPa. The injection pressure was adjusted between the given range in order to get a flow of required 50 nl per injection. Injections were made at single-cell stage in the yolk sac and the injected embryos were transferred to petri dishes containing E3 media. These eggs were raised at 28°C. Phenotype displayed post injection accurately mimicked the previously validated morphology (Fig. 4) (Drummond and Wingert, 2016; Drummond, 2005; Halbritter et al., 2013; Sukumaran and Perkins, 2009; Sun et al., 2004).

3.3.4 Dose Response Optimisation Curve for *ift172* Morpholino

Dose response curve optimisation experiments for *ift172*-MO were done to find the optimal concentration for testing the compound library. Morpholino injections in single-cell staged embryos with 50 µM, 100 µM and 500 µM concentrations were performed to produce a titration curve (Fig. 6).

3.3.5 Time Lapse Study to Determine Cytogenesis in Cystic Nephroathic Larvae

In order to determine the cystogenesis timeline in *ift172*-MO injected embryos, time lapse imaging was performed. This was done in order to expose the larvae to test compounds prior to cystic appearance and to collect the information on their effect during the course of cystogenesis. At 24 hpf, morpholino injected embryos were dorsally oriented in a microtitre plate. To avoid media evaporation during the time lapse imaging, a plastic foil was used to cover the microtitre plate. The plate so prepared was put inside the temperature controlled chamber of ACQUIFER Imaging Machine. The larvae were imaged every four hours over an interval of 24 hour span. The imaging was set to conclude at 48 hpf. This decision was based on the previous imaging experience, where I noticed only volumetric expansion of the developed cysts after this time point (Fig. 9).

3.3.6 Dose Response Optimisation Curve for Control : Rapamycin, Valproic Acid, Trichostatin A, Curcumin

Previously published cyst suppressants in zebrafish, rapamycin, Valproic Acid (VPA), Trichostatin A (TSA) and curcumin were tested for the probability to be used as potential positive control for the screen (Cao et al., 2009; Gao et al., 2011; Leonhard et al., 2011; Tobin and Beales, 2008). For this, the embryos were first injected with 50 μ M of *ift172*-MO. At 24 hpf, 15-17 dechorionated larvae were transferred to 12-well plates. These groups were treated with 25 μ M and 50 μ M of Rapamycin (Cayman Chemicals, Hamburg, Germany), 10 μ M and 50 μ M of VPA (Sigma-Aldrich, Missouri, USA), 500 nM and 1 μ M of TSA (Sigma-Aldrich, Missouri, USA) and 1 μ M and 10 μ M of Curcumin (Sigma-Aldrich, Missouri, USA) dissolved in 0.5% Dimethyl Sulfoxide (DMSO, Missouri, USA). 5mM N-2-hydroxyethylpiperazine-N-2-ethane sulfonic acid (HEPES, Merck, Berlin, Germany) buffered E3 medium with 0.003% 1-phenyl-2-thiourea (PTU, Alfa Aesar, Karlsruhe, Germany) was added to the larvae containing multi-well plate (Fig. 11, 14, 15, 16). At 72 hpf, the larvae were oriented in 96-well plate and imaged as specified in Sec. 3.3.9 and Sec. 3.4.1 respectively.

3.3.7 Drug Treatment of Zebrafish Larvae

Altman nomogram as presented in the (Whitley and Ball, 2002) was used to ascertain the sample size required for the High-Content Screening. The values were calculated by achieving a compromise between the Altman nomogram and logistical feasibility. This resulted in ascertainment of 12 test larvae per compound as an optimal number for the study. In order to have 12 larvae on the day of imaging, batches of 15-17 dechorionated larvae at 24 hpf were transferred to 12-well plates. These larval batches were treated with 25 μ M of compounds from Prestwick Chemical Library (D'Ilkirch, France) dissolved in 0.5% Dimethyl Sulfoxide (DMSO, St. Louis, Missouri, USA). There were total 1,280 FDA/EMA-approved compounds in the library. Along with the test compound, each well was also supplemented with 5 mM N-2-hydroxyethylpiperazine-N-2-ethane sulfonic acid (HEPES, Merck, Berlin, Germany) buffered E3 medium with 0.003% 1-phenyl-2-thiourea (PTU, Alfa Aesar, Karlsruhe, Germany). The treatment continued till 72 hpf, after which 12 larvae per compound were imaged in a 96-well microtitre plate. The compounds were also monitored for the overall side-effects exerted by them on the larval body during the time of exposure. This included visual analysis and documentation of pericardial edema size, yolksac necrosis and heartbeat. In the results and discussion sections, while referring to the negative impacts of the compounds, side-effects are often referred synonymously as their toxicity gradient.

3.3.8 Dose Response Studies on Hits

To cross-validate the first round of screening results and find their optimal functional range five test concentrations i.e. 1 μ M, 6.25 μ M, 12.5 μ M and 25 μ M were chosen for further analysis. The experiments were performed in the same way as mentioned in Sec. 3.3.7, Sec. 3.3.9 , Sec. 3.4.1, Sec. 3.4.2 and Sec. 3.4.4. The results obtained were analysed as in Sec. 3.5.

3.3.9 Preparation of Microtitre Plate

70 μ l of hot 1% agarose prepared in fish water was pipetted in all the rows of 96-well microtitre plate (Cat.-No. 655180, Greiner, Frickenhausen, Germany). After 3 mins incubation at room temperature, 3-D printed dorsal tool was inserted in the plate to create dorsal trough cavity. To avoid precocious solidification of agarose, the plate was kept on a heat block at 60–70°C. After 15 mins, the tool was removed and the plates were covered with damp paper towels and

put in a plastic bag, which were stored at 4°C. On the day of imaging i.e. 72 hpf, the plates were removed from the fridge and wiped with paper towels to remove condensation droplets. Larvae were oriented in the plates, under the stereomicroscope, using a lash tool. A fixed larval orientation format was used for the entire screen, according to which, Ctrl-MO and ift172-MO injected larvae were pipetted in the first and the last row, respectively. The rest of the rows contained test compound exposed larvae.

3.4 High-Content Imaging Protocols

3.4.1 Image Acquisition

ACQUIFER Imaging Machine (DITABIS AG, Pforzheim, Germany), a wide-field high-content screening microscope was used to image 96-well microtiter plates containing zebrafish embryos. The microscope was equipped with a white LED array for bright-field imaging, a LED fluorescence excitation light source, a sCMOS (2048 x 2048 pixel) camera, a stationary plate holder in combination with movable optics and a temperature-controlled incubation lid. Smart Imaging (SI) platform, also known as feedback microscopy was used to acquire data automatically in two iterations and an ACQUIFER HIVE Core M module (DITABIS AG, Pforzheim, Germany) was used to store it (Script. S.3, Fig. 17 A). In the first step, single z-slice per larvae was acquired with a 4x 0.13 objective (Nikon, Düsseldorf, Germany) in 470nm (GFP) channel. The directory containing acquired images was monitored using a Fiji macro, which processed each image directly post acquisition. Region of interest (ROI) i.e. pronephric kidneys was found in these template images by evaluating the co-ordinates of centre of mass, after automatic thresholding. These co-ordinates were further conveyed as the microscope's stage positions. The Fiji macro outputs a small script for each XY-position based on the ACQUIFER Script Language containing instructions for a higher resolution imaging job (Fig. 17B). The scripts were detected by the Smart Imaging interface and automatically executed. This led to the repositioning of the objective lens in order to focus on ROI, and acquiring of higher resolution data by the instructional execution. High-resolution ROI acquisition in both GFP and Bright-field channel utilised 10x 0.3 objective (Nikon, Düsseldorf, Germany), generating 30 z-slices ($\Delta z = 4 \mu\text{M}$) (Fig. 17 C,D). Fixed integration times of 60% relative LED intensity and 10 ms exposure time for the bright-field channel and 100% relative LED intensity and 20 ms exposure time for the GFP channel were used. Software autofocus algorithm was used to detect

focal plane in 470 nm channel. In addition to that, all plates were also imaged using 2x objective to document the larval overview. In summary, the pronephric areas were acquired using a pre-scan/re-scan procedure on the Imaging Machine Smart Imaging Interface (DITABIS AG, Pforzheim, Germany), i.e. kidney regions were robotically detected in lower resolution data and subsequently centred and imaged at higher resolution (Pandey et al., 2019). The whole process for a single 96-well plate was completed within 45-50 mins.

3.4.2 Image Pre-processing

A custom combination of Perl and Fiji written script was used to create multilayer TIFF files of 30-slices from raw images (Script. S.4; Fig. 18). Spatiotemporal resolution of the images were improved by deblurring them using Huygens Professional deconvolution software (SVI, Hilversum, The Netherlands). The software used quick maximum likelihood estimation method and a theoretical point spread function dependent on microscope's parameters. A workstation with 12 CPU cores /24 threads and 32 Gigabyte of RAM was used for batch deconvolution. The focussed slice from all image stacks were identified using "Find Focussed Slice" plugin to make a sub-stack of 8 slices (3 slices above and 4 slices below) (Tseng). The images were outlier filtered, maximum projected and cropped by placing a bounding box of size 512 x 512 around ROI. This was followed by further cropped by placing the bounding box in the centre with width equivalent to the size of the image but the height was reduced by a factor of 1.6 than that of the original frame. It was done to ensure strictly precise inclusion of the glomerular and pronephric tubular areas only. These images were thresholded using Li method implemented in Fiji (Fig. 18) (Pandey et al., 2019).

3.4.3 Blurry, Blank and Wild-Type Kidney Check

The variance for each image was calculated after background correction. Images with variance values below 400 were considered blurry and removed (Fig. 19 A-D). Similarly, blank images were detected based on variance check after Laplace filtering (Script. S.5, (Shapiro and L., 1992)). The images with variance values above 124 were considered blank and filtered out (Fig. 19 E-H).

This was followed by detection of images displaying pronephric areas resembling the wild-type phenotype using Fiji. The recropped images were subjected to Gaussian Blur ($\sigma=20$), Li auto-thresholding method and were masked. The area fraction of foreground pixels in these images

was measured and the images with value less than 100 pixels were selected (using “Create selection” function in Fiji), inverted and surrounded by bounding box. Dimensional optimisations were made to the bounding box in order to reinsure the presence of both cystic and fluorescent pronephric areas within the boundaries (Pandey et al., 2019). On the other hand, images with area fraction values equal to 100 were first inverted and then subjected to ROI selection to exclude blank images from the evaluation scheme. The bounded areas from all images were further plotted using “Plot Profile” option in Fiji. The profile values were checked for zero values, as that was an indicator of cystic presence (Fig. 20). To validate wild-type vs. cystic classification “Convex Hull” was applied on the binary images followed by “Analyze Particles” plugin to extract the length of major axis of ellipses (Fig. 20). Henceforth, images with ellipse major axis length greater than 299 pixels were classified as wild-type. Images containing more than one ellipse were scanned first to find the biggest ellipse, which was measured and used for classification purpose.

3.4.4 Image-Based Area Quantification for Morphology Gradation

All images were subjected to pronephric area calculation by measurement of all created particles using “Analyze Particles” plugin in Fiji and summing them up. After this, for cystic area calculations, all images were inverted and a convex hull was drawn around ROI separating it from the general background. Then once again ‘Analyze Particles’ plugin was applied, which generating area values for all the particles within ROI inclusive of the cystic particles. All the particles were assigned numbers by analyse particles plugin. The images were processed to get the particles of interest within a count of 10 (Fig. 21). Following this, cystic particles among others were selected by sequential investigation and selection of those particles with the Feret Diameter ≥ 70 and Particle number < 11 in each image (Script. S.5, Fig. 21). The selected particle areas were summed up to generate final cystic area value. Depending on whether or not the image was previously classified as wild-type or not during the image quality check respective areas were assigned. In wild-type images, summed pronephric areas were allocated as the total kidney area, whereas in case of cystic kidneys the sum of both pronephric and cystic areas were attributed as their total kidney area.

3.4.5 Heatmap Representation

All the csv files generated from Sec. 3.4.3 and Sec. 3.4.4 were stored in the “Analysis Folder” inside each test folder. Once the final areas were assigned to each image utilising the merging, sorting, filtering feature of Python interface, they were sorted in an array corresponding to the microtitre plate in which they were imaged. Matplotlib library of Python was used to plot these values as a heatmap using ‘Inferno’ colour scheme. According to this colour scheme, dark to light purple shades showed wild-type and suppressed cystic phenotypes, whereas orange to brighter yellow depicted the bigger cyst sizes (Fig. 12).

3.5 Statistical Test on Screened Compound Library

To account for the variations encountered during screening due to daily manual injection and genetic variability, single-plate-based normalisation was performed for the entire screen. The area results acquired after automated image quantification were stored in a csv file in “Analysis Folder”. The first step was to homogenise the area values obtained from the sample size of 12 larvae imaged per compound with respect to each other. This was done by implementing standard deviation-based normalisation. Post first step normalisation, the data was found to follow extreme value distribution (National Institute of Standards and Technology). As I was looking for overall cyst suppression in the screen, as a result, the data was optimised by filtering out all the negative and extreme positive values. The remaining values were used for the final single plate normalisation. The degree of cyst size suppression by test compounds was determined by the difference evaluated between the cystic control and test larvae. Henceforth, normalised and filtered values for ift172-MO injected larvae were averaged in each plate and used to divide the area values of the remaining compounds. The resulting values for all test sub-populations were averaged and assigned as the normalised area for that compound. These values were used to generate boxplot for the entire screen and isolate the hits.

3.6 Molecular Methods

3.6.1 RNA Extraction

At 72 hpf, 50 zebrafish embryos injected with Ctrl-MO, ift172 exon-1 splice MO and wild-type were aliquoted in 2.0 ml tubes removing as much E3 media as possible. Larvae were then ho-

mogenised in 1ml TRIZOL (Life Technologies, Germany) solution. 200 µl of chloroform (Roth, Karlsruhe, Germany) was added to the larval solution followed by centrifugation at 13000 g at 4°C for 15 minutes. The resulting supernatant aqueous phase was carefully collected in DNase and RNase free tubes and was supplemented with 500 µl of Isopropyl alcohol (Sigma-Aldrich, Deisenhofen, Germany). After 10 mins, incubation at RT, samples were centrifuged at 4°C for 10 mins. The pellet so obtained was washed with freshly prepared 75% Ethanol (Roth, Karlsruhe, Germany) and re-centrifuged. At this juncture, the supernatant was discarded and the pellet was air dried at RT. Final pellet was resuspended in 50 µl nuclease free water on ice. Concentration of RNA was measured using spectrophotometer.

3.6.2 DNase Digestion

3.6.3 *ift172* Morpholino Knockdown Quantification with RT-PCR

cDNA strand was amplified using different primer pairs designed to check morpholino knock-down at 72 hpf. 1 µl of cDNA strand was added to each reaction sample containing forward and reverse primer pair, 10x PCR Buffer, MgCl₂, dNTPs, Taq Pt Polymerase and dH₂O. Following Primers were designed to check the efficacy of MO knockdown along with EF1alpha as house-keeping gene:

ift172-Exon1 Forward: AGACTCTTTTAAACGCCTCAGGT,

ift172-Exon1 Reverse: ACTTTTGGGTCAGCAGGCTT,

EF1alpha_Forward: GTGCTGTGCTGATTGTTGCT

CTTCTCAGGCTGACT

EF1alpha_Reverse: TGTATGCGCTGACTTCCTTG

CCGCTAGCATTACCC

RT-PCR was carried out under following conditions : 2 mins denaturation at 98°C; followed by 30 cycles of 98°C, 60°C, 72°C of 30 secs each for denaturation, annealing and elongation, respectively.

3.6.4 Agarose Gel Electrophoresis

Agarose gel electrophoresis was carried out to separate post PCR fragments of different sizes in order to check the morpholino knockdown. Agarose gel with 1.8% agarose in 1x TBE buffer supplemented with 1µl/ml Gel Red solution (Biotium, Fremont, USA). Before loading, the

samples were mixed with an appropriate volume of 6x loading dye. In addition to the samples, a DNA ladder was loaded to determine the size and approximate quantity of the nucleic acid samples. The electrophoresis was carried out using 3–5V/cm gel length. Nucleic acids were visualised using an UV–Transilluminator (BioRad, Germany) (Fig. 7).

3.6.5 Fixation of Zebrafish Embryos

Zebrafish larvae were fixed at required stage by transferring them into ice-cold 4% PFA in PBS. After overnight incubation at 4°C, the embryos were dehydrated by three washes in absolute ethanol and stored in 100% ethanol at –20°C. Fixation was performed for both Ctrl and ift172-MO injected embryos at 72 hpf.

3.6.6 HE Staining and Imaging

Fixed zebrafish larvae were transferred to embedding cassette (Einbettkassetten, Cat.-No. 09-0401, Langenbrink GmbH, Emmendingen, Germany) in groups of 20 and were washed for 5 mins each in ethanol series of 70%, 96% and 100% . These cassettes were incubated in Xylene (Roth, Karlsruhe, Germany) for 3 hours and dipped in 60°C paraffin for an hour. The processed larvae were oriented in small metal trays containing melted paraffin. 5-10 larvae per tray were oriented parallel to each other and immediately solidified at 4°C. Trays were refrigerated for 48 hours and later the larvae containing part of the paraffin was carved out and embedded vertically in new metal trays to allow transverse sectioning. These final embedded blocks were loaded on the sectioning machine (Leica RM2165) and cut into 3 µM sections. Slices so generated were inspected using microscope for the presence of ROI. ROI containing slices were transferred to hot water bath maintained at 37°C to remove creases from the section, if any and saved on the glass slides. These slides were appropriately labelled and incubated overnight at 38°C. The overnight baked slides were put in slide holder tray and bathed in alcohol series. The series began by three times incubation of 5 mins each in Xylene and 99% ethanol, respectively. This was followed by 96% and 70% ethanol incubations for 5 mins each. The slides were washed in distilled water for 3 mins before being stained for 2 mins in hematoxylin. The slides were washed again after staining in lukewarm running water for 5 mins to get rid of the excess stain followed by a quick dip in distilled water bath. Acetic acid activated acidic dye Eosin G, was used to further stain the slides for 3 mins followed by short RT water dip. The slides were transferred to two fresh distilled water baths before being dipped thrice in increasing ethanol

series of 70%, 96% and 99%. They were washed twice in two separate 99% ethanol baths for 30 sec and 2 mins, respectively. The staining procedure was finalised by three rounds of xylene incubations of 5 min each. Slides were left to dry in dry, dark place at RT. In order to ensure proper sealing and preservation of slides drops of glycerine were placed on the slides, proceeded by gentle placement of glass cover slips avoiding air bubbles. The sealant was allowed to dry overnight before the slides were collected and stored in the holder. Such HE stained slides were imaged using Image Scope version 11 (v11.2.0.780) and the images were acquired using 10x objective (Fig. 8).

4 Results

4.1 Optimisations for High-Content Screening

4.1.1 Dose Response Optimisation Curve for *ift172*-MO

Cilia assembly and maintenance co-ordinating protein complex, intra flagellar transport protein (*ift172*), are often implicated in human mutational diseases such as, Jeune and Mainzer Saldino syndromes. These are grouped together as ciliopathies characterised by skeletal, renal, hepatic, or retinal abnormalities. The severe human phenotype can be replicated in loss of function phenotypes models of zebrafish (Pandey et al., 2019). Using splice-morpholinos-based knock-down of *ift172* in the *Tg(wt1b:EGFP)* transgenic line, I engendered readily scorable glomerular cysts, creating a cystic kidney disease of zebrafish (Fig. 6).

Large scale drug discovery platforms can make use of zebrafish only if it provides robust phenotypic read-outs that can be easily concatenated with automated screening assays. However, large glomerular cyst in the developing pronephroi of zebrafish are often coalesced with several other morphological alterations of the body, hence challenging the automated imaging assays in terms of variation-free data acquisition (Pandey et al., 2019). Addressing this, dose response studies were performed to find the most suited concentration of morpholino to create a cystic nephropathy model of zebrafish. The aim was to find an MO concentration capable of engendering cystic nephropathy at a stage, which is progressive enough to mimic all the disease related phenotypes, but still provides enough room for the execution of compound effect studies and consistent data acquisition. With its ability to mimic the cystic phenotype in moderation, 50 μ M was chosen out of the tested 50, 100 and 500 μ M concentrations of *ift172*-MO (Fig. 6 A-H). In addition to this, previously published phenotypic traits such as, dorsally curved body, hydroencephaly and pericardial edema were all well recapitulated without severe necrosis or toxicity leading to mortality (Fig. 6 I-L). Therefore, 50 μ M *ift172*-MO laid the foundation of this High-Content Screening project by generating the required model and providing window for further experimentation (Fig. 6 M,N).

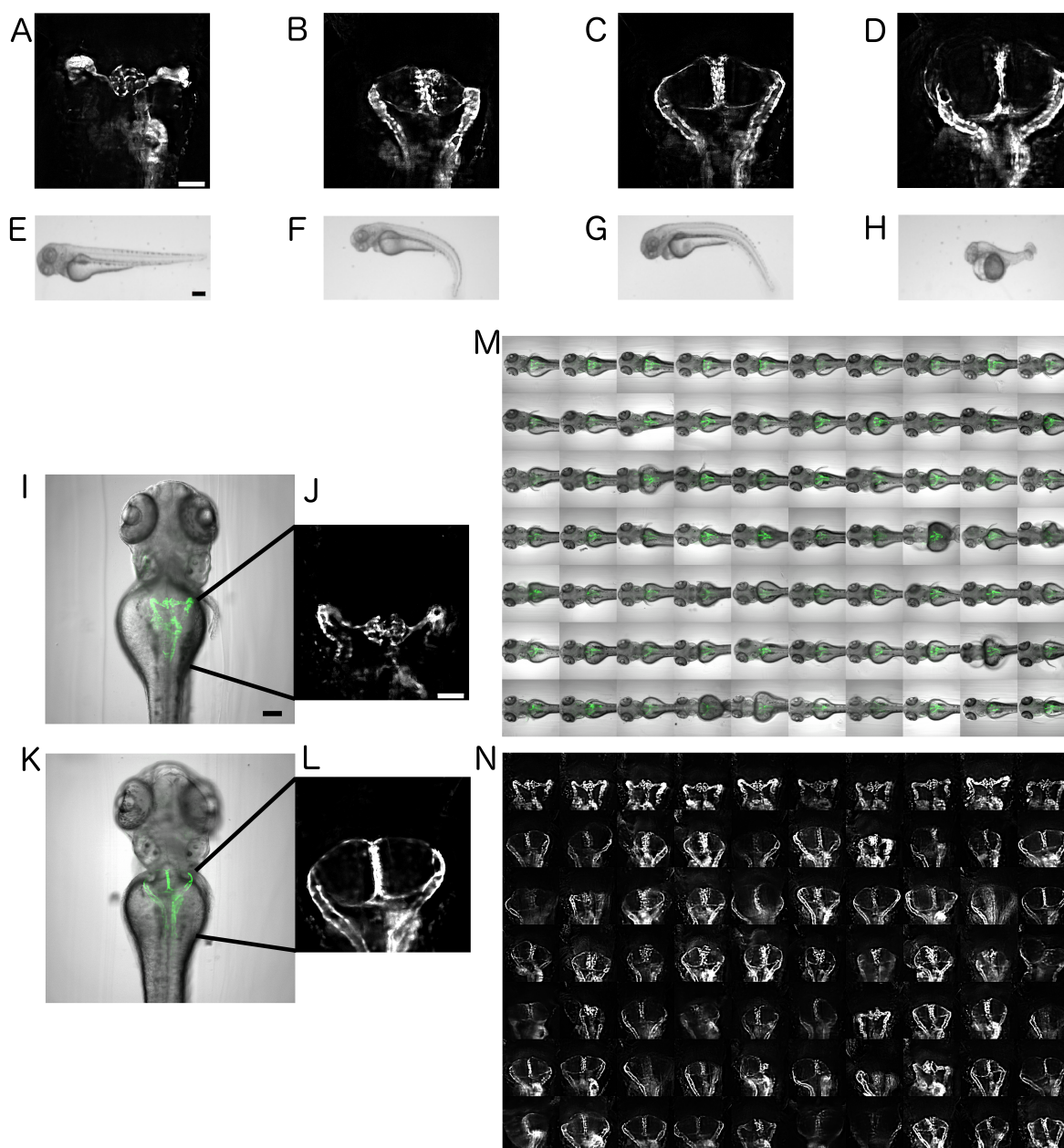


Fig. 6: Automated imaging of an *ift172*-MO-based zebrafish model for human cystic kidney disease. (A-D) Dorsal views on pronephric areas in the *Tg(wt1b:EGFP)* embryos. Scale bar is 50 μ m. (E-H) bright-field stereo microscope images of dose response curve of *ift172*-MO on 72 hpf zebrafish larvae. Scale bar is 250 μ m. (A,E) wild-type, (B,F) 50 μ M *ift172*-MO, (C,G) 100 μ M *ift172*-MO, (D,H) 500 μ M *ift172*-MO. (I,K) Overlay images of bright-field and fluorescence channels depicting wild-type and cystic pronephric phenotypes acquired with a 10x objective. Scale bar for I is 100 μ m and J is 50 μ m. (J,L) Enlarged fluorescent view of I and K. (M-N) Montage images illustrating (M) overlay images or (N) pronephric areas of dorsally oriented larvae in a microtitre plate (Pandey et al., 2019).

4.2 Morpholino Knockdown Quantification

Efficacy of the morpholino knockdown, despite mimicking all the published and validated phenotypes in morphants and mutants was once more confirmed by performing a qPCR experiment.

For this process, cDNA library from *ift172*-MO, Ctrl-MO and wild-type larvae at 72 hpf were created. As the splice morpholino used in the study targeted exon1, primers were designed to amplify this region. The cDNA from all three sample types were PCR amplified using the region specific primers. The resulting products were run on an agarose gel in an electrophoresis chamber and imaged. In cases of ctrl-MO and wild-type larvae a band of 112 bp was seen as expected, which represented the presence of amplified Exon1 region. However, in the case of *ift172*-MO injected larvae the highly diminished intensity of the band was observed. This confirmed the targeted knockdown of the exon1 in *ift172*-MO injected larvae, hence, corroborating our studies (Fig. 7). The experiment used the amplification of the housekeeping gene *EF1 α* at 461 bp as control.

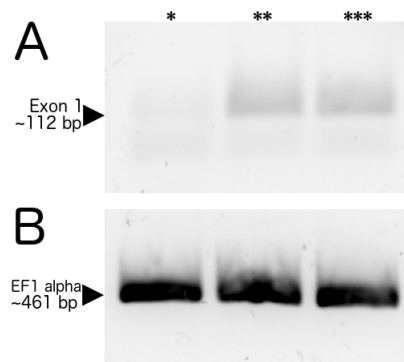


Fig. 7: **Morpholino knockdown quantification.** Gel representing quantification of exon1 of *ft172* at 112 bp position done using primer pair directed to amplify segment extending from exon1 till the beginning of exon2 in 72 hpf zebrafish larvae. *, ** and *** are *ift172*-MO, ctrl-MO and wild-type larvae, respectively. The experiment used the amplification of the housekeeping gene *EF1 α* at 461 bp as control.

4.3 Sub-cellular Phenotype Visualisation Utilising HE Stain

HE staining was performed on the *ift172*-MO injected, *ift172*-MO plus rapamycin exposed and wild-type larvae at 72 hpf to document the sub-cellular modifications in the pronephric morphology. Images from *ift172*-MO showed a wide clear lumen in place of normal intercalated glomerular fusion as seen in the Ctrl-MO larvae sections (Fig. 8 A,B). The cyst-size seen in *ift172*-MO larvae was significantly reduced in the case of rapamycin exposure, similar to the findings in the fluorescence image acquisition done on high-content screening microscope (Fig. 8C; Fig. 11). Thus, re-establishing the validated cyst creation by *ift172*-MO and its clear suppression by the activity of the positive control drug, rapamycin.

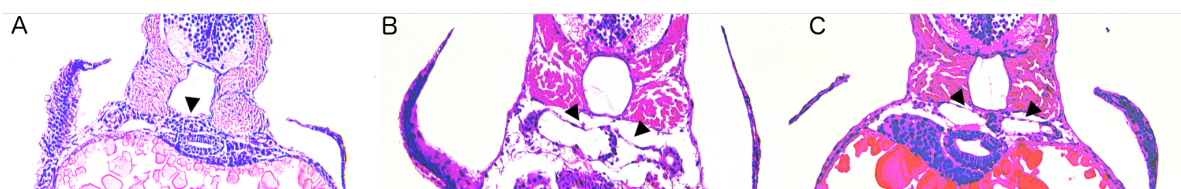


Fig. 8: **HE staining.** HE staining revealing the pronephric condition in (A) wild-type: arrow head showing fused glomerular structure, (B) ift172-MO and (C) ift172-MO injected larvae exposed to 25 μ M rapamycin at 72 hpf. The larvae showed the presence reduction in cystic lumen (shown by black arrow heads) in (C) validating the positive effect of rapamycin on cyst suppression.

4.4 Time Lapse Study to Determine Cystogenesis in Cystic Nephropathic Larvae

The library compounds tested during this High-Content Screening were determined to be introduced to the larvae culture medium before the inception of cystic invasion in order to document their effect on the entire cystogenesis process. Therefore, time lapse studies were performed to analyse the cystogenesis timeline in the ift172-MO knockdown larvae to pin down the real time of cystic emergence; followed by resolution of the optimal time for compound exposure. The time lapse studies starting from 24 hpf till 48 hpf revealed the appearance of cysts began around 40 hpf and almost doubled at 44 hpf, with 64.3% cystic population (Fig. 9, Fig. 10 A). The cystic growth kept following an upward trend with 98–100% cystic larvae at 48 hpf. Cystic growth was quite dependent on the overall larval developmental rate. During the study, the fusion of medial glomerular structure was also found to occur at 44 hpf in around 40% of the sample population (Fig. 10 B). The size of the cysts continued to enlarge till the imaged duration of 72 hpf concomitant with gradual gross morphological health degradation. This deduction led to the selection of 24 hpf as an appropriate time point for the inception of compound exposure in the culture medium. Such a method led us to comprehend the activity of the compound during the entire cyst formation rather than having just the end point effect.

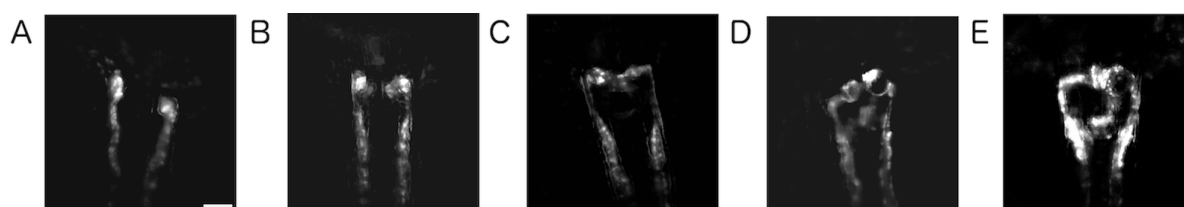


Fig. 9: **Developmental analysis of cyst formation in *ift172* morphants.** Time lapse recording performed at (A) 24 hpf, (B) 32 hpf, (C) 40 hpf, (D) 44 hpf, arrows indicate forming cysts (E) 48 hpf to analyse the cystogenesis timeline of *ift172*-MO injected *Tg(wt1b:EGFP)* zebrafish embryos. 44 hpf was seen as the critical time point for cyst development in more than 60% larvae. Scale bar for A-E is 50 μ m. (Pandey et al., 2019).

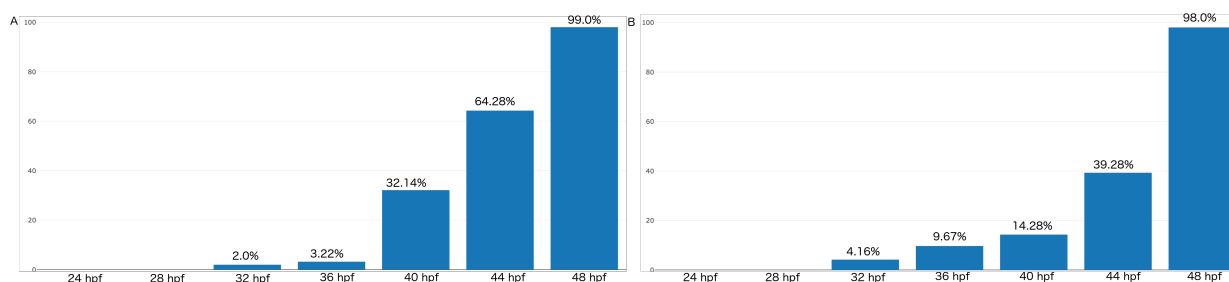


Fig. 10: **Quantitative analysis of cyst sizes upon *ift172*-MO injection.** (A) and (B) showing cystic growth and glomerular fusion percentage in *ift172*-MO injected larvae over recorded durations of 24 hpf, 32 hpf, 40 hpf, 44 hpf and 48 hpf to analyse the cystogenesis timeline in *Tg(wt1b:EGFP)* zebrafish embryos.

4.4.1 Dose Response Optimisation Curve for Positive Control : Rapamycin

In order to execute an orderly experiment and compare the effectiveness of the test compounds, it is of utmost importance to have a proper positive control. Therefore, based on thorough literature survey, I found rapamycin along with few other compounds to be a definitive cyst suppressant and implemented it here as potential positive control. Although, the mTOR inhibiting compound's application in human clinical trials resulted in subdued efficiency, it flawlessly suppresses cysts in cystic kidney models of zebrafish (Tobin and Beales, 2008).

As I wanted to test its activity as well as find an optimal working concentration, I performed a dose response study using 25 μ M and 50 μ M concentrations (Fig. 11). Embryos injected with *ift172*-MO and exposed to 25 μ M rapamycin were oriented in 96-well microtiter plates. Smart imaging workflow was implemented to image these plates and the resulting data was analysed using automated pipeline (Fig. 12A). Heatmaps were plotted for the quantified pronephric areas for quick visualisation and effective identification of cystic suppression (Fig. 12B, 13, S.1). Heatmap provided a quick and easy visualisation tool for the purpose. The drug was successful in displaying clear suppression of cysts at both doses, coupled with concentration

dependent increment in precipitate formation (Fig. 11). In cystic nephropathies, the glomerular and tubular epithelia rapidly multiplies and swells so much that phenotypically it appears as one fused structure. The application of rapamycin displayed a significant reduction in the fused and swollen glomerulo-tubular curvature, hence made the demarcation of glomerular and tubular sections clearer; bringing it closer to the wild-type phenotype (Fig. 12). On average, 92.1% larvae showed 50% depreciation in the cyst size in a population of around 170 tested subjects (Fig. S.1). At this point, factors such as lack of compound precipitation, comparable cyst suppression and lower probability of unknown side-effects led to the designation of 25 μ M as an appropriate concentration for positive control. This effective concentration was used as the base value to conduct the entire screen of 1,280 compounds. Therefore, validating the use of developed automated pipeline for the use of automatic identification of cyst-size modifying compounds in the upcoming zebrafish High-Content Screening.

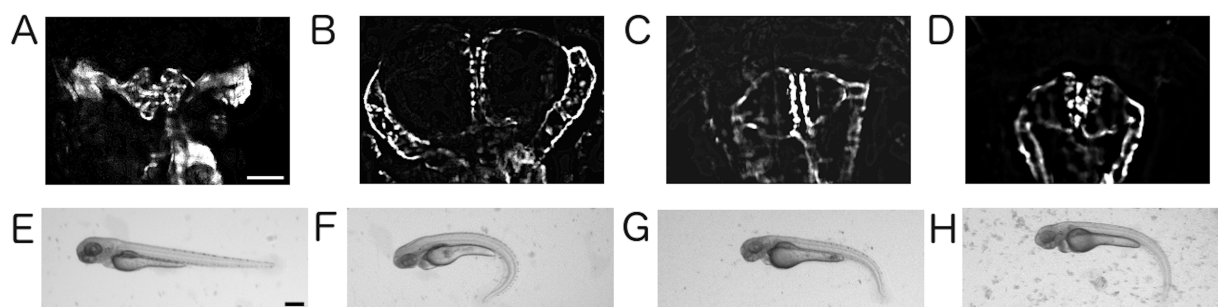


Fig. 11: **Pronephric phenotypes on rapamycin treatment.** The fluorescence and stereo microscope images of dose response experiment administering rapamycin Ctrl-MO or ift172-MO injected embryos at 72 hpf. (A,E) Control, (B,F) ift172-MO injected, (C,G) ift172-MO + 25 μ M rapamycin and (D,H) ift172-MO + 50 μ M rapamycin exposed larvae are shown. Scale bar for A-D is 50 μ m and for E-H is 250 μ m. (Pandey et al., 2019).

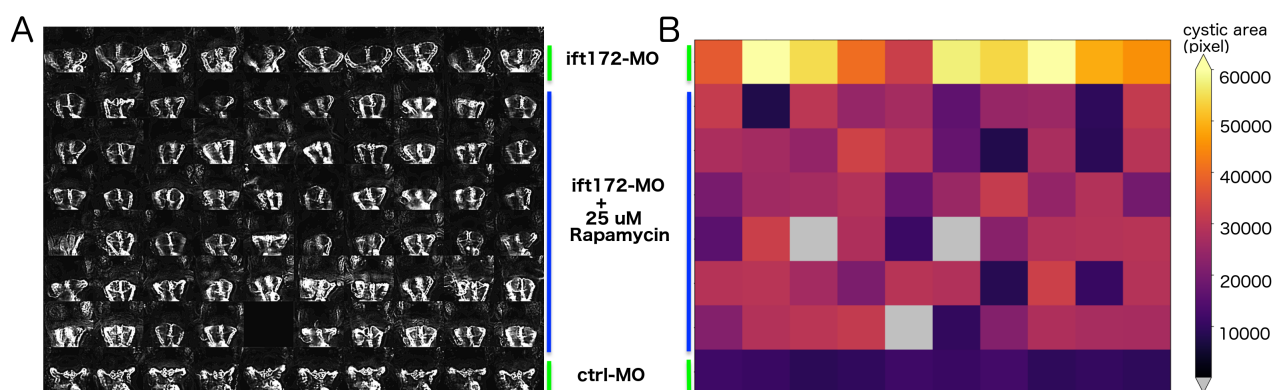


Fig. 12: **Automated scoring of pronephric phenotypes on rapamycin treatment.** Montage (A) in correspondance to the heatmap (B) representing the areas calculated from 72 hpf pronephroi in a microtitre plate; first row is ift172-MO injected, last row is wild-type and rest of the rows are 25 μ M rapamycin exposed larvae. Thus, (B) is providing an easy to read output format for faster scoring of phenotype affecting compound classes. (Pandey et al., 2019)

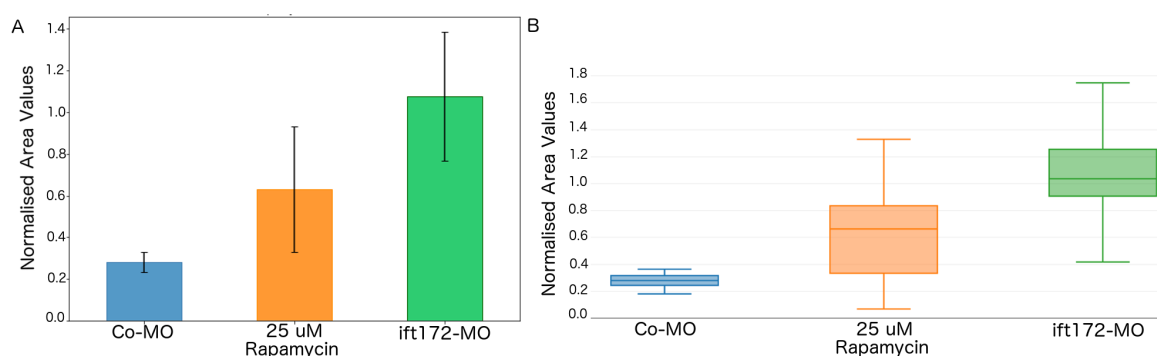


Fig. 13: **Quantitative analysis of cyst sizes upon rapamycin treatment.** (A) Bar chart showing the area quantification results of Co-MO (blue; mean=0.27, SD=0.04) , ift172-MO + 25 μ M rapamycin (orange; mean= 0.63, SD=0.3) and ift172-MO injected larvae (green; mean=1.07 , SD=0.3) at 72 hpf. The plots represent the normalised data against the plate-specific mean of negative controls (i.e. ift172-MO injected larvae). (B) Box plots indicating the distribution of individual area measurements. Whiskers indicate min-max values. (Pandey et al., 2019)

4.4.2 Dose Response Optimisation Curve for Controls : Valproic Acid and Trichostatin A

After gaining one strong positive control, in order to find other possible controls for our study, I tested few other previously tested compounds known to repress cystic aggression. In this process, based on (Cao et al., 2009)'s work, HDAC inhibitors, Valproic Acid and Trichostatin A were selected. Similar to the rapamycin test, dose response study was performed to identify the optimally effective exposure concentration. VPA responded well in micromolar range whereas, the same for TSA led to near mortality and sometimes even mortality in larvae (Fig. 14, 15). Pertaining to the difference in the effective concentration ranges of both compounds, different

scale spectrums were used. With mild toxicity and functionality, 50 μM concentration of VPA was found to be optimally active and TSA displayed effective suppression at 1 μM concentration. VPA, with its HDAC class I specific inhibition, only showed intermediate suppression on 34% of dorsally acquired pronephric phenotype. On the other hand, pronephroi at 72 hpf, under the pan-HDAC inhibitory effect of TSA resembled 40-48 hpf developmental stage, lacking midline glomerular fusion at times (Fig. 14, 15). Although, the developmental progression was hampered by the compound, the overall cyst morphology seemed subdued for around 80% population at the most effective concentration of 1 μM . This stunted pronephric development by TSA, made it difficult to ascertain the degree of suppression induced and its direct comparison with the peer control group. Despite being HDAC inhibitors, VPA and TSA belong to different structural families, which could have played a part as well and contributed to the variations seen in the cystic suppression exerted by both compounds. Other than cystic suppression, both compounds showed significant improvement in the curvature straightening of the larvae at all exposed doses (Fig. 14, 15), as was also seen previously by (Cao et al., 2009). To summarise, the effect of these compounds in our study showed a rather toxic and feeble suppression unlike rapamycin. Resultantly, they were omitted as positive control candidates for this High-Content Screening experiment.

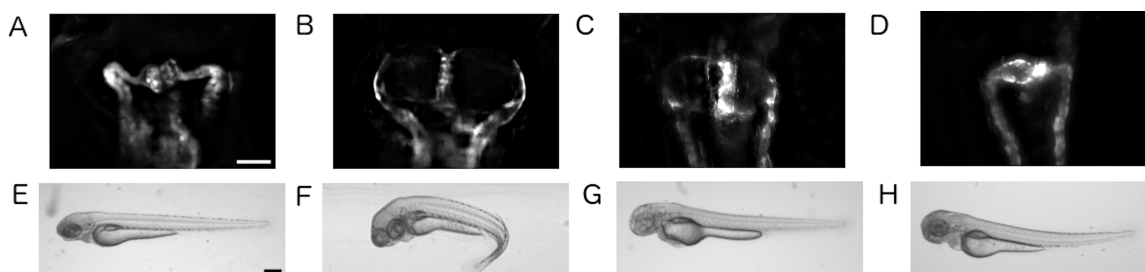


Fig. 14: **Pronephric phenotypes on VPA treatment.** Fluorescence and stereo microscopic images of dose response study of VPA on ift172-MO injected zebrafish larvae at 72 hpf. (A,E) are the wild-type ctrl, (B,F) ift172-MO injected, (C,G) and (D,H) are ift172-MO injected larvae exposed to 10 μM VPA and 50 μM respectively. Scale bar for A-D is 50 μm and for E-H is 250 μm

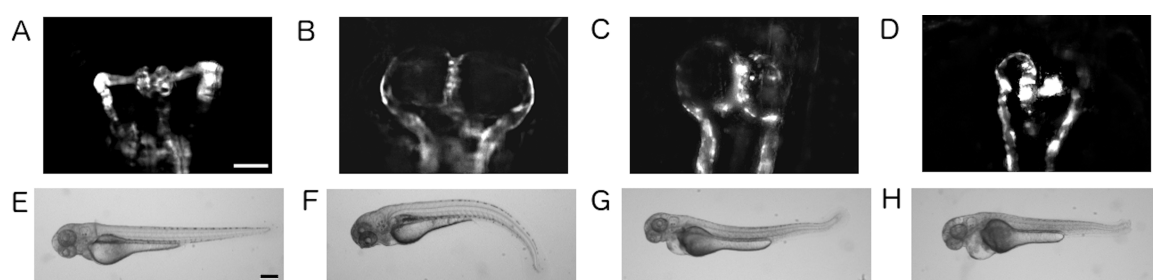


Fig. 15: **Pronephric phenotypes on TSA treatment.** Fluorescence and stereo microscopic images of dose response study of TSA on ift172-MO injected zebrafish larvae at 72 hpf. (A,E) are the wild-type ctrl, (B,F) ift172-MO injected, (C,G) and (D,H) are ift172-MO injected larvae exposed to 500 nM TSA and 1 μ M respectively. Scale bar for A-D is 50 μ m and for E-H is 250 μ m

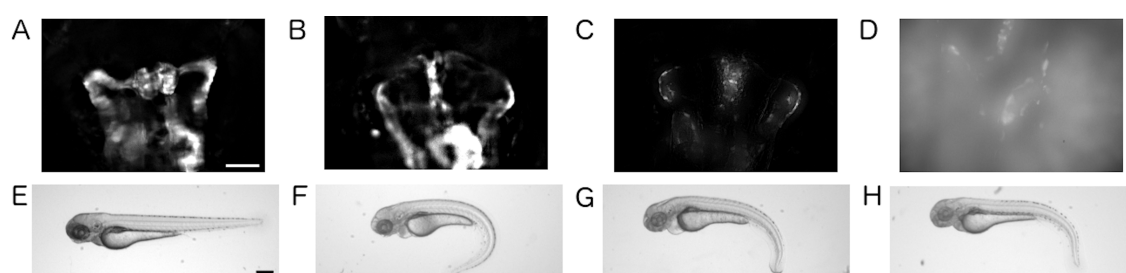


Fig. 16: **Pronephric phenotypes on curcumin treatment.** Fluorescence and stereo microscopic images of dose response study of curcumin on ift172-MO injected zebrafish larvae at 72 hpf. (A,E) are wild-type ctrl, (B,F) are ift172-MO injected (C,G) and (D,H) are ift172-MO injected larvae exposed to 1 μ M and 10 μ M curcumin respectively. Scale bar for A-D is 50 μ m and for E-H is 250 μ m

4.4.3 Dose Response Optimisation Curve for Control : Curcumin

Curcumin, similar to previously tested compounds was also investigated for its cyst suppressing activity in zebrafish model. Cyst suppressing activity of curcumin mediated by mTOR signalling has been previously reported in cell and mice models (Gao et al., 2011; Leonhard et al., 2011). To validate its effect on zebrafish larvae, a dose response study was performed using 10 and 50 μ M concentrations. In 72 hpf larvae, 10 μ M curcumin evidently displayed slight to nil cyst suppression. Effects of higher concentrations could not be ascertained because of considerable decline in the renal structure visibility, pertaining to curcumin's fluorescence. As represented in the (Fig. 16) panel, only faint outlines of the pronephric structure could be seen at 10 μ M concentration. In conclusion, the effect of curcumin at lower concentration was quite low, whereas at higher concentrations couldn't be determined due to the autofluorescence issues. Based on these cryptic results, the inclusion of this compound as an alternative positive control for the screen was omitted.

4.5 High-Content Imaging

4.5.1 Image Pre-processing

The application of low magnification objectives with large field of view, which captures low-resolution data with reduced informational content often hinders the analysis of tissue specific phenotypes in automated zebrafish imaging assays. To overcome this bottleneck a smart imaging module following a two-step imaging procedure to automatically centre and zoom-in on regions of interest (Fig. 17A) was developed here. Its implementation enabled acquisition of standardised higher resolution data of dorsal views of pronephric areas in *Tg(wt1b:EGFP)* embryos. The overview data of the entire screen with large field of views was generated using a 4x objective and a single z-plane in the GFP channel. An external “folder-watch” routine monitored this directory containing acquired images, subsequently prompting the execution of a feature recognition step ensued by caching of new experimental images. Separate Fiji macros were effectuated for the “folder-watch” routine and feature recognition step. Utilising the centre-of-mass detection after automatic thresholding the feature-recognition provides the XY-localisation of the pronephroi. The script-based smart imaging interface of the ACQUIFER Imaging Machine was executed in order to send the instructional feedback to the screening microscope and commence higher resolution imaging of localised pronephric regions. A local directory on the control computer was used to save text-files containing script commands for positioning the objective lens, software autofocus and higher resolution z-stack acquisition, corresponding to each detected pronephric region (Fig. 17B). The smart imaging interface of the command and control software of the microscope later detected and executed these “job-files”. Resultantly, automatic capturing of each pronephric region at enhanced resolution in both bright-field and GFP channel using a 10x objective and 30 z-slices with a z-slice distance of 4 μ M was attained (Fig. 17 C,D). Fiji interface was used to enforce all external software components of the smart imaging module and are available in supplementary section (S.1, (Pandey et al., 2019)).

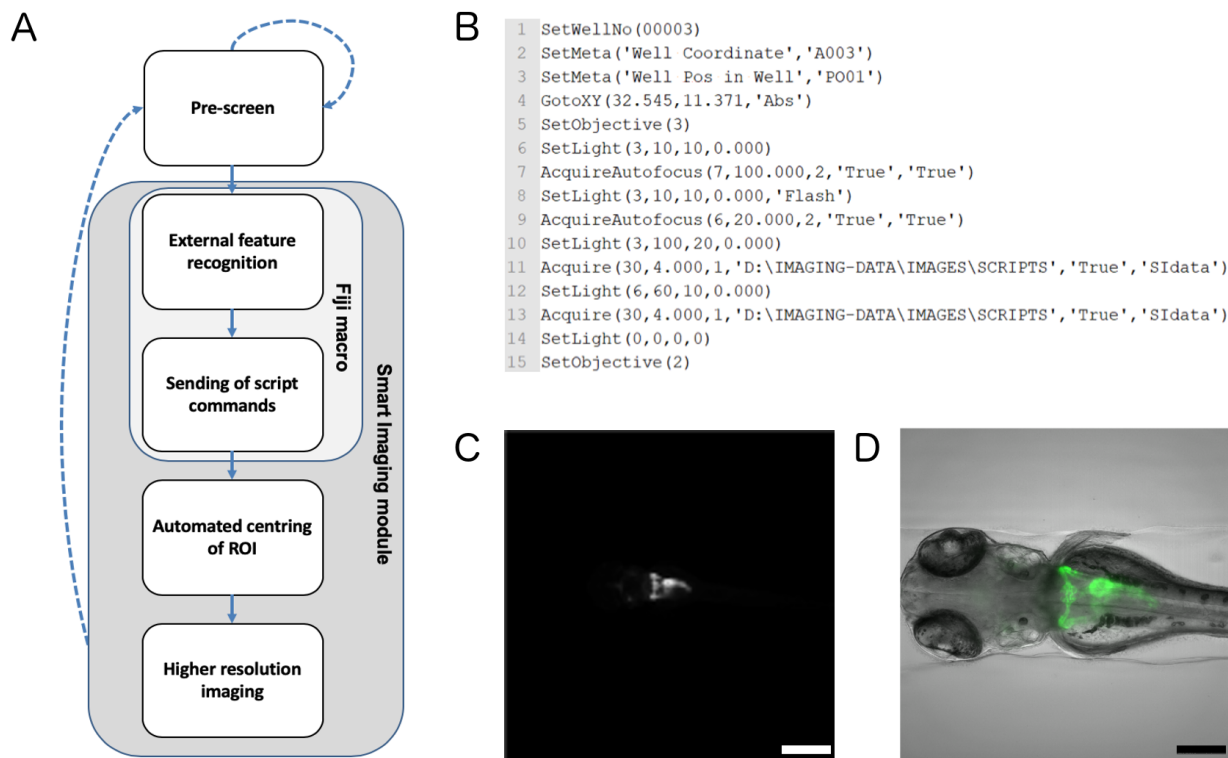


Fig. 17: High-Content Screening automated imaging workflow. (A) Workflow chart illustrating the feedback microscopy approach utilised to automatically acquire regions of interest (ROIs). Dotted arrows indicate imaging components of the pre-screen; solid arrows indicate image processing and higher resolution imaging procedures of the smart imaging module. (B) Example of script commands for a single well that are sent to the automated microscope. The script triggers automated centring of the region of interest and high-resolution acquisition. (C) Representative overview image taken with 4X objective followed by (D) centring and higher resolution imaging of the pronephric region with 10x objective. The image shows a maximum projection of the GFP channel overlaid with the bright-field channel. Scale bar in C is 500 μm and scale bar in D is 200 μm (Pandey et al., 2019).

The automated High-Content Screening acquisition module acquired around 1,200,000 raw images, including both bright-field and GFP channel, accounting for more than 13 TB data. Once the images were acquired from the two-step SI module, they were pre-processed to make them readily discernible for large scale automated quantification workflows. Each well was imaged as a set of 60 z-slices, which was comprised of two sets of BF and GFP channel with 30 z-slices each (Fig. 18A). The GFP channel z-slices were decked together as a single stack using custom written Perl script in combination with Fiji (Fig. 18B; Script. S.4). This multilayer format reduced the number of files on average from 57,600 to a mere 960 per week, hence making the process more streamlined. As the images were acquired using wide-field microscopy, they were deblurred to restore clarity by deconvolution (Fig. 18C). The deconvolution software reverses the optical distortion in the image by using theoretically calculated point spread function resulting in significantly sharp output images. Deconvolved stacks of 30 z-slices so ob-

tained were converted into sub-stacks of 8 slices around the most focussed slice (Fig. 18D). The sub-stacking step enhanced the volumetric information captured once the images underwent z-projection (Fig. 18E). Projections were outlier filtered and cropped by automated placing of a bounding box in the centre to contain the kidney region (Fig. 18 F,G). Finally, these images were recropped, thresholded and binarised based on set empirical criteria to encompass only the pronephric area with the focus on glomerular region (Fig. 18 H,I; Script. S.5) (Pandey et al., 2019).

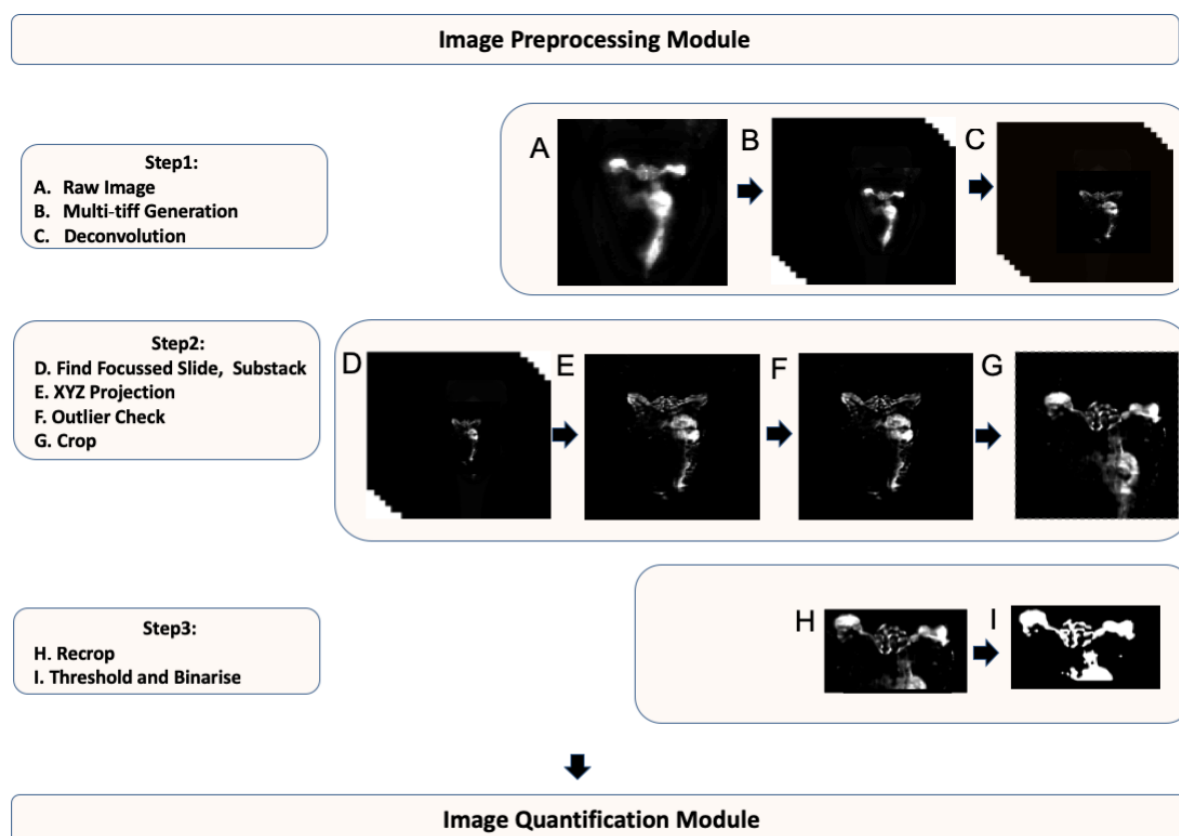


Fig. 18: **Image pre-processing module.** (A) Raw images were first converted to multi-tiff format (B) utilising Perl script and deconvolved (B). (D) These images were sub-stacked with focussed slice in the centre. Sub-stacks were then (E) XYZ-projected, (F) outlier filtered and (G) cropped localised around pronephric region. These images were then (H) recropped, (I) thresholded and binarise depending on the downstream requirements and finally sent to the image quantification module.

4.5.2 Blank, Blurry and wild-type Scoring

All the pre-processed images were run through a set of scripts devised exclusively for the automation of the image quantification module of the High-Content Screening pipeline. The module identified whether the images had features of blank, blurry or wild-type kidneys (Fig. 19, 20, Script. S.5). This check was essential in order to remove the images acquired from damaged,

GFP-negative, misaligned embryos or empty wells. While checking for the presence of blurry images, a Fiji macro was used to calculate the variance value for each image (Fig. 19 A,B; Script. S.5). Variance values so ascertained were directly proportional to the bluriness of the image. Low variance indicated higher probability of blurry or poor quality image, whereas higher values denoted crisp images (Fig. 19 C,D). The script led to the creation of csv files per image containing the variance value assigned to it. The threshold limit of 400 pixel values was used for this classification, images below this value were marked as blurry with the help of an adjoining script written in Python (Script. S.5) (Pandey et al., 2019).

On treating the images with Laplace Filter, the regions of extreme intensity variations can be underscored and this made it a useful tool for boundary detection. Therefore, in order to score blank images, Laplace Filter was applied before calculating the image variance (Fig. 19 E-H). As each outlier is recognised as a separate entity with its own outline, the presence of several kinds of indelible outliers and noise in the blank images filled them with exponentially more number of detectable edges after “Laplace Filter” application. Thus, the variance calculated for these images are usually higher than the normal images. Henceforth, images with variance above 125 were classified as blank. Blank and blur detection scripts had an overall efficiencies of 99% and 97% respectively (N = 288). In the whole primary screen, a total of 1,709 out of 20,544 acquired images were removed, which could have otherwise led to skewing of data analysis based on false positives occurring due to manual handling of thousands of embryos (Pandey et al., 2019).

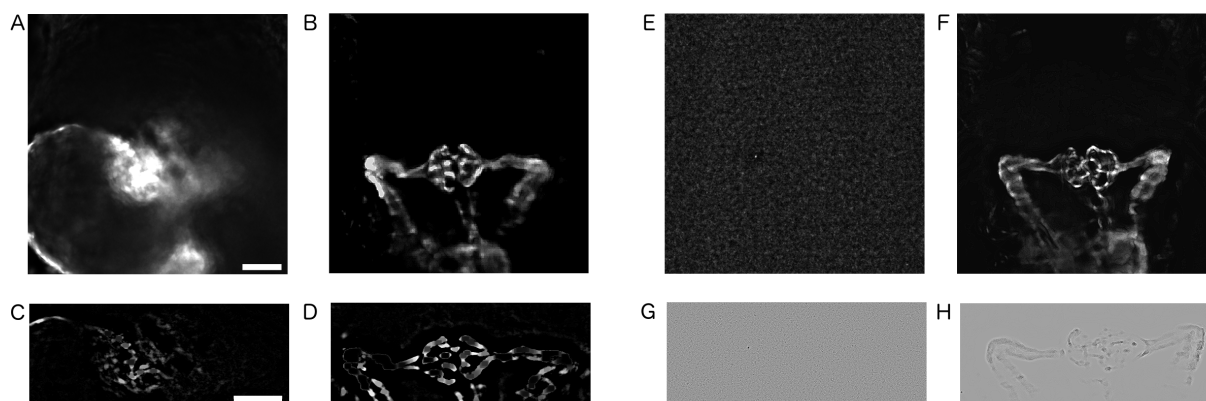


Fig. 19: **Quality control and image filtering.** (A-D) Pre-processed images used for the quality check step. In both blank and blur detection process, the images acquired with 10x objective were cropped as seen in (A,B,E,F). (C,D) In blur detection, the background noise was reduced using "Subtract Background" plugin in Fiji followed by variance calculation. Images below 400 variance value were classified as blurry. (G,H) In blank detection, "Laplace Filter" was used before variance calculation and images above 124 variance value were considered blank. Scale bar in A and C are 50 μm (Pandey et al., 2019).

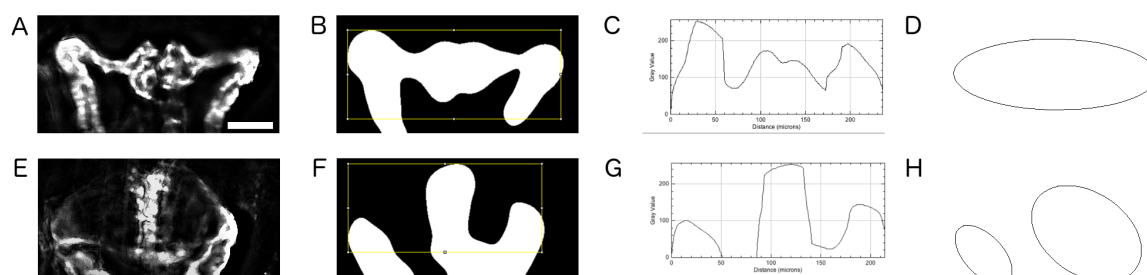


Fig. 20: **Image categorisation and phenotype detection.** Pictorial representation of (A-D) wild-type and (E-H) cystic images acquired with 10x objective and checked by pronephric phenotype detection script. (B,F) Pre-processed images were denoised and thresholded. An optimised bounding box was automatically drawn to ensure inclusion of kidney tissue. (C,G) Examples of plot profiles for control (C) and cystic kidneys (G). The difference between the resulting profiles were analysed and categorised as either wild-type or cystic kidney. (D,H) Implementation of confirmatory script to check the previously classified pronephric phenotype. Number of ellipses surrounding the ROI and ellipse major axis length of the largest ellipse was measured. Images with ellipse values above 299 pixels were classified as wild-type. Scale bar in A is 50 μm (Pandey et al., 2019).

In the screen, pronephroi were observed to resemble either the wild-type phenotype or cystic kidney phenotype (Fig. 6 I-L; Fig. 20 A,E). The former was seen in Ctrl-MO injected embryos, accidentally non-injected embryos and some hits, while the latter was seen at varying degrees of extremity depending on the compound treatment, experimental day and injections for all ift172-MO embryos. A basic phenotypic categorisation of the entire screen was performed using a workflow established on two algorithms i.e. calculation of pronephric and cystic areas of all images. First, cropped pronephric images were thresholded and an ROI with optimised dimensions was automatically placed within the images to contain the glomerular regions (Fig. 20

B,F). These ROIs were then subjected to “Plot Profile” command in Fiji. The said command displayed an array of pixel intensities inside the selection; X-axis marked the distance within the ROI, while the Y-axis marked the average of the pixel intensities. Therefore, “Plot Profile” action on a wild-type kidney resulted in pixels intensity values higher than zero. However, in the absence of a wild-type kidney, ROI covered the non-fluorescent cystic areas, generating an intensity drop resulting in zero values (Fig. 20 C,G). This principle formed the basis of cystic and wild-type type kidney classification. As this script was run independently of the blank detection script, an additional image quality check was included so that the presence of blank images did not skew the results. Processed images, post thresholding were checked for their “% Area fraction”. Images with 100 %Area value were marked as blank images and were inverted prior to their profile plot execution. This check led to the omission of falsely classified wild-type images resulting due to non-zero values generated by blank images.

An auxiliary script was run in addition to the first wild-type classification script for confirmation. The script generated a mask from binary image data, displaying the best fit ellipse of the encompassed ROI. Large ellipse in the images implied large chunks of unbroken structures, as seen in the case of wild-type pronephroi whereas, small ellipses represented tubules and marked the presence of non-fluorescent regions, which was used as a marker of cystic pronephroi. The “Major” value denoted the largest diameter of the ellipse and served as an apt parameter to quantify these results. Ellipses with major value larger than 299 pixel values were classified as a wild-type kidney (Fig. 20 D,H). This auxiliary classification was implemented in the end result only if the previous script failed to classify a given image to its respective category. The image classification script had an overall efficiency of 93.7% (N = 288) (Pandey et al., 2019). Henceforth, with the help of above three methods, low quality images were automatically excluded from the analysis pipeline with fine accuracy, without utilising any complex image recognition tools.

4.5.3 Image Processing and Pronephric Area Quantification

All the processed images were analysed to get the total pronephric area to determine the extent of cystic suppression. Pronephric area in wild-type kidneys referred to the glomerular and tubular region (Fig. 21 A-F). However, in the cystic kidneys, it included the cystic areas along with the glomerular and tubular region (Fig. 21 G-L). Therefore, scripts were run in order to calculate both pronephric and cystic areas in all images (Fig. 21 A,G). After pre-processing, due to

the presence of some unremovable outliers and noise, not all particles in the image contributed to the pronephric region. To ensure the selection of correct particles at first, the morphological descriptors of all the particles were calculated using pre-programmed “Analyze Particles” plugin in Fiji (Fig. 21 C,J,E). Henceforth, all particles passing the set number and morphological features were extracted and their areas were summed together to get the pronephric area. This operation was performed by using a Python-based script (Script. S.5). The value obtained here served as the final area for wild-type images.

In cystic kidneys, pertaining to evasion of pronephroi by tumour cells, the overall structure becomes completely disorganised as non-fluorescent tumour cell population multiplies and pushes the wild-type GFP cells away, creating a dark mass in the centre surrounded by faint and discontinuous array of fluorescent cells from glomerulo-tubular structures. (Fig. 6 K,L). Although, being blurry and unable to form closed boundaries, the fluorescence from these cells provides an overview of the tumour size. Henceforth, the cystic areas were evaluated by first inverting and then tracing a convex hull around the pronephroi (Fig. 21 D,J,K, (Landini; Pandey et al., 2019)). Convex hull, being the smallest convex containing the pre-defined pronephric boundaries precisely served the purpose of closing the structure and providing a refined overview of the cystic size. Once again, the morphological descriptors for all the particles so generated were calculated using the “Analyze Particles” plugin in Fiji, similar to the pronephric area calculation. As previously mentioned, not all the particles in the image contributed to the cystic areas. Consequently, they were filtered through the pre-defined parameter check and, the area values of cystic particles obtained were summed up and assigned as cystic area value. Although, the script was run on all images but due to significant differences in the morphology of the cystic and non-cystic images the extracted particles were mostly from the cystic images.

The two types of area calculated for each image were merged in a csv file in the “Analysis Folder” and the images were checked for their blank, blurry and wild-type status. If found in the blank/blurry category the images were disregarded from analysis and zero area value was assigned to it. In the case of wild-type kidneys, the areas calculated for the pronephric regions were considered as the final area of the pronephroi (Fig. 21F). The images in the cystic category were assigned the sum of areas calculated for both pronephric and cystic particles (Fig. 21L). Higher area values were correlated with the bigger cyst, whereas lower values suggested the presence of either wild-type or suppressed cystic phenotype. In conclusion, these automatically quantified areas represented the overall changes in pronephric morphology.

Consequently, without the implementation of any machine learning approach or complex pat-

tern recognition technique the algorithm self-sufficiently recognised phenotypic parameters accurately. It also possesses the potential to serve as a template for classification of complex objects such as, organs, tissues or whole embryo features. Additionally, the script can be easily reproduced using an open source software (Pandey et al., 2019).

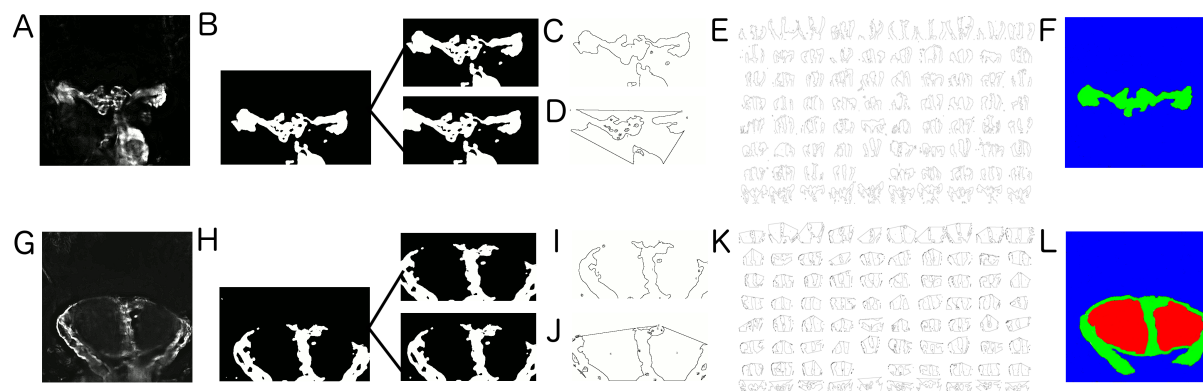


Fig. 21: **Automated measurement of pronephric and cystic areas.** (A-F) and (G-L) are the pictorial representation of wild-type and cystic area quantification method, respectively. (A,G) show the initial XYZ-projected image used by the script, which are further cropped and thresholded (B,H). These images are then recropped to focus precisely on the glomerular region. This is followed by (C,D) and (I,J), where the images are binarised and are subjected to "Analyze Particles" plugin both before (C,I) and after (D,J) drawing convex hull around ROI. (C,I) present the pronephric area whereas, (D,J) pictorially depict the cystic area acquisition. All areas once collected are filtered through selective parameters and assigned to images based on their pre-defined status (i.e. wild-type or cystic) decided earlier by the quality control step. (E,K) are the corresponding montages showing the collated binary images used for the pronephric and cystic area calculation respectively. (F,L) Green depicts GFP-positive pronephric tissue and red depicts cystic area quantified by the script.

4.5.4 Heatmaps: An Interactive Output for Compound Class Scoring

Generation of heatmaps representing the end results of quantification served as an interactive way to score for phenotype altering compounds (Fig. 12 A,B). Heatmaps were generated using matplotlib library of python. Each cell in the heatmap corresponded to the wells of the imaged microtitre plate. Cells were assigned a specific shade of colour from the 'Inferno' colour scheme, which was dependent on the pronephric area assigned to the image acquired from that particular well. Dark to light colours on the purple end of the spectrum displayed wild-type and suppressed phenotypes whereas orange to brighter yellow marked the increasing cyst size (Fig. 12B). One can interpret the efficacy of the compounds just by focussing on the row colour. Once a row with required phenotype is found one can investigate the used compound further by going to those image sets and analysing the type of effect and toxicity grade details.

4.6 High-Content Screening Results

4.6.1 Pharmacological Cyst Modifiers Identified by High-Content Screening

The High-Content Screening was performed to identify new pharmacological modifiers of cystic nephropathy, which could come to rescue in cases of successful post screen approval. The execution involved exposure of batches of 15–17 *ift172*-MO injected larvae to test compounds from the Prestwick library in a 12-well plate, starting from 24 hpf till 72 hpf. At this time point, the larvae were transferred to 96-well microtitre plate (1 larva/well), dorsally oriented and subjected to image acquisition using smart imaging workflow. The images acquired were processed and analysed with the help of automated quantification module generated for the screen. This was followed by the application of statistical tests on the automatically quantified results from the primary screen. It helped to streamline data, making it account for fluctuations documented due to daily manual injections and genetic variability. The raw data was normalised in reference to each microtitre plate specific mean of negative controls (i.e. *ift172*-MO injected larvae) and subjected to extreme value distribution test (Sec. 3.5, (National Institute of Standards and Technology)). Hinging on the identification of overall cyst suppression at a coarse level, the used test optimised data by filtering out all the extreme negative and extreme positive values. The degree of cyst size suppression by test compounds was determined by the difference evaluated between the cystic control and test larvae. On the basis of this quantification, all the compounds lying below 0.75 value were chosen as hits from the library (Fig. 22). This led to the identification of 60 hits with mild to high cyst suppressing activity.

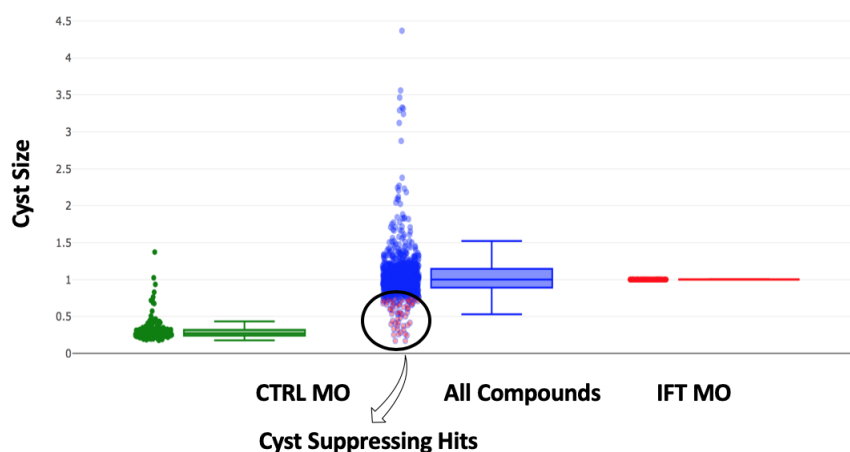


Fig. 22: Summary of the results obtained after primary round of screening Prestwick compound library. Box Plot highlighting the subset of screened compounds found as positive cystic modifiers based on the automated quantification module. The values represented were normalised to the plate-specific mean controls. This led to the selection of 60 primary hits, which were further focussed upon.

Tab. 3: Tabular representation of hits according to their activity and toxicity

		Low	Activity Intermediate	Strong	Total
Toxicity	None	12	7	1	20
	Mild	7	8	1	16
	Severe	3	11	10	24
Total		22	26	12	60

More than 45% of these compounds ranged from intermediate to high toxicity range (Tab. 3; 4). Around 90% of the highly toxic compounds had intermediate to strong cyst suppressive activity, in contrast to the low and mildly toxic compounds, where 90% of the population had low to intermediate activity range. The compounds were also classified according to the Anatomical Therapeutic Code (ATC) (Fig. 23 A,B; 24) (World Health Organization, 2017). Based on this classification, amongst the group of effective compounds a substantial majority of 30% belonged to Genito Urinary Systems and Sex Hormones (G). This class included compounds from pharmacological sub-groups of anti-infectives and antiseptics without corticosteroids, estrogen and progestogen combinations. The class G was closely followed by Anti-neoplastic and Immunomodulating Systems (L); taxanes, selective immunosuppressant, folic acid and purine analogues, formed one-tenth of the hits from this class. With compounds exerting mild to intermediate activity, the Musculo-Skeletal class (M) made the third most effective class

Tab. 4: Tabular representation of hits scored from first round of screening on Prestwick compound library. The table shows activity of the hits and their associated toxicity.

	Low	Activity Intermediate	Strong	Total
None	Tioconazole	Homatropine hydrobromide	Acetyl salicylsalicyclic acid	20
	Methiothepin maleate	Methotrexate		
	Docetaxel	Etodolac		
	Dofetilide	Dilazep dihydrochloride		
	Phenprobamate	Cyproterone Acetate		
	Misoprostol	Milrinone		
	Sulfadoxine	Bacitracin		
	Cyclopentolate hydrochloride			
	Flubendazole			
	Altretamine			
	Pramipexole dihydrochloride			
	Chlormadinone acetate			
	Toxicity Mild	Flumethasone pivalate	Flumequine	
4-aminosalicylic acid		Paclitaxel		
Verteporfin		1,8-dihydroxyanthraquinone		
Tentoprazole		Ethinylestradiol		
Famprofazone		Nelarabine		
Glycopyrrolate		Nabumetone		
Fluticasone propionate		Niridazole		
Severe	Digitoxigenin	Epiandrosterone	Clotrimazole	24
	GBR 12909 dihydrochloride	Leftunomide	Piroxicam	
	Fluspirilen	(R)-Naproxen sodium salt	Cycloheximide	
		Racecadotril	Equilin	
		Butoconazole nitrate	Ciclesonide	
		Butylparaben	Monobenzone	
		Ethynodiol acetate	Toltrazuril	
		Adapalene	Nimodipine	
		Loteprednol etabonate	Dydrogesterone	
		Sertaconazole nitrate	Omeprazole	
		Astemizole		
Total	22	26	12	60

in this list. It was populated with non-steroids, anti-inflammatory and anti-rheumatic agents such as, phenprobamate, nabumetone, etodolac, (R)-Naproxen sodium salt. The only exception to the overall mild activity of this class was shown by Piroxicam with its high level cyst suppression. The fourth position was shared by Respiratory (R), Cardiovascular, Sensory Organs (C) and Dermatologicals (D) class; with an individual contribution of 6.6% each. Respiratory compounds included obstructive airway alleviating agents such as Ciclesonide, Fluticasone propionate, Glycopyrrolate and anti-histaminic agent, Astemizole. Cardiovascular agents were comprised of therapeutic sub-group such as, cardiac stimulant-Milrinone, calcium channel blocker-Nimodipine, vasodilator-Dilazep dihydrochloride and anti-arrhythmics-Dofetilide. Sensory compounds encompassed anti-neovascularisation agent, verteporfin; anti-

cholinergics, such as, Cyclopentolate hydrochloride and Homatropine bromide along with anti-inflammatory agent, Loteprednol etabonate (corticosteroid, plain). Dermatological hits included Monobenzone, which displayed high cyst suppression; whereas topically applied preparations of Adapalene and Sertaconazole nitrate showed intermediate effect. Both Anti-infectives for Systemic Use (J) and Alimentary Tract and Metabolism (A) classes, ranked second last with their individual contributions of 5% each to the hit list. The former was mainly comprised of aminosalicyclic acid derivatives and anti-bacterials, whereas the latter included therapeutic subgroup for acid related disorders such as, Misoprostol and Omeprazole along with anti-diarrheal, Racecadotril. With the respective contribution of two compounds each, the last place was shared among Anti-parasitic, Anti-repellant, Insecticides (P); Nervous System (N) and Veterinary Use (Q) compounds. In this group, class P comprised of anti-helmentic drugs, Flubendazole and Niridazole; class N contained dopamine agonist- Pramipexole dihydrochloride and diphenylbutylpiperidine derivatives- Fluspirilen; and Toltrazuril and Sulfadoxine belonged to class Q. Toltrazuril from the veterinary section demonstrated significant suppressive activity, whereas only mild effects were shown by Sulfadoxine from this class.

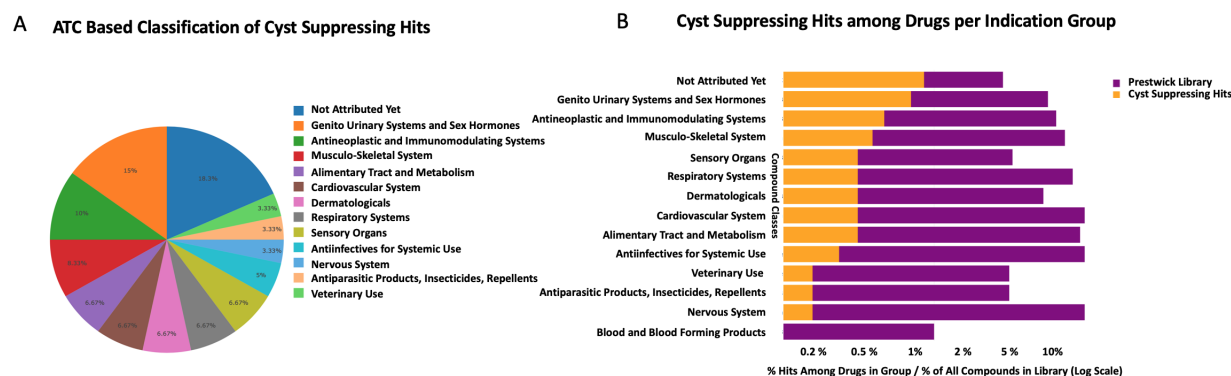


Fig. 23: ATC categorisation of compounds obtained from Prestwick library screening. (A) and (B) Pie and bar chart, respectively show the ATC-based classification of cyst suppressing compounds from the library. (A) shows the ATC-based per cent distribution of the hits. (B) shows the logarithmic scale division of the hits in reference to the available library compounds in the particular class.

Some of the scored compounds were not found in any category of ATC classification. These compounds accounted for maximum i.e. 18% of the total hits (Fig. 23D). Out of these, more than 60% showed intermediate to high level suppression. The list included high impact compounds such as, Acetylsalicylsalicylic acid, which is normally encountered as impurity during aspirin production (Bundgaard, 1974); Cycloheximide – a fungicide and Equilin – an estrogen supplement (Verbin and Farber, 1967). Intermediate and low impacting compounds included Methiothepin maleate – a serotonin receptor antagonist; Digitoxigenin – a carden-

olide, an aglycon of digitoxin; GBR 12909 dihydrochloride – a dopamine uptake inhibitor; 1,8-dihydroxyanthraquinone; Phenothiazine – a Dopamine D2 Receptor antagonist; Butylparaben – a preservative and flavoring agent also actively increasing histamine release and cell mediated immunity. Although, the library contained compounds from Blood and Blood Forming Products (B) class, but no effective hits from this category were spotted. This, concluded the list of compounds scored as hits during the first round of screening.

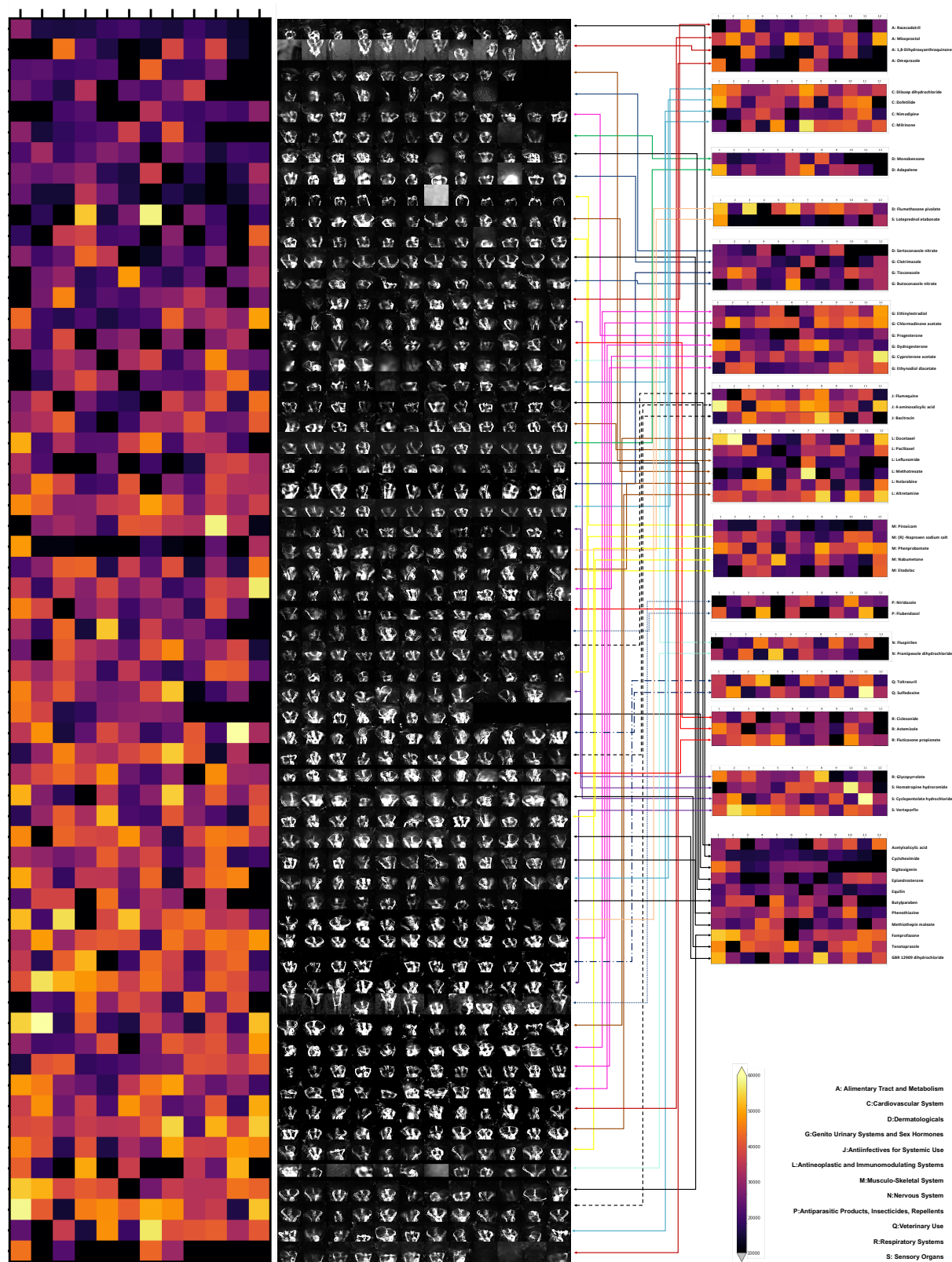


Fig. 24: Heatmaps and corresponding pronephroi of the hits identified from the primary screening of Prestwick chemical library. In the last panel heatmaps of hits from the same ATC class are grouped together.

4.6.2 Dose Response Studies on High-Content Screening Hit Compounds

In order to validate the effects of the compounds resulting from primary Prestwick compound library screening sec. 4.6.1 they were subjected to dose response studies. The larvae batches were exposed to the dilution series of hits comprised of 1 μ M, 6.25 μ M, 12.5 μ M and 25 μ M concentrations. Same protocol as in the previous section was used for this experiment, where ift172-MO injected larvae batches were exposed to the concentration series of test compounds in a 12-well plate from 24 hpf till 72 hpf. Finally, the larvae were transferred to 96-well microtitre plate (1 larva/well), dorsally oriented and subjected to image acquisition using smart imaging workflow and processed and analysed with the help of automated quantification module generated for the screen. This led to the validation of the hits and narrowing in on an optimally effective concentration of the confirmed hits with comparatively lower levels of phenotypic side-effects for each compound. Many previously effective compounds, did not show any scorable phenotypic change in this round of experiment. Around 91% of the the low effect category compounds attributed to the non-effective group. This was followed by an almost four times increase in the activity leading to 35% effective compounds in the intermediate range and 50% in the high activity class. The initial decision to include these compounds was based on two factors i.e their weak suppression effect, along with their presence within the chosen statistical threshold range. The latter being reliant on automated quantification module lacked human image recognition prowess and was prone to an error rate of 9-10%. Additionally, the major difference in the effectivity of primary and secondary screening compounds could also be due to the difference in the batches and manufacturing dates of the ordered compounds. In addition to that, the primary screen compounds were already thawed and aliquoted twice before use, this might have also resulted in the attenuation of compound activity.

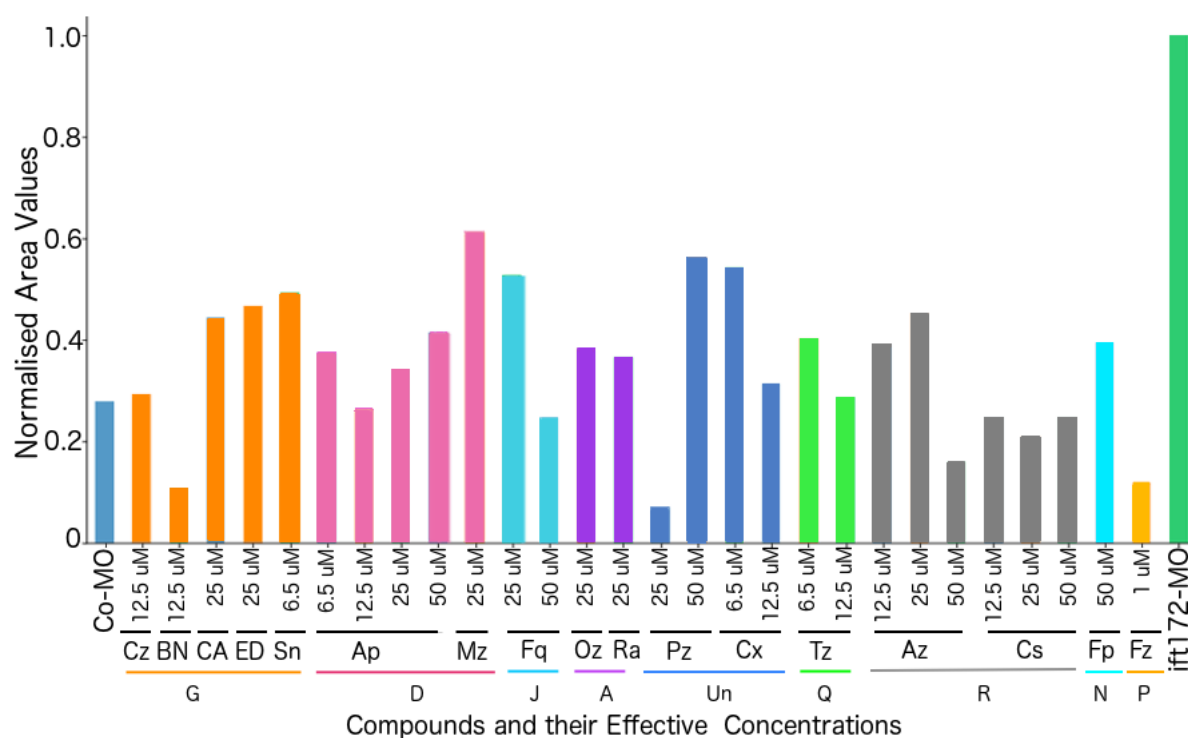


Fig. 25: **Automated qualitative analysis of cyst suppression after dose response study.** Bar plot presenting cyst areas at all effective concentrations obtained from dose response studies performed on hits identified from the first round of screening. The plot represents the normalised data against the plate-specific mean of negative controls (i.e. *ift172*-MO injected larvae). Effective concentrations of each compound are shown by black lines and the coloured lines denote their ATC.

Finally, in this process, 17 compounds showing effects ranging from strong to intermediate suppression at varied concentrations were identified as hits (Tab. 5). The compounds were: Astemizole (Az), Ciclesenoid (Cs), Adapalene (Ap), Phenothiazine (Pz), Flumequine (Fq), Fluspirilen (Fp), Cyproterone acetate (Ca), Ethynodiol diacetate (ED), Omeprazole (Oz), Racecadotril (Ra), Monobenzone (Mz), Clotrimazole (Cz), Butoconazole nitrate (BN), Cycloheximide (Cx), Toltrazuril (Tz), Sertaconazole nitrate (SN) and Flubendazol (Fz) (Fig. 25, 27, 28, 29, 30, 31, 32, 33, S.3, S.4, S.5, S.6, S.7, S.8). The hits based on plate specific normalisation against the negative control i.e. *ift172* at all their effective cyst suppressing concentrations are represented in the bar graph in Fig. 25. The individual graphs for the dose response study of each compound is present in the supplement (Fig. S.2).

Dose-Dependent Compound Effectivity

The higher end of the titration curve i.e. 50 μ M concentration was populated by class J and R representatives, Astemizole and Ciclesenoid, with twice reduced cyst sizes compared to the

Tab. 5: Tabular representation of effective hits from dose response studies done on the hits scored from first round of screening on Prestwick compound library. The table shows the level of activity of the hits and their concentration.

	Low	Activity Intermediate	Strong
Concentrations (μM)	1 μM		Flubendazole
	6.5 μM	Sertaconazole nitrate Adapalene	Toltrazuril Cycloheximide
	12.5 μM	Astemizole	Toltrazuril Cycloheximide Adapalene Butoconazole nitrate
	25 μM	Astemizole Flumenquine Cyproterone acetate Phenothiazine Ethinodiol diacetate Monobenzone Racecadotril	Omeprazole Clotrimazole Adapalene
	50 μM	Astemizole Phenothiazine Fluspirilen Ciclesenoid	Flumenquine Adapalene

control population (Fig. 30 A,B; S.3 A-D; Fig. S.2 A,B). Az, however, already had significant suppression at 25 μM. Following the trend of higher concentration effectivity, the sole representatives of class J, Flumequine; class N, Fluspirilen; and ATC unclassified hit, Phenothiazine were also operative in the range of 25 and 50 μM, with 50 μM being the most active point (Fig. 31A; 32A; 33A; S.3 G-J, S.4 A,B). Intact, but dead larvae at 50 μM concentration of Pz showed 1.6 times cystic reduction compared to cystic control, whereas an almost 2.5 times suppression was seen in the case of Fp (Fig. S.2 D,F). Flumequine treatment suppressed the cyst size strong enough to almost mimic the wild-type phenotype, however, general morphological degradation was still observed (Fig. 32A; S.3 I,J; Tab. 6). Adapalene, unlike the rest of the group, was effective at all tested concentrations showing suppression ranging from 2.5–3 times the cystic control (Fig. 28A; S.3 E,F; Fig. S.2C). The extent of cyst suppression and side-effects exerted by Ap were concentration dependent. Falling in the 25 μM suppression range, Cyproterone acetate and Ethynodiol acetate displayed clear intermediate cystic suppression by 2–2.5 times (Fig. 27 C,D; S.5 A-D; S.2 G,H). The compounds had comparatively mild side-effects. Hailing from class A, both Omeprazole and Racecadotril effectively reduced the cysts to 3 times the control size at 25 μM concentration (Fig. 29 A,B; S.6 C-F; Fig. S.2 J,K). Similar to Oz, the skin depigmenting agent Monobenzone, was also effective at 25 μM with intermediate cystic reduction similar to Pz (Fig. 28B; 29A; 31A S.6 C-D; Fig. S.2I). Butoconazole

nitrate and Clotrimazole, from class G were strongly effective at 12.5 μM and reduced the cystic size almost to the level of wild-type controls (Fig. 27 A,B; S.7 A-D; Fig. S.2 L,M). At 12.5 μM , BN was quite effective in cyst suppression, however the compound also had significant effect at 6.5 μM (Fig. S.2M). Similar to BN, Cycloheximide was equally active at both 6.5 and 12.5 μM , with its suppression activity incremented by a unit at the higher concentration (Fig. 31 B; S.7 E,F; Fig. S.2N). Toltrazuril was the only compound belonging to class Q, which was scored as a strong hit. It almost restored the cystic pronephroi to their normal wild-type state at both 6.5 μM and 12.5 μM (Fig. 32 B; S.7 G,H; Fig. S.2O). Class D compound, Sertaconazole nitrate showed intermediate level activity, resembling Mz at 6.5 μM (Fig. 27E; S.8 A,B; Fig. S.2P). SN, although in class D, belongs to the imidazole derivative group similar to BN and Cz. Despite the extreme toxicity shown by Flubendazole (Fz), its effect on the pronephric structure seen in few barely sustaining larvae resembled the wild-type kidneys (Fig. 33B; S.8 C,D; Fig. S.2Q). This phenotype amelioration by the compound led to its inclusion in the hit list.

Tab. 6: Documentation of the external phenotype displayed by larvae under the treatment of effective hits scored from dose response screening study.

		Necrosis	Phenotype Heartbeat	Edema	Curved Body
50 μM	Astemizole	+	-	+	+
	Ciclesonide	+	-	+	+
	Adapalene	+	-	+	+
	Phenothiazine	+	-	+	+
	Flumequine	+	+	+	+
	Fluspirilen	+	-	+	+
25 μM	Cyproterone acetate	+	-	+	+
	Ethinodiol acetate	+	-	+	+
	Monobenzone	+	+	+	+
	Omeprazole	+	+	+	+
	Racecadotril	+	+	-	+
12.5 μM	Clotrimazole	+	-	+	+
	Butoconazole nitrate	+	-	+	+
	Cycloheximide	-	+	+	+
	Toltrazuril	+	-	+	+
6.5 μM	Sertaconazole nitrate	+	+	+	+
1 μM	Flubendazole	+	-	+	+

(+) present; (-) absent

Compound Toxicity

All compounds irrespective of their ATC groups showed toxic effects to a certain extent. Class

G compounds Cz, CA and ED treated larvae showed signs of edema, necrosis and hydroencephalus. However unlike Cz, CA and ED had normal heartbeat (Fig. 26, 27 A,C,D; Tab. 6). BN from this class had a survival rate of 33% at 12.5 μ M, which increased up to 80% with comparatively lower toxicity at slightly less effective concentration of 6.5 μ M (Fig. 26, 27B; Tab. 6). SN delineated heavy toxicity with complete mortality at tested concentrations of 50, 25 and 12.5 μ M. Larvae were able to survive only at the low concentrations of 6.5 and 1 μ M (Fig. 26, 27E; Tab. 6). Secondary effects displayed by Ap from class D were in direct correlation to the concentration; 1 μ M showed intermediate suppression with smaller pericardial edema and yolksac necrosis, while the rest of the concentrations presented higher suppression concomitant with bigger edema size and yolksac necrosis. At 50 μ M concentration, Ap exposed larvae had no heartbeat (Fig. 26, 28A; Tab. 6). Mz from the same class had a single effective concentration causing necrosis and 16% mortality (Fig. 28B). Exposure of both compounds from class A, Oz and Ra led to heavy necrosis (Fig. 26, 29; Tab. 6). Although Ra exposure unlike Oz led to slight to no edema in tested larvae. Effective at high concentrations of 50 and 25 μ M, Az from class R showed concentration dependent increment in the phenotypic toxicity, displaying only 50% survival rate at 50 μ M (Fig. 26, 30A; Tab. 6). Ciclesonide although effective in the same range showed extreme necrosis and intense dorsal curvature, along with no heartbeat at the functional concentration (Fig. 26, 30B; Tab. 6). Phenothiazine and Fluspirilen exposed larvae showed no heartbeat, huge edema, high necrosis, hydroencephalus and were mostly dead at 25 μ M concentration (Fig. 31A; 33A). On the other hand, effective at the same concentration Flumequine from class N did not cause heartbeat blockade (Fig. 32A, 26; Tab. 6). ATC unclassified compound Cx had concentration dependent exacerbation of visible side-effects causing 16% mortality at 72 hpf at 12.5 μ M (Fig. 31 B; S.7 E,F; Fig. S.2N). Both effective concentrations of the only class Q compound Tz showed high levels of edema, necrosis and hydroencephaly with an increment of 50% in mortality rate at 12.5 μ M (Fig. 26, 32 B; Tab. 6). Flubendazole (Fz), unlike rest of the hits led to more than 90% mortality at the lowest tested concentration of 1 μ M in the series (Fig. 33B; 26; Tab. 6).

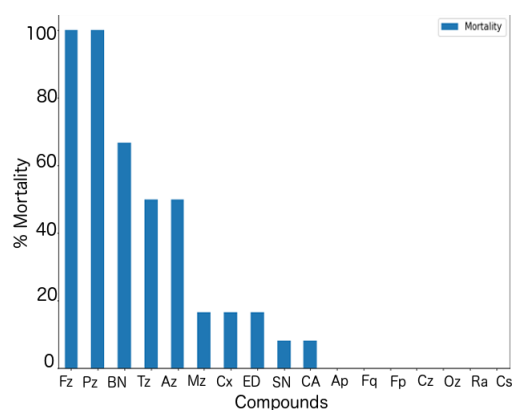
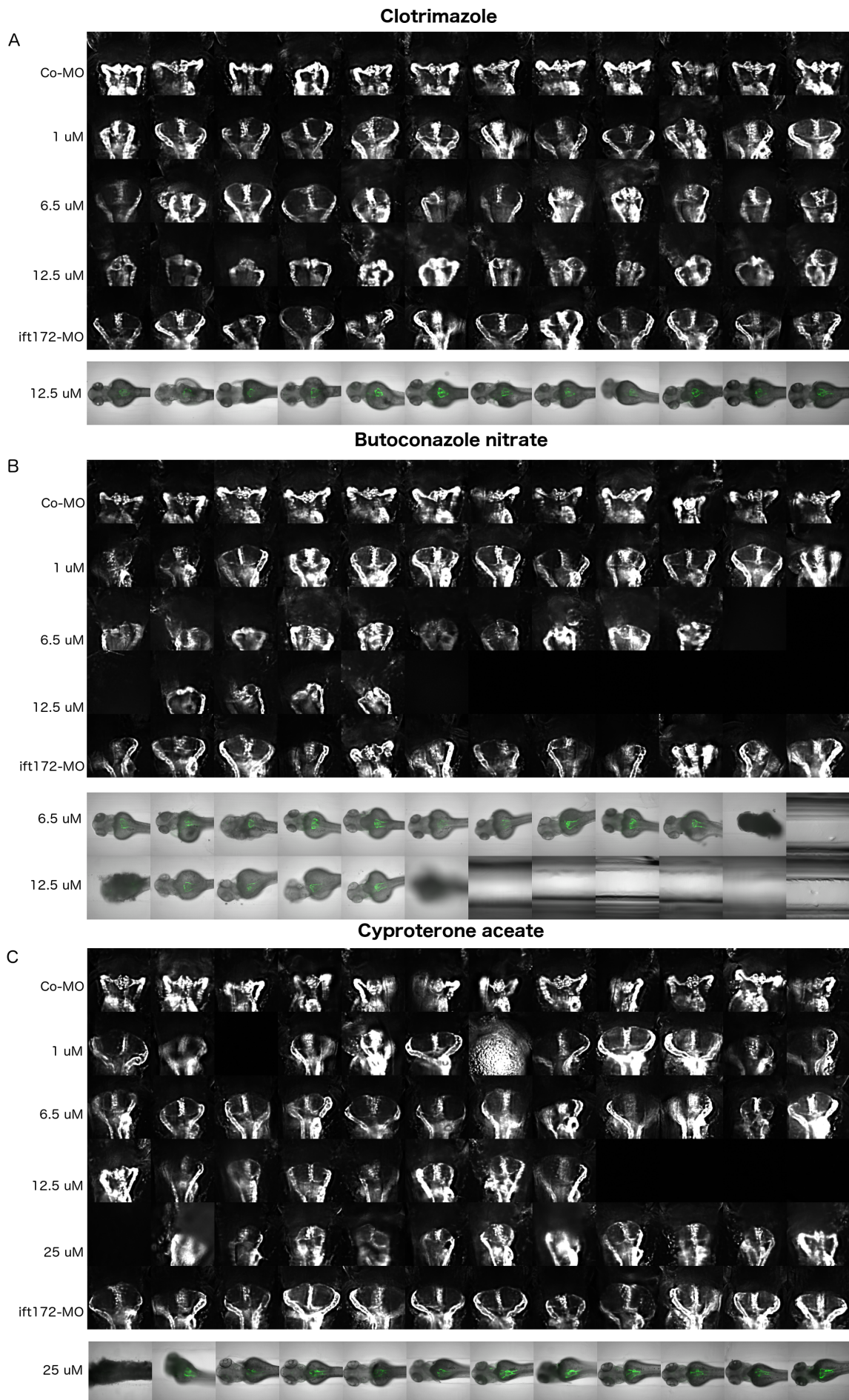


Fig. 26: **Mortality by compound.** Mortality rate shown by the most effective concentrations of the hits during dose response study

To summarise, the dose response study on the primary hits led to the identification of total 17 hits. Out of which, 13 showed intermediate to high level suppression and 7 had extremely strong suppression activity (Tab. 5). These compounds with their cyst suppressive effect shed light on several known and some lesser studied pathways associated with cystic nephropathy. Further investigation of these compounds in controlled molecular environment might assist in unraveling the mechanistic approaches exploited by these FDA approved drugs in alleviating the cyst formation.



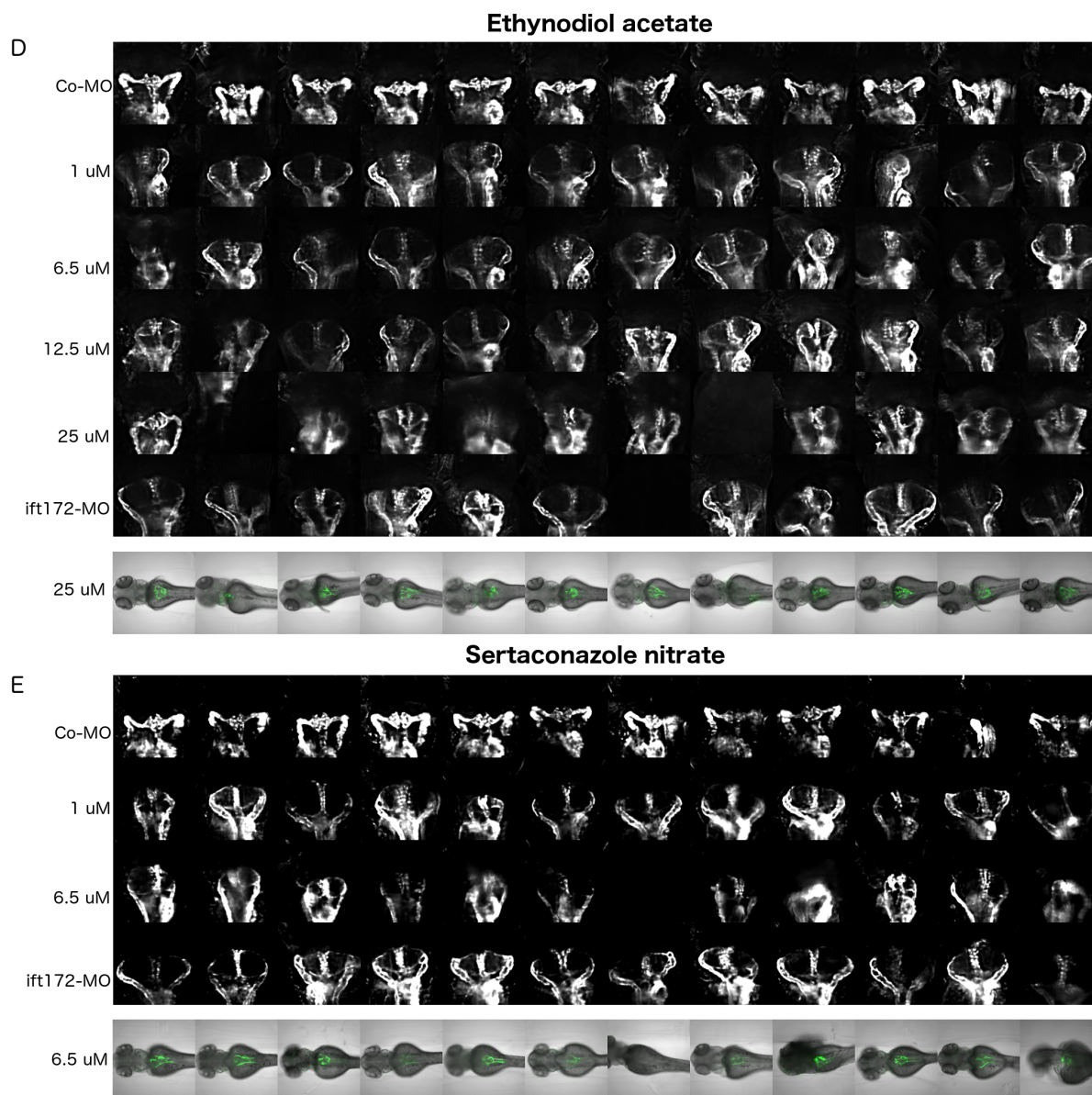


Fig. 27: **Hits effective from class G.** Fluorescent and bright-field overlaid montages of the effective concentrations of (A) Clotrimazole (B) Butoconazole nitrate (C) Cyproterone acetate (D) Ethynodiol acetate (E) Sertaconazole nitrate.

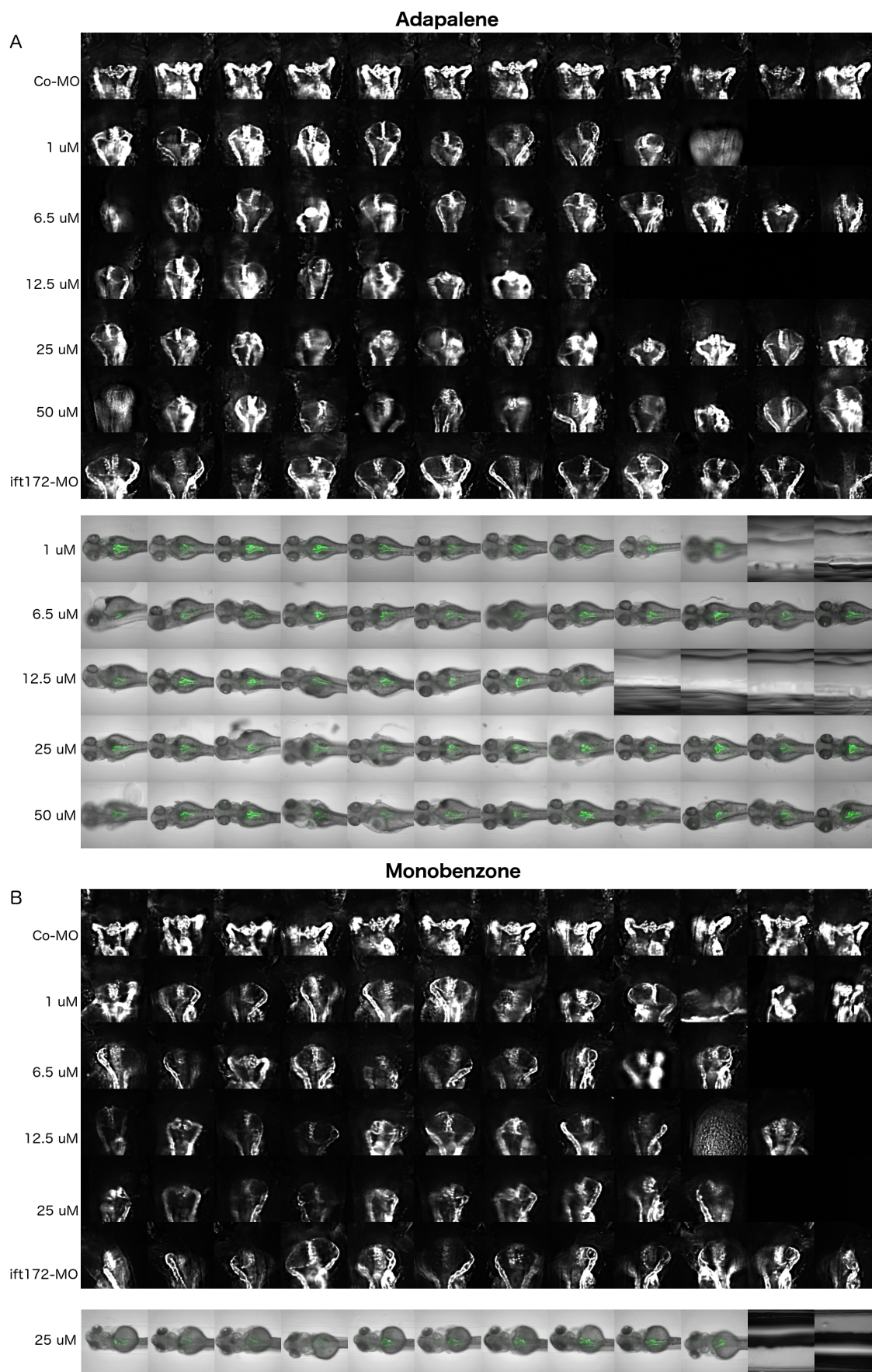


Fig. 28: **Hits effective from class D.** Fluorescent and bright-field overlaid montages of the effective concentrations of (A) Adapalene (B) Monobenzone.

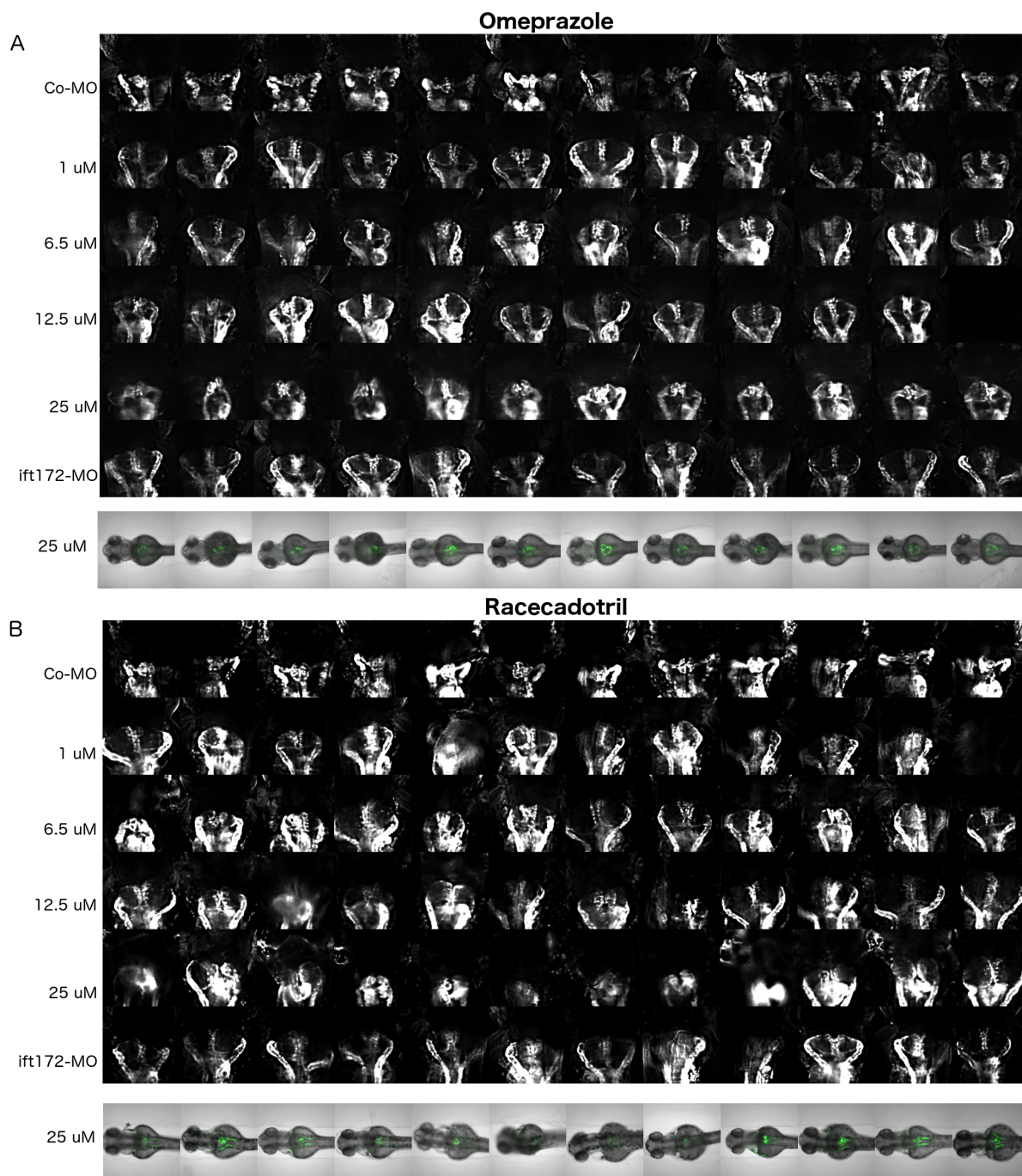


Fig. 29: **Hits effective from class A.** Fluorescent and bright-field overlaid montages of the effective concentrations of (A) Omeprazole (B) Racecadotril.

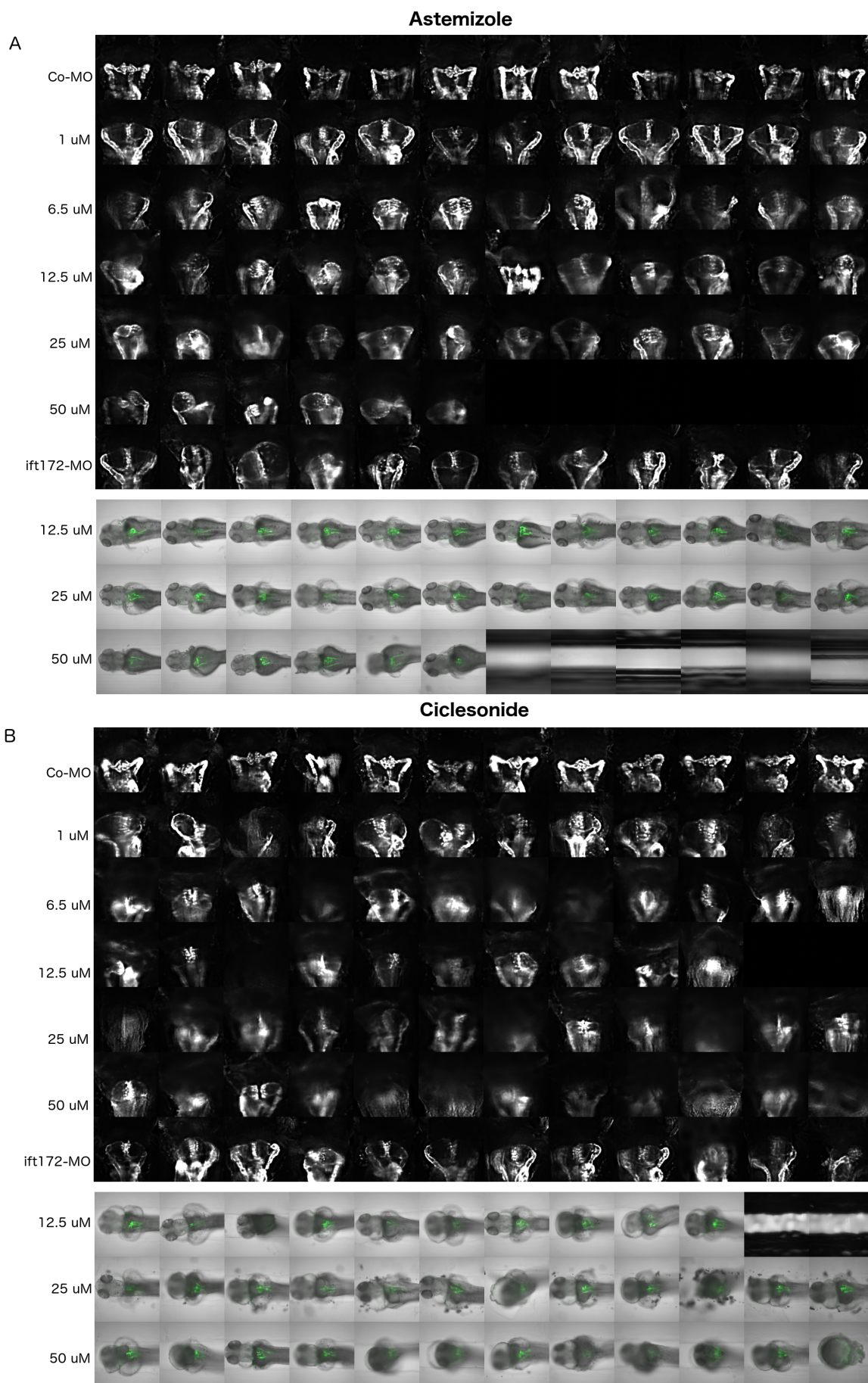


Fig. 30: **Hits effective from class R.** Fluorescent and bright-field overlaid montages of the effective concentrations of (A) Astemizole (B) Ciclesonide.

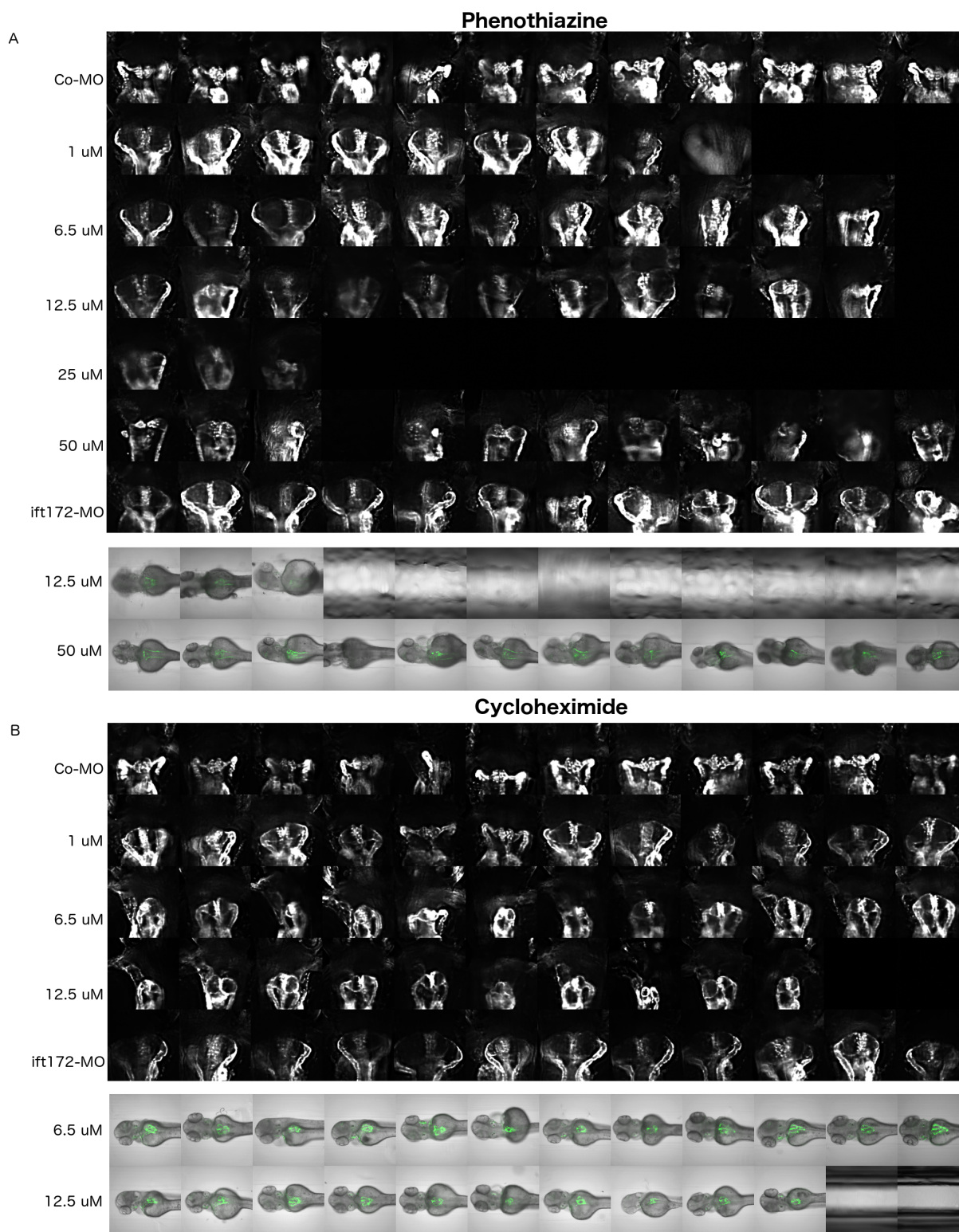


Fig. 31: Hits effective from class Un. Fluorescent and bright-field overlaid montages of the effective concentrations of (A) Phenothiazine (B) Cycloheximide.

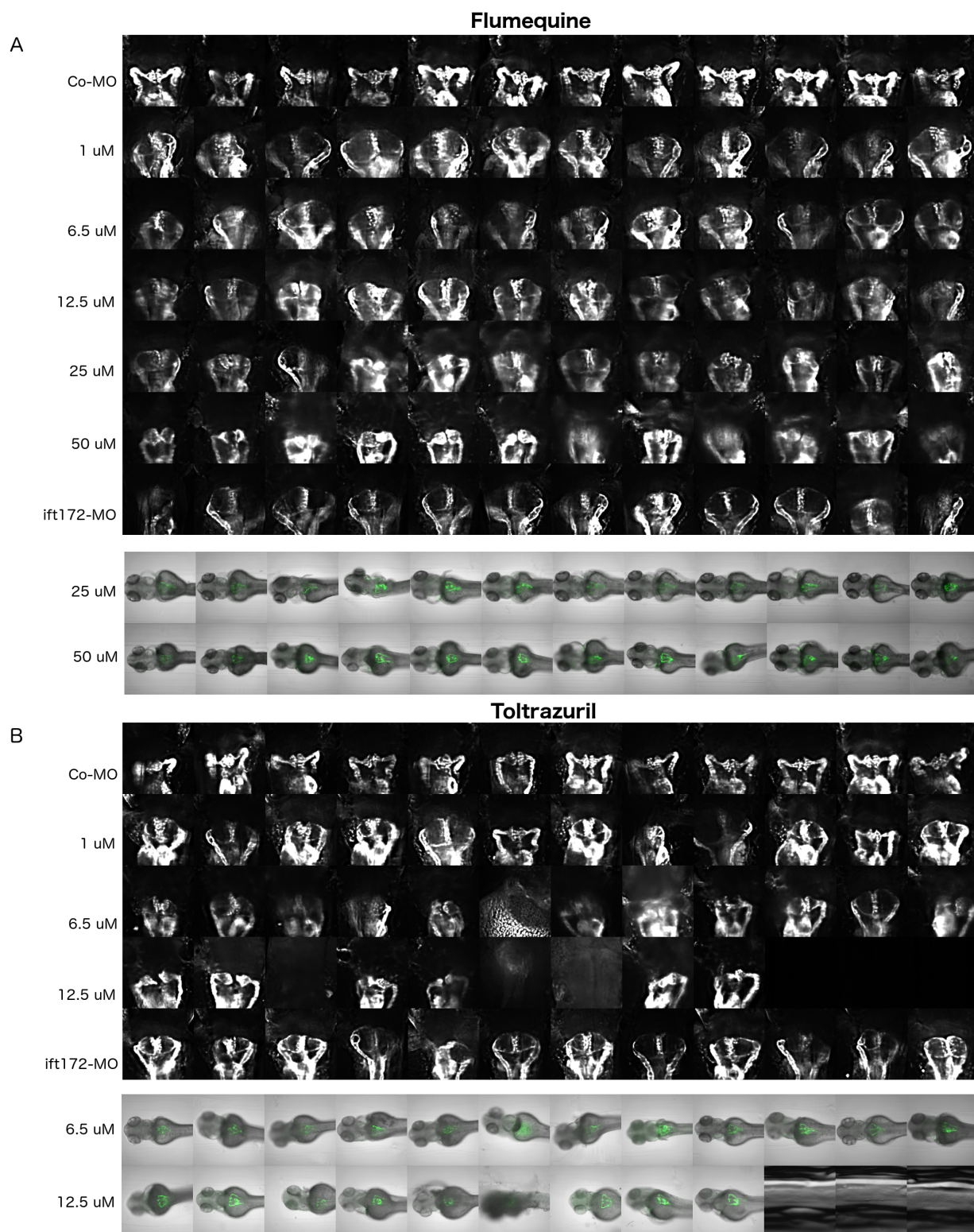


Fig. 32: **Hits effective from class J, Q.** Fluorescent and bright-field overlaid montages of the effective concentrations of (A) Fumequine (B) Toltrazuril.

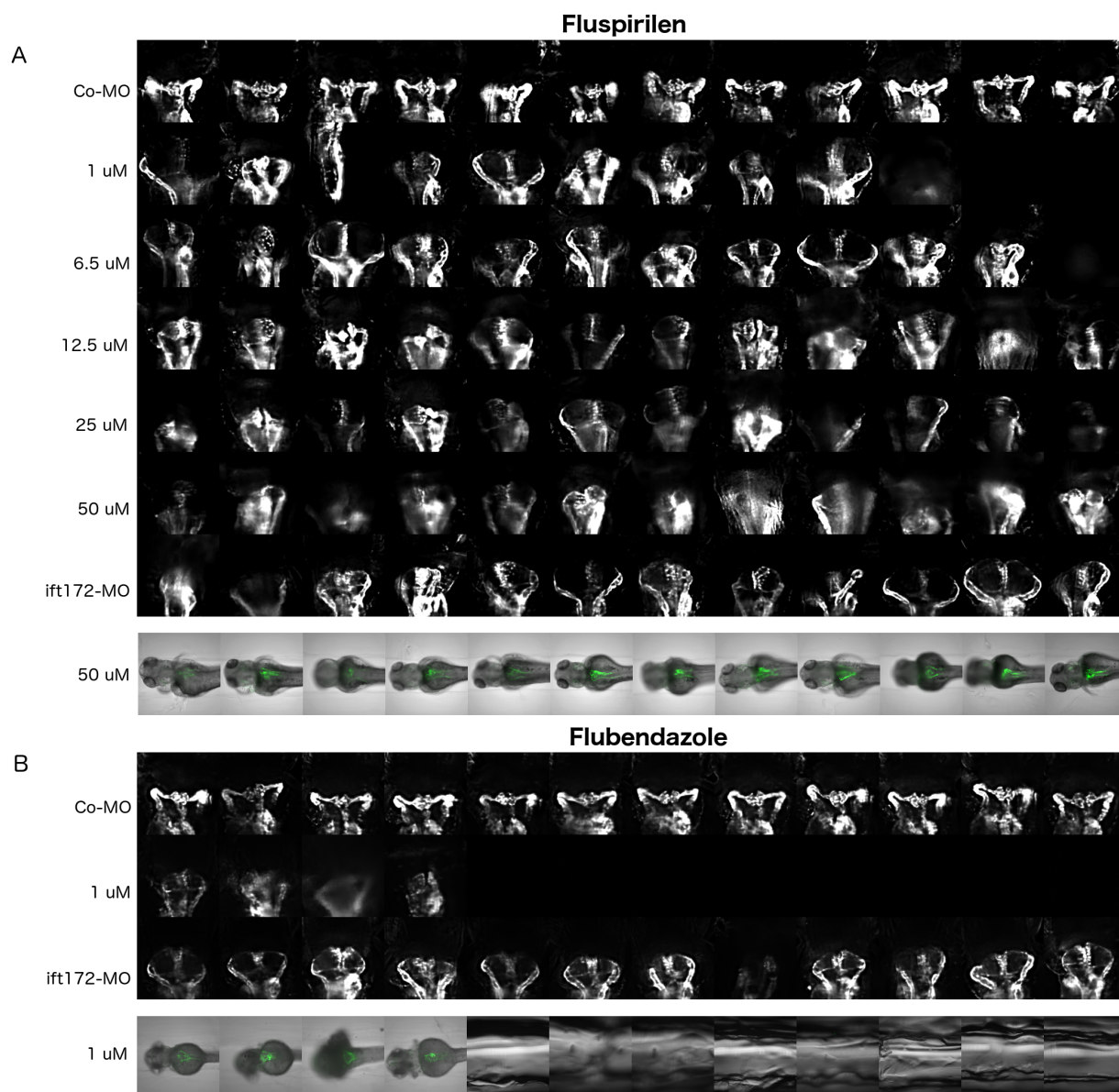


Fig. 33: **Hits effective from class N, P.** Fluorescent and bright-field overlaid montages of the effective concentrations of (A) Fluspirilen (B) Flubendazole.

5 Discussion

Cystic kidney diseases, affecting 12.5 million people annually across the world, are still considered a largely untreatable group of disorders that inevitably progress to end-stage kidney disease, although the mechanisms of pathogenesis and progression are quite well understood (Harris and Torres, 2009; Torres et al., 2007). Recently, Tolvaptan, a vasopressin V2-receptor antagonist, has been approved as the first effective treatment of autosomal dominant PKD (Otsuka America Pharmaceutical, 2009; US Food and Drug Administration, 2018). However, the effect of the drug on cyst progression is relatively weak and its tolerability is limited by polyuria and hepatotoxicity. Hence, there is a persistent medical need for novel therapies of cystic kidney diseases.

High-throughput compound screening is an efficient way to explore potential therapeutic effects of known and novel chemical compounds. Robotic capabilities allowing fast and efficient sample handling and analysis comes into play. Careful complementation of such an automated High-Content Screening (HCS) with a scalable human disease mimicking animal model equips it with the possibility to be studied in statistically relevant population size. The past three decades of advancement in zebrafish studies have proved it to be an excellent subject for these studies.

However, the efficient utilisation of zebrafish in large scale screens requires stringent workflows, that will efficiently make use of the HCS friendly features of the model from concept to practice (Pandey et al., 2019). Models of cystic nephropathy in zebrafish often present challenging phenotypes, which makes it difficult to acquire and evaluate the features correctly in a HCS setting. There are many studies conceptualising such protocols in the field but very few successfully executed screening studies. Proper application of zebrafish as an HCS tool requires addition of robust phenotypic read-outs along with efficient screening assays. Underscoring all these points of sample and protocol handling, an automated small molecule screening platform has been implemented here. The HCS is focussed on cystic nephropathies and aims to reduce the average time spent on preliminary screening of potential drug candidates by automating the imaging, improving the resolution of acquired images and simultaneously reducing the unnecessary details by capturing the ROI and automating the phenotype quantification (Fig. 5). The developed pipeline was tested by evaluating the *in vivo* of several interesting small molecules with known and unknown functions in human cystic nephropathy mimicking model of

zebrafish.

5.1 Choice of the Disease Model

ift complex with 48 coding sequences in both human and zebrafish shows close resemblance to each other. With an overall difference of 4 amino acids in numbers, a protein BLAST revealed 75% similarity between the *ift* transcripts of both organisms. In addition to that, partial protein alignment of the gene also demonstrated the conservation of mutational sites in case of Jeune asphyxiating thoracic dystrophy (JATD) (Halbritter et al., 2013). All these similarities were in turn complemented by the molecular and functional homology at pronephric level between the two. Originating as a coelomic invagination in the IM, zebrafish pronephroi present a simple yet complete model of renal architecture mimicking human cystic nephropathy (Fig. 2). Despite the lack of developed metanephros in adult zebrafish, the embryonic pronephroi are remarkably similar at both molecular and functional levels to higher vertebrate kidneys (Westhoff et al., 2013).

The GFP masked pronephric region of the *Tg(wt1b:EGFP)* transgenic line represents a useful tool to study developmental changes during larval stages of zebrafish (Fig. 4) (Perner et al., 2007). *ift172* gene abnormalities in humans lead to renal, hepatic, retinal and thoracic phenotypes (Halbritter et al., 2013), which are remarkably well replicated in zebrafish. Mutant and morphant models of *ift172* display cystic kidneys, pericardial edema, hydroencephalus and dorsally curved body (Cao et al., 2010).

For the large scale compound screening planned in this project, a **morpholino-based disease model** appeared more feasible under logistic aspects than the use of a transgenic fish line. Due to the lethality induced by the homozygous gene deletion only a heterozygous mutant could have been used which would have generated only 25% of progeny with cysts, multiplying our egg production demands by four times - i.e. around 200,000 more eggs than required with the morpholino strategy. Moreover, it would have been impossible to pre-screen these eggs to ensure the presence of cystic disease before exposing them to test compounds, which would have led to a massive waste of chemicals and animal resources.

In order to ascertain the efficacy of the morpholino-based knockdown, translational and splice inducing morpholinos were tested and both were found to be similarly effective. Further optimisation was achieved by **dose response studies**, which demonstrated a reliable cystic kidney phenotype at 50 μ M concentration with an ample scope for exposing the larvae to test com-

pounds and evaluating their effects.

In order to find a valid **time point** to expose the larvae to test compounds, I studied the inception of cystogenesis during embryonic development from 24 to 48 hpf. Tracking of cyst growth revealed 40-44 hpf as a crucial period. Cyst development was also found to depend on the overall developmental progress of the larval body. Previous published studies had shown a similar time course of cyst development, lending further support to our observations (Drummond et al., 1998; Le Corre et al., 2014). Accounting for the developmental variability in individual larvae, 48 hpf was ascertained as an optimal time for exposing larvae to compounds and study their effect on the entire process of cyst creation and expansion. Since at 48 hpf cysts were still relatively small limiting the detecting moderate-degree phenotypes at large scale, cyst formation was followed on at 24 hour intervals hpf. Larvae at 72 hpf exhibited decent cyst sizes. Beyond 72 hpf cystic mass escalation was observed, which was coupled with external phenotype deterioration due to increment in necrosis and body curvature. These changes made it difficult to orient the larvae dorsally in microtitre format needed for proper capturing of the pronephric structure. We concluded from these observations that the 72 hpf time point was a reasonable timepoint to obtain the readings since the cysts were distended enough to provide clear and easily scorable morphology while body shape distortions were still absent.

5.2 Development of the High-Content Screening System

Following the successful optimisation of the disease model, we focused on the technical aspects of the High-Content Screening. Although zebrafish with its pronephric similarity to humans, transparent and microtitre compatible body made it a perfect HCS model, its efficient utilisation in the HCS frequently requires read-outs that cannot be readily scored at high-throughput scale. In our study the glomerular cysts constituted a straightforward phenotype, but the alterations due to genetic manipulations and compound exposure lead to malformations of the larval body. Such samples impede both image acquisition and quantification and present challenges to HCS automation (Pandey et al., 2019). To address these bottlenecks, I worked on the automation of acquisition and quantification in HCS.

5.2.1 Image Acquisition

Often, High-Content Screening suffers from low-resolution image capturing with lower detectability of details, due to conventional usage of a wide-field of view to enable acquisition of

regions of interest in all acquired images. To overcome this problem, I implemented the acquisition of dorsal views of the *Tg(wt1b:EGFP)* fish pronephroi. To ensure such an acquisition it is required to properly align the larvae, which in itself is a gigantic task mostly due to larval body structure and motility in *in vivo* imaging. For this purpose, I used a 3D printed orientation tool developed in our lab (Wittbrodt et al., 2014). The tool, when pressed on top of agarose filled microtitre plate generated dorsal cavities allowing systemic orientation of the larvae using simple lash tool. The tool, when pressed on top of an agarose filled microtitre plate, generates dorsal cavities allowing systematic orientation of the larvae using a simple lash tool. This greatly facilitated setting of the acquisition parameters for each plate and provided an approximate overview area for finding pronephroi.

However, as in our case the goal was to meet the extensive demands of HCS, imaging was completely automated using a smart imaging module including a two-step pre-scan/re-scan protocol on ACQUIFER Imaging Machine (Fig. 17A). This protocol allowed for automatic centering and zooming in on the region of interest. In the pre-scan step, the overview data of the image is captured using a 4x objective with a single GFP channel z-plane. The images acquired were monitored using an external “Folder watch” procedure, which triggered the region of interest search after caching them. These external scripts were written utilising an open source software Fiji’s programming environment and are available in the supplement (Script. S.3). The XY-location of pronephroi in the image was detected after thresholding and detecting their centre of mass. This was followed by a crucial interactional step, sending the feedback instruction to the ACQUIFER Imaging Machine and requesting the inception of high-resolution acquisition of the identified ROI in a re-scan step. Each detected pronephric region entailed a text file with instructional information regarding positioning of the objective lens and software autofocus to facilitate higher resolution z-stack acquisition and saving to the local directory (Fig. 17B). These jobs were discerned and executed in both bright-field and GFP channels capturing 30 slices in each channel using a 10x objective (Pandey et al., 2019).

More than 60,000 zebrafish embryos were acquired using this approach of automatic image acquisition. Such a consistent high-resolution image collection procedure based on the XY-location of the pronephric fluorescence distribution was of extreme assistance in formulating succeeding image analysis routines for glomerular detection, phenotype quantification and image categorisation, while eliminating the presence of necessary details. This feedback microscopy is written completely in Fiji’s macro language. The software presents a user-friendly environment with simple instructional syntax, thus abrogating the need for advance program-

ming environments or deep programming edification.

Additionally, the script provides the capacity to modify and append the acquisition platform with the downstream image processing phenotype quantification modules in Fiji. Therefore, the whole approach can be adapted by non-microscopy experts and implemented in a wide variety of specimen studied at a relatively large scale.

5.2.2 Image Pre-processing

The established SI pipeline was successfully used to screen all 1,280 compounds of the library. The images were stored in TIFF format and were converted to multilayer TIFF format (Fig. 18 A-B, Script. S.4). The multilayer TIFF format reduced an average of 5,760 image files generated per week to 960 files, allowing easy manipulation of the image for subsequent profiling. The automated microscope utilised here is based on a wide-field platform. Wide-field microscopy provides quick scanning and acquisition in shorter times compared to other approaches as the process is independent of the scan speed of the detectors and is solely dependent on the exposure times, number of channels and the z-slices chosen. This also prolongs the sample life by limiting the exposure time and thus, reducing the photobleaching.

All these factors make it worthwhile to use this approach in the context of High-Content Screening, where efficient and swift screening is of utter importance. However, the lack of pinhole in the wide-field approach necessitates image restoration in order to obtain maximum spatiotemporal information and make full use of the acquired details, which brought us to the pre-processing module of the pipeline. At this stage, the wide-field z-stacks were deblurred using Huygens Professional deconvolution software with a theoretically calculated point spread function. This was ensued by elimination of out-of-focus images containing non-pronephric regions from the stack by generating a sub-stack of 8 slices around the focussed z-slice. To make the images even more precise for glomerular cyst quantification, the stacks were automatically XY-cropped, centering the pronephric glomerular and tubular areas. These cropped stacks were Z-projected and used for further analysis.

This pre-processing workflow truncated the overall raw data of more than 1,200,000 images equivalent to >10 Terabyte, to one XYZ-cropped maximum projection for each of the approximately 20,000 larvae analysed and hence, reducing storing space to approximately 8 Gigabyte (Pandey et al., 2019). The pre-processing of data not only reduced the data volume but also provided a streamlined overview concerning data handling, visualisations and on upcoming

phenotype scoring and quantification steps.

5.2.3 Image Filtering

The actual data quantification was performed on these pre-processed images beginning with the deletion of the erroneous data i.e. blank and blurry images acquired during screening as a result of GFP-negative, misaligned or damaged larvae or due to empty wells. These images were categorised and removed with the combined implementation of edge detection and variance calculation approaches. These checks had an overall efficiency rate of 99% (N = 288) for blank detection and 97% (N = 288) for blur detection. It led to an automatic removal of 1,709 outliers among 20,440 images acquired, due to manual handling errors during fluorescence sorting and mounting thousands of embryos, which could skew the automated quantification analysis (Pandey et al., 2019).

The basic phenotypes observed during the course of the entire screen could be broadly classified in two major categories, i.e. the ones resembling the wild-type pronephroi and those with the cystic kidney phenotype. The former were mostly the result of control morpholino injections, accidentally non-injected embryos and some as a result of test compound effectiveness. The effect was also dependent on the injection day and certainly on the treatment experienced by the particular batch of larvae. The cropped images were thresholded and the region encompassing the glomerular region was selected in the binarised images. These selections were subjected to horizontal average intensity profiling, which demarcated the changes in the wild-type and cystic images. The former displayed a fluorescence signal across the entire region whereas the presence of glomerular cysts led to black image areas visible as regions of zero intensity in image profiles.

A secondary script was used to confirm the results obtained from this primary categorisation. Here, the mask from binary image data was generated representing the best fit ellipse of the detected objects. Images converted to single large ellipse were considered wild-type, while two or multiple ellipses in single image indicated the cystic presence.

With these scripts, wild-type and cystic kidney classification was obtained with up to 92% (N = 169) accuracy. Thus, we successfully established a basic image parameter-based phenotype separation with high accuracy, without any need for complicated pattern recognition techniques or machine learning approaches. The algorithm developed here can also be used as a template for classifying complex objects such as tissue, organs or whole embryo body features, and is

readily reproducible on open source software.

5.2.4 Image Quantification

Once the outlier data was removed, the actual quantification of cyst areas was performed. This process involved cropping the glomerular areas and binarising them using global thresholding. The binarised images were scored for their foreground particles to learn about the extent of the GFP positive areas. The particles were filtered out based on their size, morphology and the ones that remained were considered the pronephric particles. A convex hull circumscribing the foreground pixels was formed and the particles enclosed were analysed. For the images previously categorised as cystic kidney, the background area within the convex hull was quantified, as it represented the cyst area. For the wild-type kidneys, the background was excluded, as it represented only the non-pronephric background area. Thus, the total tissue area consisted of pronephric tissue for wild-type kidneys, and pronephric tissue plus cyst area for cystic kidneys. The entire area quantification module can be easily run in an hour to analyse seven to ten 96-well microtitre plates and hence, identify phenotype-modifying agents quite quickly. Despite the multiple checks, outlier elimination and stringent image refinement techniques applied on the images, some outliers/noises leading to false positive signals could not be avoided. The rate of such occurrences amounted to 9% for the entire screen. Improvements to overcome these flaws in the script could be added by complementing them with more advanced supervised training and progressing it towards unsupervised training using convolutional and neural network approaches, as first applied by (Cario et al., 2011).

However, such approaches require huge amounts of training data along with deep expertise in the field, which would have been beyond the scope of this project, which was to provide a reliable yet uncomplicated automated platform which enables bioinformatic/programming non-experts to quickly sort the hits from the first round of screening with the added flexibility to easily modify steps as required.

5.2.5 Empowering High-Content Screening by Smart Imaging

In conclusion of the aforesaid, the engendered automated platform with simple, efficient and swift modules caters the needs of High-Content Screening without expansive time and resource depletion. The platform developed by our group focuses on organ-based phenotype studies in contrast to conventional cell / sub-cellular workflows (Kimmel et al., 1995; Vogt et al.,

2009). Many such combinations of imaging systems with automated analysis workflows such as VAST-HTS, ARQiv-HTS along with custom made tools have been previously used in HCS experiments (Chen et al., 2011; Kimmel et al., 1995; Mikut et al., 2013; Patton and Zon, 2001). However, they focused mainly on sub-cellular imaging and the workflows were executed for over an hour for a single 96-well plate with one larva per well (Peal et al., 2011). In zebrafish larvae imaging time could be a limiting factor, as the development is quite accelerated during these phases and slow processing could lead to capturing of a completely different developmental stage by the last well of microtitre plate (Torres et al., 2017). In our SI platform, acquisition of a whole 96-well plate with 60 z-slices per well took 45 minutes, thus overcoming the issue of long image acquisition times. The sophisticated handling and orienting of whole organisms on a large scale is a major challenge in whole-organism-based *in vivo* HCS. Automated sample handling using capillary action force and pre-sorting of embryos using image recognition are becoming more and more common solutions to the problem, but still are very expensive (Chapman et al., 2010; Peterson et al., 2000) and yet compromised by slow acquisition rates. This issue was systematically dealt with here by the use of custom printed orientation tools on a desktop 3-D printer (Wittbrodt et al., 2014). Thus, allowing homogenous alignment of larvae per well and providing a sound platform for downstream image-based applications.

The Smart Imaging methodology added efficiency to the image acquisition by automatically detecting and capturing high-resolution images of the ROI. The high quality data captured at this point with lesser noise makes it a much easier target for robotic analysis workflow construction. Most whole-organism/tissue-based studies aimed at understanding behavioural patterns, locomotion, heartbeat detection, sleep/wake cycles, body deformation, dead/alive, regeneration and toxicology make use of cognitive recognition networks, supervised and unsupervised machine learning, video tracking techniques supplemented with MATLAB, Python, and ImageJ scripts (Caroli et al., 2013; Kenneth et al., 1997; Kimmel et al., 1995; Liu et al., 2016; Paul et al., 2010; Pulak, 2016; Walz et al., 2010; Yu et al., 2015). The results generated from these workflows often make use of complex mathematical operations to quantify the image descriptors. Such a system makes it much complicated for a non-expert experimentalist to configure the protocols without intensive training in the field. Contrastingly, the platform used here quantifies *in vivo* pronephric phenotype using simple macro instructions from Fiji and Python. The entire process can essentially be run without manual intervention. Each sub-module is designed in compatibility with High-Content Screening.

The analysis performed here rendered a clear overview about the phenotypic changes exerted

by the compounds on each larvae based on the calculated area. Many studies prefer to use fluorescence as an end-point output (Chen et al., 2011; Creton, 2009; Gehrig et al., 2018; Omer et al., 2017; Swinney and Anthony, 2011). In fluorescence-based analysis results vary in every clutch of heterozygous *Tg(wt1b:EGFP)* fish, an effect that becomes even more relevant when complemented with genetic manipulations as in our application. Consequently, usage of cyst area provides us with a better and more robust answer to the problem in question.

5.3 Choice of Control Compounds

In order to have a proper experimental analysis, it is essential to have positive controls to which the effect of test compounds could be referred to and compared with. An extensive literature survey yielded several candidate control compounds, which included rapamycin, TSA, Valproic acid and curcumin. All these compounds were tested for their effectivity on suppressing the cystic phenotype with the compound exposure beginning from 48 hpf and imaging at 72 hpf. The most significant and best reproducible cyst inhibition was achieved with rapamycin, a compound utilised successfully in another zebrafish model *ift80* (Tobin and Beales, 2008). The effect of rapamycin is most probably exerted by suppressing the hyperactivation of mTOR caused by PC1 mislocalisation. The cyst suppressive effect of the drug was also confirmed by analysing HE stained slides. These slides showed reduced cystic lumen by significant proportions compared to the *ift172* samples (Fig. 8). Albeit human clinical trials demonstrated limited efficacy of rapamycin as a therapeutic drug, the reliable cyst size reduction by 50% obtained in our and previous model prompted us to chose this compound as positive control for this High-Content Screening (Fig. S.1).

The HDAC inhibitor valproic acid (VPA) induced intermediate cyst suppression at 50 μ M and TSA arrested pronephroi development with comparatively smaller cysts at 1 μ M. A previous study (Cao et al., 2009) with these compounds demonstrated effective suppression of cysts in PKD1 morphant models. The observed effects could be related to the partial HDAC inhibition by VPA and the complete inhibition of HDAC achieved with TSA. Whereas VPA, which inhibits only class I HDAC, displayed slight cyst suppression and lower toxicity, TSA, which indiscriminately inhibits both HDAC classes, might have led to multiple non-specific vital pathway inhibition leading to arrested pronephric development along with increased necrosis and pericardial edema.

I also evaluated cyst suppression by **curcumin**. The compound showed interesting rates of

suppression in previous studies on mice kidneys (Gao et al., 2011; Leonhard et al., 2011). Curcumin, a widely used spice, was of particular interest due to its largely absent toxicity. However, the compound, due to its yellow colour, generated much autofluorescence, hindering clear pronephric image acquisition.

5.4 High-Content Screening

Once the controls were tested and validated, the actual screening was performed on the **Prestwick chemical library**. This library contains a well balanced list of 1,280 small-molecular compounds including mechanistically interesting targets in the context of cyst development and growth, such as Cyclooxygenase, beta-adrenergic receptors, voltage gated sodium and L-type calcium channels, glucocorticoid, progesterone and estrogen receptors. Another key argument to select this library was that most of the compounds are approved pharmacological agents with little or absent human toxicity. Hence, the identification of cyst inhibitory effects could rapidly lead to human studies and extension of existing indications to cystic kidney disease.

Twelve larvae per compound were tested based on the Altman nomogram (Whitley and Ball, 2002). This statistically relevant sample size was chosen to account for the manual injection differences and the genetic variability within single clutches of embryos.

Our **screening strategy** comprised an initial assessment of all 1,280 compounds, followed by a second screen studying the dose-effect relationships of the candidate compounds detected in the first round. During the first round of screen, around 60 compounds with apparent cyst suppressive activity were identified. The majority of these compounds are genito-urinary and sex hormone therapeutics (class G of the ATC classification). However, many of the initial hits were not confirmed in the second screening round, which yielded 17 final hits with solid dose-response relationships.

The unconfirmed compounds were deemed as cyst suppressive in the first place based on their presence within the chosen statistical threshold range of 0.75 units after automatic quantification. Selected to maximise sensitivity of detection, the chosen threshold led to the inclusion of compounds with low or intermediate effects. Low-level cyst suppressive effects could sometimes also be seen due to weekly injection differences or genetic variations combined with outlier prone skewing in area quantification by the script. Additional factors to be considered include differences in the batches and manufacturing dates of the used chemical sets.

Chemical screens have a tendency to be biased for compounds with cell permeability, admiss-

ible pharmacokinetic and pharmacodynamic profile and lower toxicity. Therefore, the lead compounds identified in the High-Content Screening are to be subjected to dose-response studies and further investigation in other disease models and systems to ascertain their validity.

5.4.1 Pharmacological Modifiers of Cystic Nephropathy Identified from High-Content Screening

Following the lines of primary screen, concentration gradient studies also had maximum number of hits from class G. Due to organ of activity-based classification provided by ATC, despite of having stark differences several types of compounds were pooled in the same class. On doing extensive literature survey, significant variations in the modes of action of these compounds were delineated. These mode of action-based similarities will be utilised here to further re-group and analyse the hits.

5.4.1.1 Clotrimazole, Butoconazole nitrate and Sertaconazole nitrate

Clotrimazole, Butoconazole and Sertaconazole are molecules of the imidazole family, which are widely used anti-fungal agents and are commonly referred to as azoles. Imidazoles target the sterol 14α -demethylase (CYP51) enzyme, an evolutionarily well conserved, P450-based housekeeping protein involved in several key metabolic steps in sterol biosynthesis (Lepesheva and Waterman, 2007) including the formation of ergosterol, an essential membrane component in fungi (Lupetti et al., 2002; Zhang et al., 2002). The Zebrafish homolog of CYP51, also referred to as CYP51ZF, functions similarly as its mammalian counterpart and is expressed in zebrafish intestine, liver, brain, kidney and heart (Morrison et al., 2014).

Apart from this anti-fungal action, azoles have anti-estrogenic properties. In animal models, azoles lowered estradiol and estrogen levels leading to impaired oocyte maturation, increased masculinisation and sperm count in testis, sexual behavioural change, and impaired ossification (Lee et al., 1995; Schieweck et al., 1993). Azoles have a clinical role in the management of estrogen dependent breast cancer (Murray, 2001; Santen and Harvey, 1999; Zarn et al., 2003). The anti-estrogenic action of azole compounds is believed to be exerted by partial or complete inhibition of tissue aromatase (CYP19) (Trosken et al., 2006). Aromatase is a member of the P450 family, as is CYP51. Aromatase catalyses the cleavage of the methyl group of androstenedione and testosterone, resulting in estrone and estradiol formation (Conley et al., 2001; Egbuta et al., 2014). Azole administration suppresses estrogen formation in aromatase express-

ing tumours, leading to shrinkage of tumour size (Bulun et al., 2009; Conley et al., 2001; Reed and Purohit, 2001).

The cyst suppressive class effect of the azoles in our zebrafish model may either be mediated via an action on the conserved CYP51ZF enzyme or on inhibition of aromatase activity. The fact that in addition to the azoles, two other screened compounds with anti-estrogen lowering activity were found to be effective in the screen (see below), points to the possibility that aromatase inhibition may be the relevant mechanism of action of the azole compounds. Estrogens might impact on cyst volume by their regulatory activity on transepithelial ion channels via both non-genomic and genomic mechanisms (Bulun et al., 2009; Conley et al., 2001; Reed and Purohit, 2001).

Testing this hypothesis will require further studies including the assessment of temporal and tissue specific aromatase expression in developing zebrafish larvae, inhibition of aromatase activity by other compounds devoid of CYP51 blocking activity, and phenotype rescue by estrogen supplementation during azole treatment.

Moreover, the findings need to be reproduced in mammalian models of cyst development before human studies can be envisioned. The role of estrogen in rodent and human cystic nephropathy is controversial. In human ADPKD and PKD rats, females with intact estrogen status show slower disease progression than males; this difference is abolished after menopause and by experimental ovariectomy (Stringer et al., 2005). On the other hand, estrogen therapy in postmenopausal women with ADPKD accelerates the growth of liver, albeit not kidney, cysts (Sherstha et al., 1997).

5.4.1.2 Cyproterone acetate and Ethynodiol acetate

Cyproterone acetate (CA) and Ethynodiol acetate (ED) act as antagonists of the androgen and progesterone receptor, respectively. Furthermore, they inhibit the CYP51 and CYP19 members of the P450 family of enzymes. CA, an efficient androgen receptor blocker, might also be functional in inhibiting androgenic aromatisation by targeting CYP19 (Beijer et al., 2018). In other fish species, the latter action leads to lowered estrogen levels (Beijer et al., 2018), which are integral for cystogenesis. This promoted the speculation that it might also be responsible for the anti-cystic mechanism seen in the pronephric cysts of zebrafish larvae. Similarly, the increase of progesterone tone induced by ED decreases estrogen receptor expression (Cherubini et al., 2002; Hochmann, 2007). This attribute of ED might be of importance when targeting

estrogen-dependent cystic tissues. Hence, as outlined above for the potential mechanism of azoles action, also CA and ED could modify the cystic phenotype via lowering the estrogen tone. Further experimental efforts will be required to corroborate this hypothesis for each class of drugs.

5.4.1.3 Astemizole and Ciclesonoid

The neuroactive ligand-receptor interaction pathway participants Astemizole (Az) and Ciclesonoid (Cs) showed an intermediate effect with a 50% depreciation in cyst size. Az is an H1 receptor antagonist and also interacts with H3 receptors. Cs is a glucocorticoid receptor agonist approved as an anti-asthmatic and anti-inflammatory drug. Both drugs are substrates of cytochrome P450 family 3 sub-family A (Inoue et al., 1992; Kanehisa and Goto, 2000; Kanehisa et al., 2016, 2017).

Mammalian kidneys are known to house several histamine receptors including H1 and H2 (Banks et al., 1978). The anti-histaminic drug Az might exert its cyst suppressing activity in pronephroi via its competitive H1-receptor binding activity. In zebrafish, the presence of H1, H2 and H3 receptors has been demonstrated for brain, but their expression in kidney is unknown (Peitsaro et al., 2007). The antagonistic activity of Az here might be leading to increase in urine flow and chloride, which is followed by rise in GFR rates and thus, decrease in the cystic size (Banks et al., 1978; Ichikawa and Brenner, 1979). On the other hand, Az is also known to interact with the H3 receptor and H3 receptor interacting drugs have been shown to modulate renal homeostasis by decrease in urine flow and chloride release (Yamasaki et al., 2001). One might speculate that the intermediate cyst suppression observed with Az is the net result of opposite effects exerted via the H1 and H3 receptors respectively. Unfortunately, Az when taken with CYP3A4 inhibiting compounds causes arrhythmia, which has even led to banning of the drug (Knox et al., 2011). If a major anti-cyst effect of the compound can be corroborated in further model studies, re-approval of the drug for the specific indication of cystic kidney disease might be considered.

Glucocorticoid receptors are ubiquitously expressed in zebrafish as well as humans. They are involved in Na^+ - K^+ -ATPase-rich cells-mediated calcium uptake (Cruz et al., 2013; Schaaf et al., 2008). Despite the controversial role of calcium channels in cystic kidney disease (Harris and Torres, 2014) this could be a potential mechanism by which Cs mildly reduced the cystic phenotype in the larval pronephroi. The aberrant ciliary structure present in ift complex dis-

orders dysregulates multiple flow sensing pathways in kidneys, leading to aberrant intracellular calcium levels (Praetorius and Spring, 2003). The glucocorticoid agonist Cs might assist in excretion of this extra calcium, thereby increasing glomerular filtration rate, renal plasma flow and water diuresis (Cruz et al., 2013; McKay and Cidlowski, 2003). However, it is unclear why the cyst suppressive effect was observed with Cs but not other glucocorticoid receptor agonists represented in the Prestwick library, leaving room for speculation about a potential glucocorticoid receptor independent action of the compound. Cs is used as an intranasal corticosteroid for allergic rhinitis (Williams et al., 2008) but has poor oral bioavailability (Knox et al., 2011). As a result, little is known about systemic and organ-specific actions of the compound and more research is required.

5.4.1.4 Omeprazole

Omeprazol (Oz) was highly efficacious in inhibited cyst growth, leading to a two third reduction of cyst area. Oz is a proton pump inhibitor, commonly prescribed in the clinics to treat duodenal ulcer, gastric ulcer, gastroesophageal reflux disease, Zollinger-Ellison syndrome and multiple endocrine adenomas. The drug interacts with the H⁺/K⁺ ATPase (adenosine triphosphatase), resulting in reduced acidic secretion by parietal cells (Ward and Kearns, 2013). In humans, H⁺/K⁺ ATPase is responsible for H⁺ excretion in all segments of the kidney along with K⁺ uptake in the collecting duct region against the gradient (Gumz et al., 2010). Additionally, the channel also maintains potassium and sodium homeostasis. In zebrafish, during larval development skin plays a major role in body homeostasis regulation. The apical V-type H⁺-ATPase pumps out H⁺ and builds up an electrical gradient for Na⁺ uptake in gill epithelial cells prior to attainment of complete functionality by specialised organs such as, kidneys and gills (Lin et al., 2006). A potential mechanism of the observed pronephric cyst suppression by two thirds upon Oz exposure could be the resumption of acid-base balance by amplified acid excretion from the cystic epithelia, analogously to its effect on the gill epithelia.

Oz has several off-target effects. It potently inhibits CYP3A4 and CYP2C19 (Zvyaga et al., 2012) and has been associated with renal malformations and acute kidney injury (Ward and Kearns, 2013; Yang et al., 2017). 2013). Oz has also been shown to cause skin lightening by melanocyte reduction in cells, which could exacerbate vitiligo in patients (Shin et al., 2014). Oz might suppress melanogenesis by inhibiting anti-tyrosinase activity, where an intramelanosomal pH switch must occur to promote and regulate melanogenesis, or by inducing ox-

oxidative stress via accumulation of hydrogen peroxide or by blocking ATP7A trafficking (Fuller et al., 2001; Lin et al., 2018; Matsui et al., 2015). Notwithstanding these off-target effects, Oz is one of the most widely prescribed anti-acidic drugs with an excellent overall safety profile. The strong inhibition of the cystic phenotype achieved with Oz in our zebrafish model certainly makes this compound a highly attractive target of further research regarding the impact of proton pump inhibition on cystogenesis in mammalian cystic kidney disease models.

5.4.1.5 Monobenzone

Monobenzone (Mz) exhibited an intermediate cyst suppressive activity. Mz, like Oz, is a skin lightening agent assumed to function by inactivating tyrosinase enzyme by quinone-hapten formation (van den Boorn et al., 2010, 2011). Along with its depigmentation effect, Mz induces autophagy in melanocytes and potential cyst elimination in mice studies (Hariharan et al., 2010; van den Boorn et al., 2010). By the formation of quinone-haptens to the tyrosinase protein, Mz is also capable of specific CD8⁺T-cell immunity in melanocytes (van den Boorn et al., 2011). Of note in this context, T-cell mediated therapy has recently been proposed as a potential therapeutic approach in autosomal cystic nephropathy (Kleczo et al., 2018).

As Mz shares an anti-tyrosinase activity with Oz, it appears possible that this property is a mechanism of action underlying the cyst suppressive activity of both compounds.

5.4.1.6 Racecadotril

Racecadotril (Ra) is an approved anti-diarrheal drug. It is a prodrug which is converted to two active forms, Thiorphan and Acetyl thiorphan, which are mostly eliminated by the renal route (Eberlin et al., 2012). The S and R stereoisomer structures of Ra are known as ecadotril and retorphan respectively. The active form of Ra inhibits membrane-metalloendopeptidase, i.e. neutral endopeptidase, also known as Enkephalinase. Neutral endopeptidases cleave not only enkephalins but also many other peptides such as atrial natriuretic peptide (ANP), brain natriuretic peptide, substance P, neurotensins, and neuropeptide Y. Therefore, the effects seen upon compound administration could be due to the potential accumulation of any of these peptides. Enkephalinase inhibitors including Ra increase diuresis and natriuresis by amplifying ANP and urinary guanosine 3',5'-cyclic monophosphate (cGMP) and decreasing distal tubular reabsorption of sodium (Dussaule et al., 1993; Gros et al., 1989; Lecomte et al., 1990; Schmitt et al., 1994). The clinical effects of neutral endopeptidase inhibitors include increased glomerular fil-

tration rate, reduced renal mass and vasodilation without any impact on the renin-angiotensin system (Dussaule et al., 1993; Lecomte et al., 1990) making them interesting targets to treat renal failure, hypertension and hepatorenal syndrome.

So far, no studies assessed the *in vivo* effects of Ra or other Enkephalinase inhibitors on zebrafish. As already mentioned, both in humans and zebrafish, the pathophysiology of *ift* gene induced cystic nephropathies includes an impaired urine flow leading to fluid filled cystic sac creation due to loss of fluid flow sensing. The observed cyst suppressive effect on the larval pronephroi might have been mediated by an increase in ANP and cGMP leading to increased urine flow. Hence, endopeptidase inhibition may be an attractive therapeutic approach as it combines a specific anti-cystic action with general nephroprotective effects such as blood pressure lowering and GFR stimulation.

5.4.1.7 Adapalene

Adapalene (Ap) is a retinoic acid receptor (RAR) agonist and approved for acne treatment. Retinoic acid (RA) exerts its effect on target genes by binding to cytosolic RARs and heterodimerizes with retinoid X receptors (RXR), which in turn activates RA response elements (RARE) (Lehrke et al., 2002; Mendelsohn et al., 1999; Oseto et al., 2003; Perner et al., 2007; Vaughan et al., 2005; Wingert et al., 2007).

In ciliary cystogenesis studies, RA induced a reduction in cyst size by targeting PKD1, demonstrating its potential to ameliorate renal ciliopathies such as the one studied here (Altieri et al., 1999; Islam et al., 2008; Muto et al., 2002). The functionality of RA is well conserved between zebrafish and mammalian species, making compounds interacting with RA signalling a highly interesting target for the treatment of human disease (Bollig et al., 2009).

We observed an impressive 60-70% reduction in cyst area with Ap. Due to the involvement of RA in multiple developmental pathways it is difficult to narrow in on the particular mode of action utilised in the suppression of cystic phenotype. While being quite effective and showing great potential in treating cystic kidney disease, the use of RA is potentially compromised by toxicity issues. Although to our knowledge there have not been any renal toxicity reports associated with the use of Ap, this could be due to the lack of studies of renal effects of the compound altogether. In an effort to overcome the drawback of RA toxicity, boronic acid retinoid (BD4), a novel derivative of RAR α agonist with increased affinity and reportedly reduced toxicity was recently introduced (Zhong et al., 2011).

5.4.1.8 Cycloheximide

Cycloheximide (Cx), an antibiotic produced from *Streptomyces griseus* strain, is prominently known for its protein synthesis inhibition. It exhibits a wide range of fungicidal, anti-psoriatic and has even anti-tumorigenic properties. Cx hampers protein synthesis by interrupting the transfer of amino acids from amino acyl-soluble RNA to the site of peptide bond synthesis on the ribosome (Verbin and Farber, 1967). In the field of renal studies, Cx administration on rat kidneys before perfusion reduced renin release (Vandongen, 1976). It has also been effective in assisting body curvature correction in pkd1 mutant models by clearing accumulated collagen II (Le Corre et al., 2014). Along with that, Cx had no impact on the foxj1a transcription factor, integral for ciliary mobility in the zebrafish nephronophthisis model (Hellman et al., 2010). Cx decelerates the G1 phase of the cell cycle concomitant with prolongation of subsequent S and G2 phases (Okuda and Kimura, 1988). The powerful suppressive effect of Cx on cyst size could be attributed to this cell-cycle prolonging property, blocking epithelial cell proliferation followed by cAMP-dependent cell differentiation (Liu et al., 2010). Whereas Cx does not affect the mitosis phase progression in already dividing cells, it blocks new cells from entering the division cycle. In addition to this potential mechanism on tubulo-epithelial cell mitosis, Cx conditionally suppresses cAMP induced P450, which in turn could play an important role in obliterating cystic cells (Payne and Sha, 1991).

5.4.1.9 Phenothiazine

Phenothiazine (Pz) has a characteristic alkyl side chain skeleton structure with a nitrogen ring present on the 10th position, which attributes for a wide range of receptor binding activities presented by the compound and its family members. This promiscuous receptor binding behaviour of Pz leads to multiple off-target/adverse effects. Some of the well studied activities shown by the compound include: anti-histaminergic, anti-dopaminergic, anti-serotonergic, anti-cholinergic, anti-glutamnergic, alpha-adrenergic receptor-blocking, anti-bacterial, anti-protozoal, anti-fungal, anti-viral, anti-prion and anti-tumorigenic effects. The anti-tumorigenic effect exerted by Pz is through several modes of action such as, apoptosis induction, efflux pump blockade, angiogenesis blockade or anti-cancer stem cell activity (Varga et al., 2017).

Perphenazine, a phenothiazine member, showed a new mode of action in a small molecule screen conducted on a T-cell acute lymphoblastic leukaemia zebrafish model. By means of this mechanism, PP2A is dephosphorylated at an accelerated pace subjecting the cells to apoptosis

along with growth repression. The mechanism has been suggested as a treatment avenue for Notch triggered cancers (Gutierrez et al., 2014). In a recent publication, direct correlation of Notch3 signalling dysregulation and cystogenesis has been established in both ARPKD and ADPKD mouse models (Idowu et al., 2018). Therefore, one possible way of Pz's effect in our study might have been due to the PP2A-based cellular apoptosis and tumor growth inhibition. Additionally, mammalian Wilms' tumour protein *wt* with functional homology to fish *wt*, plays an integral part in the development and functioning of podocytes (Bollig et al., 2009; Perner et al., 2007). It is highly expressed during development and mutations in this gene could also lead to cystic nephropathy, among other anomalies such as nephroblastoma and renal fibrosis. PP2A levels correlate with *wt* expression and are increased in Wilms' tumours (Carlson et al., 1998). One could speculate about aberrations in PP2A levels pertaining to overexpressed *wt* along with other growth factors followed by unchecked cell multiplication in kidney tissue (Armstrong et al., 1993; Perner et al., 2007). Application of Pz in such a scenario would lead to faster dephosphorylation of PP2A and hampered tumour development.

Levomepromazine, a member compound of Pz family has been shown to suppress CYP450 isozymes CYP1A2, CYP2D6 and CYP3A4 in *in vitro* studies, which have been also one of the probable modes of cyst inhibition reported earlier (Basinska-Ziobron et al., 2015). Pronephric development is a highly orchestrated biological process, which makes pinpointing aberrations responsible for a specific etiology in this process almost like finding a needle in a haystack. Therefore, I present multiple potential mechanisms by which this "dirty drugs" compound could interfere with cystic development and progression.

5.4.1.10 Fluspirilen

Fluspirilene (Fs), a diphenylbutylpiperidine derivative and calcium channel blocker, is an anti-psychotic compound. It has also been found effective in autophagy by reducing intracellular calcium levels which in turn incremented the levels of Autophagy Related 5(ATG) and ATG12-ATG5 protein conjugates (Xia et al., 2010). Additionally, ATG is responsible for phosphorylation of CDK1 and CHEK2, two essential checkpoints required for cell-cycle obstruction (Simon and Friis, 2014). Combinatorial effects of ATG ultimately cause cell-cycle arrest. In case of cystic nephropathies, the increase in calcium levels can be explained based on the mistargeting of ciliary assembly protein followed by interactional jam. Both *ift*-A and B complex, along with other proteins help in the proper establishment of the cilia. *ift*-B complex is formed by nine

core (*ift88/81/74/70/52/46/27/25/22*) and six peripheral subunits (*ift172/80/57/54/20*). In functional *ift*-B complex, *ift54/20* couple together and interact with *ift80* and co-dimerised *ift57/38*; *ift57/38* in turn interacts with *ift80* and *ift172*. In case of mutations in the peripheral members of *ift*-B subunit, the inter-subunit conversation is altered, followed by blocked interaction of the former two with the cation channel PC-2 at the basal body responsible for primary ciliary assembly (Jurczyk et al., 2004; Taschner and Lorentzen, 2016). Moreover, PC-1 and PC-2 interact with each other for proper signalling in wild-type kidneys whereas this association often lacks in cystic kidney diseases (Cantiello, 2004). Such gaps in proper structural connections with PC-1 and *ift* at times cause PC-1 independent activation of PC-2 in renal epithelia, leading to a rise in cytosolic calcium levels and its improper extracellular efflux (Cantiello, 2004). F_s exposure in such an ambience might have lead to the depletion of accumulated calcium levels ensued by autophagic response in cystic cells due to ATG5 cues. This could have progressed the cells towards an arrested state at G₂/M phase, resulting in a mitotic blockade (Simon and Friis, 2014).

5.4.1.11 Flumequine

Flumequine (Fq), a quinolone compound, is an anti-bacterial agent which interferes with bacterial cell division by prohibiting the DNA unwinding topoisomerase (TOP) type IV enzyme (Schena et al., 1988). In mammals, Topoisomerase II α (TOPO II) is an essential enzyme present at the replication fork, enabling decatenation of sister chromatids by introducing double strand breaks for proper progression of cells into M phase (McClendon and Osheroff, 2007). Targeting TOPO II inhibition has led to the development of a major class of anti-tumorigenic compounds, known as TOPO II poisons (McClendon and Osheroff, 2007), which lead to accumulation of DNA fragments causing cell death (Montecucco and Biamonti, 2007). 2007). In cystic kidney disease, uncontrolled proliferation of epithelia similar to neoplastic disorders leads to the creation of cysts. In order to facilitate this process, several checkpoints of cell-cycle are overcome causing accelerated genetic material replication proceeded by cell division. Accretion of TOPO II α might be a critical factor in this process.

Similar to mammals, zebrafish embryos express two isoforms of topoisomerase i.e. Top2a and Top2b; where Top2a is associated with the chromatid decatenation at G₂/M cell-cycle checkpoint (Sapetto-Rebow et al., 2011). We speculate that treatment with Fq in this study might have imposed a block on the increased TOPO II α activity and thereby ameliorated the condition. The

detailed mode of action the mode of blocking the cleavage by the enzyme in zebrafish is currently cryptic and further investigation will be required to clarify the exact pathways involved. Notably, Fq has also been shown to confer resistance when used persistently on zebrafish and electric eels, leaving the possibility of treatment tolerance of cystic epithelia upon long term Fq exposure (Cantas et al., 2012; van der Heijden et al., 1996).

5.4.1.12 Toltrazuril

Toltrazuril (Tz) was the only veterinary drug that emerged as a strong hit in our screen. Mostly used as a coccidiostat agent or for protozoal myeloencephalitis treatment in animals, not much is known about its mode of action (Furr et al., 2000; Kanehisa and Goto, 2000; Kanehisa et al., 2016, 2017). However, in one published report Tz was shown to interfere with mitochondrial respiration based on the assessment of succinate-cytochrome C reductase, NADH oxidase and succinate oxidase from mouse liver (Harder and Haberkorn, 1989). In another report, the use of 1% Tz diet in adult goldfish suffering from kidney enlargement disease created no significant reduction in the kidney size of the diseased fish (Yokoyama H. and Wakabayashi, 1990). Based on the sparse literature available on the compound no concrete hypothesis about its functioning in zebrafish pronephroi could be deduced. We speculate that the strong effect almost restoring the wild-type could be due to the complete cell activity arrest, similar to when it is used as a coccidiostat (Fig. 32B; S.7 G,H; S.2O), which would lead to shedding of cystic epithelia in the larval pronephroi.

5.4.1.13 Flubendazole

Flubendazole (Fz) appeared as an extremely toxic cyst suppressive compound which led to larval mortality by 72 hpf at 1 μ M concentration. Fz is an anti-protozoal benzimidazole derivative with a broad anti-helminthic range. It is mostly used in veterinary medicine and only rarely applied in humans. Fz impacts on the cell-cycle by binding at the colchicine binding site of tubulin, hampering its polymerisation along with microtubule formation and thereby disrupting mitosis (Spagnuolo et al., 2010; Tweats et al., 2016). Given this mode of action the drug has been classified as a potent aneugenic agent (Tweats et al., 2016). However, no carcinogenicity has been documented to date. The high toxicity of Fz has greatly hampered *in vivo* studies to explore its mechanisms of action (European Medicines Agency, 2006) and evaluate phenotypic modifications. Additionally, Fz has relatively poor bioavailability upon oral intake. Taking in

account all these points, coupling Fz with a milder agent that might dampen its potency and possibly improve its uptake in a way that its impact is dwindled just enough to keep the subjects alive could be helpful in deducing the compound's regulated pathways and potential phenotype modifying effects.

5.5 Concluding Remarks

The High-Content Screening analysis module developed in this work addresses the bottlenecks created due to acquisition of terabytes of imaging data, demanding labor and resource intensive analysis to produce meaningful results. Once established, the largely automated workflow of image pre-processing, outlier removal, ROI capture, and phenotype scoring provided an optimal setting for the large-scale *in vivo* screening in search of compounds modifying the cystic phenotype.

The hit compounds confirmed in a two-stage screening procedure provide a basis for future research into novel pathways involved in the pathogenesis and therapeutic modification of cystic kidney disease. The 17 compounds partially converge on distinct molecular pathways of cytochrome P450 family enzymes, retinoid X receptors, proton pump and adenosine triphosphatase channels, enkephalinase, glucocorticoid, tyrosinase and histamine receptors. These findings require further exploration both in the zebrafish and in mammalian models to learn which disease pathways are common to different ciliopathies and were conserved in evolution. Based on this next step of research, a few drug classes may turn out suitable for the development of novel therapies for human cystic kidney diseases.

6 ZUSAMMENFASSUNG

In dieser Arbeit beschreibe ich technische und biologische Aspekte eines Hochdurchsatz-Screening-Experiments, das durchgeführt wurde, um pharmakologische Modifikatoren einer humanen zystischen Nierenerkrankung an einem Zebrafischmodell zu identifizieren. Die zystische Nephropathie wurde mittels Morpholino-Knockdown des *ift172*-Gens induziert. IFT172 ist Teil des sogenannten intraflagellaren Transportkomplexes; sein Fehlen beeinträchtigt die Funktion der primären Zilien, was zu einem beeinträchtigten Urinfluss und zur Ausbildung von Zysten führt.

Eine automatisierte Pipeline wurde entwickelt, um die Handhabung der Akquisition, Quantifizierung und Analyse großer Mengen von Bildmaterial zu optimieren. Spezielle Hard- und Softwarewerkzeuge wurden entwickelt, um Probleme im Zusammenhang mit der räumlichen Orientierung von Larven in Mikrotiterplatten, der automatisierten Bild-Erfassung, Datenvorverarbeitung und Befundquantifizierung zu lösen. Nach erfolgreicher Implementierung der High-Content-Screening-Plattform untersuchte ich 1,280 bekannte kleinmolekulare pharmakologische Substanzen aus der Prestwick-Bibliothek anhand von 12 Larven pro Substanz. Das initiale Screening erbrachte 60 Kandidaten-Substanzen mit potenzieller Zysten-inhibierender Aktivität. Diese wurden mittels Dosis-Wirkungs-Studien weiter validiert, was zur endgültigen Bestätigung von 17 Wirksubstanzen führte.

Die identifizierten Substanzen wirken teilweise über bisher in der Ciliopathieforschung wenig bekannte zelluläre Signalwege, darunter Östrogen-Antagonismus, Hemmung neutraler Endopeptidasen, Protonenpumpenhemmung, Anti-Tyrosinase-Aktivität, Calciumkanal-Regulation, Retinoid-Rezeptor-Aktivierung und Topoisomerase-Blockade.

Zusammenfassend konnten wir durch die Etablierung und Durchführung eines automatisierten Hochdurchsatz-Screeningverfahrens in einem genetisch modifizierten Zebrafischmodell mehrere vielversprechende neue pharmakologische Targets identifizieren, die im Hinblick auf ihre zystenhemmende Aktivität und Eignung für den Einsatz bei menschlichen zystischen Nierenerkrankungen weiter untersucht werden können.

Summary: *in English*

In this work, I describe technical and biological aspects of a High-Content Screening experiment conducted to identify pharmacological modifiers of human cystic kidney disease in zebrafish larvae. Human cystic nephropathy was mimicked in zebrafish larvae with the help of morpholino-mediated knockdown of the *ift172* gene. IFT172 is part of the ciliary intra flagellar transport complex; its deficiency impairs the function of the primary cilia, resulting in impaired urine flow and the development of fluid filled cysts.

An automated pipeline was developed to optimise large scale sample handling, image acquisition, quantification and analysis. Dedicated hardware and software tools were developed to solve issues associated with the spatial orientation of larvae in microtitre plates, automated Image capture, data pre-processing and quantification. After successful implementation of the high-content screening platform, I screened 1,280 known small-molecular pharmacological compounds from the Prestwick library in 12 larvae per compound. The initial screen yielded 60 candidate compounds with potential cyst suppressive activity. The hits were further validated in dose response studies, which led to the final confirmation of 17 target compounds. These compounds share several interesting putative modes of action, including estrogen antagonism, enkephalinase and proton pump inhibition, anti-tyrosinase activity, calcium channel regulation, retinoic acid receptor interactions and topoisomerase blockade.

In conclusion, the establishment and execution of an automated High-Content Screening in a transgenic zebrafish model yielded several promising novel pharmacological targets that can be further explored with regards to their cyst-suppressing activity and suitability for use in human cystic kidney diseases.

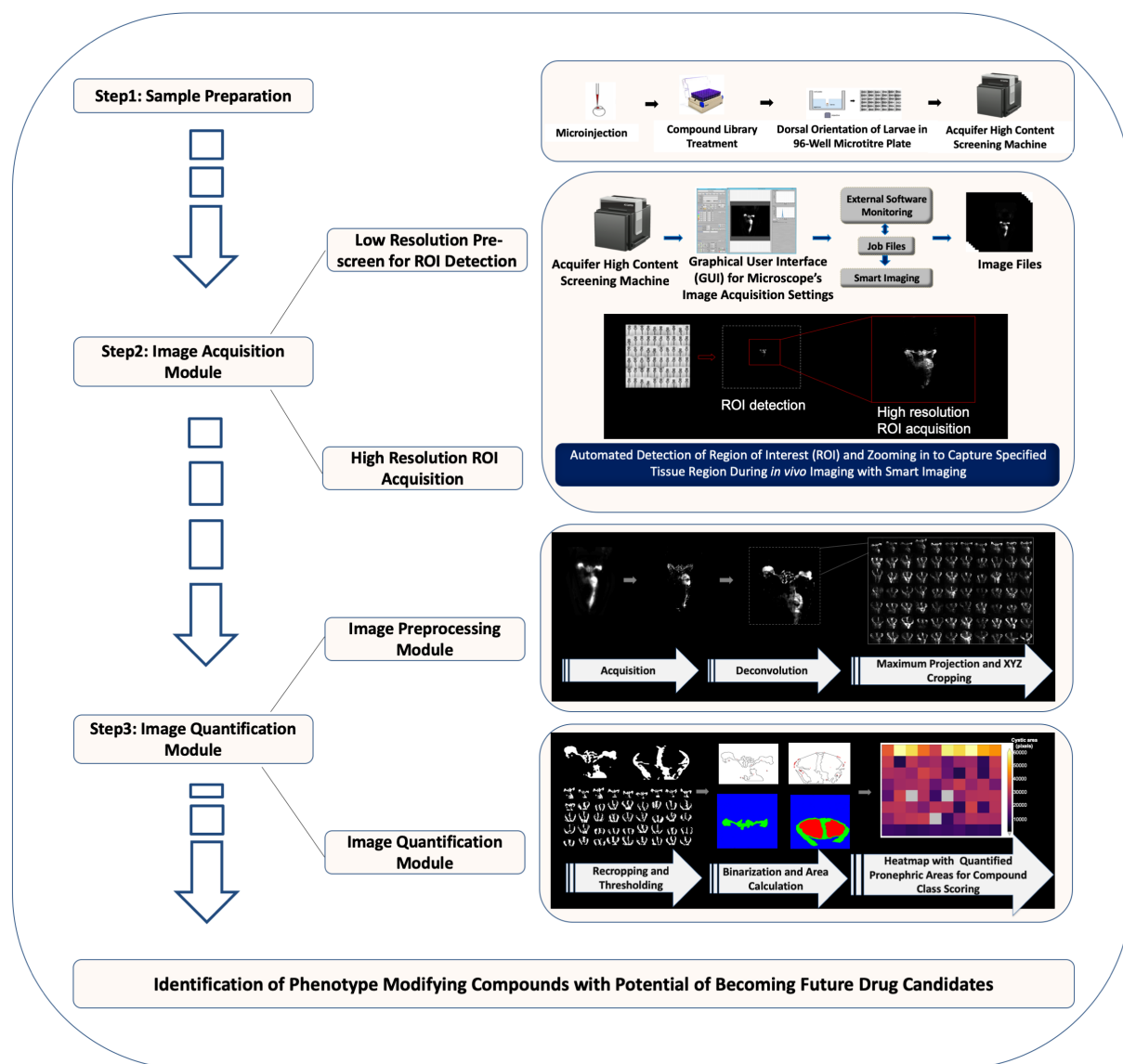


Fig. 34: **Graphical Abstract:** Development of an Automated High-Content Screening Pipeline for Identification of Cystic Kidney Disease Modifying Substances in Zebrafish Model.

7 References

- Altieri, P., Caridi, G., Chiesa, V., Ponzoni, M., and Ghiggeri, G. M. N-(4-hydroxyphenyl) retinamide inhibits cystogenesis by polycystic epithelial cell lines in vitro. *Life Sci*, 64(22):PL259–65, 1999. ISSN 0024-3205 (Print) 0024-3205 (Linking). URL <https://www.ncbi.nlm.nih.gov/pubmed/10374933>.
- Alvarez, Y., Cederlund, M. L., Cottell, D. C., Bill, B. R., Ekker, S. C., Torres-Vazquez, J., Weinstein, B. M., Hyde, D. R., Vihtelic, T. S., and Kennedy, B. N. Genetic determinants of hyaloid and retinal vasculature in zebrafish. *BMC Dev Biol*, 7:114, 2007. ISSN 1471-213X (Electronic) 1471-213X (Linking). doi: 10.1186/1471-213X-7-114. URL <https://www.ncbi.nlm.nih.gov/pubmed/17937808>.
- Alvarez, Y., Astudillo, O., Jensen, L., Reynolds, A. L., Waghorne, N., Brazil, D. P., Cao, Y., O'Connor, J. J., and Kennedy, B. N. Selective inhibition of retinal angiogenesis by targeting pi3 kinase. *PLoS One*, 4(11):e7867, 2009. ISSN 1932-6203 (Electronic) 1932-6203 (Linking). doi: 10.1371/journal.pone.0007867. URL <https://www.ncbi.nlm.nih.gov/pubmed/19924235>.
- Armstrong, J. F., Pritchard-Jones, K., Bickmore, W. A., Hastie, N. D., and Bard, J. B. The expression of the wilms' tumour gene, wt1, in the developing mammalian embryo. *Mech Dev*, 40(1-2):85–97, 1993. ISSN 0925-4773 (Print) 0925-4773 (Linking). URL <https://www.ncbi.nlm.nih.gov/pubmed/8382938>.
- Ashraf, S., Gee, H. Y., Woerner, S., Xie, L. X., Vega-Warner, V., Lovric, S., Fang, H., Song, X., Cattran, D. C., Avila-Casado, C., Paterson, A. D., Nitschke, P., Bole-Feysot, C., Cochat, P., Esteve-Rudd, J., Haberberger, B., Allen, S. J., Zhou, W., Airik, R., Otto, E. A., Barua, M., Al-Hamed, M. H., Kari, J. A., Evans, J., Bierzynska, A., Saleem, M. A., Bockenbauer, D., Kleta, R., El Desoky, S., Hacıhamdioglu, D. O., Gok, F., Washburn, J., Wiggins, R. C., Choi, M., Lifton, R. P., Levy, S., Han, Z., Salviati, L., Prokisch, H., Williams, D. S., Pollak, M., Clarke, C. F., Pei, Y., Antignac, C., and Hildebrandt, F. Adck4 mutations promote steroid-resistant nephrotic syndrome through coq10 biosynthesis disruption. *J Clin Invest*, 123(12):5179–89, 2013. ISSN 1558-8238 (Electronic) 0021-9738 (Linking). doi: 10.1172/JCI69000. URL <https://www.ncbi.nlm.nih.gov/pubmed/24270420>.
- Banks, R. O., Fondacaro, J. D., Schwaiger, M. M., and Jacobson, E. D. Renal histamine h1 and h2 receptors: characterization and functional significance. *Am J Physiol*, 235(6):F570–5, 1978. ISSN 0002-9513 (Print) 0002-9513 (Linking). doi: 10.1152/ajprenal.1978.235.6.F570. URL <https://www.ncbi.nlm.nih.gov/pubmed/736141>.
- Basinska-Ziobron, A., Daniel, W. A., and Wojcikowski, J. Inhibition of human cytochrome p450 isoenzymes by a phenothiazine neuroleptic levomepromazine: An in vitro study. *Pharmacol Rep*, 67(6):1178–82, 2015. ISSN 1734-1140 (Print) 1734-1140 (Linking). doi: 10.1016/j.pharep.2015.04.005. URL <https://www.ncbi.nlm.nih.gov/pubmed/26481538>.
- Beales, P. L., Bland, E., Tobin, J. L., Bacchelli, C., Tuysuz, B., Hill, J., Rix, S., Pearson, C. G., Kai, M., Hartley, J., Johnson, C., Irving, M., Elcioglu, N., Winey, M., Tada, M., and Scambler, P. J. Ift80, which encodes a conserved intraflagellar transport protein, is mutated in jeune asphyxiating thoracic dystrophy. *Nat Genet*, 39(6):727–9, 2007. ISSN 1061-4036 (Print) 1061-4036 (Linking). doi: 10.1038/ng2038. URL <https://www.ncbi.nlm.nih.gov/pubmed/17468754>.
- Beijer, K., Jonsson, M., Shaik, S., Behrens, D., Brunstrom, B., and Brandt, I. Azoles additively inhibit cytochrome p450 1 (erod) and 19 (aromatase) in rainbow trout (oncorhynchus mykiss). *Aquat Toxicol*, 198:73–81, 2018. ISSN 1879-1514 (Electronic) 0166-445X (Linking). doi: 10.1016/j.aquatox.2018.02.016. URL <https://www.ncbi.nlm.nih.gov/pubmed/29522952>.
- Berbari, N. F., O'Connor, A. K., Haycraft, C. J., and Yoder, B. K. The primary cilium as a complex signaling center. *Curr Biol*, 19(13):R526–35, 2009. ISSN 1879-0445 (Electronic) 0960-9822 (Linking). doi: 10.1016/j.cub.2009.05.025. URL <https://www.ncbi.nlm.nih.gov/pubmed/19602418>.
- Bollig, F., Perner, B., Besenbeck, B., Kothe, S., Ebert, C., Taudien, S., and Englert, C. A highly conserved retinoic acid responsive element controls wt1a expression in the zebrafish pronephros. *Development*, 136(17):2883–92, 2009. ISSN 1477-9129 (Electronic) 0950-1991 (Linking). doi: 10.1242/dev.031773. URL <https://www.ncbi.nlm.nih.gov/pubmed/19666820>.

REFERENCES

- Booij, T. H., Bange, H., Leonhard, W. N., Yan, K., Fokkelman, M., Kunnen, S. J., Dauwerse, J. G., Qin, Y., van de Water, B., van Westen, G. J. P., Peters, D. J. M., and Price, L. S. High-throughput phenotypic screening of kinase inhibitors to identify drug targets for polycystic kidney disease. *SLAS Discov*, 22(8):974–984, 2017. ISSN 2472-5560 (Electronic) 2472-5552 (Linking). doi: 10.1177/2472555217716056. URL <https://www.ncbi.nlm.nih.gov/pubmed/28644734>.
- Briggs, J. P. The zebrafish: a new model organism for integrative physiology. *Am J Physiol Regul Integr Comp Physiol*, 282(1):R3–9, 2002. ISSN 0363-6119 (Print) 0363-6119 (Linking). doi: 10.1152/ajpregu.00589.2001. URL <https://www.ncbi.nlm.nih.gov/pubmed/11742817>.
- Buchser, W., Collins, M., Garyantes, T., Guha, R., Haney, S., Lemmon, V., Z., L., and O. Joseph Trask, B. Assay development guidelines for image-based high content screening, high content analysis and high content imaging, 2012. URL <https://www.ncbi.nlm.nih.gov/books/NBK100913/>. [accessed: 21-09-2018].
- Bulun, S. E., Lin, Z., Zhao, H., Lu, M., Amin, S., Reierstad, S., and Chen, D. Regulation of aromatase expression in breast cancer tissue. *Ann N Y Acad Sci*, 1155:121–31, 2009. ISSN 1749-6632 (Electronic) 0077-8923 (Linking). doi: 10.1111/j.1749-6632.2009.03705.x. URL <https://www.ncbi.nlm.nih.gov/pubmed/19250199>.
- Bundgaard, H. Acetylsalicylsalicylic acid: a potentially immunogenic impurity in acetylsalicylic acid. *J Pharm Pharmacol*, 26(1):18–22, 1974. ISSN 0022-3573 (Print) 0022-3573 (Linking). URL <https://www.ncbi.nlm.nih.gov/pubmed/4150928>.
- Cachat, J., Stewart, A., Utterback, E., Hart, P., Gaikwad, S., Wong, K., Kyzar, E., Wu, N., and Kalueff, A. V. Three-dimensional neurophenotyping of adult zebrafish behavior. *PLoS One*, 6(3):e17597, 2011. ISSN 1932-6203 (Electronic) 1932-6203 (Linking). doi: 10.1371/journal.pone.0017597. URL <https://www.ncbi.nlm.nih.gov/pubmed/21408171>.
- Cantas, L., Midtlyng, P. J., and Sorum, H. Impact of antibiotic treatments on the expression of the r plasmid tra genes and on the host innate immune activity during *prsl* bearing *aeromonas hydrophila* infection in zebrafish (*danio rerio*). *BMC Microbiol*, 12:37, 2012. ISSN 1471-2180 (Electronic) 1471-2180 (Linking). doi: 10.1186/1471-2180-12-37. URL <https://www.ncbi.nlm.nih.gov/pubmed/22429905>.
- Cantiello, H. F. Regulation of calcium signaling by polycystin-2. *Am J Physiol Renal Physiol*, 286(6):F1012–29, 2004. ISSN 1931-857X (Print) 1522-1466 (Linking). doi: 10.1152/ajprenal.00181.2003. URL <https://www.ncbi.nlm.nih.gov/pubmed/15130895>.
- Cao, Y., Semanchik, N., Lee, S. H., Somlo, S., Barbano, P. E., Coifman, R., and Sun, Z. Chemical modifier screen identifies hdac inhibitors as suppressors of pkd models. *Proc Natl Acad Sci U S A*, 106(51):21819–24, 2009. ISSN 1091-6490 (Electronic) 0027-8424 (Linking). doi: 10.1073/pnas.0911987106. URL <https://www.ncbi.nlm.nih.gov/pubmed/19966229>.
- Cao, Y., Park, A., and Sun, Z. Intraflagellar transport proteins are essential for cilia formation and for planar cell polarity. *J Am Soc Nephrol*, 21(8):1326–33, 2010. ISSN 1533-3450 (Electronic) 1046-6673 (Linking). doi: 10.1681/ASN.2009091001. URL <https://www.ncbi.nlm.nih.gov/pubmed/20576807>.
- Cario, C. L., Farrell, T. C., Milanese, C., and Burton, E. A. Automated measurement of zebrafish larval movement. *J Physiol*, 589(Pt 15): 3703–8, 2011. ISSN 1469-7793 (Electronic) 0022-3751 (Linking). doi: 10.1113/jphysiol.2011.207308. URL <https://www.ncbi.nlm.nih.gov/pubmed/21646414>.
- Carlson, S. G., Eng, E., Kim, E. G., Perlman, E. J., Copeland, T. D., and Ballermann, B. J. Expression of set, an inhibitor of protein phosphatase 2a, in renal development and wilms’ tumor. *J Am Soc Nephrol*, 9(10):1873–80, 1998. ISSN 1046-6673 (Print) 1046-6673 (Linking). URL <https://www.ncbi.nlm.nih.gov/pubmed/9773788>.
- Caroli, A., Perico, N., Perna, A., Antiga, L., Brambilla, P., Pisani, A., Visciano, B., Imbriaco, M., Messa, P., Cerutti, R., Dugo, M., Cancian, L., Buongiorno, E., De Pascalis, A., Gaspari, F., Carrara, F., Rubis, N., Prandini, S., Remuzzi, A., Remuzzi, G., Ruggenti, P., and group, A. s. Effect of longacting somatostatin analogue on kidney and cyst growth in autosomal dominant polycystic kidney disease (aladin): a randomised, placebo-controlled, multicentre trial. *Lancet*, 382(9903):1485–95, 2013. ISSN 1474-547X (Electronic) 0140-6736 (Linking). doi: 10.1016/S0140-6736(13)61407-5. URL <https://www.ncbi.nlm.nih.gov/pubmed/23972263>.

- Chapman, A. B., Torres, V. E., Perrone, R. D., Steinman, T. I., Bae, K. T., Miller, J. P., Miskulin, D. C., Rahbari Oskoui, F., Masoumi, A., Hogan, M. C., Winklhofer, F. T., Braun, W., Thompson, P. A., Meyers, C. M., Kelleher, C., and Schrier, R. W. The halt polycystic kidney disease trials: design and implementation. *Clin J Am Soc Nephrol*, 5(1):102–9, 2010. ISSN 1555-905X (Electronic) 1555-9041 (Linking). doi: 10.2215/CJN.04310709. URL <https://www.ncbi.nlm.nih.gov/pubmed/20089507>.
- Chen, S., Borowiak, M., Fox, J. L., Maehr, R., Osafune, K., Davidow, L., Lam, K., Peng, L. F., Schreiber, S. L., Rubin, L. L., and Melton, D. A small molecule that directs differentiation of human escs into the pancreatic lineage. *Nat Chem Biol*, 5(4):258–65, 2009. ISSN 1552-4469 (Electronic) 1552-4450 (Linking). doi: 10.1038/nchembio.154. URL <https://www.ncbi.nlm.nih.gov/pubmed/19287398>.
- Chen, S., Zhu, Y., Xia, W., Xia, S., and Xu, X. Automated analysis of zebrafish images for phenotypic changes in drug discovery. *J Neurosci Methods*, 200(2):229–36, 2011. ISSN 1872-678X (Electronic) 0165-0270 (Linking). doi: 10.1016/j.jneumeth.2011.06.015. URL <https://www.ncbi.nlm.nih.gov/pubmed/21767568>.
- Chen, S. A., Besman, M. J., Sparkes, R. S., Zollman, S., Klisak, I., Mohandas, T., Hall, P. F., and Shively, J. E. Human aromatase: cdna cloning, southern blot analysis, and assignment of the gene to chromosome 15. *DNA*, 7(1):27–38, 1988. ISSN 0198-0238 (Print) 0198-0238 (Linking). doi: 10.1089/dna.1988.7.27. URL <https://www.ncbi.nlm.nih.gov/pubmed/3390233>.
- Cherubini, M., Baxa, P., and Guarino, G. The oestrogen-progesterone receptor ratio: an indicator of breast cancer evolution. *Chir Ital*, 54(4):423–8, 2002. ISSN 0009-4773 (Print) 0009-4773 (Linking). URL <https://www.ncbi.nlm.nih.gov/pubmed/12239750>.
- Cirio, M. C., de Caestecker, M. P., and Hukriede, N. A. Zebrafish models of kidney damage and repair. *Curr Pathobiol Rep*, 3(2):163–170, 2015. ISSN 2167-485X (Print) 2167-485X (Linking). doi: 10.1007/s40139-015-0080-4. URL <https://www.ncbi.nlm.nih.gov/pubmed/28690924>.
- Conley, A., Mapes, S., Corbin, C. J., Greger, D., Walters, K., Trant, J., and Graham, S. A comparative approach to structure-function studies of mammalian aromatases. *J Steroid Biochem Mol Biol*, 79(1-5):289–97, 2001. ISSN 0960-0760 (Print) 0960-0760 (Linking). URL <https://www.ncbi.nlm.nih.gov/pubmed/11850235>.
- Creton, R. Automated analysis of behavior in zebrafish larvae. *Behav Brain Res*, 203(1):127–36, 2009. ISSN 1872-7549 (Electronic) 0166-4328 (Linking). doi: 10.1016/j.bbr.2009.04.030. URL <https://www.ncbi.nlm.nih.gov/pubmed/19409932>.
- Cruz, S. A., Lin, C. H., Chao, P. L., and Hwang, P. P. Glucocorticoid receptor, but not mineralocorticoid receptor, mediates cortisol regulation of epidermal ionocyte development and ion transport in zebrafish (*danio rerio*). *PLoS One*, 8(10):e77997, 2013. ISSN 1932-6203 (Electronic) 1932-6203 (Linking). doi: 10.1371/journal.pone.0077997. URL <https://www.ncbi.nlm.nih.gov/pubmed/24205060>.
- de Groh, E. D., Swanhart, L. M., Cosentino, C. C., Jackson, R. L., Dai, W., Kitchens, C. A., Day, B. W., Smithgall, T. E., and Hukriede, N. A. Inhibition of histone deacetylase expands the renal progenitor cell population. *J Am Soc Nephrol*, 21(5):794–802, 2010. ISSN 1533-3450 (Electronic) 1046-6673 (Linking). doi: 10.1681/ASN.2009080851. URL <https://www.ncbi.nlm.nih.gov/pubmed/20378823>.
- Devuyst, O., Knoers, N. V., Remuzzi, G., Schaefer, F., Board of the Working Group for Inherited Kidney Diseases of the European Renal, A., European, D., and Transplant, A. Rare inherited kidney diseases: challenges, opportunities, and perspectives. *Lancet*, 383(9931):1844–59, 2014. ISSN 1474-547X (Electronic) 0140-6736 (Linking). doi: 10.1016/S0140-6736(14)60659-0. URL <https://www.ncbi.nlm.nih.gov/pubmed/24856029>.
- Drummond, B. E. and Wingert, R. A. Insights into kidney stem cell development and regeneration using zebrafish. *World J Stem Cells*, 8(2):22–31, 2016. ISSN 1948-0210 (Print) 1948-0210 (Linking). doi: 10.4252/wjsc.v8.i2.22. URL <https://www.ncbi.nlm.nih.gov/pubmed/26981168>.
- Drummond, I. Making a zebrafish kidney: a tale of two tubes. *Trends Cell Biol*, 13(7):357–65, 2003. ISSN 0962-8924 (Print) 0962-8924 (Linking). URL <https://www.ncbi.nlm.nih.gov/pubmed/12837606>.
- Drummond, I. A. Kidney development and disease in the zebrafish. *J Am Soc Nephrol*, 16(2):299–304, 2005. ISSN 1046-6673 (Print) 1046-6673 (Linking). doi: 10.1681/ASN.2004090754. URL <https://www.ncbi.nlm.nih.gov/pubmed/15647335>.

REFERENCES

- Drummond, I. A. and Davidson, A. J. Zebrafish kidney development. *Methods Cell Biol*, 134:391–429, 2016. ISSN 0091-679X (Print) 0091-679X (Linking). doi: 10.1016/bs.mcb.2016.03.041. URL <https://www.ncbi.nlm.nih.gov/pubmed/27312500>.
- Drummond, I. A., Majumdar, A., Hentschel, H., Elger, M., Solnica-Krezel, L., Schier, A. F., Neuhauss, S. C., Stemple, D. L., Zwartkruis, F., Rangini, Z., Driever, W., and Fishman, M. C. Early development of the zebrafish pronephros and analysis of mutations affecting pronephric function. *Development*, 125(23):4655–67, 1998. ISSN 0950-1991 (Print) 0950-1991 (Linking). URL <https://www.ncbi.nlm.nih.gov/pubmed/9806915>.
- Dussaule, J. C., Michel, C., Peraldi, M. N., Lecomte, J. M., Gros, C., Mignon, F., and Ardaillou, R. Inhibition of neutral endopeptidase stimulates renal sodium excretion in patients with chronic renal failure. *Clin Sci (Lond)*, 84(1):31–9, 1993. ISSN 0143-5221 (Print) 0143-5221 (Linking). URL <https://www.ncbi.nlm.nih.gov/pubmed/8382131>.
- Early, J. J., Cole, K. L., Williamson, J. M., Swire, M., Kamadurai, H., Muskavitch, M., and Lyons, D. A. An automated high-resolution in vivo screen in zebrafish to identify chemical regulators of myelination. *Elife*, 7, 2018. ISSN 2050-084X (Electronic) 2050-084X (Linking). doi: 10.7554/eLife.35136. URL <https://www.ncbi.nlm.nih.gov/pubmed/29979149>.
- Ebarasi, L., He, L., Hultenby, K., Takemoto, M., Betsholtz, C., Tryggvason, K., and Majumdar, A. A reverse genetic screen in the zebrafish identifies *crb2b* as a regulator of the glomerular filtration barrier. *Dev Biol*, 334(1):1–9, 2009. ISSN 1095-564X (Electronic) 0012-1606 (Linking). doi: 10.1016/j.ydbio.2009.04.017. URL <https://www.ncbi.nlm.nih.gov/pubmed/19393641>.
- Eberlin, M., Muck, T., and Michel, M. C. A comprehensive review of the pharmacodynamics, pharmacokinetics, and clinical effects of the neutral endopeptidase inhibitor racecadotril. *Front Pharmacol*, 3:93, 2012. ISSN 1663-9812 (Electronic) 1663-9812 (Linking). doi: 10.3389/fphar.2012.00093. URL <https://www.ncbi.nlm.nih.gov/pubmed/22661949>.
- Eckardt, K. U., Coresh, J., Devuyt, O., Johnson, R. J., Kottgen, A., Levey, A. S., and Levin, A. Evolving importance of kidney disease: from subspecialty to global health burden. *Lancet*, 382(9887):158–69, 2013. ISSN 1474-547X (Electronic) 0140-6736 (Linking). doi: 10.1016/S0140-6736(13)60439-0. URL <https://www.ncbi.nlm.nih.gov/pubmed/23727165>.
- Egbuta, C., Lo, J., and Ghosh, D. Mechanism of inhibition of estrogen biosynthesis by azole fungicides. *Endocrinology*, 155(12):4622–8, 2014. ISSN 1945-7170 (Electronic) 0013-7227 (Linking). doi: 10.1210/en.2014-1561. URL <https://www.ncbi.nlm.nih.gov/pubmed/25243857>.
- European Medicines Agency. Flubendazole (extrapolation to poultry), summary report (4). committee for medicinal products for veterinary use, 2006. URL http://www.ema.europa.eu/docs/en_GB/document_library/Maximum_Residue_Limits_-_Report/2009/11/WC500014292.pdf. [accessed: 9-12-2018].
- Fukuyo, Y., Nakamura, T., Bubenshchikova, E., Powell, R., Tsuji, T., Janknecht, R., and Obara, T. Nephric and podocin functions are highly conserved between the zebrafish pronephros and mammalian metanephros. *Mol Med Rep*, 9(2):457–65, 2014. ISSN 1791-3004 (Electronic) 1791-2997 (Linking). doi: 10.3892/mmr.2013.1844. URL <https://www.ncbi.nlm.nih.gov/pubmed/24337247>.
- Fuller, B. B., Spaulding, D. T., and Smith, D. R. Regulation of the catalytic activity of preexisting tyrosinase in black and caucasian human melanocyte cell cultures. *Exp Cell Res*, 262(2):197–208, 2001. ISSN 0014-4827 (Print) 0014-4827 (Linking). doi: 10.1006/excr.2000.5092. URL <https://www.ncbi.nlm.nih.gov/pubmed/11139343>.
- Furr, M. O., Quance, J., and Kennedy, T. A 10-day toxicity study of toltrazuril 5 *Vet Ther*, 1(4):245–51, 2000. ISSN 1528-3593 (Print) 1528-3593 (Linking). URL <https://www.ncbi.nlm.nih.gov/pubmed/19757571>.
- Gao, J., Zhou, H., Lei, T., Zhou, L., Li, W., Li, X., and Yang, B. Curcumin inhibits renal cyst formation and enlargement in vitro by regulating intracellular signaling pathways. *Eur J Pharmacol*, 654(1):92–9, 2011. ISSN 1879-0712 (Electronic) 0014-2999 (Linking). doi: 10.1016/j.ejphar.2010.12.008. URL <https://www.ncbi.nlm.nih.gov/pubmed/21187084>.
- Gao, Y., Chan, R. H., Chow, T. W., Zhang, L., Bonilla, S., Pang, C. P., Zhang, M., and Leung, Y. F. A high-throughput zebrafish screening method for visual mutants by light-induced locomotor response. *IEEE/ACM Trans Comput Biol Bioinform*, 11(4):693–701, 2014. ISSN 1557-9964 (Electronic) 1545-5963 (Linking). doi: 10.1109/TCBB.2014.2306829. URL <https://www.ncbi.nlm.nih.gov/pubmed/26356340>.

- Gbadegesin, R., Hinkes, B. G., Hoskins, B. E., Vlangos, C. N., Heeringa, S. F., Liu, J., Loirat, C., Ozaltin, F., Hashmi, S., Ulmer, F., Cleper, R., Ettenger, R., Antignac, C., Wiggins, R. C., Zenker, M., and Hildebrandt, F. Mutations in *plec1* are a major cause of isolated diffuse mesangial sclerosis (idms). *Nephrol Dial Transplant*, 23(4):1291–7, 2008. ISSN 1460-2385 (Electronic) 0931-0509 (Linking). doi: 10.1093/ndt/gfm759. URL <https://www.ncbi.nlm.nih.gov/pubmed/18065803>.
- Gee, H. Y., Saisawat, P., Ashraf, S., Hurd, T. W., Vega-Warner, V., Fang, H., Beck, B. B., Gribouval, O., Zhou, W., Diaz, K. A., Natarajan, S., Wiggins, R. C., Lovric, S., Chernin, G., Schoeb, D. S., Ovunc, B., Frishberg, Y., Soliman, N. A., Fathy, H. M., Goebel, H., Hoefele, J., Weber, L. T., Innis, J. W., Faul, C., Han, Z., Washburn, J., Antignac, C., Levy, S., Otto, E. A., and Hildebrandt, F. Arhgdia mutations cause nephrotic syndrome via defective rho gtpase signaling. *J Clin Invest*, 123(8):3243–53, 2013. ISSN 1558-8238 (Electronic) 0021-9738 (Linking). doi: 10.1172/JCI69134. URL <https://www.ncbi.nlm.nih.gov/pubmed/23867502>.
- Gee, H. Y., Zhang, F., Ashraf, S., Kohl, S., Sadowski, C. E., Vega-Warner, V., Zhou, W., Lovric, S., Fang, H., Nettleton, M., Zhu, J. Y., Hoefele, J., Weber, L. T., Podracka, L., Boor, A., Fehrenbach, H., Innis, J. W., Washburn, J., Levy, S., Lifton, R. P., Otto, E. A., Han, Z., and Hildebrandt, F. Kank deficiency leads to podocyte dysfunction and nephrotic syndrome. *J Clin Invest*, 125(6):2375–84, 2015. ISSN 1558-8238 (Electronic) 0021-9738 (Linking). doi: 10.1172/JCI79504. URL <https://www.ncbi.nlm.nih.gov/pubmed/25961457>.
- Gehrig, J., Reischl, M., Kalmar, E., Ferg, M., Hadzhiev, Y., Zaucker, A., Song, C., Schindler, S., Liebel, U., and Muller, F. Automated high-throughput mapping of promoter-enhancer interactions in zebrafish embryos. *Nat Methods*, 6(12):911–6, 2009. ISSN 1548-7105 (Electronic) 1548-7091 (Linking). doi: 10.1038/nmeth.1396. URL <https://www.ncbi.nlm.nih.gov/pubmed/19898487>.
- Gehrig, J., Pandey, G., and Westhoff, J. H. Zebrafish as a model for drug screening in genetic kidney diseases. *Front Pediatr*, 6:183, 2018. ISSN 2296-2360 (Print) 2296-2360 (Linking). doi: 10.3389/fped.2018.00183. URL <https://www.ncbi.nlm.nih.gov/pubmed/30003073>.
- Geisler, R., Rauch, G. J., Geiger-Rudolph, S., Albrecht, A., van Bebber, F., Berger, A., Busch-Nentwich, E., Dahm, R., Dekens, M. P., Dooley, C., Elli, A. F., Gehring, I., Geiger, H., Geisler, M., Glaser, S., Holley, S., Huber, M., Kerr, A., Kirn, A., Knirsch, M., Konantz, M., Kuchler, A. M., Maderspacher, F., Neuhauss, S. C., Nicolson, T., Ober, E. A., Praeg, E., Ray, R., Rentzsch, B., Rick, J. M., Rief, E., Schuarte, H. E., Schepp, C. P., Schonberger, U., Schonhaler, H. B., Seiler, C., Sidi, S., Sollner, C., Wehner, A., Weiler, C., and Nusslein-Volhard, C. Large-scale mapping of mutations affecting zebrafish development. *BMC Genomics*, 8:11, 2007. ISSN 1471-2164 (Electronic) 1471-2164 (Linking). doi: 10.1186/1471-2164-8-11. URL <https://www.ncbi.nlm.nih.gov/pubmed/17212827>.
- Geisler, R., Borel, N., Ferg, M., Maier, J. V., and Strahle, U. Maintenance of zebrafish lines at the european zebrafish resource center. *Zebrafish*, 13 Suppl 1:S19–23, 2016. ISSN 1557-8542 (Electronic) 1545-8547 (Linking). doi: 10.1089/zeb.2015.1205. URL <https://www.ncbi.nlm.nih.gov/pubmed/27351617>.
- Giuliano, K. A., Haskins, J. R., and Taylor, D. L. Advances in high content screening for drug discovery. *Assay Drug Dev Technol*, 1(4): 565–77, 2003. ISSN 1540-658X (Print) 1540-658X (Linking). doi: 10.1089/154065803322302826. URL <https://www.ncbi.nlm.nih.gov/pubmed/15090253>.
- Goessling, W., Allen, R. S., Guan, X., Jin, P., Uchida, N., Dovey, M., Harris, J. M., Metzger, M. E., Bonifacino, A. C., Stroncek, D., Stegner, J., Armant, M., Schlaeger, T., Tisdale, J. F., Zon, L. I., Donahue, R. E., and North, T. E. Prostaglandin e2 enhances human cord blood stem cell xenotransplants and shows long-term safety in preclinical nonhuman primate transplant models. *Cell Stem Cell*, 8(4):445–58, 2011. ISSN 1875-9777 (Electronic) 1875-9777 (Linking). doi: 10.1016/j.stem.2011.02.003. URL <https://www.ncbi.nlm.nih.gov/pubmed/21474107>.
- Graf, S. F., Hotzel, S., Liebel, U., Stemmer, A., and Knapp, H. F. Image-based fluidic sorting system for automated zebrafish egg sorting into multiwell plates. *J Lab Autom*, 16(2):105–11, 2011. ISSN 2211-0690 (Electronic) 2211-0682 (Linking). doi: 10.1016/j.jala.2010.11.002. URL <https://www.ncbi.nlm.nih.gov/pubmed/21609691>.
- Grantham, J. J. Polycystic kidney disease: huge kidneys, huge problems, huge progress. *Trans Am Clin Climatol Assoc*, 108:165–70; discussion 170–2, 1997. ISSN 0065-7778 (Print) 0065-7778 (Linking). URL <https://www.ncbi.nlm.nih.gov/pubmed/9108675>.

REFERENCES

- Gros, C., Souque, A., Schwartz, J. C., Duchier, J., Cournot, A., Baumer, P., and Lecomte, J. M. Protection of atrial natriuretic factor against degradation: diuretic and natriuretic responses after in vivo inhibition of enkephalinase (ec 3.4.24.11) by acetorphan. *Proc Natl Acad Sci U S A*, 86(19):7580–4, 1989. ISSN 0027-8424 (Print) 0027-8424 (Linking). URL <https://www.ncbi.nlm.nih.gov/pubmed/2529543>.
- Gumz, M. L., Lynch, I. J., Greenlee, M. M., Cain, B. D., and Wingo, C. S. The renal h⁺-k⁺-atpases: physiology, regulation, and structure. *Am J Physiol Renal Physiol*, 298(1):F12–21, 2010. ISSN 1522-1466 (Electronic) 1522-1466 (Linking). doi: 10.1152/ajprenal.90723.2008. URL <https://www.ncbi.nlm.nih.gov/pubmed/19640897>.
- Gutierrez, A., Pan, L., Groen, R. W., Baleyrier, F., Kentsis, A., Marineau, J., Grebliunaite, R., Kozakewich, E., Reed, C., Pflumio, F., Poglio, S., Uzan, B., Clemons, P., VerPlank, L., An, F., Burbank, J., Norton, S., Tolliday, N., Steen, H., Weng, A. P., Yuan, H., Bradner, J. E., Mitsiades, C., Look, A. T., and Aster, J. C. Phenothiazines induce pp2a-mediated apoptosis in t cell acute lymphoblastic leukemia. *J Clin Invest*, 124(2):644–55, 2014. ISSN 1558-8238 (Electronic) 0021-9738 (Linking). doi: 10.1172/JCI65093. URL <https://www.ncbi.nlm.nih.gov/pubmed/24401270>.
- Haffter, P., Granato, M., Brand, M., Mullins, M. C., Hammerschmidt, M., Kane, D. A., Odenthal, J., van Eeden, F. J., Jiang, Y. J., Heisenberg, C. P., Kelsh, R. N., Furutani-Seiki, M., Vogelsang, E., Beuchle, D., Schach, U., Fabian, C., and Nusslein-Volhard, C. The identification of genes with unique and essential functions in the development of the zebrafish, danio rerio. *Development*, 123:1–36, 1996. ISSN 0950-1991 (Print) 0950-1991 (Linking). URL <https://www.ncbi.nlm.nih.gov/pubmed/9007226>.
- Hagedorn, E. J., Durand, E. M., Fast, E. M., and Zon, L. I. Getting more for your marrow: boosting hematopoietic stem cell numbers with pge2. *Exp Cell Res*, 329(2):220–6, 2014. ISSN 1090-2422 (Electronic) 0014-4827 (Linking). doi: 10.1016/j.yexcr.2014.07.030. URL <https://www.ncbi.nlm.nih.gov/pubmed/25094063>.
- Halbritter, J., Bizet, A. A., Schmidts, M., Porath, J. D., Braun, D. A., Gee, H. Y., McInerney-Leo, A. M., Krug, P., Filhol, E., Davis, E. E., Airik, R., Czarnecki, P. G., Lehman, A. M., Trnka, P., Nitschke, P., Bole-Feysot, C., Schueler, M., Knebelmann, B., Burtey, S., Szabo, A. J., Tory, K., Leo, P. J., Gardiner, B., McKenzie, F. A., Zankl, A., Brown, M. A., Hartley, J. L., Maher, E. R., Li, C., Leroux, M. R., Scambler, P. J., Zhan, S. H., Jones, S. J., Kayserili, H., Tuysuz, B., Moorani, K. N., Constantinescu, A., Krantz, I. D., Kaplan, B. S., Shah, J. V., Consortium, U. K., Hurd, T. W., Doherty, D., Katsanis, N., Duncan, E. L., Otto, E. A., Beales, P. L., Mitchison, H. M., Saunier, S., and Hildebrandt, F. Defects in the ift-b component ift172 cause jeune and mainzer-saldino syndromes in humans. *Am J Hum Genet*, 93(5):915–25, 2013. ISSN 1537-6605 (Electronic) 0002-9297 (Linking). doi: 10.1016/j.ajhg.2013.09.012. URL <https://www.ncbi.nlm.nih.gov/pubmed/24140113>.
- Hanke, N., King, B. L., Vaske, B., Haller, H., and Schiffer, M. A fluorescence-based assay for proteinuria screening in larval zebrafish (danio rerio). *Zebrafish*, 12(5):372–6, 2015. ISSN 1557-8542 (Electronic) 1545-8547 (Linking). doi: 10.1089/zeb.2015.1093. URL <https://www.ncbi.nlm.nih.gov/pubmed/26125680>.
- Harder, A. and Haberkorn, A. Possible mode of action of toltrazuril: studies on two eimeria species and mammalian and ascaris suum enzymes. *Parasitol Res*, 76(1):8–12, 1989. ISSN 0932-0113 (Print) 0932-0113 (Linking). URL <https://www.ncbi.nlm.nih.gov/pubmed/2560189>.
- Hariharan, V., Klarquist, J., Reust, M. J., Koshoffer, A., McKee, M. D., Boissy, R. E., and Le Poole, I. C. Monobenzyl ether of hydroquinone and 4-tertiary butyl phenol activate markedly different physiological responses in melanocytes: relevance to skin depigmentation. *J Invest Dermatol*, 130(1):211–20, 2010. ISSN 1523-1747 (Electronic) 0022-202X (Linking). doi: 10.1038/jid.2009.214. URL <https://www.ncbi.nlm.nih.gov/pubmed/19657355>.
- Harris, P. C. and Torres, V. E. Polycystic kidney disease. *Annu Rev Med*, 60:321–37, 2009. ISSN 1545-326X (Electronic) 0066-4219 (Linking). doi: 10.1146/annurev.med.60.101707.125712. URL <https://www.ncbi.nlm.nih.gov/pubmed/18947299>.
- Harris, P. C. and Torres, V. E. Genetic mechanisms and signaling pathways in autosomal dominant polycystic kidney disease. *J Clin Invest*, 124(6):2315–24, 2014. ISSN 1558-8238 (Electronic) 0021-9738 (Linking). doi: 10.1172/JCI72272. URL <https://www.ncbi.nlm.nih.gov/pubmed/24892705>.

- Hellman, N. E., Liu, Y., Merkel, E., Austin, C., Le Corre, S., Beier, D. R., Sun, Z., Sharma, N., Yoder, B. K., and Drummond, I. A. The zebrafish foxj1a transcription factor regulates cilia function in response to injury and epithelial stretch. *Proc Natl Acad Sci U S A*, 107(43): 18499–504, 2010. ISSN 1091-6490 (Electronic) 0027-8424 (Linking). doi: 10.1073/pnas.1005998107. URL <https://www.ncbi.nlm.nih.gov/pubmed/20937855>.
- Hinkes, B., Wiggins, R. C., Gbadegesin, R., Vlangos, C. N., Seelow, D., Nurnberg, G., Garg, P., Verma, R., Chaib, H., Hoskins, B. E., Ashraf, S., Becker, C., Hennies, H. C., Goyal, M., Wharram, B. L., Schachter, A. D., Mudumana, S., Drummond, I., Kerjaschki, D., Waldherr, R., Dietrich, A., Ozaltin, F., Bakkaloglu, A., Cleper, R., Basel-Vanagaite, L., Pohl, M., Griebel, M., Tsygin, A. N., Soyly, A., Muller, D., Sorli, C. S., Bunney, T. D., Katan, M., Liu, J., Attanasio, M., O'Toole J. F., Hasselbacher, K., Mucha, B., Otto, E. A., Airik, R., Kispert, A., Kelley, G. G., Smrcka, A. V., Gudermann, T., Holzman, L. B., Nurnberg, P., and Hildebrandt, F. Positional cloning uncovers mutations in *plce1* responsible for a nephrotic syndrome variant that may be reversible. *Nat Genet*, 38(12):1397–405, 2006. ISSN 1061-4036 (Print) 1061-4036 (Linking). doi: 10.1038/ng1918. URL <https://www.ncbi.nlm.nih.gov/pubmed/17086182>.
- Hochmann, J. Ratio of concentrations of estrogen receptors to progesterone receptors (er/pr) in the cytosol of breast cancers (stratification by forming of groups differing in pr). *Neoplasma*, 54(4):290–6, 2007. ISSN 0028-2685 (Print) 0028-2685 (Linking). URL <https://www.ncbi.nlm.nih.gov/pubmed/17822318>.
- Huangfu, D., Liu, A., Rakeman, A. S., Murcia, N. S., Niswander, L., and Anderson, K. V. Hedgehog signalling in the mouse requires intraflagellar transport proteins. *Nature*, 426(6962):83–7, 2003. ISSN 1476-4687 (Electronic) 0028-0836 (Linking). doi: 10.1038/nature02061. URL <https://www.ncbi.nlm.nih.gov/pubmed/14603322>.
- Huiting, L. N., Laroche, F., and Feng, H. The zebrafish as a tool to cancer drug discovery. *Austin J Pharmacol Ther*, 3(2):1069, 2015. ISSN 2373-6208 (Print) 2373-6208 (Linking). URL <https://www.ncbi.nlm.nih.gov/pubmed/26835511>.
- Hultman, K. A., Budi, E. H., Teasley, D. C., Gottlieb, A. Y., Parichy, D. M., and Johnson, S. L. Defects in *erbb*-dependent establishment of adult melanocyte stem cells reveal independent origins for embryonic and regeneration melanocytes. *PLoS Genet*, 5(7):e1000544, 2009. ISSN 1553-7404 (Electronic) 1553-7390 (Linking). doi: 10.1371/journal.pgen.1000544. URL <https://www.ncbi.nlm.nih.gov/pubmed/19578401>.
- Ichikawa, I. and Brenner, B. M. Mechanisms of action of hisamine and histamine antagonists on the glomerular microcirculation in the rat. *Circ Res*, 45(6):737–45, 1979. ISSN 0009-7330 (Print) 0009-7330 (Linking). URL <https://www.ncbi.nlm.nih.gov/pubmed/498437>.
- Idowu, J., Home, T., Patel, N., Magenheimer, B., Tran, P. V., Maser, R. L., Ward, C. J., Calvet, J. P., Wallace, D. P., and Sharma, M. Aberrant regulation of notch3 signaling pathway in polycystic kidney disease. *Sci Rep*, 8(1):3340, 2018. ISSN 2045-2322 (Electronic) 2045-2322 (Linking). doi: 10.1038/s41598-018-21132-3. URL <https://www.ncbi.nlm.nih.gov/pubmed/29463793>.
- Inoue, K., Inazawa, J., Nakagawa, H., Shimada, T., Yamazaki, H., Guengerich, F. P., and Abe, T. Assignment of the human cytochrome p-450 nifedipine oxidase gene (*cyp3a4*) to chromosome 7 at band q22.1 by fluorescence in situ hybridization. *Jpn J Hum Genet*, 37(2): 133–8, 1992. ISSN 0916-8478 (Print) 0916-8478 (Linking). doi: 10.1007/BF01899734. URL <https://www.ncbi.nlm.nih.gov/pubmed/1391968>.
- Islam, M. R., Puri, S., Rodova, M., Magenheimer, B. S., Maser, R. L., and Calvet, J. P. Retinoic acid-dependent activation of the polycystic kidney disease-1 (*pkd1*) promoter. *Am J Physiol Renal Physiol*, 295(6):F1845–54, 2008. ISSN 1931-857X (Print) 1522-1466 (Linking). doi: 10.1152/ajprenal.90355.2008. URL <https://www.ncbi.nlm.nih.gov/pubmed/18922886>.
- Jarque, S., Fetter, E., Veneman, W. J., Spaink, H. P., Peravali, R., Strahle, U., and Scholz, S. An automated screening method for detecting compounds with goitrogenic activity using transgenic zebrafish embryos. *PLoS One*, 13(8):e0203087, 2018. ISSN 1932-6203 (Electronic) 1932-6203 (Linking). doi: 10.1371/journal.pone.0203087. URL <https://www.ncbi.nlm.nih.gov/pubmed/30157258>.
- Jonassen, J. A., SanAgustin, J., Baker, S. P., and Pazour, G. J. Disruption of ift complex a causes cystic kidneys without mitotic spindle misorientation. *J Am Soc Nephrol*, 23(4):641–51, 2012. ISSN 1533-3450 (Electronic) 1046-6673 (Linking). doi: 10.1681/ASN.2011080829. URL <https://www.ncbi.nlm.nih.gov/pubmed/22282595>.

REFERENCES

- Jurczyk, A., Gromley, A., Redick, S., San Agustin, J., Witman, G., Pazour, G. J., Peters, D. J., and Doxsey, S. Pericentrin forms a complex with intraflagellar transport proteins and polycystin-2 and is required for primary cilia assembly. *J Cell Biol*, 166(5):637–43, 2004. ISSN 0021-9525 (Print) 0021-9525 (Linking). doi: 10.1083/jcb.200405023. URL <https://www.ncbi.nlm.nih.gov/pubmed/15337773>.
- Kalueff, A. V., Stewart, A. M., and Gerlai, R. Zebrafish as an emerging model for studying complex brain disorders. *Trends Pharmacol Sci*, 35(2):63–75, 2014. ISSN 1873-3735 (Electronic) 0165-6147 (Linking). doi: 10.1016/j.tips.2013.12.002. URL <https://www.ncbi.nlm.nih.gov/pubmed/24412421>.
- Kanehisa, M. and Goto, S. Kegg: kyoto encyclopedia of genes and genomes. *Nucleic Acids Res*, 28(1):27–30, 2000. ISSN 0305-1048 (Print) 0305-1048 (Linking). URL <https://www.ncbi.nlm.nih.gov/pubmed/10592173>.
- Kanehisa, M., Sato, Y., Kawashima, M., Furumichi, M., and Tanabe, M. Kegg as a reference resource for gene and protein annotation. *Nucleic Acids Res*, 44(D1):D457–62, 2016. ISSN 1362-4962 (Electronic) 0305-1048 (Linking). doi: 10.1093/nar/gkv1070. URL <https://www.ncbi.nlm.nih.gov/pubmed/26476454>.
- Kanehisa, M., Furumichi, M., Tanabe, M., Sato, Y., and Morishima, K. Kegg: new perspectives on genomes, pathways, diseases and drugs. *Nucleic Acids Res*, 45(D1):D353–D361, 2017. ISSN 1362-4962 (Electronic) 0305-1048 (Linking). doi: 10.1093/nar/gkw1092. URL <https://www.ncbi.nlm.nih.gov/pubmed/27899662>.
- Katoh, Y., Terada, M., Nishijima, Y., Takei, R., Nozaki, S., Hamada, H., and Nakayama, K. Overall architecture of the intraflagellar transport (ift)-b complex containing cluap1/ift38 as an essential component of the ift-b peripheral subcomplex. *J Biol Chem*, 291(21):10962–75, 2016. ISSN 1083-351X (Electronic) 0021-9258 (Linking). doi: 10.1074/jbc.M116.713883. URL <https://www.ncbi.nlm.nih.gov/pubmed/26980730>.
- Kenneth, A. G., Robbin, L. D., Dunlay, R. T., Albert, G., Joanne, M. V., Joseph, Z., George, N. P., and Taylor, D. L. High-content screening: A new approach to easing key bottlenecks in the drug discovery process. *Journal of Biomolecular Screening*, 2(4):249–259, 1997. doi: 10.1177/108705719700200410.
- Kimmel, C. B., Ballard, W. W., Kimmel, S. R., Ullmann, B., and Schilling, T. F. Stages of embryonic development of the zebrafish. *Dev Dyn*, 203(3):253–310, 1995. ISSN 1058-8388 (Print) 1058-8388 (Linking). doi: 10.1002/aja.1002030302. URL <https://www.ncbi.nlm.nih.gov/pubmed/8589427>.
- Kleczo, E. K., Marsh, K. H., Tyler, L. C., Furgeson, S. B., Bullock, B. L., Altmann, C. J., Miyazaki, M., Gitomer, B. Y., Harris, P. C., Weiser-Evans, M. C. M., Chonchol, M. B., Clambey, E. T., Nemenoff, R. A., and Hopp, K. Cd8(+) t cells modulate autosomal dominant polycystic kidney disease progression. *Kidney Int*, 94(6):1127–1140, 2018. ISSN 1523-1755 (Electronic) 0085-2538 (Linking). doi: 10.1016/j.kint.2018.06.025. URL <https://www.ncbi.nlm.nih.gov/pubmed/30249452>.
- Knox, C., Law, V., Jewison, T., Liu, P., Ly, S., Frolkis, A., Pon, A., Banco, K., Mak, C., Neveu, V., Djoumbou, Y., Eisner, R., Guo, A. C., and Wishart, D. S. Drugbank 3.0: a comprehensive resource for 'omics' research on drugs. *Nucleic Acids Res*, 39(Database issue):D1035–41, 2011. ISSN 1362-4962 (Electronic) 0305-1048 (Linking). doi: 10.1093/nar/gkq1126. URL <https://www.ncbi.nlm.nih.gov/pubmed/21059682>.
- Kokel, D., Bryan, J., Laggner, C., White, R., Cheung, C. Y., Mateus, R., Healey, D., Kim, S., Werdich, A. A., Haggarty, S. J., Macrae, C. A., Shoichet, B., and Peterson, R. T. Rapid behavior-based identification of neuroactive small molecules in the zebrafish. *Nat Chem Biol*, 6(3):231–237, 2010. ISSN 1552-4469 (Electronic) 1552-4450 (Linking). doi: 10.1038/nchembio.307. URL <https://www.ncbi.nlm.nih.gov/pubmed/20081854>.
- Kotb, A. M., Muller, T., Xie, J., Anand-Apte, B., Endlich, K., and Endlich, N. Simultaneous assessment of glomerular filtration and barrier function in live zebrafish. *Am J Physiol Renal Physiol*, 307(12):F1427–34, 2014. ISSN 1522-1466 (Electronic) 1522-1466 (Linking). doi: 10.1152/ajprenal.00029.2014. URL <https://www.ncbi.nlm.nih.gov/pubmed/25298528>.
- Kramer-Zucker, A. G., Wiessner, S., Jensen, A. M., and Drummond, I. A. Organization of the pronephric filtration apparatus in zebrafish requires nephrin, podocin and the ferm domain protein mosaic eyes. *Dev Biol*, 285(2):316–29, 2005. ISSN 0012-1606 (Print) 0012-1606 (Linking). doi: 10.1016/j.ydbio.2005.06.038. URL <https://www.ncbi.nlm.nih.gov/pubmed/16102746>.

- Landini, G. Convex hull plugin. URL <https://blog.bham.ac.uk/intellimic/g-landini-software/>. [accessed: 23-11-2016].
- Le Corre, S., Eyre, D., and Drummond, I. A. Modulation of the secretory pathway rescues zebrafish polycystic kidney disease pathology. *J Am Soc Nephrol*, 25(8):1749–59, 2014. ISSN 1533-3450 (Electronic) 1046-6673 (Linking). doi: 10.1681/ASN.2013101060. URL <https://www.ncbi.nlm.nih.gov/pubmed/24627348>.
- Lecomte, J. M., Baumer, P., Lim, C., Duchier, J., Cournot, A., Dussaule, J. C., Ardaillou, R., Gros, C., Chaignon, B., Souque, A., and et al. Stereoselective protection of exogenous and endogenous atrial natriuretic factor by enkephalinase inhibitors in mice and humans. *Eur J Pharmacol*, 179(1-2):65–73, 1990. ISSN 0014-2999 (Print) 0014-2999 (Linking). URL <https://www.ncbi.nlm.nih.gov/pubmed/2163851>.
- Lee, H. W., Khan, S. Q., Faridi, M. H., Wei, C., Tardi, N. J., Altintas, M. M., Elshabrawy, H. A., Mangos, S., Quick, K. L., Sever, S., Reiser, J., and Gupta, V. A podocyte-based automated screening assay identifies protective small molecules. *J Am Soc Nephrol*, 26(11):2741–52, 2015. ISSN 1533-3450 (Electronic) 1046-6673 (Linking). doi: 10.1681/ASN.2014090859. URL <https://www.ncbi.nlm.nih.gov/pubmed/25858967>.
- Lee, K., Macaulay, V. M., Nicholls, J. E., Detre, S., Ashworth, A., and Dowsett, M. An in vivo model of intratumoural aromatase using aromatase-transfected mcf7 human breast cancer cells. *Int J Cancer*, 62(3):297–302, 1995. ISSN 0020-7136 (Print) 0020-7136 (Linking). URL <https://www.ncbi.nlm.nih.gov/pubmed/7628871>.
- Leet, J. K., Lindberg, C. D., Bassett, L. A., Isales, G. M., Yozzo, K. L., Raftery, T. D., and Volz, D. C. High-content screening in zebrafish embryos identifies butafenacil as a potent inducer of anemia. *PLoS One*, 9(8):e104190, 2014. ISSN 1932-6203 (Electronic) 1932-6203 (Linking). doi: 10.1371/journal.pone.0104190. URL <https://www.ncbi.nlm.nih.gov/pubmed/25090246>.
- Lehrke, I., Schaier, M., Schade, K., Morath, C., Waldherr, R., Ritz, E., and Wagner, J. Retinoid receptor-specific agonists alleviate experimental glomerulonephritis. *Am J Physiol Renal Physiol*, 282(4):F741–51, 2002. ISSN 1931-857X (Print) 1522-1466 (Linking). doi: 10.1152/ajprenal.00026.2001. URL <https://www.ncbi.nlm.nih.gov/pubmed/11880336>.
- Leonhard, W. N., van der Wal, A., Novalic, Z., Kunnen, S. J., Gansevoort, R. T., Breuning, M. H., de Heer, E., and Peters, D. J. Curcumin inhibits cystogenesis by simultaneous interference of multiple signaling pathways: in vivo evidence from a pkd1-deletion model. *Am J Physiol Renal Physiol*, 300(5):F1193–202, 2011. ISSN 1522-1466 (Electronic) 1522-1466 (Linking). doi: 10.1152/ajprenal.00419.2010. URL <https://www.ncbi.nlm.nih.gov/pubmed/21345977>.
- Lepesheva, G. I. and Waterman, M. R. Sterol 14alpha-demethylase cytochrome p450 (cyp51), a p450 in all biological kingdoms. *Biochim Biophys Acta*, 1770(3):467–77, 2007. ISSN 0006-3002 (Print) 0006-3002 (Linking). doi: 10.1016/j.bbagen.2006.07.018. URL <https://www.ncbi.nlm.nih.gov/pubmed/16963187>.
- Lin, F., Hiesberger, T., Cordes, K., Sinclair, A. M., Goldstein, L. S., Somlo, S., and Igarashi, P. Kidney-specific inactivation of the kif3a subunit of kinesin-ii inhibits renal ciliogenesis and produces polycystic kidney disease. *Proc Natl Acad Sci U S A*, 100(9):5286–91, 2003. ISSN 0027-8424 (Print) 0027-8424 (Linking). doi: 10.1073/pnas.0836980100. URL <https://www.ncbi.nlm.nih.gov/pubmed/12672950>.
- Lin, L. Y., Horng, J. L., Kunkel, J. G., and Hwang, P. P. Proton pump-rich cell secretes acid in skin of zebrafish larvae. *Am J Physiol Cell Physiol*, 290(2):C371–8, 2006. ISSN 0363-6143 (Print) 0363-6143 (Linking). doi: 10.1152/ajpcell.00281.2005. URL <https://www.ncbi.nlm.nih.gov/pubmed/16148031>.
- Lin, M. Z., Chai, W. M., Ou-Yang, C., Huang, Q., Xu, X. H., and Peng, Y. Y. Antityrosinase mechanism of omeprazole and its application on the preservation of fresh-cut fuji apple. *Int J Biol Macromol*, 117:538–545, 2018. ISSN 1879-0003 (Electronic) 0141-8130 (Linking). doi: 10.1016/j.ijbiomac.2018.05.172. URL <https://www.ncbi.nlm.nih.gov/pubmed/29803745>.
- Liu, H., Chen, S., Huang, K., Kim, J., Mo, H., Iovine, R., Gendre, J., Pascal, P., Li, Q., Sun, Y., Dong, Z., Arkin, M., Guo, S., and Huang, B. A high-content larval zebrafish brain imaging method for small molecule drug discovery. *PLoS One*, 11(10):e0164645, 2016. ISSN 1932-6203 (Electronic) 1932-6203 (Linking). doi: 10.1371/journal.pone.0164645. URL <https://www.ncbi.nlm.nih.gov/pubmed/27732643>.

REFERENCES

- Liu, X., Yang, J. M., Zhang, S. S., Liu, X. Y., and Liu, D. X. Induction of cell cycle arrest at g1 and s phases and camp-dependent differentiation in c6 glioma by low concentration of cycloheximide. *BMC Cancer*, 10:684, 2010. ISSN 1471-2407 (Electronic) 1471-2407 (Linking). doi: 10.1186/1471-2407-10-684. URL <https://www.ncbi.nlm.nih.gov/pubmed/21159181>.
- Lunt, S. C., Haynes, T., and Perkins, B. D. Zebrafish ift57, ift88, and ift172 intraflagellar transport mutants disrupt cilia but do not affect hedgehog signaling. *Dev Dyn*, 238(7):1744–59, 2009. ISSN 1058-8388 (Print) 1058-8388 (Linking). doi: 10.1002/dvdy.21999. URL <https://www.ncbi.nlm.nih.gov/pubmed/19517571>.
- Lupetti, A., Danesi, R., Campa, M., Del Tacca, M., and Kelly, S. Molecular basis of resistance to azole antifungals. *Trends Mol Med*, 8(2): 76–81, 2002. ISSN 1471-4914 (Print) 1471-4914 (Linking). URL <https://www.ncbi.nlm.nih.gov/pubmed/11815273>.
- MacRae, C. A. and Peterson, R. T. Zebrafish-based small molecule discovery. *Chem Biol*, 10(10):901–8, 2003. ISSN 1074-5521 (Print) 1074-5521 (Linking). URL <https://www.ncbi.nlm.nih.gov/pubmed/14583256>.
- Mangos, S., Lam, P. Y., Zhao, A., Liu, Y., Mudumana, S., Vasilyev, A., Liu, A., and Drummond, I. A. The adpdk genes pkd1a/b and pkd2 regulate extracellular matrix formation. *Dis Model Mech*, 3(5-6):354–65, 2010. ISSN 1754-8411 (Electronic) 1754-8403 (Linking). doi: 10.1242/dmm.003194. URL <https://www.ncbi.nlm.nih.gov/pubmed/20335443>.
- Mathew, L. K., Sengupta, S., Kawakami, A., Andreasen, E. A., Lohr, C. V., Loynes, C. A., Renshaw, S. A., Peterson, R. T., and Tanguay, R. L. Unraveling tissue regeneration pathways using chemical genetics. *J Biol Chem*, 282(48):35202–10, 2007. ISSN 0021-9258 (Print) 0021-9258 (Linking). doi: 10.1074/jbc.M706640200. URL <https://www.ncbi.nlm.nih.gov/pubmed/17848559>.
- Matsui, M. S., Petris, M. J., Niki, Y., Karaman-Jurukovska, N., Muizzuddin, N., Ichihashi, M., and Yarosh, D. B. Omeprazole, a gastric proton pump inhibitor, inhibits melanogenesis by blocking atp7a trafficking. *J Invest Dermatol*, 135(3):834–841, 2015. ISSN 1523-1747 (Electronic) 0022-202X (Linking). doi: 10.1038/jid.2014.461. URL <https://www.ncbi.nlm.nih.gov/pubmed/25337692>.
- McCampbell, K. K. and Wingert, R. A. Renal stem cells: fact or science fiction? *Biochem J*, 444(2):153–68, 2012. ISSN 1470-8728 (Electronic) 0264-6021 (Linking). doi: 10.1042/BJ20120176. URL <https://www.ncbi.nlm.nih.gov/pubmed/22574774>.
- McClendon, A. K. and Osheroff, N. Dna topoisomerase ii, genotoxicity, and cancer. *Mutat Res*, 623(1-2):83–97, 2007. ISSN 0027-5107 (Print) 0027-5107 (Linking). doi: 10.1016/j.mrfmmm.2007.06.009. URL <https://www.ncbi.nlm.nih.gov/pubmed/17681352>.
- McGown, A., Shaw, D. P., and Ramesh, T. Znstress: a high-throughput drug screening protocol for identification of compounds modulating neuronal stress in the transgenic mutant sod1g93r zebrafish model of amyotrophic lateral sclerosis. *Mol Neurodegener*, 11(1):56, 2016. ISSN 1750-1326 (Electronic) 1750-1326 (Linking). doi: 10.1186/s13024-016-0122-3. URL <https://www.ncbi.nlm.nih.gov/pubmed/27460825>.
- McKay, L. and Cidlowski, J. Physiologic and pharmacologic effects of corticosteroids, 2003. URL <https://www.ncbi.nlm.nih.gov/books/NBK13780/>. [accessed: 15-06-2018].
- McKee, R. A. and Wingert, R. A. Zebrafish renal pathology: Emerging models of acute kidney injury. *Curr Pathobiol Rep*, 3(2):171–181, 2015. ISSN 2167-485X (Print) 2167-485X (Linking). doi: 10.1007/s40139-015-0082-2. URL <https://www.ncbi.nlm.nih.gov/pubmed/25973344>.
- Mendelsohn, C., Batourina, E., Fung, S., Gilbert, T., and Dodd, J. Stromal cells mediate retinoid-dependent functions essential for renal development. *Development*, 126(6):1139–48, 1999. ISSN 0950-1991 (Print) 0950-1991 (Linking). URL <https://www.ncbi.nlm.nih.gov/pubmed/10021334>.
- Mikut, R., Dickmeis, T., Driever, W., Geurts, P., Hamprecht, F. A., Kausler, B. X., Ledesma-Carbayo, M. J., Maree, R., Mikula, K., Pantazis, P., Ronneberger, O., Santos, A., Stotzka, R., Strahle, U., and Peyrieras, N. Automated processing of zebrafish imaging data: a survey. *Zebrafish*, 10(3):401–21, 2013. ISSN 1557-8542 (Electronic) 1545-8547 (Linking). doi: 10.1089/zeb.2013.0886. URL <https://www.ncbi.nlm.nih.gov/pubmed/23758125>.

- Miyake, N., Tsukaguchi, H., Koshimizu, E., Shono, A., Matsunaga, S., Shiina, M., Mimura, Y., Imamura, S., Hirose, T., Okudela, K., Nozu, K., Akioka, Y., Hattori, M., Yoshikawa, N., Kitamura, A., Cheong, H. I., Kagami, S., Yamashita, M., Fujita, A., Miyatake, S., Tsurusaki, Y., Nakashima, M., Saitsu, H., Ohashi, K., Imamoto, N., Ryo, A., Ogata, K., Iijima, K., and Matsumoto, N. Biallelic mutations in nuclear pore complex subunit nup107 cause early-childhood-onset steroid-resistant nephrotic syndrome. *Am J Hum Genet*, 97(4):555–66, 2015. ISSN 1537-6605 (Electronic) 0002-9297 (Linking). doi: 10.1016/j.ajhg.2015.08.013. URL <https://www.ncbi.nlm.nih.gov/pubmed/26411495>.
- Molina, G., Vogt, A., Bakan, A., Dai, W., Queiroz de Oliveira, P., Znosko, W., Smithgall, T. E., Bahar, I., Lazo, J. S., Day, B. W., and Tsang, M. Zebrafish chemical screening reveals an inhibitor of dusp6 that expands cardiac cell lineages. *Nat Chem Biol*, 5(9):680–7, 2009. ISSN 1552-4469 (Electronic) 1552-4450 (Linking). doi: 10.1038/nchembio.190. URL <https://www.ncbi.nlm.nih.gov/pubmed/19578332>.
- Montecucco, A. and Biamonti, G. Cellular response to etoposide treatment. *Cancer Lett*, 252(1):9–18, 2007. ISSN 0304-3835 (Print) 0304-3835 (Linking). doi: 10.1016/j.canlet.2006.11.005. URL <https://www.ncbi.nlm.nih.gov/pubmed/17166655>.
- Morrison, A. M., Goldstone, J. V., Lamb, D. C., Kubota, A., Lemaire, B., and Stegeman, J. J. Identification, modeling and ligand affinity of early deuterostome cyp51s, and functional characterization of recombinant zebrafish sterol 14alpha-demethylase. *Biochim Biophys Acta*, 1840(6):1825–36, 2014. ISSN 0006-3002 (Print) 0006-3002 (Linking). doi: 10.1016/j.bbagen.2013.12.009. URL <https://www.ncbi.nlm.nih.gov/pubmed/24361620>.
- Murphey, R. D., Stern, H. M., Straub, C. T., and Zon, L. I. A chemical genetic screen for cell cycle inhibitors in zebrafish embryos. *Chem Biol Drug Des*, 68(4):213–9, 2006. ISSN 1747-0277 (Print) 1747-0277 (Linking). doi: 10.1111/j.1747-0285.2006.00439.x. URL <https://www.ncbi.nlm.nih.gov/pubmed/17105485>.
- Murray, R. Role of anti-aromatase agents in postmenopausal advanced breast cancer. *Cancer Chemother Pharmacol*, 48(4):259–65, 2001. ISSN 0344-5704 (Print) 0344-5704 (Linking). URL <https://www.ncbi.nlm.nih.gov/pubmed/11710624>.
- Muto, S., Aiba, A., Saito, Y., Nakao, K., Nakamura, K., Tomita, K., Kitamura, T., Kurabayashi, M., Nagai, R., Higashihara, E., Harris, P. C., Katsuki, M., and Horie, S. Pioglitazone improves the phenotype and molecular defects of a targeted pkd1 mutant. *Hum Mol Genet*, 11(15):1731–42, 2002. ISSN 0964-6906 (Print) 0964-6906 (Linking). URL <https://www.ncbi.nlm.nih.gov/pubmed/12095915>.
- National Institute of Standards and Technology. Nist/sematech e-handbook of statistical methods, 06/01/2003 . URL <https://www.itl.nist.gov/div898/handbook/>. [accessed: 09-05-2018].
- Niaudet, P. and Gubler, M. C. Wt1 and glomerular diseases. *Pediatr Nephrol*, 21(11):1653–60, 2006. ISSN 0931-041X (Print) 0931-041X (Linking). doi: 10.1007/s00467-006-0208-1. URL <https://www.ncbi.nlm.nih.gov/pubmed/16927106>.
- Nichane, M., Van Campenhout, C., Pendeville, H., Voz, M. L., and Bellefroid, E. J. The na+/po4 cotransporter slc20a1 gene labels distinct restricted subdomains of the developing pronephros in xenopus and zebrafish embryos. *Gene Expr Patterns*, 6(7):667–72, 2006. ISSN 1567-133X (Print) 1567-133X (Linking). doi: 10.1016/j.modgep.2006.01.005. URL <https://www.ncbi.nlm.nih.gov/pubmed/16531124>.
- North, T. E., Goessling, W., Walkley, C. R., Lengerke, C., Kopani, K. R., Lord, A. M., Weber, G. J., Bowman, T. V., Jang, I. H., Grosser, T., Fitzgerald, G. A., Daley, G. Q., Orkin, S. H., and Zon, L. I. Prostaglandin e2 regulates vertebrate haematopoietic stem cell homeostasis. *Nature*, 447(7147):1007–11, 2007. ISSN 1476-4687 (Electronic) 0028-0836 (Linking). doi: 10.1038/nature05883. URL <https://www.ncbi.nlm.nih.gov/pubmed/17581586>.
- Okuda, A. and Kimura, G. Non-specific elongation of cell cycle phases by cycloheximide in rat 3y1 cells, and specific reduction of g1 phase elongation by simian virus 40 large t antigen. *J Cell Sci*, 91 (Pt 2):295–302, 1988. ISSN 0021-9533 (Print) 0021-9533 (Linking). URL <https://www.ncbi.nlm.nih.gov/pubmed/2855804>.
- Omer, I., Sajith Kecheril, S., and Carolina, W. Deep fish: Deep learningbased classification of zebrafish deformation for high-throughput screening. *SLAS DISCOVERY: Advancing Life Sciences R&D*, 22(1):102–107, 2017. doi: 10.1177/1087057116667894.

REFERENCES

- OpenStax. Anatomy & physiology, 2016. URL <http://cnx.org/contents/14fb4ad7-39a1-4eee-ab6e-3ef2482e3e22@8.24>. [accessed: 10-12-2018].
- Oseto, S., Moriyama, T., Kawada, N., Nagatoya, K., Takeji, M., Ando, A., Yamamoto, T., Imai, E., and Hori, M. Therapeutic effect of all-trans retinoic acid on rats with anti-gbm antibody glomerulonephritis. *Kidney Int*, 64(4):1241–52, 2003. ISSN 0085-2538 (Print) 0085-2538 (Linking). doi: 10.1046/j.1523-1755.2003.00219.x. URL <https://www.ncbi.nlm.nih.gov/pubmed/12969142>.
- Otsuka America Pharmaceutical, I. Samsca (tolvaptan), package insert. Rockville, MD, 2009. [accessed: 12-10-2018].
- Pandey, G., Westhoff, J., Schaefer, F., and Gehrig, J. A smart imaging workflow for organ-specific screening in a cystic kidney zebrafish disease model. *Int. J. Mol. Sci.*, 20(6), 1290, 2019. doi: <https://doi.org/10.3390/ijms20061290>. URL <https://www.mdpi.com/1422-0067/20/6/1290>.
- Patton, E. E. and Zon, L. I. The art and design of genetic screens: zebrafish. *Nat Rev Genet*, 2(12):956–66, 2001. ISSN 1471-0056 (Print) 1471-0056 (Linking). doi: 10.1038/35103567. URL <https://www.ncbi.nlm.nih.gov/pubmed/11733748>.
- Paul, B. M. and Vanden Heuvel, G. B. Kidney: polycystic kidney disease. *Wiley Interdiscip Rev Dev Biol*, 3(6):465–87, 2014. ISSN 1759-7692 (Electronic) 1759-7684 (Linking). doi: 10.1002/wdev.152. URL <https://www.ncbi.nlm.nih.gov/pubmed/25186187>.
- Paul, S. M., Mytelka, D. S., Dunwiddie, C. T., Persinger, C. C., Munos, B. H., Lindborg, S. R., and Schacht, A. L. How to improve r&d productivity: the pharmaceutical industry’s grand challenge. *Nat Rev Drug Discov*, 9(3):203–14, 2010. ISSN 1474-1784 (Electronic) 1474-1776 (Linking). doi: 10.1038/nrd3078. URL <https://www.ncbi.nlm.nih.gov/pubmed/20168317>.
- Payne, A. H. and Sha, L. L. Multiple mechanisms for regulation of 3 beta-hydroxysteroid dehydrogenase/delta 5—delta 4-isomerase, 17 alpha-hydroxylase/c17-20 lyase cytochrome p450, and cholesterol side-chain cleavage cytochrome p450 messenger ribonucleic acid levels in primary cultures of mouse leydig cells. *Endocrinology*, 129(3):1429–35, 1991. ISSN 0013-7227 (Print) 0013-7227 (Linking). doi: 10.1210/endo-129-3-1429. URL <https://www.ncbi.nlm.nih.gov/pubmed/1874181>.
- Pazour, G. J. Intraflagellar transport and cilia-dependent renal disease: the ciliary hypothesis of polycystic kidney disease. *J Am Soc Nephrol*, 15(10):2528–36, 2004. ISSN 1046-6673 (Print) 1046-6673 (Linking). doi: 10.1097/01.ASN.0000141055.57643.E0. URL <https://www.ncbi.nlm.nih.gov/pubmed/15466257>.
- Peal, D. S., Mills, R. W., Lynch, S. N., Mosley, J. M., Lim, E., Ellinor, P. T., January, C. T., Peterson, R. T., and Milan, D. J. Novel chemical suppressors of long qt syndrome identified by an in vivo functional screen. *Circulation*, 123(1):23–30, 2011. ISSN 1524-4539 (Electronic) 0009-7322 (Linking). doi: 10.1161/CIRCULATIONAHA.110.003731. URL <https://www.ncbi.nlm.nih.gov/pubmed/21098441>.
- Peitsaro, N., Sundvik, M., Anichtchik, O. V., Kaslin, J., and Panula, P. Identification of zebrafish histamine h1, h2 and h3 receptors and effects of histaminergic ligands on behavior. *Biochem Pharmacol*, 73(8):1205–14, 2007. ISSN 0006-2952 (Print) 0006-2952 (Linking). doi: 10.1016/j.bcp.2007.01.014. URL <https://www.ncbi.nlm.nih.gov/pubmed/17266939>.
- Peravali, R., Gehrig, J., Giselsbrecht, S., Lutjohann, D. S., Hadzhiev, Y., Muller, F., and Liebel, U. Automated feature detection and imaging for high-resolution screening of zebrafish embryos. *Biotechniques*, 50(5):319–24, 2011. ISSN 1940-9818 (Electronic) 0736-6205 (Linking). doi: 10.2144/000113669. URL <https://www.ncbi.nlm.nih.gov/pubmed/21548893>.
- Perner, B., Englert, C., and Bollig, F. The wilms tumor genes wt1a and wt1b control different steps during formation of the zebrafish pronephros. *Dev Biol*, 309(1):87–96, 2007. ISSN 0012-1606 (Print) 0012-1606 (Linking). doi: 10.1016/j.ydbio.2007.06.022. URL <https://www.ncbi.nlm.nih.gov/pubmed/17651719>.
- Peterson, R. T., Link, B. A., Dowling, J. E., and Schreiber, S. L. Small molecule developmental screens reveal the logic and timing of vertebrate development. *Proc Natl Acad Sci U S A*, 97(24):12965–9, 2000. ISSN 0027-8424 (Print) 0027-8424 (Linking). doi: 10.1073/pnas.97.24.12965. URL <https://www.ncbi.nlm.nih.gov/pubmed/11087852>.

- Peterson, R. T., Shaw, S. Y., Peterson, T. A., Milan, D. J., Zhong, T. P., Schreiber, S. L., MacRae, C. A., and Fishman, M. C. Chemical suppression of a genetic mutation in a zebrafish model of aortic coarctation. *Nat Biotechnol*, 22(5):595–9, 2004. ISSN 1087-0156 (Print) 1087-0156 (Linking). doi: 10.1038/nbt963. URL <https://www.ncbi.nlm.nih.gov/pubmed/15097998>.
- Praetorius, H. A. and Spring, K. R. Removal of the mdck cell primary cilium abolishes flow sensing. *J Membr Biol*, 191(1):69–76, 2003. ISSN 0022-2631 (Print) 0022-2631 (Linking). doi: 10.1007/s00232-002-1042-4. URL <https://www.ncbi.nlm.nih.gov/pubmed/12532278>.
- Pulak, R. Tools for automating the imaging of zebrafish larvae. *Methods*, 96:118–126, 2016. ISSN 1095-9130 (Electronic) 1046-2023 (Linking). doi: 10.1016/j.ymeth.2015.11.021. URL <https://www.ncbi.nlm.nih.gov/pubmed/26631716>.
- Pyati, U. J., Cooper, M. S., Davidson, A. J., Nechiporuk, A., and Kimelman, D. Sustained bmp signaling is essential for cloaca development in zebrafish. *Development*, 133(11):2275–84, 2006. ISSN 0950-1991 (Print) 0950-1991 (Linking). doi: 10.1242/dev.02388. URL <https://www.ncbi.nlm.nih.gov/pubmed/16672335>.
- Reed, M. J. and Purohit, A. Aromatase regulation and breast cancer. *Clin Endocrinol (Oxf)*, 54(5):563–71, 2001. ISSN 0300-0664 (Print) 0300-0664 (Linking). URL <https://www.ncbi.nlm.nih.gov/pubmed/11380485>.
- Reiser, J., Lee, H. W., Gupta, V., and Altintas, M. M. A high-content screening technology for quantitatively studying podocyte dynamics. *Adv Chronic Kidney Dis*, 24(3):183–188, 2017. ISSN 1548-5609 (Electronic) 1548-5595 (Linking). doi: 10.1053/j.ackd.2017.04.001. URL <https://www.ncbi.nlm.nih.gov/pubmed/28501082>.
- Rennekamp, A. J. and Peterson, R. T. 15 years of zebrafish chemical screening. *Curr Opin Chem Biol*, 24:58–70, 2015. ISSN 1879-0402 (Electronic) 1367-5931 (Linking). doi: 10.1016/j.cbpa.2014.10.025. URL <https://www.ncbi.nlm.nih.gov/pubmed/25461724>.
- Rider, S. A., Tucker, C. S., del Pozo, J., Rose, K. N., MacRae, C. A., Bailey, M. A., and Mullins, J. J. Techniques for the in vivo assessment of cardio-renal function in zebrafish (*Danio rerio*) larvae. *J Physiol*, 590(8):1803–9, 2012. ISSN 1469-7793 (Electronic) 0022-3751 (Linking). doi: 10.1113/jphysiol.2011.224352. URL <https://www.ncbi.nlm.nih.gov/pubmed/22331420>.
- Rihel, J., Prober, D. A., Arvanites, A., Lam, K., Zimmerman, S., Jang, S., Haggarty, S. J., Kokel, D., Rubin, L. L., Peterson, R. T., and Schier, A. F. Zebrafish behavioral profiling links drugs to biological targets and rest/wake regulation. *Science*, 327(5963):348–51, 2010. ISSN 1095-9203 (Electronic) 0036-8075 (Linking). doi: 10.1126/science.1183090. URL <https://www.ncbi.nlm.nih.gov/pubmed/20075256>.
- Sanker, S., Cirio, M. C., Vollmer, L. L., Goldberg, N. D., McDermott, L. A., Hukriede, N. A., and Vogt, A. Development of high-content assays for kidney progenitor cell expansion in transgenic zebrafish. *J Biomol Screen*, 18(10):1193–202, 2013. ISSN 1552-454X (Electronic) 1087-0571 (Linking). doi: 10.1177/1087057113495296. URL <https://www.ncbi.nlm.nih.gov/pubmed/23832868>.
- Sans-Atxer, L. and Joly, D. Tolvaptan in the treatment of autosomal dominant polycystic kidney disease: patient selection and special considerations. *Int J Nephrol Renovasc Dis*, 11:41–51, 2018. ISSN 1178-7058 (Print) 1178-7058 (Linking). doi: 10.2147/IJNRD.S125942. URL <https://www.ncbi.nlm.nih.gov/pubmed/29430193>.
- Santen, R. J. and Harvey, H. A. Use of aromatase inhibitors in breast carcinoma. *Endocr Relat Cancer*, 6(1):75–92, 1999. ISSN 1351-0088 (Print) 1351-0088 (Linking). URL <https://www.ncbi.nlm.nih.gov/pubmed/10732791>.
- Sapetto-Rebow, B., McLoughlin, S. C., O’Shea, L. C., O’Leary, O., Willer, J. R., Alvarez, Y., Collery, R., O’Sullivan, J., Van Eeden, F., Hensey, C., and Kennedy, B. N. Maternal topoisomerase ii alpha, not topoisomerase ii beta, enables embryonic development of zebrafish top2a^{-/-} mutants. *BMC Dev Biol*, 11:71, 2011. ISSN 1471-213X (Electronic) 1471-213X (Linking). doi: 10.1186/1471-213X-11-71. URL <https://www.ncbi.nlm.nih.gov/pubmed/22111588>.
- Saydmohammed, M., Vollmer, L. L., Onuoha, E. O., Vogt, A., and Tsang, M. A high-content screening assay in transgenic zebrafish identifies two novel activators of fgf signaling. *Birth Defects Res C Embryo Today*, 93(3):281–7, 2011. ISSN 1542-9768 (Electronic) 1542-975X (Linking). doi: 10.1002/bdrc.20216. URL <https://www.ncbi.nlm.nih.gov/pubmed/21932436>.

REFERENCES

- Schaaf, M. J., Champagne, D., van Laanen, I. H., van Wijk, D. C., Meijer, A. H., Meijer, O. C., Spink, H. P., and Richardson, M. K. Discovery of a functional glucocorticoid receptor beta-isoform in zebrafish. *Endocrinology*, 149(4):1591–9, 2008. ISSN 0013-7227 (Print) 0013-7227 (Linking). doi: 10.1210/en.2007-1364. URL <https://www.ncbi.nlm.nih.gov/pubmed/18096659>.
- Schena, F. P., Gesualdo, L., and Caracciolo, G. A multicentre study of flumequine in the treatment of urinary tract infections. *J Antimicrob Chemother*, 21(1):101–6, 1988. ISSN 0305-7453 (Print) 0305-7453 (Linking). URL <https://www.ncbi.nlm.nih.gov/pubmed/3356617>.
- Schieweck, K., Bhatnagar, A. S., Batzl, C., and Lang, M. Anti-tumor and endocrine effects of non-steroidal aromatase inhibitors on estrogen-dependent rat mammary tumors. *J Steroid Biochem Mol Biol*, 44(4-6):633–6, 1993. ISSN 0960-0760 (Print) 0960-0760 (Linking). URL <https://www.ncbi.nlm.nih.gov/pubmed/8476774>.
- Schmidts, M., Hou, Y., Cortes, C. R., Mans, D. A., Huber, C., Boldt, K., Patel, M., van Reeuwijk, J., Plaza, J. M., van Beersum, S. E., Yap, Z. M., Letteboer, S. J., Taylor, S. P., Herridge, W., Johnson, C. A., Scambler, P. J., Ueffing, M., Kayserili, H., Krakow, D., King, S. M., Uk10K, Beales, P. L., Al-Gazali, L., Wicking, C., Cormier-Daire, V., Roepman, R., Mitchison, H. M., and Witman, G. B. Tctex1d2 mutations underlie jeune asphyxiating thoracic dystrophy with impaired retrograde intraflagellar transport. *Nat Commun*, 6:7074, 2015. ISSN 2041-1723 (Electronic) 2041-1723 (Linking). doi: 10.1038/ncomms8074. URL <https://www.ncbi.nlm.nih.gov/pubmed/26044572>.
- Schmitt, F., Martinez, F., Ikeni, A., Savoie, C., Natov, S., Laborde, K., Lacour, B., Grunfeld, J. P., and Hannedouche, T. Acute renal effects of neutral endopeptidase inhibition in humans. *Am J Physiol*, 267(1 Pt 2):F20–7, 1994. ISSN 0002-9513 (Print) 0002-9513 (Linking). doi: 10.1152/ajprenal.1994.267.1.F20. URL <https://www.ncbi.nlm.nih.gov/pubmed/7519405>.
- Serra, A. L., Poster, D., Kistler, A. D., Krauer, F., Raina, S., Young, J., Rentsch, K. M., Spanaus, K. S., Senn, O., Kristanto, P., Scheffel, H., Weishaupt, D., and Wuthrich, R. P. Sirolimus and kidney growth in autosomal dominant polycystic kidney disease. *N Engl J Med*, 363(9):820–9, 2010. ISSN 1533-4406 (Electronic) 0028-4793 (Linking). doi: 10.1056/NEJMoa0907419. URL <https://www.ncbi.nlm.nih.gov/pubmed/20581391>.
- Shah, A. N., Davey, C. F., Whitebirch, A. C., Miller, A. C., and Moens, C. B. Rapid reverse genetic screening using crispr in zebrafish. *Nat Methods*, 12(6):535–40, 2015. ISSN 1548-7105 (Electronic) 1548-7091 (Linking). doi: 10.1038/nmeth.3360. URL <https://www.ncbi.nlm.nih.gov/pubmed/25867848>.
- Shapiro, R. H. and L. *Computer and Robot Vision*, volume 1. Addison-Wesley Publishing Company, 1992.
- Sherstha, R., McKinley, C., Russ, P., Scherzinger, A., Bronner, T., Showalter, R., and Everson, G. T. Postmenopausal estrogen therapy selectively stimulates hepatic enlargement in women with autosomal dominant polycystic kidney disease. *Hepatology*, 26(5):1282–6, 1997. ISSN 0270-9139 (Print) 0270-9139 (Linking). doi: 10.1002/hep.510260528. URL <https://www.ncbi.nlm.nih.gov/pubmed/9362373>.
- Shi, J., Bezabhe, R., and Szkudlinska, A. Further evaluation of a flow cytometric in vitro micronucleus assay in cho-k1 cells: a reliable platform that detects micronuclei and discriminates apoptotic bodies. *Mutagenesis*, 25(1):33–40, 2010. ISSN 1464-3804 (Electronic) 0267-8357 (Linking). doi: 10.1093/mutage/geb040. URL <https://www.ncbi.nlm.nih.gov/pubmed/19843589>.
- Shi, Y., Su, Y., Lipschutz, J. H., and Lobo, G. P. Zebrafish as models to study ciliopathies of the eye and kidney. *Clin Nephrol Res*, 1(1):6–9, 2017. URL <https://www.ncbi.nlm.nih.gov/pubmed/29553143>.
- Shimada, Y., Hirano, M., Nishimura, Y., and Tanaka, T. A high-throughput fluorescence-based assay system for appetite-regulating gene and drug screening. *PLoS One*, 7(12):e52549, 2012. ISSN 1932-6203 (Electronic) 1932-6203 (Linking). doi: 10.1371/journal.pone.0052549. URL <https://www.ncbi.nlm.nih.gov/pubmed/23300705>.
- Shin, J. M., Lee, J. Y., Lee, D. Y., Yoon, T. Y., Lee, J. C., Lim, E. H., Sohn, K. C., Lee, Y. H., Im, M., Seo, Y. J., Kim, C. D., Lee, J. H., and Lee, Y. Proton pump inhibitors as a possible cause of vitiligo: an in vivo and in vitro study. *J Eur Acad Dermatol Venereol*, 28(11):1475–9, 2014. ISSN 1468-3083 (Electronic) 0926-9959 (Linking). doi: 10.1111/jdv.12317. URL <https://www.ncbi.nlm.nih.gov/pubmed/24236446>.

- Simon, H. U. and Friis, R. Atg5: a distinct role in the nucleus. *Autophagy*, 10(1):176–7, 2014. ISSN 1554-8635 (Electronic) 1554-8627 (Linking). doi: 10.4161/auto.26916. URL <https://www.ncbi.nlm.nih.gov/pubmed/24248263>.
- Singla, V. and Reiter, J. F. The primary cilium as the cell's antenna: signaling at a sensory organelle. *Science*, 313(5787):629–33, 2006. ISSN 1095-9203 (Electronic) 0036-8075 (Linking). doi: 10.1126/science.1124534. URL <https://www.ncbi.nlm.nih.gov/pubmed/16888132>.
- Sipes, N. S., Padilla, S., and Knudsen, T. B. Zebrafish: as an integrative model for twenty-first century toxicity testing. *Birth Defects Res C Embryo Today*, 93(3):256–67, 2011. ISSN 1542-9768 (Electronic) 1542-975X (Linking). doi: 10.1002/bdrc.20214. URL <https://www.ncbi.nlm.nih.gov/pubmed/21932434>.
- Solnica-Krezel, L., Schier, A. F., and Driever, W. Efficient recovery of enu-induced mutations from the zebrafish germline. *Genetics*, 136(4): 1401–20, 1994. ISSN 0016-6731 (Print) 0016-6731 (Linking). URL <https://www.ncbi.nlm.nih.gov/pubmed/8013916>.
- Spagnuolo, P. A., Hu, J., Hurren, R., Wang, X., Gronda, M., Sukhai, M. A., Di Meo, A., Boss, J., Ashali, I., Beheshti Zavareh, R., Fine, N., Simpson, C. D., Sharmeen, S., Rottapel, R., and Schimmer, A. D. The antihelminthic flubendazole inhibits microtubule function through a mechanism distinct from vinca alkaloids and displays preclinical activity in leukemia and myeloma. *Blood*, 115(23):4824–33, 2010. ISSN 1528-0020 (Electronic) 0006-4971 (Linking). doi: 10.1182/blood-2009-09-243055. URL <https://www.ncbi.nlm.nih.gov/pubmed/20348394>.
- Spaink, H. P., Cui, C., Wiweger, M. I., Jansen, H. J., Veneman, W. J., Marin-Juez, R., de Sonnevile, J., Ordas, A., Torraca, V., van der Ent, W., Leenders, W. P., Meijer, A. H., Snaar-Jagalska, B. E., and Dirks, R. P. Robotic injection of zebrafish embryos for high-throughput screening in disease models. *Methods*, 62(3):246–54, 2013. ISSN 1095-9130 (Electronic) 1046-2023 (Linking). doi: 10.1016/j.ymeth.2013.06.002. URL <https://www.ncbi.nlm.nih.gov/pubmed/23769806>.
- Stainier, D. Y., Fouquet, B., Chen, J. N., Warren, K. S., Weinstein, B. M., Meiler, S. E., Mohideen, M. A., Neuhauss, S. C., Solnica-Krezel, L., Schier, A. F., Zwartkruis, F., Stemple, D. L., Malicki, J., Driever, W., and Fishman, M. C. Mutations affecting the formation and function of the cardiovascular system in the zebrafish embryo. *Development*, 123:285–92, 1996. ISSN 0950-1991 (Print) 0950-1991 (Linking). URL <https://www.ncbi.nlm.nih.gov/pubmed/9007248>.
- Stainier, D. Y. R., Raz, E., Lawson, N. D., Ekker, S. C., Burdine, R. D., Eisen, J. S., Ingham, P. W., Schulte-Merker, S., Yelon, D., Weinstein, B. M., Mullins, M. C., Wilson, S. W., Ramakrishnan, L., Amacher, S. L., Neuhauss, S. C. F., Meng, A., Mochizuki, N., Panula, P., and Moens, C. B. Guidelines for morpholino use in zebrafish. *PLoS Genet*, 13(10):e1007000, 2017. ISSN 1553-7404 (Electronic) 1553-7390 (Linking). doi: 10.1371/journal.pgen.1007000. URL <https://www.ncbi.nlm.nih.gov/pubmed/29049395>.
- Stern, H. M., Murphey, R. D., Shepard, J. L., Amatruda, J. F., Straub, C. T., Pfaff, K. L., Weber, G., Tallarico, J. A., King, R. W., and Zon, L. I. Small molecules that delay s phase suppress a zebrafish bmyb mutant. *Nat Chem Biol*, 1(7):366–70, 2005. ISSN 1552-4450 (Print) 1552-4450 (Linking). URL <https://www.ncbi.nlm.nih.gov/pubmed/16372403>.
- Streisinger, G., Walker, C., Dower, N., Knauber, D., and Singer, F. Production of clones of homozygous diploid zebra fish (*brachydanio rerio*). *Nature*, 291(5813):293–6, 1981. ISSN 0028-0836 (Print) 0028-0836 (Linking). URL <https://www.ncbi.nlm.nih.gov/pubmed/7248006>.
- Stringer, K. D., Komers, R., Osman, S. A., Oyama, T. T., Lindsley, J. N., and Anderson, S. Gender hormones and the progression of experimental polycystic kidney disease. *Kidney Int*, 68(4):1729–39, 2005. ISSN 0085-2538 (Print) 0085-2538 (Linking). doi: 10.1111/j.1523-1755.2005.00589.x. URL <https://www.ncbi.nlm.nih.gov/pubmed/16164649>.
- Su, X., Driscoll, K., Yao, G., Raed, A., Wu, M., Beales, P. L., and Zhou, J. Bardet-biedl syndrome proteins 1 and 3 regulate the ciliary trafficking of polycystic kidney disease 1 protein. *Hum Mol Genet*, 23(20):5441–51, 2014. ISSN 1460-2083 (Electronic) 0964-6906 (Linking). doi: 10.1093/hmg/ddu267. URL <https://www.ncbi.nlm.nih.gov/pubmed/24939912>.
- Sukumaran, S. and Perkins, B. D. Early defects in photoreceptor outer segment morphogenesis in zebrafish ift57, ift88 and ift172 intraflagellar transport mutants. *Vision Res*, 49(4):479–89, 2009. ISSN 1878-5646 (Electronic) 0042-6989 (Linking). doi: 10.1016/j.visres.2008.12.009. URL <https://www.ncbi.nlm.nih.gov/pubmed/19136023>.

REFERENCES

- Sun, Z., Amsterdam, A., Pazour, G. J., Cole, D. G., Miller, M. S., and Hopkins, N. A genetic screen in zebrafish identifies cilia genes as a principal cause of cystic kidney. *Development*, 131(16):4085–93, 2004. ISSN 0950-1991 (Print) 0950-1991 (Linking). doi: 10.1242/dev.01240. URL <https://www.ncbi.nlm.nih.gov/pubmed/15269167>.
- Swinney, D. C. and Anthony, J. How were new medicines discovered? *Nat Rev Drug Discov*, 10(7):507–19, 2011. ISSN 1474-1784 (Electronic) 1474-1776 (Linking). doi: 10.1038/nrd3480. URL <https://www.ncbi.nlm.nih.gov/pubmed/21701501>.
- Taschner, M. and Lorentzen, E. The intraflagellar transport machinery. *Cold Spring Harb Perspect Biol*, 8(10), 2016. ISSN 1943-0264 (Electronic) 1943-0264 (Linking). doi: 10.1101/cshperspect.a028092. URL <https://www.ncbi.nlm.nih.gov/pubmed/27352625>.
- Tobin, J. L. and Beales, P. L. Restoration of renal function in zebrafish models of ciliopathies. *Pediatr Nephrol*, 23(11):2095–9, 2008. ISSN 0931-041X (Print) 0931-041X (Linking). doi: 10.1007/s00467-008-0898-7. URL <https://www.ncbi.nlm.nih.gov/pubmed/18604564>.
- Torres, V. E., Harris, P. C., and Pirson, Y. Autosomal dominant polycystic kidney disease. *Lancet*, 369(9569):1287–1301, 2007. ISSN 1474-547X (Electronic) 0140-6736 (Linking). doi: 10.1016/S0140-6736(07)60601-1. URL <https://www.ncbi.nlm.nih.gov/pubmed/17434405>.
- Torres, V. E., Chapman, A. B., Devuyt, O., Gansevoort, R. T., Perrone, R. D., Koch, G., Ouyang, J., McQuade, R. D., Blais, J. D., Czerwiec, F. S., Sergeeva, O., and Investigators, R. T. Tolvaptan in later-stage autosomal dominant polycystic kidney disease. *N Engl J Med*, 377(20):1930–1942, 2017. ISSN 1533-4406 (Electronic) 0028-4793 (Linking). doi: 10.1056/NEJMoa1710030. URL <https://www.ncbi.nlm.nih.gov/pubmed/29105594>.
- Trosken, E. R., Fischer, K., Volkel, W., and Lutz, W. K. Inhibition of human cyp19 by azoles used as antifungal agents and aromatase inhibitors, using a new lc-ms/ms method for the analysis of estradiol product formation. *Toxicology*, 219(1-3):33–40, 2006. ISSN 0300-483X (Print) 0300-483X (Linking). doi: 10.1016/j.tox.2005.10.020. URL <https://www.ncbi.nlm.nih.gov/pubmed/16330141>.
- Truong, L., Gonnerman, G., Simonich, M. T., and Tanguay, R. L. Assessment of the developmental and neurotoxicity of the mosquito control larvicide, pyriproxyfen, using embryonic zebrafish. *Environ Pollut*, 218:1089–1093, 2016. ISSN 1873-6424 (Electronic) 0269-7491 (Linking). doi: 10.1016/j.envpol.2016.08.061. URL <https://www.ncbi.nlm.nih.gov/pubmed/27593350>.
- Tseng, Q. Find focussed slice plugin. URL <https://sites.google.com/site/qingzongtseng/find-focus#contact>. [accessed: 16-09-2016].
- Tweats, D. J., Johnson, G. E., Scandale, I., Whitwell, J., and Evans, D. B. Genotoxicity of flubendazole and its metabolites in vitro and the impact of a new formulation on in vivo aneugenicity. *Mutagenesis*, 31(3):309–21, 2016. ISSN 1464-3804 (Electronic) 0267-8357 (Linking). doi: 10.1093/mutage/gev070. URL <https://www.ncbi.nlm.nih.gov/pubmed/26443851>.
- US Food and Drug Administration. New molecular entity (nme) drug and new biologic approvals. URL <https://www.fda.gov/drugs/developmentapprovalprocess/howdrugsaredevelopedandapproved/drugandbiologicapprovalreports/ndaandblaapprovalreports/ucm373420.htm>. [accessed: 9-12-2018].
- US Food and Drug Administration. Approval package for tolvaptan, 2018. URL https://www.accessdata.fda.gov/drugsatfda_docs/nda/2018/204441Orig1s000Approv.pdf. [accessed: 9-12-2018].
- van den Boorn, J. G., Konijnenberg, D., Tjin, E. P., Picavet, D. I., Meeuwenoord, N. J., Filippov, D. V., van der Veen, J. P., Bos, J. D., Melief, C. J., and Luiten, R. M. Effective melanoma immunotherapy in mice by the skin-depigmenting agent monobenzone and the adjuvants imiquimod and cpg. *PLoS One*, 5(5):e10626, 2010. ISSN 1932-6203 (Electronic) 1932-6203 (Linking). doi: 10.1371/journal.pone.0010626. URL <https://www.ncbi.nlm.nih.gov/pubmed/20498710>.
- van den Boorn, J. G., Picavet, D. I., van Swieten, P. F., van Veen, H. A., Konijnenberg, D., van Veelen, P. A., van Capel, T., Jong, E. C., Reits, E. A., Drijfhout, J. W., Bos, J. D., Melief, C. J., and Luiten, R. M. Skin-depigmenting agent monobenzone induces potent t-cell autoimmunity toward pigmented cells by tyrosinase haptenation and melanosome autophagy. *J Invest Dermatol*, 131(6):1240–51, 2011. ISSN 1523-1747 (Electronic) 0022-202X (Linking). doi: 10.1038/jid.2011.16. URL <https://www.ncbi.nlm.nih.gov/pubmed/21326294>.

- van der Heijden, M. H., Helders, G. M., Booms, G. H., Huisman, E. A., Rombout, J. H., and Boon, J. H. Influence of flumequine and oxytetracycline on the resistance of the european eel against the parasitic swimbladder nematode *anguillicola crassus*. *Vet Immunol Immunopathol*, 52(1-2):127–34, 1996. ISSN 0165-2427 (Print) 0165-2427 (Linking). URL <https://www.ncbi.nlm.nih.gov/pubmed/8807782>.
- Vandongen, R. Suppression of renin secretion in the isolated rat kidney by cycloheximide. *Eur J Pharmacol*, 40(1):179–81, 1976. ISSN 0014-2999 (Print) 0014-2999 (Linking). URL <https://www.ncbi.nlm.nih.gov/pubmed/991924>.
- Varga, B., Csonka, A., Csonka, A., Molnar, J., Amaral, L., and Spengler, G. Possible biological and clinical applications of phenothiazines. *Anticancer Res*, 37(11):5983–5993, 2017. ISSN 1791-7530 (Electronic) 0250-7005 (Linking). doi: 10.21873/anticancer.12045. URL <https://www.ncbi.nlm.nih.gov/pubmed/29061777>.
- Varshney, G. K., Pei, W., LaFave, M. C., Idol, J., Xu, L., Gallardo, V., Carrington, B., Bishop, K., Jones, M., Li, M., Harper, U., Huang, S. C., Prakash, A., Chen, W., Sood, R., Ledin, J., and Burgess, S. M. High-throughput gene targeting and phenotyping in zebrafish using *crispr/cas9*. *Genome Res*, 25(7):1030–42, 2015. ISSN 1549-5469 (Electronic) 1088-9051 (Linking). doi: 10.1101/gr.186379.114. URL <https://www.ncbi.nlm.nih.gov/pubmed/26048245>.
- Vaughan, M. R., Pippin, J. W., Griffin, S. V., Krofft, R., Fleet, M., Haseley, L., and Shankland, S. J. ATRA induces podocyte differentiation and alters nephrin and podocin expression in vitro and in vivo. *Kidney Int*, 68(1):133–44, 2005. ISSN 0085-2538 (Print) 0085-2538 (Linking). doi: 10.1111/j.1523-1755.2005.00387.x. URL <https://www.ncbi.nlm.nih.gov/pubmed/15954902>.
- Veldman, M. B. and Lin, S. Zebrafish as a developmental model organism for pediatric research. *Pediatr Res*, 64(5):470–6, 2008. ISSN 1530-0447 (Electronic) 0031-3998 (Linking). doi: 10.1203/PDR.0b013e318186e609. URL <https://www.ncbi.nlm.nih.gov/pubmed/18679162>.
- Verbin, R. S. and Farber, E. Effect of cycloheximide on the cell cycle of the crypts of the small intestine of the rat. *J Cell Biol*, 35(3):649–58, 1967. ISSN 0021-9525 (Print) 0021-9525 (Linking). URL <https://www.ncbi.nlm.nih.gov/pubmed/6064368>.
- Vogt, A., Cholewinski, A., Shen, X., Nelson, S. G., Lazo, J. S., Tsang, M., and Hukriede, N. A. Automated image-based phenotypic analysis in zebrafish embryos. *Dev Dyn*, 238(3):656–63, 2009. ISSN 1058-8388 (Print) 1058-8388 (Linking). doi: 10.1002/dvdy.21892. URL <https://www.ncbi.nlm.nih.gov/pubmed/19235725>.
- Vogt, A., Codore, H., Day, B. W., Hukriede, N. A., and Tsang, M. Development of automated imaging and analysis for zebrafish chemical screens. *J Vis Exp*, (40), 2010. ISSN 1940-087X (Electronic) 1940-087X (Linking). doi: 10.3791/1900. URL <https://www.ncbi.nlm.nih.gov/pubmed/20613708>.
- Walker, S. L., Ariga, J., Mathias, J. R., Coothankandaswamy, V., Xie, X., Distel, M., Koster, R. W., Parsons, M. J., Bhalla, K. N., Saxena, M. T., and Mumm, J. S. Automated reporter quantification in vivo: high-throughput screening method for reporter-based assays in zebrafish. *PLoS One*, 7(1):e29916, 2012. ISSN 1932-6203 (Electronic) 1932-6203 (Linking). doi: 10.1371/journal.pone.0029916. URL <https://www.ncbi.nlm.nih.gov/pubmed/22238673>.
- Walz, G., Budde, K., Manna, M., Nurnberger, J., Wanner, C., Sommerer, C., Kunzendorf, U., Banas, B., Horl, W. H., Obermuller, N., Arns, W., Pavenstadt, H., Gaedeke, J., Buchert, M., May, C., Gschaidmeier, H., Kramer, S., and Eckardt, K. U. Everolimus in patients with autosomal dominant polycystic kidney disease. *N Engl J Med*, 363(9):830–40, 2010. ISSN 1533-4406 (Electronic) 0028-4793 (Linking). doi: 10.1056/NEJMoa1003491. URL <https://www.ncbi.nlm.nih.gov/pubmed/20581392>.
- Wang, X., Wu, Y., Ward, C. J., Harris, P. C., and Torres, V. E. Vasopressin directly regulates cyst growth in polycystic kidney disease. *J Am Soc Nephrol*, 19(1):102–8, 2008. ISSN 1533-3450 (Electronic) 1046-6673 (Linking). doi: 10.1681/ASN.2007060688. URL <https://www.ncbi.nlm.nih.gov/pubmed/18032793>.
- Wang, X. T., Sun, X. J., Li, C., Liu, Y., Zhang, L., Li, Y. D., Wu, Q. H., Li, S. Y., and Li, Y. Establishing a cell-based high-content screening assay for tcm compounds with anti-renal fibrosis effects. *Evid Based Complement Alternat Med*, 2018:7942614, 2018. ISSN 1741-427X (Print) 1741-427X (Linking). doi: 10.1155/2018/7942614. URL <https://www.ncbi.nlm.nih.gov/pubmed/30050593>.

REFERENCES

- Wang, Y., Sun, Z. H., Zhou, L., Li, Z., and Gui, J. F. Grouper tshbeta promoter-driven transgenic zebrafish marks proximal kidney tubule development. *PLoS One*, 9(6):e97806, 2014. ISSN 1932-6203 (Electronic) 1932-6203 (Linking). doi: 10.1371/journal.pone.0097806. URL <https://www.ncbi.nlm.nih.gov/pubmed/24905828>.
- Warashina, M., Min, K. H., Kuwabara, T., Huynh, A., Gage, F. H., Schultz, P. G., and Ding, S. A synthetic small molecule that induces neuronal differentiation of adult hippocampal neural progenitor cells. *Angew Chem Int Ed Engl*, 45(4):591–3, 2006. ISSN 1433-7851 (Print) 1433-7851 (Linking). doi: 10.1002/anie.200503089. URL <https://www.ncbi.nlm.nih.gov/pubmed/16323231>.
- Ward, R. M. and Kearns, G. L. Proton pump inhibitors in pediatrics : mechanism of action, pharmacokinetics, pharmacogenetics, and pharmacodynamics. *Paediatr Drugs*, 15(2):119–31, 2013. ISSN 1179-2019 (Electronic) 1174-5878 (Linking). doi: 10.1007/s40272-013-0012-x. URL <https://www.ncbi.nlm.nih.gov/pubmed/23512128>.
- Westhoff, J. H., Giselbrecht, S., Schmidts, M., Schindler, S., Beales, P. L., Tonshoff, B., Liebel, U., and Gehrig, J. Development of an automated imaging pipeline for the analysis of the zebrafish larval kidney. *PLoS One*, 8(12):e82137, 2013. ISSN 1932-6203 (Electronic) 1932-6203 (Linking). doi: 10.1371/journal.pone.0082137. URL <https://www.ncbi.nlm.nih.gov/pubmed/24324758>.
- Westwick, J. K. and Lamerdin, J. E. Improving drug discovery with contextual assays and cellular systems analysis. *Methods Mol Biol*, 756: 61–73, 2011. ISSN 1940-6029 (Electronic) 1064-3745 (Linking). doi: 10.1007/978-1-61779-160-4_3. URL <https://www.ncbi.nlm.nih.gov/pubmed/21870220>.
- Whitley, E. and Ball, J. Statistics review 4: sample size calculations. *Crit Care*, 6(4):335–41, 2002. ISSN 1364-8535 (Print) 1364-8535 (Linking). URL <https://www.ncbi.nlm.nih.gov/pubmed/12225610>.
- Wickstrom, M., Danielsson, K., Rickardson, L., Gullbo, J., Nygren, P., Isaksson, A., Larsson, R., and Lovborg, H. Pharmacological profiling of disulfiram using human tumor cell lines and human tumor cells from patients. *Biochem Pharmacol*, 73(1):25–33, 2007. ISSN 0006-2952 (Print) 0006-2952 (Linking). doi: 10.1016/j.bcp.2006.08.016. URL <https://www.ncbi.nlm.nih.gov/pubmed/17026967>.
- Williams, B., Smith, W. B., and Kette, F. E. Intranasal ciclesonide for allergic rhinitis. *J Asthma Allergy*, 1:49–54, 2008. ISSN 1178-6965 (Print) 1178-6965 (Linking). URL <https://www.ncbi.nlm.nih.gov/pubmed/21436985>.
- Wingert, R. A. and Davidson, A. J. The zebrafish pronephros: a model to study nephron segmentation. *Kidney Int*, 73(10):1120–7, 2008. ISSN 1523-1755 (Electronic) 0085-2538 (Linking). doi: 10.1038/ki.2008.37. URL <https://www.ncbi.nlm.nih.gov/pubmed/18322540>.
- Wingert, R. A., Selleck, R., Yu, J., Song, H. D., Chen, Z., Song, A., Zhou, Y., Thisse, B., Thisse, C., McMahon, A. P., and Davidson, A. J. The cdx genes and retinoic acid control the positioning and segmentation of the zebrafish pronephros. *PLoS Genet*, 3(10):1922–38, 2007. ISSN 1553-7404 (Electronic) 1553-7390 (Linking). doi: 10.1371/journal.pgen.0030189. URL <https://www.ncbi.nlm.nih.gov/pubmed/17953490>.
- Wittbrodt, J. N., Liebel, U., and Gehrig, J. Generation of orientation tools for automated zebrafish screening assays using desktop 3d printing. *BMC Biotechnol*, 14:36, 2014. ISSN 1472-6750 (Electronic) 1472-6750 (Linking). doi: 10.1186/1472-6750-14-36. URL <https://www.ncbi.nlm.nih.gov/pubmed/24886511>.
- World Health Organization. Methodology-who collaborating centre for drug statistics, guidelines for atc classification and ddd assignment, 2018. 2017. [accessed: 02-04-2018].
- Xia, H. G., Zhang, L., Chen, G., Zhang, T., Liu, J., Jin, M., Ma, X., Ma, D., and Yuan, J. Control of basal autophagy by calpainI mediated cleavage of atg5. *Autophagy*, 6(1):61–6, 2010. ISSN 1554-8635 (Electronic) 1554-8627 (Linking). URL <https://www.ncbi.nlm.nih.gov/pubmed/19901552>.
- Yamasaki, T., Tamai, I., and Matsumura, Y. Activation of histamine h3 receptors inhibits renal noradrenergic neurotransmission in anesthetized dogs. *Am J Physiol Regul Integr Comp Physiol*, 280(5):R1450–6, 2001. ISSN 0363-6119 (Print) 0363-6119 (Linking). doi: 10.1152/ajpregu.2001.280.5.R1450. URL <https://www.ncbi.nlm.nih.gov/pubmed/11294767>.

- Yang, Y., George, K. C., Shang, W. F., Zeng, R., Ge, S. W., and Xu, G. Proton-pump inhibitors use, and risk of acute kidney injury: a meta-analysis of observational studies. *Drug Des Devel Ther*, 11:1291–1299, 2017. ISSN 1177-8881 (Electronic) 1177-8881 (Linking). doi: 10.2147/DDDT.S130568. URL <https://www.ncbi.nlm.nih.gov/pubmed/28479851>.
- Yoder, B. K. Role of primary cilia in the pathogenesis of polycystic kidney disease. *J Am Soc Nephrol*, 18(5):1381–8, 2007. ISSN 1046-6673 (Print) 1046-6673 (Linking). doi: 10.1681/ASN.2006111215. URL <https://www.ncbi.nlm.nih.gov/pubmed/17429051>.
- Yokoyama H., O. K. and Wakabayashi, H. Chemotherapy with fumagillin and toltrazuril against kidney enlargement disease of goldfish caused by myxosporean hoferellus carassii. *Fish Pathol*, (25):157–163, 1990.
- Yu, A. S. L., El-Ters, M., and Winkhofer, F. T. Clinical trials in autosomal dominant polycystic kidney disease, 2015. URL <https://www.ncbi.nlm.nih.gov/pubmed/27512781>. [accessed: 21-09-2018].
- Zarn, J. A., Bruschweiler, B. J., and Schlatter, J. R. Azole fungicides affect mammalian steroidogenesis by inhibiting sterol 14 alpha-demethylase and aromatase. *Environ Health Perspect*, 111(3):255–61, 2003. ISSN 0091-6765 (Print) 0091-6765 (Linking). doi: 10.1289/ehp.5785. URL <https://www.ncbi.nlm.nih.gov/pubmed/12611652>.
- Zhang, W., Ramamoorthy, Y., Kilicarslan, T., Nolte, H., Tyndale, R. F., and Sellers, E. M. Inhibition of cytochromes p450 by antifungal imidazole derivatives. *Drug Metab Dispos*, 30(3):314–8, 2002. ISSN 0090-9556 (Print) 0090-9556 (Linking). URL <https://www.ncbi.nlm.nih.gov/pubmed/11854151>.
- Zhong, Y., Wu, Y., Liu, R., Li, Z., Chen, Y., Evans, T., Chuang, P., Das, B., and He, J. C. Novel retinoic acid receptor alpha agonists for treatment of kidney disease. *PLoS One*, 6(11):e27945, 2011. ISSN 1932-6203 (Electronic) 1932-6203 (Linking). doi: 10.1371/journal.pone.0027945. URL <https://www.ncbi.nlm.nih.gov/pubmed/22125642>.
- Zhou, W. and Hildebrandt, F. Inducible podocyte injury and proteinuria in transgenic zebrafish. *J Am Soc Nephrol*, 23(6):1039–47, 2012. ISSN 1533-3450 (Electronic) 1046-6673 (Linking). doi: 10.1681/ASN.2011080776. URL <https://www.ncbi.nlm.nih.gov/pubmed/22440901>.
- Zhou, X., Fan, L. X., Sweeney, W. E., J., Denu, J. M., Avner, E. D., and Li, X. Sirtuin 1 inhibition delays cyst formation in autosomal-dominant polycystic kidney disease. *J Clin Invest*, 123(7):3084–98, 2013. ISSN 1558-8238 (Electronic) 0021-9738 (Linking). doi: 10.1172/JCI64401. URL <https://www.ncbi.nlm.nih.gov/pubmed/23778143>.
- Zvyaga, T., Chang, S. Y., Chen, C., Yang, Z., Vuppugalla, R., Hurley, J., Thorndike, D., Wagner, A., Chimalakonda, A., and Rodrigues, A. D. Evaluation of six proton pump inhibitors as inhibitors of various human cytochromes p450: focus on cytochrome p450 2c19. *Drug Metab Dispos*, 40(9):1698–711, 2012. ISSN 1521-009X (Electronic) 0090-9556 (Linking). doi: 10.1124/dmd.112.045575. URL <https://www.ncbi.nlm.nih.gov/pubmed/22648560>.

8 Publication and Awards

8.1 Original Publications

Pandey G., Westhoff J.H., Schaefer F., Jochen G. A Smart Imaging Workflow for Organ-Specific Screening in a Cystic Kidney Zebrafish Disease Model. *Int. J. Mol. Sci.* 2019, 20, 1290. doi: 10.3390/ijms20061290.

Gehrig J., **Pandey G.**, Westhoff J.H. Zebrafish as a Model for Drug Screening in Genetic Kidney Diseases. *Frontiers in Pediatrics.* 2018;6:183. doi: 10.3389/fped.2018.00183.

Pandey G., Westhoff J.H., Schaefer F., Jochen G. An automated high content screen for identification of cystic kidney disease modifying substances in human cystic kidney disease model of zebrafish. (In preparation).

Steenbergen P., Heigwer J., **Pandey G.**, Gehrig J., Westhoff J.H. A multi-parametric semi-automated pipeline development for filtration barrier function study on zebrafish. (In preparation).

8.2 Abstracts

Thomas L., **Pandey G.**, Westhoff J.H., Schaefer F., Jochen G. Large scale feature extraction and image classification for high content screening microscopy. QBI, 01/2019, Le Couvent des Jacobins in Rennes, France- Poster Presentation

Pandey G., Westhoff J.H., Schaefer F., Jochen G. An Automated High Content Screening Platform for Identification of Cystic Kidney Disease-Modifying Substances in Zebrafish. Fish and Amphibian Embryos as Alternative Models in Toxicology and Teratology, 11/2018, Paris, France- Oral Presentation

Pandey G., Westhoff J.H., Schaefer F., Jochen G. An Automated High Content Screening Platform for Identification of Cystic Kidney Disease-Modifying Substances in Zebrafish. Gesellschaft für Entwicklungsbiologie School, 10/2018, Günzburg, Germany- Poster Presentation

Pandey G., Westhoff J.H., Schaefer F., Jochen G. An Automated High Content Screening Platform for Identification of Cystic Kidney Disease-Modifying Substances in Zebrafish. ZDM'11, 07/2018, Leiden, Netherlands- Poster Presentation

Pandey G., Westhoff J.H., Schaefer F., Jochen G. An Automated High-Content Platform for Cyst-Modifying Compound Screening in Zebrafish Cystic Nephropathy Models. ERA-EDTA Congress, 05/2018, Copenhagen, Denmark- Oral Presentation

Pandey G., Westhoff J.H., Schaefer F., Jochen G. An Automated High Content Screening Platform for Identification of Cystic Kidney Disease-Modifying Substances in Zebrafish. Regional Fish Meeting, 04/2017, Heidelberg, Germany- Poster Presentation

Thomas L., **Pandey G.**, Jochen G. A smart imaging platform for automated high- resolution imaging of zebrafish. Regional Fish Meeting, 04/2017, Heidelberg, Germany- Poster Presentation

Pandey G., Westhoff J.H., Schaefer F., Jochen G. An Automated High Content Screening Platform for Identification of Cystic Kidney Disease-Modifying Substances in Zebrafish. RenalTract Conference, 04/2017, Manchester, UK- Poster Presentation

Pandey G., Westhoff J.H., Schaefer F., Jochen G. An Automated High Content Screening Platform to Identify Cystic Kidney Disease-Modifying Substances in Zebrafish. Acquirer HTS Workshop, 03/2018, Griefswald, Germany- Oral Presentation

Pandey G., Westhoff J.H., Schaefer F., Jochen G. An Automated High Content Screening Platform to Identify Cystic Kidney Disease-Modifying Substances in Zebrafish. Acquirer HTS Workshop, 10/2017, Tübingen, Germany- Oral Presentation

Pandey G., Westhoff J.H., Schaefer F., Jochen G. Development of an Automated High Content Screening Platform to Identify Cystic Kidney Disease-Modifying Substances in Zebrafish. EuRenOmics, 05/2017, Berlin, Germany- Oral and Poster Presentation

Pandey G., Westhoff J.H., Schaefer F., Jochen G. Development of an Automated High Content Screening Platform to Identify Cystic Kidney Disease-Modifying Substances in Zebrafish. RenalTract Workshop, 03/2017, Marseille, France- Poster Presentation

Pandey G., Westhoff J.H., Schaefer F., Jochen G. Development of an Automated High Content Screening Platform to Identify Cystic Kidney Disease-Modifying Substances in Zebrafish. RenalTract Workshop, 06/2016, Glasgow, Scotland- Oral Presentation

Pandey G., Westhoff J.H., Schaefer F., Jochen G. Development of an Automated High Content Screening Platform to Identify Cystic Kidney Disease-Modifying Substances in Zebrafish. EuRenOmics, 05/2016, Paris, France- Oral Presentation

9 Supplement

9.1 Materials

9.1.1 High-Content Drug Screening

<u>Materials</u>	<u>Company</u>
Petridish	Sarstedt, Nümbrecht, Germany
12-well plates	Falcon Corning, New York, USA
Borosilicate Glass Capillaries	World Precision Instruments, Florida, USA
Flaming/Brown Micropipette puller	Sutter Instruments, California, USA
FemtoJet Microinjector	Eppendorf, Wesseling-Berzdorf, Germany
Fluorescence Screening Microscope	Nikon SMZ18, Düsseldorf, Germany
Stereomicroscope	Nikon SM745T, Düsseldorf, Germany
<u>Compounds, Buffers and Solutions</u>	
<u>E3 Media</u>	
Sodium chloride	Sigma-Aldrich, Missouri, USA
Potassium chloride	Sigma-Aldrich, Missouri, USA
Calcium chloride dihydrate	Sigma-Aldrich, Missouri, USA
Magnesium sulfate heptahydrate	Sigma-Aldrich, Missouri, USA
1-pheny-2-thiourea (PTU)	Alfa Aesar, Karlsruhe, Germany
HEPES	Merck, Berlin, Germany
Protease Type XIV	Sigma-Aldrich Chemie GmbH, Schnelldorf, Germany
Ethyl 3-aminobenzoate methanesulfonate (Tricaine)	Sigma-Aldrich, Missouri, USA
DMSO	Sigma-Aldrich, Missouri, USA
Rapamycin	Cayman Chemicals, Biomol GmbH, Hamburg, Germany
Valproic Acid	Sigma-Aldrich, Missouri, USA
Trichostatin A	Sigma-Aldrich, Missouri, USA
Curcumin	Sigma-Aldrich, Missouri, USA
Prestwick Drug Library	Prestwick Chemical, Illkirch, France
Morpholinos	Gene Tools, LLC, Oregon, USA

Morpholino Sequences

<u>Morpholino Name</u>	<u>Sequence</u>
IFT-MO	5'-ACGTCGTCAATATTTTACCTGAGGC-3'
Ctrl-MO	5'-CCTCTTACCTCAGTTACAATTTATA-3'

9.1.2 High-Content Imaging

<u>Materials</u>	<u>Company</u>
Acquifer High-Content Imaging Machine-IM04	DITABIS AG, Pforzheim, Germany
ACQUIFER HIVE Core M module	DITABIS AG, Pforzheim, Germany

10x,4x,2x objective	Nikon, Düsseldorf, Germany
96-well plates	Greiner, Frickenhausen, Germany
<u>Buffers and Solutions</u>	
Agarose NEEO ultra-quality	Roth, Karlsruhe, Germany

9.1.3 RNA, cDNA Extraction and Agarose Gel Electrophoresis

<u>Materials</u>	<u>Company</u>
Thermo cycler	BioRad, Rüdigheim, Germany
UV Transilluminator	BioRad, Rüdigheim, Germany
Needles	Sarstedt, Nümbrecht, Germany
<u>Buffers and Solutions</u>	
TRIZOL	Life Technologies, Darmstadt, Germany
Phenol	Roth, Karlsruhe, Germany
Chloroform	Roth, Karlsruhe, Germany
iScript cDNA Synthesis Kit	BioRad, California, USA
6X Loading Dye	Thermo Scientific, Karlsruhe, Germany
Gene Ruler	Thermo Scientific, Karlsruhe, Germany
Agarose NEEO ultra-quality	Roth, Karlsruhe, Germany
Primers	Eurofins Genomics, Ebersberg, Germany

Primer Sequences

Gene	Name	Sequence
ift	Forward	5'-CTTGGGCTCCAAACAATGCAA-3'
	Reverse	5'-GGGTCAGCAGGCTTTGTTGTA-3'
EF1-alpha	Forward	5'-GTGCTGTGCTGATTGTTGCT-3'
	Reverse	5'-TGTATGCGCTGACTTCCTTG-3'

9.1.4 HE Staining

<u>Materials</u>	<u>Company</u>
Einbettkassetten	Langenbrink GmbH, Emmendingen, Germany
Glass slides	Marienfild, Lauda-Königshofen, Germany
Microtome	Leica Microsystems, Heerbrugg, Switzerland
Hisotology Machine	Leica Microsystems, Heerbrugg, Switzerland

Leica S8 APO stereo microscope Leica, Microsystems, Heerbrugg, Switzerland

Buffers and Solutions

PFA Sigma-Aldrich, Missouri, USA

PBS Sigma-Aldrich, Missouri, USA

Ethanol 99,9% Roth, Karlsruhe, Germany

Ethanol 96% Roth, Karlsruhe, Germany

Ethanol 70% Roth, Karlsruhe, Germany

Xylene Roth, Karlsruhe, Germany

Hematoxylin Roth, Karlsruhe, Germany

Eosin G Roth, Karlsruhe, Germany

Acetic Acid Sigma-Aldrich, Missouri, USA

9.2 Figures

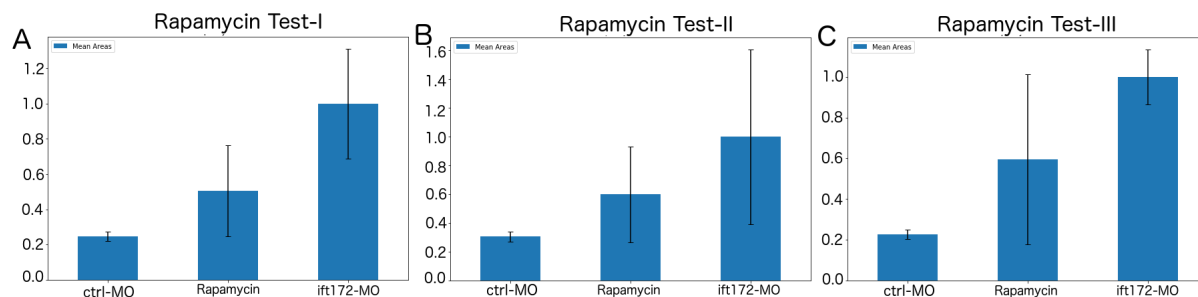


Fig. S.1: Bar charts representing three tests (A,B,C) done on automated cyst suppressive effect assessment of 25 μM rapamycin on ift172-MO injected larvae at 72 hpf. The graphs show around 50% suppression in each test population.

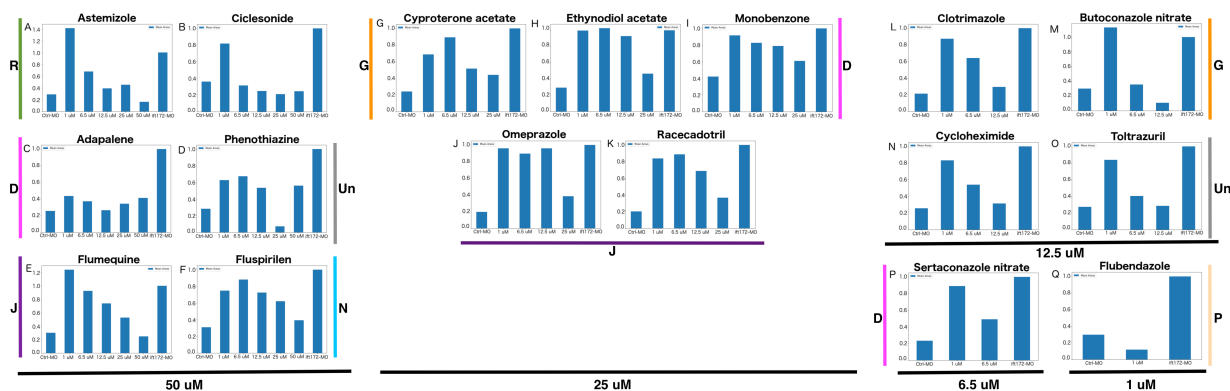


Fig. S.2: Bar charts presenting cystic suppression quantified by the automated script. The graphs have been normalised against ift172-MO control. The x and y-axis display the concentrations used i.e. 1 μM , 6.5 μM , 12.5 μM , 25 μM , 50 μM and normalised areas values respectively. The compounds have been grouped according to their most effective concentration and their ATC classes area displayed by colour coded lines and bold capital letters (for letter description refer to: Fig. 24)

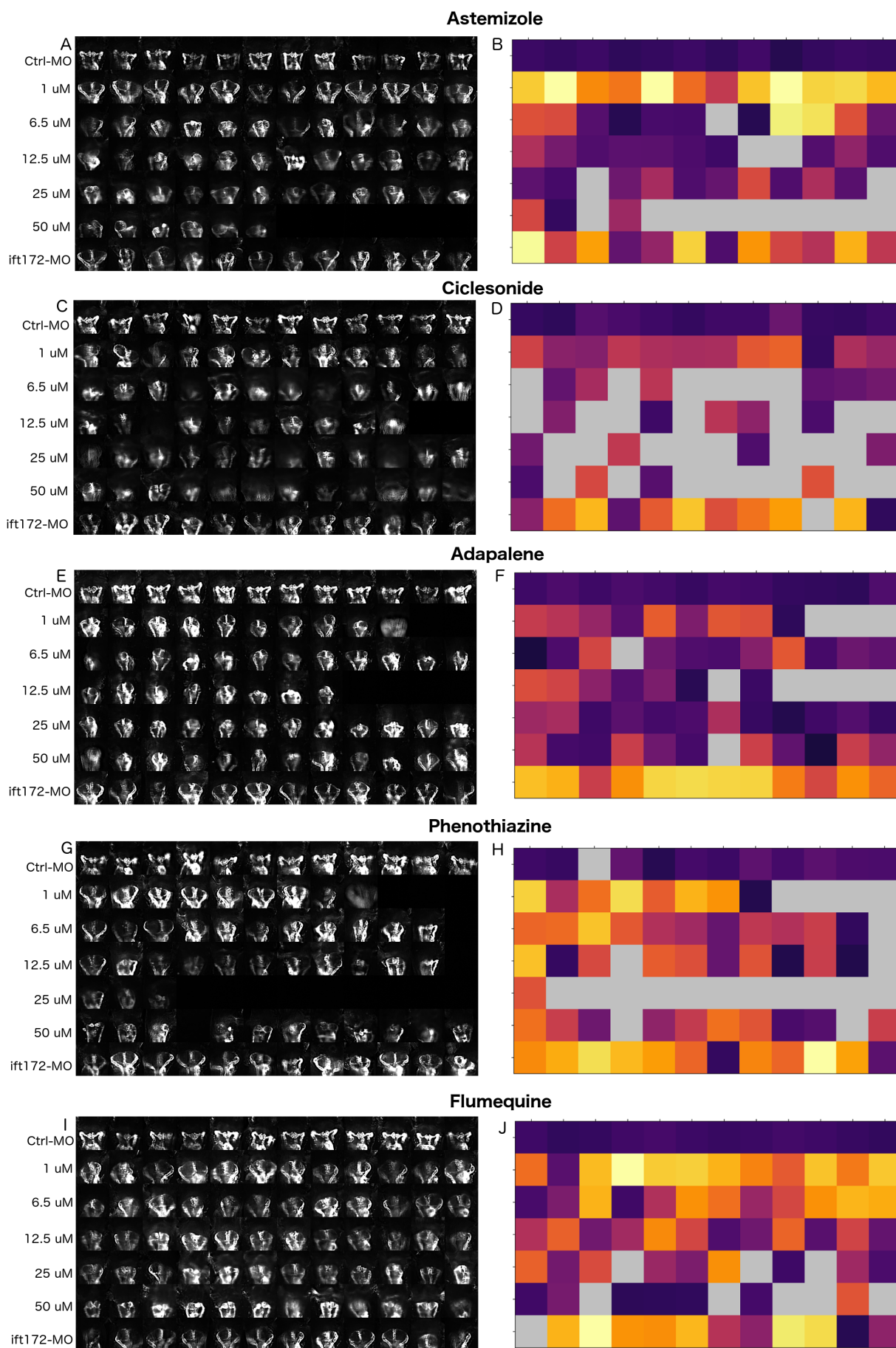


Fig. S.3: **Hits effective at 50 μ M.** Montages of hits with 50 μ M as primary effective concentration corresponding to their heatmaps displaying automatically quantified areas. The annotated heatmap scale is shown in S.8.

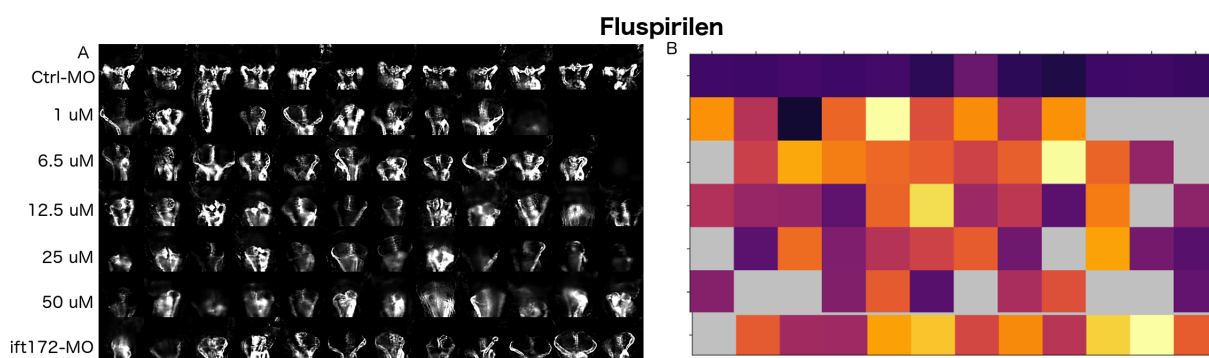


Fig. S.4: **Hits effective at 50 µM.** Montages of hits with 50 µM as primary effective concentration corresponding to their heatmaps displaying automatically quantified areas. The annotated heatmap scale is shown in S.8.

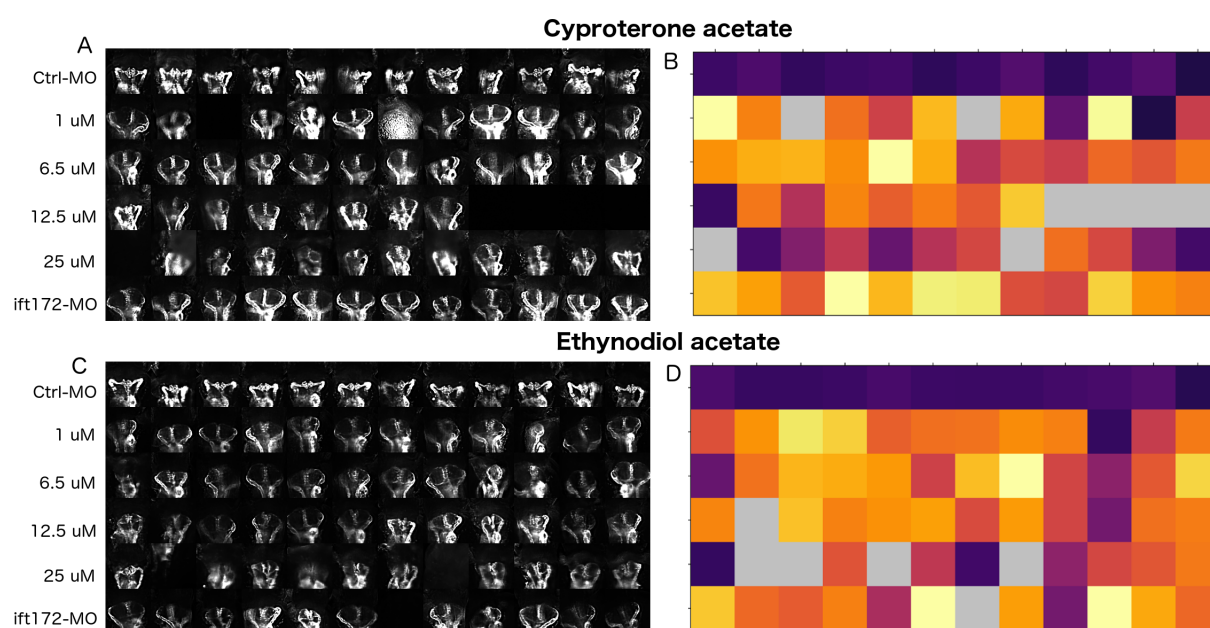


Fig. S.5: **Hits effective at 25 µM.** Montages of hits with 25 µM as primary effective concentration corresponding to their heatmaps displaying automatically quantified areas. The annotated heatmap scale is shown in S.8.

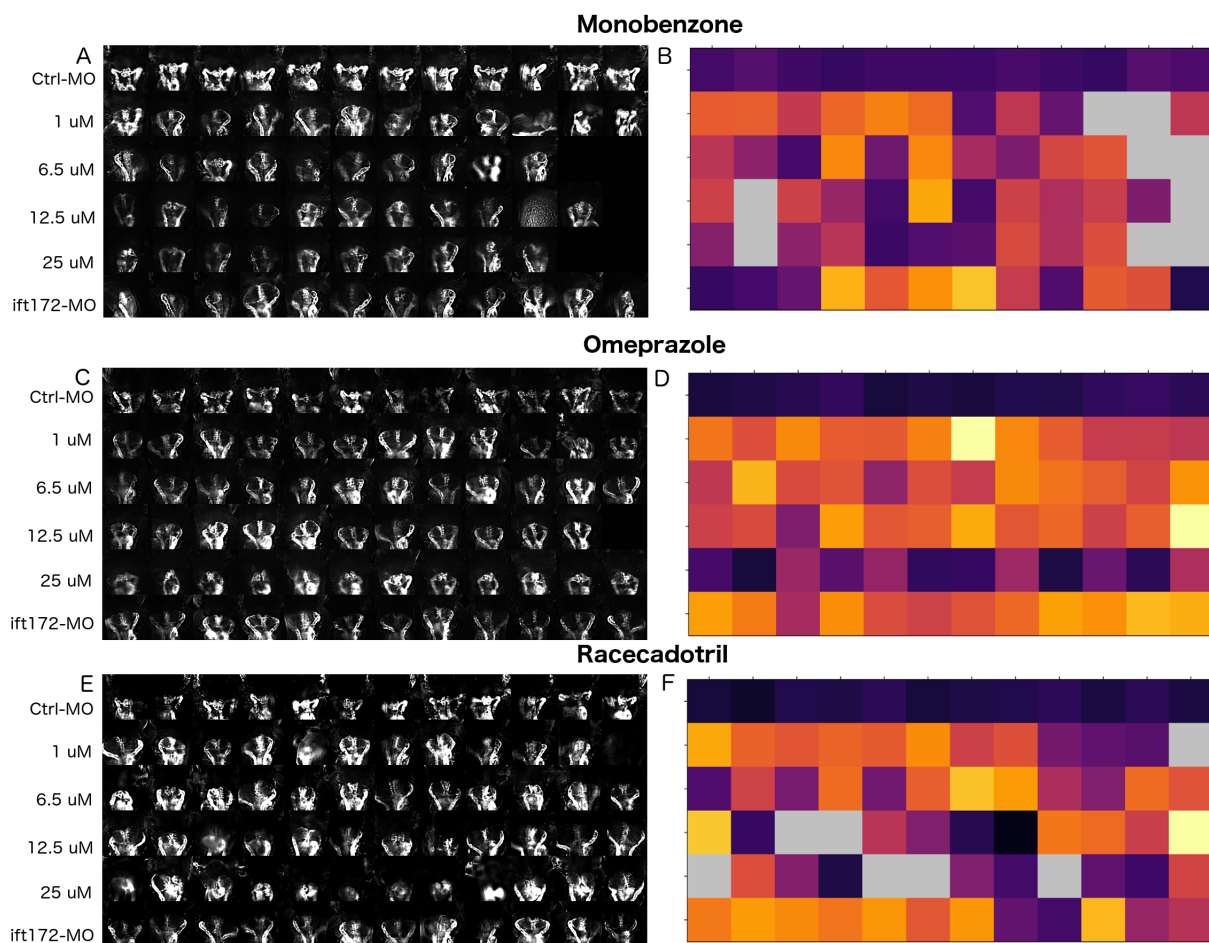


Fig. S.6: **Hits effective at 25 μ M.** Montages of hits with 25 μ M as primary effective concentration corresponding to their heatmaps displaying automatically quantified areas. The annotated heatmap scale is shown in S.8.

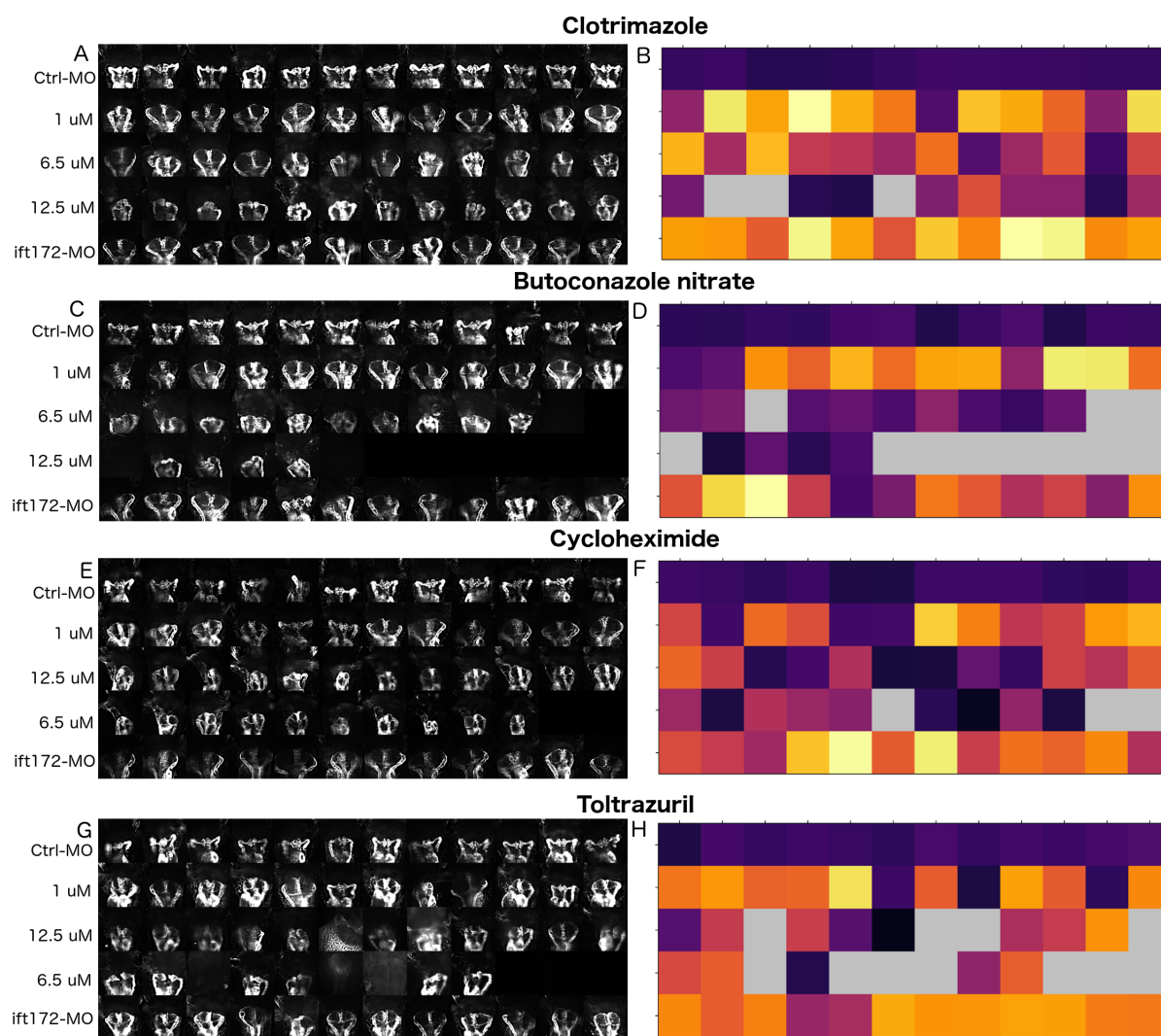


Fig. S.7: **Hits effective at 12.5 μ M, 6.5 μ M and 1 μ M.** Montages of hits up to 12.5 μ M, 6.5 μ M and 1 μ M effective concentrations corresponding to their heatmaps displaying automatically quantified areas. The annotated heatmap scale is shown in the S.8.

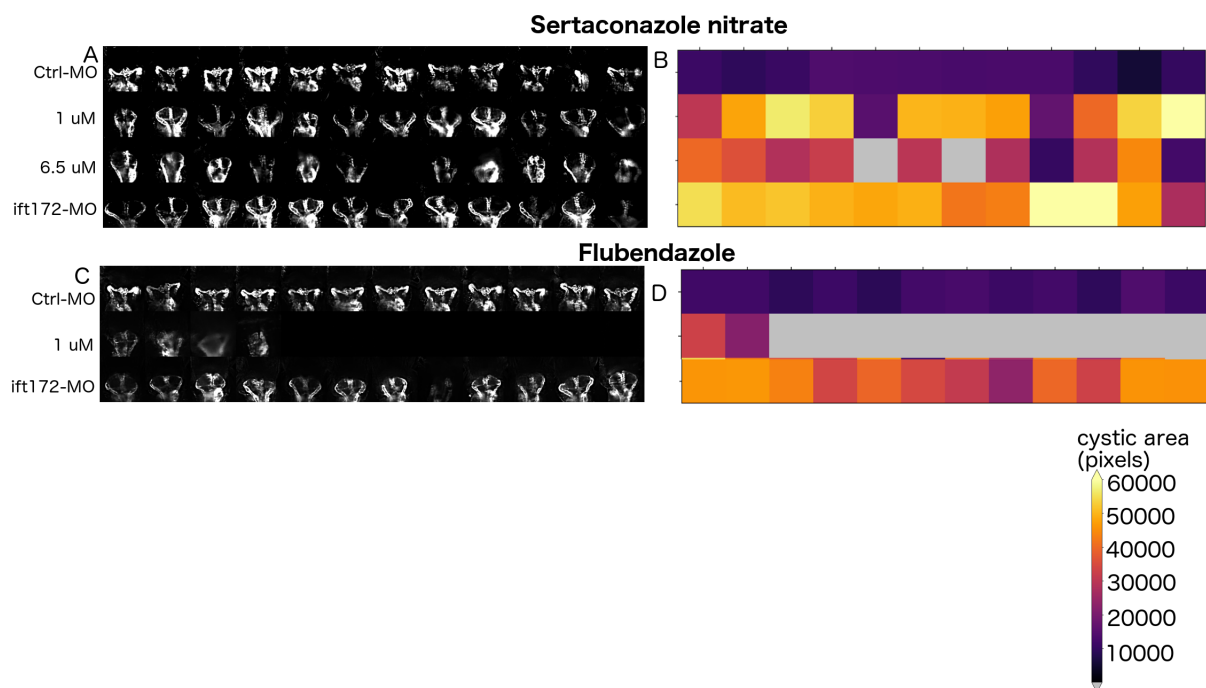


Fig. S.8: **Hits effective at 6.5 μ M and 1 μ M.** Montages of hits up to 12.5 μ M, 6.5 μ M and 1 μ M effective concentrations corresponding to their heatmaps displaying automatically quantified areas. The annotated heatmap scale is shown in the end.

9.3 Scripts

S.1 Step-by-step execution of smart-imaging workflow for organ-specific screening in a cystic kidney zebrafish disease model

Download all the script files from the supplementary folder. If you wish to make no changes to the script and execute the scripts in their given state, please install all the dependencies mentioned at the end of the document.

Automated image acquisition script:

1. Download: Supplementary folder >> Smart Imaging sub-folder >> “SmartImaging_macro.ijm” script.
2. Launch the control software of the ACQUIFER Imaging Machine along with the smart imaging (SI) interface.
3. Configure the required imaging parameters for the pre-screen on the Graphical User Interface (GUI), such as, integration time, objective, channels etc.
4. Launch the Fiji software and install the “SmartImaging_macro.ijm” as plugin under Fiji >> Plugins >> Install.
5. Start the pre-screen experiment on the ACQUIFER Imaging Machine by clicking on “Generate Script” and then “Start”.
6. As the imaging commences, go to the “Jobs Folder (..\JOBS)” in the file explorer and wait for the file “Image_Location.pth” to appear and then, execute the pre-installed SI macro in the Fiji plugins section to begin automated feature detection and acquisition of region of interest (ROI).

Note: SI script parameters can be easily modified to fit the demands of the project, for example: cells, tissues, organs etc. could be captured.

7. All images will be saved in the predefined project folder.

Image pre-processing module:

Automated multi-layer generation

1. Download: Supplementary folder >> Multilayer Generation sub-folder >> “MultilayerTiff-Script.pl”.
2. Pool all the imaged folders requiring multi-layer generation in a single folder.

3. Launch Fiji and the multilayer generating Perl script.

Note: The Perl script can be modified, For example: channels subjected to multilayer tiff generation can be decided from the list of acquired channels, folder location change etc.

4. Copy the address of the target folder in the Perl window >> press enter.
5. Go to the target folder >> find “makemulti-macro.ijm” >> drag and drop to Fiji window >> run script.
6. All folders will end up with a new “multitiff” folder with sub-folders for all imaged channels and multilayer tiff files for the channel subjected to the script.

Image restoration

1. Launch Huygens 3D deconvolution software.
2. Open a single image >> parameter window >> find theoretical PSF (Point Spread Function) >> enter other required settings >> save the settings file for batch deconvolution later.
3. Open batch processing mode >> select target folder >> create save folder >> execute pre-generated with defined parameters as deconvolution script.
4. All deconvolved images will end in the pre-defined save folder, ready for further processing.

Automated quantification script:

1. Download: Supplementary folder >> Image Analysis sub-folder >> “AllFijiScripts.ijm”.
2. Launch Fiji >> Open scripts >> Run “Script1” >> Select folder.
3. Script will create the specified folder sub-folders >> Crop >> Recrop >> 1) Cyst, 2)Kidney and 3)Analysis Folder
4. Upon “Script1” execution, the “Crop” folder contains cropped and Z-projected versions of the images that were sub-stacked around their focal plan using “Find Focussed Slide” plugin.

Note: All parameters involved in this sub-module can be changed as per project requirements. For example: focal plane settings, Z-projection settings, number of slides used for sub-stacking, ROI selection etc.

5. The “Recrop” folder contains recropped, thresholded and outlier filtered images from the “Crop” folder.

Note: All parameters involved in this sub-module can be changed as per project requirements. For example: threshold chosen, denoising threshold, ROI selection etc.

6. “Cyst” folder contains the results of cystic area calculation in “.csv” format for all the images from “Recrop” folder.
7. “Kidney” folder contains the results of kidney area calculation in “.csv” format for all the images from “Recrop” folder.

Note: The location of convex hull drawn is ROI dependent and can be modified as per ROI in question, along with other following parameters in *Steps 6 and 7*.

8. Open “Blank Detection” script >> Run script.
9. The script will create a sub-folder in the “Recrop” folder and save the variance results in “.csv” format for all the images from the “Crop” folder.
10. Open “Blur Detection” script >> Run script.
11. The script will create a sub-folder in the “Recrop” folder and save the variance results after “Subtract background” plugin execution in “.csv” format for all the images from the “Crop” folder.
12. Open “Wild type Detection” script >> Run script.
13. The script will create a sub-folder in the “Crop” folder and save the “Plot profile” results in “.csv” format for all the images from the “Crop” folder.
14. Open “Wild type/Cyst Detection re-check” script >> Run script.
15. The script will create a sub-folder in the wild type detection folder and save the “Analyze particles” >> Ellipse measurement results in “.csv” format for all the images from the “Crop” folder.
16. For the upcoming steps, Python 3.0 was used in “Jupyter notebook” environment on Windows 10 platform. The script can also be run on a Mac system with some modifications.

Note: The script has the capacity to be executed in other Python environments, but I have not tried that here.

17. Launch the “Jupyter notebook” using windows command prompt and execute the python script >> “PythonMethods.ipynb”. The script will stepwise go through all the results folders with “.csv” files.

18. The areas from individual “Kidney” files will be added and collated together in a single file against the file name. This collated file with kidney areas for all imaged wells is copied to the “Analysis Folder”.
19. The individual “Cyst” files will be filtered to screen for particles with desired cystic morphology and collated and saved in a new file against the file name as its cystic area. The collated file with cyst areas for all imaged wells are copied to the “Analysis Folder”.
20. The individual “Blank” and “Blur” files will be screened and the well names clearing set threshold limit will be collated. These lists with the filenames will be copied to the “Analysis Folder”.
21. The individual files from wild type detection folders will be checked and the well names clearing the set “Plot profile” parameters will be collated. These lists with the filenames will be copied to the “Analysis Folder”.
22. The results from “Kidney”, ‘Cyst’, “Blank”, “Blur”, “wild type” lists for each file ~ well will be merged in a single “.csv” file.

Note: All the threshold values are subject to the ROI in question and can be changed depending on the required end-point in *Steps 17–21*.

23. The python script will go through each column in a row i.e. Blank, Blur, wild type and check for the assigned status. Based on which, the final kidney value will assigned to that well. For instance: a wild type kidney will be assigned only pronephric area value, whereas cystic kidney will be assigned pronephric area + cystic area values. On the contrary, blank and blur images will be assigned zero-area values, in order to prevent data skewing due to false positives.
24. These assigned area values will be further plotted as heatmap corresponding to the 96-well plate format imaged using ‘Matplotlib’ library. The heatmap labelled by the name of the folder analysed will be saved in the “Analysis Folder” location.

Note: The location of the folders can be changed to any preferred location.

Dependencies required for the script execution: Certain plugins which are not part of the default Fiji library are used and must be installed in advance for the script execution:

- “Find Focussed Slice”
- “Convex Hull Plus”
- “Laplace Filter”
- Python 3.0 was used in “Jupyter notebook” environment on Windows 10 platform.

S.2 Script codes

S.3 Smart Imaging

```
/* this set of macros can be used to carry out Smart Imaging applications on an ACQUIFER
   Imaging Machine IM04. The first macro "SmartImaging_400_11" watches a directory reported
   by the IM04 to D:\\IMAGING-DATA\\JOBS\\Image_Location.pth. Each image is then processed
   by the second macro "centerofmass_400_11", which detects the center of mass after
   thresholding and generates a IM04 job file with script commands for altering the
   screening run. */
macro "SmartImaging_400_11" {
  setBatchMode (true);
  filestring=File.openAsString("D:\\IMAGING-DATA\\JOBS\\Image_Location.pth");
  rows=split(filestring, "\\n");
  directory=replace(rows[0], "\\\\", "\\\\\\\\\\\\\\\\\\")+"\\\\";
  print (directory);
  File.makeDirectory(""+directory+"dest");
  // get the initial list (without opening the files)
  fulllist = getFileList(directory);
  Array.sort(fulllist);

  //push only images into the list array
  list = newArray();
  for (jj=0; jj<fulllist.length; jj++){
    if (endsWith (fulllist[jj], ".tif")){
      list = Array.concat(fulllist[jj], list);
    }
  }
  Array.sort(list);
  Array.print(list);

  //execute command for each image file
  for (ii=0; ii<list.length; ii++){
    if (endsWith (list[ii], ".tif")){
      print (list[ii]);
      open(directory + list[ii]);
      selectWindow(list[ii]);
      run("centerofmass_400_11");
      close();
    }
  }
  //watch folder
  for (;;) {
    previousList = list;
    fulllist = getFileList(directory);
    //push only images into the list array
    list = newArray();
    for (jjj=0; jjj<fulllist.length; jjj++){
      if (endsWith (fulllist[jjj], ".tif")){
```

```

    list = Array.concat(fulllist[jjj], list);
  }}
  if (previousList.length != list.length) {
    //sort both lists
    Array.sort(list);
  Array.sort(previousList);
    // walk both lists
    j = 0;
    for (i = 0; i < list.length; i++) {
      stopJ = previousList.length;
      while (j < stopJ)
        if (previousList[j] < list[i]) {
          j++;
        }else{
          stopJ = j; }
      if (j >= previousList.length && endsWith (list[i], ".tif")){
        //wait(200);
        open(directory + list[i]);
        selectWindow(list[i]);
        run("centerofmass_400_11");
        close();
      } else if (list[i] != previousList[j] && endsWith (list[i], ".tif")) {
        //wait(200);
        open(directory + list[i]);
        selectWindow(list[i]);
        run("centerofmass_400_11");
        close(); }}
    }
    wait(1000); // wait a second
  } }
macro "centerofmass_400_11"{
run("Set Measurements...", "center redirect=None decimal=0");
run("Properties...", "channels=1 slices=1 frames=1 unit=pixel pixel_width=1.0000
    pixel_height=1.0000 voxel_depth=1.0000 frame=[0 sec] origin=0,0");

a = getInfo("image.filename");
print (a);
dir = getInfo("image.directory");
print (dir);
File.makeDirectory(""+dir+"dest");
setBatchMode(true);
run("Duplicate...", "title=b duplicate range=1-130");
run("Invert");
run("8-bit");
run("Auto Threshold", "method=Otsu ignore_white");
run("Select None");

getPixelSize(unit, pixelWidth, pixelHeight);
x=newArray(1); y=newArray(1);
run("Measure");

```

```

x[0] = round(getResult("XM")/pixelWidth);
y[0] = round(getResult("YM")/pixelHeight);

selectWindow(a);
makeRectangle(x[0]-256, y[0]-256, 512, 512);
run("Crop");
saveAs("Tiff", ""+dir+"\\dest\\cropped--"+a+"");
selectWindow("b");
close();

f = File.open("D:\\IMAGING-DATA\\JOBS\\"+a+".lck");
newName = replace(a, "--", "#");
name = split(newName, "#");
Array.print(name);
//Array.print(name);
XLabel = split(name[9], "X");
YLabel = split(name[10], "Y");
XAbs = XLabel[0];
YAbs = YLabel[0];
print("X: "+XAbs+", Y: "+YAbs+"");
offsetX = (x[0]-1024)*(6.5/4); //set to (6.5/2) for 2x
print("offsetX :"+offsetX+"");
offsetY = (1024-y[0])*(6.5/4); //set to (6.5/2) for 2x
print("offsetY :"+offsetY+"");
NewXCoord = (round((XAbs)+(offsetX)))/1000;
NewYCoord = (round((YAbs)+(offsetY)))/1000;
print("New X: "+NewXCoord+"");
print("New Y: "+NewYCoord+"");
WellNo = split(name[13], "WE");
WellNoCleaned = split(WellNo[0], ".tif");
print(f, "SetWellNo("+WellNoCleaned[0]+")");
WellCoordinate = split(name[0], "-");
print(f, "SetMeta('Well Coordinate','"+WellCoordinate[0]+"')");
SubPos = split(name[1], "SU");
print(f, "SetMeta('Well Pos in Well','"+SubPos[0]+"')");
print(f, "GotoXY("+NewXCoord+", "+NewYCoord+', 'Abs')");
print(f, "SetObjective(3)");
/////10x/////
print(f, "SetLight(3,10,10,0.000)");
print(f, "AcquireAutofocus(7,100.000,2,'True','True')");
print(f, "SetLight(3,10,10,0.000,'Flash')");
print(f, "AcquireAutofocus(6,20.000,2,'True','True')");
print(f, "SetLight(3,100,20,0.000)");
print(f, "Acquire(30,4.000,1,'D:\\IMAGING-DATA\\IMAGES\\SCRIPTS','True','SIdata')"); // 30
    slices 4um
print(f, "SetLight(6,60,10,0.000)");
print(f, "Acquire(30,4.000,1,'D:\\IMAGING-DATA\\IMAGES\\SCRIPTS','True','SIdata')"); // 30
    slices 4um
print(f, "SetLight(0,0,0,0)");
print(f, "SetObjective(2)"); //set to SetObjective(1) for 2x

```

```

File.close(f);
File.rename("D:\\IMAGING-DATA\\JOBS\\"+a+".lck", "D:\\IMAGING-DATA\\JOBS\\"+a+".job");
}

```

S.4 Multilayer TIFF Generation

```

use strict;
print "Choose experimental folder:\nUSAGE: x:\\a\\b\\c\n(right_click -> paste)";
my $choice = <STDIN>;          #flexible input of directory
chomp $choice;
(my $parentdir = $choice);
#print "$parentdir\n";
chdir($parentdir);
opendir(DIR1, $parentdir) or die "can't opendir $parentdir: $!";
my @listdir = readdir (DIR1);  #reads all the experiment directories
my @experiment_folders;
my %folder_structure;
my @macros;
open OUT, ">$parentdir/makemulti-macro.ijm" or die $!,"\\n" ;
print OUT qq(setBatchMode(true));
foreach my $folder (@listdir){
#makes the needed destination folders within the experimental folders and pushes the
  experiment folders into an array
  if ($folder !~ /\.|macros|max|deconvolved|multi/ig) {
    #print $folder,"\\n";
    mkdir("$folder/multi_tiff", 0777) || print $!;
    mkdir("$folder/multi_tiff/CO1", 0777) || print $!;
    mkdir("$folder/multi_tiff/CO2", 0777) || print $!;
    mkdir("$folder/multi_tiff/CO3", 0777) || print $!;
    mkdir("$folder/multi_tiff/CO4", 0777) || print $!;
    mkdir("$folder/multi_tiff/CO5", 0777) || print $!;
    mkdir("$folder/multi_tiff/CO6", 0777) || print $!;
    my $experiment = $parentdir."\\\\".$folder;
    push @experiment_folders, ($experiment);
  }
}
foreach my $exp_folder (@experiment_folders) {
  print "$exp_folder\\n";
  my @tags = split (/\\/, $exp_folder);
  my $tag = $tags[-1];
  #print "$tag\\n\\n";
  my $$SIdata = $exp_folder."\\SIdata";
  print "$$SIdata\\n";
  chdir($$SIdata);
  opendir(DIR3, $$SIdata) or die "can't opendir $$SIdata: $!";
  my @listfiles = readdir (DIR3);
  #print "@listfiles";
  my %wellhash;

```

```
my @wellarray;
while (my $file = shift @listfiles){
    #iterates over the filenames, splits the filenames and loads the well and rest into an
    hash
    my ($coord, $subpos, $loop, $color, $slice, $px, $pw, $int, $tm, $x, $y, $z, $t,
        $well) = split ('--', $file);
    $wellhash{$coord."--".$subpos."--".$loop."--".$color} = "$slice" unless $file !~
        /\.tif/ig;      #is using only *.tif files
}
while ( (my $key,my $value) = each %wellhash){#makes an sorted array of the wells present
    in the folder (the hash was used to find unique wells, so it ignores the number of
    images per well
    push @wellarray, ("$key");
    #print "$key\n";
}
my @sorted_wellarray = sort @wellarray;
#print "@sorted_wellarray";
while (my $line = shift @sorted_wellarray) {
    my ($coord, $subpos, $loop, $color) = split ('--', $line);
    #print "$coord, $subpos, $loop, $color\n";
    (my $modparent = $SIdata) =~ s/\\/\\\\/g;
    (my $moddest = $exp_folder) =~ s/\\/\\\\/g;
print "Coord: $coord Subpos: $subpos Loop: $loop Color: $color\n";
#print "$color\n";
if ($color =~ /CO3/ig){
#print "$color\n";
    print OUT qq(
        run("Image Sequence...", "open=$modparent\\\\anyimage.tif number=1000 starting=1
            increment=1 scale=100 file=($coord--$subpos--$loop--$color--SL...) sort");
        saveAs("Tiff",
            "$moddest\\\\multi_tiff\\\\$color\\\\$coord--$subpos--$loop--MULTI--$color");
        run("Close All");
    );}
}
}
```

S.5 Image Analysis

```
%\lstset{language=ijm}
//Script1
//The following script was run on an entire folder of 96 deconvolved multi-tiff images of 30
    slices each
//The script can also be run on non deconvolved stacks with minor modifications
//Main functions of the script include preprocessing and assigning of pronephric areas to the
    images
dir =getDirectory("Choose a directory");
setBatchMode(true);
```

```

function main(dir) // creates output folders to save resulting csv and images
    files
{
    print("Running entire process on: "+dir);
    // STEP 0: CROP
    cropDir = dir + "Crop/";
    File.makeDirectory(cropDir);
    step0_crop(dir, cropDir);
    // STEP 1: RECROP
    recropDir = cropDir + "Recrop/";
    File.makeDirectory(recropDir);
    step1_recrop(cropDir, recropDir);
    // STEP 2.1: CYST DETECTION
    cystDir = recropDir + "Cyst/";
    File.makeDirectory(cystDir);
    step2a_cysts(recropDir, cystDir);
    // STEP 2.2: KIDNEY_DETECTION
    kidneyDir = recropDir + "Kidney/";
    File.makeDirectory(kidneyDir);
    step2b_kidneys(recropDir, kidneyDir);
}
function closeAll() // close all open windows
{
    run("Close All");
    windows = getList("window.titles");
    for ( i=0; i < windows.length; i++ )
    {
        window = windows[i];
        selectWindow(window);
        run("Close");
    }
}
/** Goes through all the multilayer tif files, z-projects and crops it and saves the output
    to respective folder */
function step0_crop( dir, outDir )
{
    files = getFileList(dir);
    for( i=0; i < files.length; i++ )
    {
        file = files[i];
        if(
            endsWith(file, ".tif")
            || endsWith(file, ".tiff")
        )
        {
            print(" Cropping: "+file);
            open(dir+file);
            crop();
            saveAs("tiff", outDir+file);
            closeAll();
        }
    }
}

```

```
    }
  }
}

/** Auto crops the image to minimize the black border and then cuts off the
 * lower part of the image and saves the output to respective folder */
function step1_recrop( dir, outDir )
{
  files = getFileList(dir);
  for( i=0; i < files.length; i++ )
  {
    file = files[i];
    if(
      endsWith(file, ".tif")
      || endsWith(file, ".tiff")
    )
    {
      open(dir+file);
      recrop();
      saveAs("tiff", outDir+file);
      closeAll();
    }
  }
}

/** Finds all the potential cyst "particle" areas and saves the output to respective folder*/
function step2a_cysts( dir, outDir )
{
  files = getFileList(dir);
  for( i=0; i < files.length; i++ )
  {
    file = files[i];
    if(
      endsWith(file, ".tif")
      || endsWith(file, ".tiff")
    )
    {
      open(dir+file);
      Title = File.nameWithoutExtension();
      detectCysts();
      saveAs("tiff", outDir+file);
      saveAs("Measurements", outDir + Title + ".csv");
      closeAll();
    }
  }
}

/** Finds all the potential kidney "particle" areas and saves the output to respective
 * folder*/
function step2b_kidneys( dir, outDir )
{
  files = getFileList(dir);
```

```

for( i=0; i < files.length; i++ )
{
  file = files[i];
  if(
    endsWith(file, ".tif")
    || endsWith(file, ".tiff")
  )
  {
    open(dir+file);
    Title = File.nameWithoutExtension();
    detectKidneys();
    saveAs("tiff", outDir+file);
    saveAs("Measurements", outDir + Title + ".csv");
    closeAll();
  }
}

setBatchMode(true);
function crop()
{
  sliceCount = nSlices();
  run("Rotate 90 Degrees Right");
  sourceWindow = getTitle();
  run("Find focused slices", "select=100 variance=0.000");
  label = getMetadata("Label"); // get the subtitle
  l1 = lengthOf("Z_");
  l2 = indexOf(label, "Z_");
  str1 = substring(label, l1+l2);
  str2 = substring(label, 0, l2);
  focus = parseInt(str1+str2); // convert string into integer, fs: focussed slide
  print(" Focussed Slice: " + focus);
  slice_first= focus - 4;
  slice_last = focus + 3;
  if( slice_first< 1 ) slice_first= 1;
  if( slice_last > sliceCount) slice_last = sliceCount;
  selectWindow(sourceWindow);
  run("Make Substack...", " slices=" + slice_first + "-" + slice_last);
  substackWindow = getTitle();
  run("Duplicate...", "duplicate");
  run("Remove Outliers...", "radius=1 threshold=50 which=Bright stack");
  run("Z Project...", "projection=[Max Intensity]");
  run("Canvas Size...", "width=512 height=512 position=Center");
}
function recrop()
{
  run("Duplicate...", " ");
  run("Auto Threshold", "method=Li white");
  run("Canvas Size...", "width=" + getWidth() + " height=" + getHeight()/1.6 + "
    position=Center");
}

```

```

    run("Remove Outliers...", "radius=6 threshold=50 which=Bright stack");
}
function detectCysts()
{
    run("Canvas Size...", "width=" + getWidth()/1.11 + " height=" + getHeight()/1.38+ "
        position=Bottom-Center");
    run("Canvas Size...", "width=" + getWidth()/1.09 + " height=" + getHeight()+ "
        position=Bottom-Right");
    run("Remove Outliers...", "radius=22 threshold=50 which=Bright");
    run("Invert");
    run("Clear Results");
    run("Set Measurements...", "area mean standard modal min centroid center perimeter bounding
        fit shape feret's integrated median skewness kurtosis area_fraction redirect=None
        decimal=3");
    run("Convex Hull Plus", "mode=[Convex Hull selection] log");
    if (isOpen("Exception")) {
        selectWindow("Exception");
        run("Close"); }
    run("Analyze Particles...", " show=Outlines display include");
}
function detectKidneys()
{
    run("Canvas Size...", "width=" + getWidth()/1.11 + " height=" + getHeight()/1.38+ "
        position=Bottom-Center");
    run("Clear Results");
    run("Set Measurements...", "area mean standard modal min centroid center perimeter bounding
        fit shape feret's integrated median skewness kurtosis area_fraction redirect=None
        decimal=3");
//Creates an empty row in results table in case of blank well with no particles
    setResult("Area",nResults,"0");setResult("Mean",0,"0");setResult("StdDev",0,"0");setResult("Mode",0,"0");setR
    setResult("Width",nResults,"0");setResult("Height",nResults,"0");setResult("Major",nResults,"0");setResult("M
    setResult("%Area",nResults,"0");setResult("RawIntDen",nResults,"0");setResult("FeretX",nResults,"0");setResul
    run("Analyze Particles...", " show=Outlines display include");
}
main(dir);
//Blank Detection
//The following script was run on an entire folder of 96 preprocessed images obtained from
    crop folder of script1 to find blank images
setBatchMode(true);
dir = getDirectory("Choose a Directory");
list = getFileList(dir);
dirName = File.getName(dir);
outDir = dir+File.separator+"Recrop"+File.separator+"/BlankDetection"+File.separator; //
    create output folder to save resulting csv and images files
File.makeDirectory(outDir);
function cyst() // function execution for filter application and variance
    measurement
{
    run("Clear Results");
TargetTitle= File.nameWithoutExtension();

```

```

run("8-bit");
run("Canvas Size...", "width=512 height=320 position=Bottom-Center");
run("Canvas Size...", "width=412 height=200 position=Top-Center");
run("Laplace Filter");
run("8-bit");
run("Clear Results");
run("Set Measurements...", " mean redirect=None decimal=5");
run("Measure");
mean = getResult("Mean");
selectWindow("Results");
run("Close");
W = getWidth();
H = getHeight();
b = 0;
Var = 0;                                     // Set to 0 which is out of focus
for (j=0; j<H; j++) {
  for (i=0; i<W; i++) {
    p = getPixel(i, j);
    t = (p-mean)*(p-mean);
    b += t;
  }
}
Var = b/(H*W);                               // Maximum value is best-focused, decreasing as defocus increases
print(Var);
}
for (i=0; i<list.length; i++)                // saving resulting images and csv files in the
  output folder
{
  showProgress(i+1, list.length);
  if (endsWith(list[i], ".tif") || endsWith(list[i], ".TIF"))
  {
    print(dir+list[i]);
    open(dir+list[i]);
    cyst();
    TargetTitle= File.nameWithoutExtension();
    saveAs("TIFF", outDir+TargetTitle);
    selectWindow("Log");
    saveAs("Text", outDir+TargetTitle+".csv");
  }
}
//Blur Detection
//The following script was run on an entire folder of 96 preprocessed images obtained from
  crop folder of script1 to find blurry images
setBatchMode(true);
dir = getDirectory("Choose a Directory");
list = getFileList(dir);
dirName = File.getName(dir);
outDir = dir+File.separator+"Recrop"+File.separator+"BlurDetection"+File.separator; //
  create output folder to save resulting csv and images files
File.makeDirectory(outDir);

```

```

function cyst() // function execution for background subtraction and variance
    measurement
{
run("Clear Results");
TargetTitle= File.nameWithoutExtension();
run("8-bit");
run("Canvas Size...", "width=512 height=320 position=Bottom-Center");
run("Canvas Size...", "width=412 height=200 position=Top-Center");
run("Unsharp Mask...", "radius=10 mask=0.90");
run("Subtract Background...", "rolling=5");
run("Clear Results");
run("Set Measurements...", " mean redirect=None decimal=5");
run("Measure");
mean = getResult("Mean");
selectWindow("Results");
run("Close");
W = getWidth();
H = getHeight();
b = 0;
Var = 0; // Set to 0 which is out of focus
for (j=0; j<H; j++) {
    for (i=0; i<W; i++) {
        p = getPixel(i, j);
        t = (p-mean)*(p-mean);
        b += t;
    }
}
Var = b/(H*W); // Maximum value is best-focused, decreasing as defocus
                increases
print(Var);
}
for (i=0; i<list.length; i++) // saving resulting images and csv
    files in the output folder
{
    showProgress(i+1, list.length);
    if (endsWith(list[i], "tif") || endsWith(list[i], "TIF"))
    {
        print(dir+list[i]);
        open(dir+list[i]);
        cyst();
        TargetTitle= File.nameWithoutExtension();
        saveAs("TIFF", outDir+TargetTitle);
        selectWindow("Log");
        saveAs("Text", outDir+TargetTitle+".csv");
    }
}
//Wild type/Cyst Detection
//The following script was run on an entire folder of 96 preprocessed images obtained from
    crop folder of script1 to detect the presence of wild type/cystic images
dir =getDirectory("Choose a directory");
setBatchMode(true);
function main(dir)

```

```

{
    print("Running entire process on: "+dir);    // create output folders to save resulting
        csv and images files
    // STEP 1: Wt_Preprocess
    Wt_preprocessDir = dir + "Wt_preprocess/";
    File.makeDirectory(Wt_preprocessDir);
    step1_Wt_preprocess(dir,Wt_preprocessDir);
    // STEP 2: Wt_FilePlot
    Wt_FilePlotDir = Wt_preprocessDir + "Wt_FilePlot/";
    File.makeDirectory(Wt_FilePlotDir);
    step2_Wt_FilePlot(Wt_preprocessDir,Wt_FilePlotDir);
}
function closeAll()                                // close all open windows
{
    run("Close All");
    windows = getList("window.titles");
    for ( i=0; i < windows.length; i++ )
    {
        window = windows[i];
        selectWindow(window);
        run("Close");
    }
}
function step1_Wt_preprocess(dir, outDir)
{
    files = getFileList(dir);
    for( i=0; i < files.length; i++ )
    {
        file = files[i];
        if(
            endsWith(file, ".tif")
            || endsWith(file, ".tiff")
        )
        {
            print(" Wt_Preprocess: "+file);
            open(dir+file);
            Wt_preprocess();
            saveAs("tiff", outDir+file);
        } }
}
function step2_Wt_FilePlot( dir, outDir )
{
    files = getFileList(dir);
    for( i=0; i < files.length; i++ )
    {
        file = files[i];
        if(
            endsWith(file, ".tif")
            || endsWith(file, ".tiff")
        )
    }
}

```

```
{
    open(dir+file);
    Wt_FilePlot();
    closeAll();
}}
}
setBatchMode(true);
function Wt_preprocess() // image preprocessing
{
    run("8-bit");
    run("Canvas Size...", "width=512 height=320 position=Bottom-Center");
    run("Canvas Size...", "width=412 height=200 position=Top-Center");
    run("Gaussian Blur...", "sigma=15");
    setAutoThreshold("Li dark");
    run("Convert to Mask");
}
function Wt_FilePlot()
{
    TargetTitle= File.nameWithoutExtension();
    run("Clear Results");
    run("Measure");
    WholeImage_Area = getResult("%Area",0); // internal blank image check
    if (WholeImage_Area == 100)
    {
        run("Invert");
        run("Select All");
        profile = getProfile();
        run("Clear Results");
        saveAs("TIFF", outDir+TargetTitle+"plot");
        run("Clear Results");
        profile = getProfile();
        for (i=0; i<profile.length; i++) {
            setResult("Value", i, profile[i]);
            updateResults();
        }
        saveAs("Measurements", outDir+TargetTitle+".csv");
    }
    else { // if not a blank image wild type image check performed
        run("Create Selection"); // enclosing pronephroi in bounding box of optimal size
        run("Make Inverse");
        run("To Bounding Box");
        run("Clear Results");
        run("Set Measurements...", "mean standard modal centroid center perimeter bounding fit
            shape feret's integrated median skewness kurtosis area_fraction redirect=None
            decimal=5");
        run("Measure");
        boundingbox_width = getResult("Width",0);
        boundingbox_widthNew = boundingbox_width-2;
        boundingbox_height= getResult("Height",0);
        boundingbox_heightNew = 98;
        boundingbox_bx = getResult("BX",0);
    }
}
```

```

    boundingbox_by = getResult("BY",0);
    if (boundingbox_height > 98)
    {
        arguments = "width="+boundingbox_widthNew+" height="+boundingbox_heightNew+"
            x="+boundingbox_bx +" y="+boundingbox_by+ " scaled";
        run("Specify...", arguments);
    }
profile = getProfile(); // running plot profile
run("Clear Results");
saveAs("TIFF", outDir+TargetTitle+"plot");
run("Clear Results");
profile = getProfile();
for (i=0; i<profile.length; i++) {
    setResult("Value", i, profile[i]);
    updateResults();
    saveAs("Measurements", outDir+TargetTitle+".csv"); // saving resulting images and csv
        files in the output folder
    } }
}
main(dir);
//Wild type/Cyst Detection re-check
//The following script was run on an entire folder of 96 preprocessed images obtained from
    crop folder of script1 to re-check the preclassified wild type/cystic images
setBatchMode(true);
dir = getDirectory("Choose a Directory");
list = getFileList(dir);
dirName = File.getName(dir);
outDir = dir+"/MajorCheck"+File.separator;
File.makeDirectory(outDir); // create output folder to save resulting csv and images
    files
function cyst()
{
TargetTitle= File.nameWithoutExtension(); // execution of function to process and draw
    ellipse on pronephroi
run("Clear Results");
run("Set Measurements...", "area mean standard modal min centroid center perimeter bounding
    fit shape feret's integrated median skewness kurtosis area_fraction redirect=None
    decimal=3");
run("Convex Hull Plus", "mode=[Convex Hull selection] log");
if (isOpen("Exception")) {
    selectWindow("Exception");
    run("Close"); }
    run("Analyze Particles...", " show=Ellipses display include");
}
for (i=0;i<list.length;i++) // saving resulting images and csv files in the output
    folder
{
    showProgress(i+1, list.length);
    if (endsWith(list[i],".tif") || endsWith(list[i],".TIF"))
    {

```

```

        print(dir+list[i]);
    open(dir+list[i]);
        cyst();
    TargetTitle= File.nameWithoutExtension();
    saveAs("TIFF", outDir+TargetTitle);
        saveAs("Results", outDir+TargetTitle+".csv");
    }
}

```

```

# The following script was run on folder containing multiple subfolders each containing 96
  well plate data. The script goes to the folders and finds the csv files created by the
  Fiji routine. This data is filtered and processed for final kidney area assignment and
  plotting of the corresponding heatmap #
# Importing relevant libraries #
import matplotlib.pyplot as plt
import os
import pandas as pd
import glob
import csv
import numpy as np
import re
import glob
import shutil
import subprocess
import ntpath
import re
from itertools import chain
import json
import os.path
import fnmatch
import matplotlib.pyplot as plt
import matplotlib as mpl
import plotly
# Entering each subfolder of the directory #
path_pattern = r'path\to\recropped\image\folder\*'
for path in glob.glob(os.path.join(path_pattern), recursive=True):
    print(path)
#Pronephric areas present as separate particle values are summed together#
#and extracted from all images in the kidney folder and copied as a single#
##### value in a new csv file corresponding to their well names #####
writeHeader = True
All_Files = []
# checking and entering for kidney folder in each recrop subfolder #
for path in glob.glob(os.path.join(path_pattern), recursive=True):
    print(path)
    kidney_folder = glob.glob( os.path.join(path, 'Kidney\\') )
    print (kidney_folder)
    if 1 != len(kidney_folder):
        print('SKIPPING: '+path)
        continue

```

```

kidney_folder = kidney_folder[0]
# Reading all files #
kidney_paths = glob.glob( os.path.join(kidney_folder, '*.csv') )
writeHeader = True
for csv_path in kidney_paths:
    df = pd.read_csv(csv_path)
    head, tail = os.path.split(csv_path)
    df.insert(loc=0, column='Filename', value=tail, allow_duplicates=False)
    # Removing unnecessary information #
    df.drop(df.columns[[1,3,4,5,6,7,8,9,10,11,12,13,14,15,16,17,18,19,20,21,22,23,24,25,26,27,28,29]],
            axis=1, inplace=True)
    # Summing up the praticles to get kidney areas #
    df_grouped = df.groupby(['Filename']).agg({'Area':'sum'})
    df_grouped = df_grouped.reset_index()
    # Copying data to a new csv file #
    if writeHeader is True:
        df_grouped.to_csv(os.path.join(kidney_folder, 'kidney.csv'), mode='a', header=True,
                           index=False)
        writeHeader = False
    else:
        df_grouped.to_csv(os.path.join(kidney_folder, 'kidney.csv'), mode='a', header=False,
                           index=False)

# Copying the single csv file from kidney folder to a newly created Analysis folder #
All_Files = []
for path in glob.glob(os.path.join(path_pattern), recursive=True):
    kidney_folder, = glob.glob( os.path.join(path, 'Kid*\\') )
    if not os.path.exists( os.path.join(path, 'Analysis_folder') ):
        os.makedirs( os.path.join(path, 'Analysis_folder') )
    shutil.copy(os.path.join(kidney_folder, 'kidney.csv'), os.path.join(path, 'Analysis_folder'))
# Cystic areas present as separate particle values are filtered based on certain parameters
  and copied as one or two values depending on the single or double cysts detected in a new
  csv file corresponding to their well names #
cyst_area = []
writeHeader = True
All_Files = []
# checking and entering for kidney folder in each recrop subfolder #
for path in glob.glob(os.path.join(path_pattern), recursive=True):
    print(path)
    cyst_folder = glob.glob( os.path.join(path, 'Cyst*\\') )
    if 1 != len(cyst_folder):
        print('SKIPPING: '+path)
        continue
    cyst_folder =cyst_folder[0]
    cyst_paths = glob.glob( os.path.join(cyst_folder, '*.csv') )
    writeHeader = True
    for csv_path in cyst_paths:
        df = pd.read_csv(csv_path)
        head, tail = os.path.split(csv_path)
        # Filtering cyst values #

```

```

potential_cyst = df.loc[(df['MinFerret'] >= 70) & (df[' ' ] < 11)]
potential_cyst.insert(loc=0, column='Filename', value=tail, allow_duplicates=False)
# Removing unnecessary information #
    potential_cyst.drop(potential_cyst.columns[[3,4,5,6,7,8,9,10,11,12,13,14,15,16,17,18,19,20,21,22,23,24],
    axis=1, inplace=True)
# Checking for number of cysts as the script was not allowed to select more than two
    cystic particles by default #
total_rows = potential_cyst.shape[0]
if((total_rows) > 2):
    potential_cyst = potential_cyst.drop(potential_cyst[potential_cyst[' ' ] > 11].index)
    total_rows = potential_cyst.shape[0]
else:
    total_rows = potential_cyst.shape[0]
if((total_rows) > 2):
    potential_cyst = potential_cyst.drop(potential_cyst[potential_cyst[' ' ] > 9].index)
    total_rows = potential_cyst.shape[0]
else:
    total_rows = potential_cyst.shape[0]
if((total_rows) > 2):
    potential_cyst = potential_cyst.drop(potential_cyst[potential_cyst[' ' ] > 8].index)
    total_rows = potential_cyst.shape[0]
else:
    total_rows = potential_cyst.shape[0]
if ((total_rows) > 2):
    potential_cyst = potential_cyst.drop(potential_cyst[potential_cyst[' ' ] > 7].index)
    total_rows = potential_cyst.shape[0]
else:
    total_rows = potential_cyst.shape[0]
if ((total_rows) > 2):
    potential_cyst = potential_cyst.drop(potential_cyst[potential_cyst[' ' ] > 6].index)
    total_rows = potential_cyst.shape[0]
else:
    total_rows = potential_cyst.shape[0]
if ((total_rows) > 2):
    potential_cyst = potential_cyst.drop(potential_cyst[potential_cyst['MinFerret'] <=
        95].index)
    total_rows = potential_cyst.shape[0]
else:
    total_rows = potential_cyst.shape[0]
# Copying and saving data to a new csv file #
if writeHeader is True:
    potential_cyst.to_csv(os.path.join(cyst_folder, 'cyst_area.csv'), mode='a',
        header=True, index=False)
    writeHeader = False
else:
    potential_cyst.to_csv(os.path.join(cyst_folder, 'cyst_area.csv'), mode='a',
        header=False, index=False)
# Copying the single csv file from cyst folder to a newly created Analysis folder #
for path in glob.glob(os.path.join(path_pattern), recursive=True):
    cyst_folder, = glob.glob( os.path.join(path, 'Cyst\\') )

```

```

shutil.copy(os.path.join(cyst_folder, 'cyst_area.csv'),
            os.path.join(path, 'Analysis_folder'))
# The cystic area values are checked, if more than one value present, due to the presence of
  2 cysts, they were merged in the same row as 'list' to avoid multiple occurrences of same
  filename #
for path in glob.glob(os.path.join(path_pattern), recursive=True):
    Analysis_folder = glob.glob(os.path.join(path, 'Analysis_folder*\\'))
    if 1 != len(Analysis_folder):
        print('SKIPPING: '+path)
        continue
    Analysis_folder = Analysis_folder[0]
    print(Analysis_folder)
    Analysis_path = glob.glob(os.path.join(Analysis_folder, 'cyst_area.csv'))
    print(Analysis_path)
    df = [pd.read_csv(cyst_area) for cyst_area in glob.glob(os.path.join(Analysis_folder,
        'cyst_area.csv'))]
    df1 = pd.concat(df, axis=0)
    # Checking for multiple filename occurrence and regrouping as one #
    df1 = df1.rename(columns={' ': "Count"})
    df1.drop(df1.columns[[1,3]], axis=1, inplace=True)
    df2 = df1.groupby('Filename')['Area'].apply(list)
    # Saving as a new csv file with single filenames with multiple area values present as
    'list' #
    df2.to_csv(os.path.join(Analysis_folder, 'Cyst_Area_onerow.csv'))
# The values saved as list were converted to dataframe with column names #
##### for cystic areas detected i.e. Areal and Area2 #####
for path in glob.glob(os.path.join(path_pattern), recursive=True):
    Analysis_folder = glob.glob(os.path.join(path, 'Analysis_folder*\\'))
    if 1 != len(Analysis_folder):
        print('SKIPPING: '+path)
        continue
    Analysis_folder = Analysis_folder[0]
    Analysis_path = glob.glob(os.path.join(Analysis_folder, 'Cyst_Area_onerow.csv'))
    # Reading all files with cystic areas #
    df = pd.read_csv(os.path.join(Analysis_folder, 'Cyst_Area_onerow.csv'),
                    names = ["Filename", "Area1"])
    # Checking for Areal and Area2 and splitting them into two columns #
    df['Area2'] = df.Area1.apply(lambda x: x.split(',')[1] if len(x.split(','))>1 else '')
    df.Area1 = df.Area1.apply(lambda x: x.split(',')[0])
    df.Area1 = df.Area1.str.replace(r"\([.*]*\)", "").str.extract("([0-9]+)", expand=False)
    df.Area2 = df.Area2.str.replace(r"\([.*]*\)", "").str.extract("([0-9]+)", expand=False)
    df = df.fillna(0)
    #Saving as a new csv file with cystic area columns as a dataframe #
    df.to_csv(os.path.join(Analysis_folder, 'Cyst_Areal_Area2.csv'), index=False)
# Finally, each image is assigned single cystic value by summing up the cystic values, in
  case present #
for path in glob.glob(os.path.join(path_pattern), recursive=True):
    Analysis_folder = glob.glob(os.path.join(path, 'Analysis_folder*\\'))
    if 1 != len(Analysis_folder):
        print('SKIPPING: '+path)

```

```

    continue
Analysis_folder = Analysis_folder[0]
Analysis_path = glob.glob(os.path.join(Analysis_folder, 'Cyst_Areal_Area2.csv'))
# Reading files with all cystic areas #
df = pd.read_csv(os.path.join(Analysis_folder, 'Cyst_Areal_Area2.csv'))
# Summing up cystic areas and assigning them to a new column #
df['Area_Sum'] = df['Areal'] + df['Area2']
# Saving final cystic values as a new csv file #
df.to_csv(os.path.join(Analysis_folder, 'Cyst_Areas_Sum.csv'), index=False)
# Total kidney area is assigned here by summing up the given pronephric and cystic area to
  each image and saving the result in a new csv file #
for path in glob.glob (os.path.join(path_pattern), recursive=True):
    Analysis_folder = glob.glob(os.path.join(path, 'Analysis_folder*\\'))
    if 1 != len(Analysis_folder):
        print ('SKIPPING: '+path)
        continue
    Analysis_folder = Analysis_folder[0]
    Analysis_path = glob.glob(os.path.join(Analysis_folder, 'kidney.csv'))
    # Reading files with summed kidney areas #
    df = pd.read_csv(os.path.join(Analysis_folder, 'kidney.csv'))
    # Reading files with summed cystic areas #
    df2 = pd.read_csv(os.path.join(Analysis_folder, 'Cyst_Areas_Sum.csv'))
    # Merging them together #
    df3 = pd.merge(df, df2, on='Filename', how='left')
    df3.fillna(0, inplace=True)
    # In the screen ctrls were always pipetted in first 12 columns #
    ##### therefore, they were assigned only kidney areas here #####
    df3.iloc[:,12, 2:5] *= 0
    # All the areas were merged and summed in a new column #
    df3['TotalKidney_Area'] = df3['Area'] + df3['Area_Sum']
    # Saving all areas and their sum in a new csv file #
    df3.to_csv(os.path.join(Analysis_folder, 'MergedAreas_Sum_WholeKidney_Final.csv'),
              index=False)
# Checking for the blank images in the blank folder and copying their names in a file #
blank_path = r'path\to\recropped\image\folder\'
# checking and entering for kidney folder in each recrop subfolder #
for path in glob.glob (os.path.join(blank_path), recursive=True):
    Blank_folder = glob.glob(os.path.join(path, 'Blank*\\'))
    if 1 != len(Blank_folder):
        print ('SKIPPING: '+path)
        continue
    Blank_folder = Blank_folder[0]
    blank_filepath = glob.glob(os.path.join(Blank_folder, '*.csv'), recursive=True)
    last_blank_file = max(blank_filepath, key=os.path.getmtime)
    # Reading all blank folder files and scanning their variance #
    with open(last_blank_file, 'r') as f:
        words=csv.reader(f,delimiter=',')
        merged = list(chain.from_iterable(words))
        blank_dic= dict(zip(merged[:,2], merged[1::2]))
        str1 = str(blank_dic)

```

```

blank_dic_str = eval(str1)
with open("blank_file.csv", 'w') as outfile:
    root = csv.writer(outfile, delimiter=',')
    root.writerow(["Filename", "Variance"])
    for i,j in blank_dic_str.items():
        root.writerow([i, j])
writeHeader = True
blank_imgs=[]
df = pd.read_csv("blank_file.csv")
df["Filename"] = df["Filename"].apply(lambda x:
    os.path.splitext(os.path.basename(x))[0])
# Filtering files based on variance value #
blank_img = df.loc[(df['Variance'] >= 125)]
print (blank_img)
# Check for the presence of null variance value #
if blank_img.empty:
    blank_img = pd.DataFrame(index=[0,], columns=['Filename', 'Variance'])
    blank_img = blank_img.fillna(0)
    blank_img
for b_path in glob.glob(os.path.join(Blank_folder), recursive=True):
    print(b_path)
# Saving data to a new csv file #
if writeHeader is True:
    blank_img.to_csv(os.path.join(b_path, 'blank_images.csv'), mode='a', header=True,
        index=False)
    writeHeader = False
else:
    blank_img.to_csv(os.path.join(b_path, 'blank_images.csv'), mode='a', header=False,
        index=False)
# Copying the single csv file from blank folder to a newly created Analysis folder #
for path in glob.glob(os.path.join(path_pattern), recursive=True):
    blank_folder, = glob.glob( os.path.join(path, 'Blank*\\') )
    shutil.copy(os.path.join(blank_folder,'blank_images.csv'),
        os.path.join(path,'Analysis_folder'))
## All blank images were assigned an outlier area value of 0 ##
for path in glob.glob (os.path.join(path_pattern), recursive=True):
    Analysis_folder = glob.glob(os.path.join(path, 'Analysis_folder*\\'))
    if 1 != len(Analysis_folder):
        print ('SKIPPING: '+path)
        continue
    Analysis_folder = Analysis_folder[0]
    Analysis_path = glob.glob(os.path.join(Analysis_folder,
        'MergedAreas_Sum_WholeKidney_Final.csv'))
# Opening files containing kidney and cystic area information #
df = pd.read_csv(os.path.join(Analysis_folder, 'MergedAreas_Sum_WholeKidney_Final.csv'))
df["Filename"] = df["Filename"].apply(lambda x: os.path.splitext(os.path.basename(x))[0])
# Opening files containing blank image information #
df2 = pd.read_csv(os.path.join(Analysis_folder, 'blank_images.csv'))
# Merging the two files #
df3 = df.merge(df2, how='left', on= 'Filename')

```

```

df3.fillna(0, inplace=True)
# Checking for blank images and if positive assigning them 0 values #
df3.loc[df3.Variance != 0, 'TotalKidney_Area'] = 0
# Saving as a new csv file with blank checked images #
df3.to_csv(os.path.join(Analysis_folder, 'Blank_Area.csv'), index=False)
# Checking for the blurry images in the blur folder and copying their names in a file #
blur_path = r'path\to\recropped\image\folder\*'
# checking and entering for kidney folder in each recrop subfolder #
for path in glob.glob(os.path.join(blur_path), recursive=True):
    Blur_folder = glob.glob(os.path.join(path, 'Blur*\'))
    if 1 != len(Blur_folder):
        print ('SKIPPING: '+path)
        continue
    Blur_folder = Blur_folder[0]
    blur_filepath = glob.glob(os.path.join(Blur_folder, '*.csv'), recursive=True)
    last_blur_file = max(blur_filepath, key=os.path.getmtime)
    # Reading all blur folder files and scanning their variance #
    with open(last_blur_file, 'r') as f:
        words=csv.reader(f,delimiter=',')
        merged = list(chain.from_iterable(words))
        blur_dic= dict(zip(merged[::2], merged[1::2]))
        str1 = str(blur_dic)
        blur_dic_str = eval(str1)
        with open("blur_file.csv", 'w') as outfile:
            root = csv.writer(outfile, delimiter=',')
            root.writerow(["Filename", "Variance"])
            for i,j in blur_dic_str.items():
                root.writerow([i, j])
        writeHeader = True
        blurry_imgs=[]
        df = pd.read_csv("blur_file.csv")
        df["Filename"] = df["Filename"].apply(lambda x:
            os.path.splitext(os.path.basename(x))[0])
        # Filtering images based on variance value #
        blurry_img = df.loc[(df['Variance'] < 400)]
        print (blurry_img)
        # Check for the presence of null variance value #
        if blurry_img.empty:
            blurry_img = pd.DataFrame(index=[0,], columns=['Filename', 'Variance'])
            blurry_img = blurry_img.fillna(0)
            blurry_img
    for blu_path in glob.glob(os.path.join(Blur_folder), recursive=True):
        print (blu_path)
    # Saving data to a new csv file #
    if writeHeader is True:
        blurry_img.to_csv(os.path.join(blu_path, 'blurry_images.csv'), mode='a', header=True,
            index=False)
        writeHeader = False
    else:
        blurry_img.to_csv(os.path.join(blu_path, 'blurry_images.csv'), mode='a', header=False,

```

```

        index=False)
# Copying the single csv file from blur folder to a newly created Analysis folder #
for path in glob.glob(os.path.join(path_pattern), recursive=True):
    blur_folder, = glob.glob( os.path.join(path, 'Blur*\\') )
    shutil.copy(os.path.join(blur_folder,'blurry_images.csv'),
                os.path.join(path,'Analysis_folder'))
## All blur images were assigned an outlier area value of 0 ##
for path in glob.glob (os.path.join(path_pattern), recursive=True):
    Analysis_folder = glob.glob(os.path.join(path, 'Analysis_folder*\\'))
    if 1 != len(Analysis_folder):
        print ('SKIPPING: '+path)
        continue
    Analysis_folder = Analysis_folder[0]
    # Opening file with pre-assigned blank checked images #
    Analysis_path = glob.glob(os.path.join(Analysis_folder, 'Blank_Area.csv'))
    # Opening the file with blurry image information #
    df = pd.read_csv(os.path.join(Analysis_folder, 'Blank_Area.csv'))
    df["Filename"] = df["Filename"].apply(lambda x: os.path.splitext(os.path.basename(x))[0])
    df2 = pd.read_csv(os.path.join(Analysis_folder, 'blurry_images.csv'))
    # Merging the two files
    df3 = df.merge(df2, how='left', on= 'Filename')
    df3.fillna(0, inplace=True)
    # Checking for blurry images and if positive assigning them 0 values #
    df3.loc[df3.Variance_y != 0, 'TotalKidney_Area'] = 0
    # Saving as a new file with blur-blank checked images #
    df3.to_csv(os.path.join(Analysis_folder, 'Blur_Area_Final.csv'), index=False)
# Filtering, detecting and copying all wildtype kidney image names to a new csv file #
writeHeader = True
wt_filenames = []
path_p = r'path\to\wild type\image\check\folder*'
# checking and entering for wildtype check folder in each crop subfolder #
for p in glob.glob (os.path.join(path_p), recursive=True):
    wt_folder = glob.glob(os.path.join(p, 'Wt_F*\\'))
    if 1 != len(wt_folder):
        print ('SKIPPING: '+path)
        continue
    wt_filenames = []
    writeHeader = True
    wt_folder = wt_folder[0]
    # Opening each csv file attached with the image #
    wt_paths = glob.glob(os.path.join(wt_folder, '*.csv'))
    for csv_path in wt_paths:
        print (csv_path)
        df = pd.read_csv(csv_path)
        # Filtering files based on the presence of 0s in plot profile data #
        df.loc[df.index[0], 'Value'] = 1
        zero_csv = df.loc[(df['Value'] == 0)]
        if zero_csv.empty:
            head, tail = os.path.split(csv_path)
            wt_filenames.append(tail)

```

```

df1 = pd.DataFrame(wt_filenames, columns=["Filename"])
# Saving data to a new csv file #
if writeHeader is True:
    df1.to_csv(os.path.join(wt_folder, 'wtFileNames.csv'), mode='a', header=True,
               index=False)
    writeHeader = False
else:
    df1.to_csv(os.path.join(wt_folder, 'wtFileNames.csv'), mode='a', header=False,
               index=False)
# Copying the single csv file from wildtype check folder to a newly created Analysis folder #
path_pat = r'path\to\wildtype\image\check\folder\*'
for wt_path in glob.glob(os.path.join(path_pat), recursive=True):
    print('FROM: ' + wt_path)
    wt_folder, = glob.glob( os.path.join(wt_path, 'Wt_F\'))
    shutil.copy(
        os.path.join(wt_folder, 'wtFileNames.csv'),
        os.path.join(wt_folder, '..', '..', 'Recrop', 'Analysis_folder')
    )
None
# Filtering and copying all the wildtype re-check in a new csv file #
writeHeader = True
All_Files = []
path_partcle = r'path\to\wildtype\image\re-check\folder\*'
# checking and entering for wildtype recheck folder in each wttype check subfolder #
for p in glob.glob( os.path.join(path_partcle), recursive=True):
    partcle_folder = glob.glob(os.path.join(p, 'MajorCheck\'))
    if 1 != len(partcle_folder):
        print ('SKIPPING: '+path)
        continue
All_Files = []
writeHeader = True
partcle_folder = partcle_folder[0]
# Opening each csv file attached with the image #
partcle_paths = glob.glob(os.path.join(partcle_folder, '*.csv'))
for csv_path in partcle_paths:
    df = pd.read_csv(csv_path)
    head, tail = os.path.split(csv_path)
    # Selecting the highest ellipse are in case of more than one present #
    imax = df['Area'].argmax()
    df = df.iloc[imax:imax+1]
    df['Filename'] = tail
    All_Files.append(df)
    df_all = pd.concat(All_Files).set_index('Filename')
# Saving data to a new csv file #
if writeHeader is True:
    df_all.to_csv(os.path.join(partcle_folder, 'MajorCheck.csv'), mode='a', header=True,
                  index=True)
    writeHeader = False
else:
    df_all.to_csv(os.path.join(partcle_folder, 'MajorCheck.csv'), mode='a', header=False,

```

```

        index=True)
# Copying the single csv file from wildtype re-check folder to a newly created Analysis
  folder #
path_pat = r'path\to\wildtype\image\re-check\folder\*'
for wt_path in glob.glob(os.path.join(path_pat), recursive=True):
    print('FROM: ' + wt_path)
    wt_folder, = glob.glob( os.path.join(wt_path, 'Major*\\'))
    shutil.copy(
        os.path.join(wt_folder, 'MajorCheck.csv'),
        os.path.join(wt_folder, '..', '..', 'Recrop', 'Analysis_folder')
    )
None
# Both primary and rec-checked wild type detections are assigned and the area values are
  finalised here #
path_pattern = r'path\to\recropped\image\folder\*'
# checking and entering for analysis folder in each recrop subfolder #
for path in glob.glob( os.path.join(path_pattern), recursive=True):
    print (path)
    Analysis_folder = glob.glob(os.path.join(path, 'Analysis_folder*\\'))
    if 1 != len(Analysis_folder):
        print ('SKIPPING: '+path)
        continue
    Analysis_folder = Analysis_folder[0]
    # Opening csv file with areas assigned after blur-blank ascertainment #
    Analysis_path = glob.glob(os.path.join(Analysis_folder, 'Blur_Area_Final.csv'))
    df = pd.read_csv(os.path.join(Analysis_folder, 'Blur_Area_Final.csv'))
    # Checking wildtype check list against pre-assigned area values #
    # All wildtype detected kidneys are assigned non-cystic value here #
    df2 = pd.read_csv(os.path.join(Analysis_folder, 'wtFileNames.csv'))
    df2['Filename'] = df2['Filename'].map(lambda x: str(x)[:35])
    df2['Wt_Kidney'] = 0
    df3 = df.merge(df2, how='left', on= 'Filename')
    # Checking wildtype re-check list against pre-assigned area values #
    # In case any kidney was unassigned as wildtype it's corrected here#
    df4 = pd.read_csv(os.path.join(Analysis_folder, 'MajorCheck.csv'))
    df4['Filename'] = df4['Filename'].map(lambda x: str(x)[:35])
    df4.drop(df4.columns[[1,2,3,4,5,6,7,8,9,10,11,12,13,14,15,16,18,19,20,21,22,23,24,25,26,27,28,29,30,31,32,33,34,35]],
        axis=1, inplace=True)
    df5 = df3.merge(df4, how='left', on= 'Filename')
    df5= df5.drop_duplicates()
    after_11 = df5.index > 12
    not_nan = ~pd.isnull(df5.Wt_Kidney)
    major_check = df5['Major'] > 299
    df5.loc[after_11 & not_nan & major_check]
    kidney_area = df5['TotalKidney_Area'] != 0
    df5.loc[after_11 & not_nan & major_check & kidney_area, 'TotalKidney_Area'] = df5.Area
    # Saving finally assigned area file as a new csv file #
    df5.to_csv(os.path.join(Analysis_folder, 'MajorBlur_Area_wt.csv'), index=False)
# Plotting heatmap based on the finally assigned areas to the images in correspondance to the
  microtitre plate imaged #

```

```
for path in glob.glob (os.path.join(path_pattern), recursive=True):
    Analysis_folder = glob.glob(os.path.join(path, 'Analysis_folder*\\'))
    if 1 != len(Analysis_folder):
        print ('SKIPPING: '+path)
        continue
    Analysis_folder = Analysis_folder[0]
    # Reading each final area file of the respective subfolder #
    df3 = pd.read_csv(os.path.join(Analysis_folder, 'MajorBlur_Area_wt.csv'), decimal=b'.')
    colormap = df3['TotalKidney_Area'].values.reshape([8,12])
    threshold = 60000
    print (colormap)
    # Colour scheme of the heatmap #
    cmap = mpl.cm.inferno
    # Assigning plot area #
    fig = plt.figure()
    sub = fig.add_subplot(1,1,1)
    fig.suptitle('Kidney Whole Area', fontsize=16, fontweight='bold')
    norm = mpl.colors.Normalize(vmin=80, vmax=threshold)
    cmap.set_under('silver')
    sub.set_aspect('equal')
    cb_sub=fig.add_axes([0.95, 0.1, 0.03, 0.8])
    img = sub.imshow(colormap, cmap=cmap, norm=norm, interpolation='none')
    cb = mpl.colorbar.ColorbarBase(cb_sub, cmap=cmap, norm=norm, extend='both')
    # Sets size of entire heatmap
    fig.set_size_inches(10.5,8.5, forward=True)
    # Assigning labels and ticks to the heatmap #
    x = ['1','2','3','4','5','6','7','8','9','10','11','12']
    y = ['A','B','C','D','E','F','G','H']
    sub.set_xticklabels([]+x, minor=False)
    sub.set_yticklabels([]+y, minor=False)
    sub.set_yticks(np.arange(colormap.shape[0]), minor=False)
    sub.set_xticks(np.arange(colormap.shape[1]), minor=False)
    sub.xaxis.tick_top()
    # Heatmap plotted #
    plt.show()
    # Assigning heatmap name of the folder #
    split_path = path.split('\\')
    split_path[3]
    Heatmap_name = 'Heatmap_wt'+ '_' +split_path[3]+' .png'
    # Saving heatmap as png file #
    fig.savefig(os.path.join(Analysis_folder,Heatmap_name), format='png', dpi=600)
```

10 CURRICULUM VITAE

Personal data

Name	Gunjan Pandey
Date of birth	02.07.1991
Place of birth	Sitapur, India
Nationality	Indian

Contact information

Address	Fritz-Frey Strasse 8, 69121 Heidelberg, Germany
Telephone	+49 172 4375011
E-mail	gunjan.pandey@med.uni-heidelberg.de

Education

Jan. 2019 – present	University Hospital Heidelberg, Germany, Researcher Neocyst: Network for Early Onset Cystic Kidney Disease
Jan. 2016 – Jan. 2019	University Hospital Heidelberg, Germany, Early Stage Researcher in Marie Curie Initial Training Network and research in High-Content Screening on Cystic Kidney Disease Model of Zebrafish (RenalTract),
Aug. 2015 – Jan. 2016	University of Helsinki, Finland, study on role of LAMP-2 in autophagosome maturation
Mar. 2015 – Aug. 2015	University of Helsinki, Finland, study on salivary proteases in VEGF-C cleavage
Aug. 2013 – Oct. 2015	Jyväskylä University, Finland, Masters degree in Nanoscience
Jul. 2012 – Apr. 2013	National Institute of Oceanography, India, study on phytochemicals in sea slug <i>Elysia abangantawaensis</i>
Aug. 2008 – Dec. 2012	Amity University, India, Bachelors degree in Biotechnology
till – 2008	Elementary School in India

11 Acknowledgement

Firstly, I am thankful to Prof. Franz Schaefer and Dr. Jochen Gehrig, for accepting me as a PhD researcher in this exciting project. Their continued guidance and stirring discussions catalysed this project. Dr. Jens H. Westhoff, for their encouragement, guidance and helpful discussions. Dr. Jochen Wittbrodt (Centre for Organismal Studies (COS) Heidelberg) and Felix Loosli (Karlsruhe Institute of Technology) for general animal facility support. Prof. Christoph Englert for kindly providing us with *Tg(wt1b:EGFP)* fish line. Dirk Toewe, for their support in Python programming. Peter Steenbergen, for help in developing zebrafish screening protocols and providing a cheerful lab environment. Yu Liang, for introducing me to the iridescent world of transgenic zebrafish and teaching me the basic techniques.

I am grateful to Marie Sklodowska-Curie grant for funding this project under the RENALTRACT ITN project from the European Union's Horizon 2020 research and innovation programme and forming this wonderful research network, brimming with scientific opportunities.

I am grateful to all of those with whom I have had the pleasure to work during this project in Kinderklinik, Acquifer and KIT. Sincere thanks to Ms. Barbara Rodenbeck, Mrs. Brigitte Joggerst, Laurent Thomas, Jana Heigwer and Tanja Wlodkowski.

I am profoundly grateful to my grandfather and mother for bringing me up in such a remarkable scholastic environment that led me here. My heartfelt thanks to my brothers – Siddharth and Akshay Dixit for great counselling and support in times of need. I extend my gratitude to my grandmother, father, uncle and aunt for their enriching influence and motivation. Last but not the least, I would like to thank Vincent Debierre for his scientific and analytical inputs along with the emotional support and encouragement during this period. In the end, I would like to thank anyone and everyone who has been helpful in contributing towards the success of this work.

12 EIDESSTATTLICHE VERSICHERUNG IN DEUTSCHER SPRACHE

1. Bei der eingereichten Dissertation zu dem Thema

Development of An Automated High-Content Screening Platform for Identification of Cystic Kidney Disease Modifying Substances in Zebrafish Model of Human Cystic Kidney Disease

handelt es sich um meine eigenständig erbrachte Leistung.

2. Ich habe nur die angegebenen Quellen und Hilfsmittel benutzt und mich keiner unzulässigen Hilfe Dritter bedient. Insbesondere habe ich wörtlich oder sinngemäß aus anderen Werken übernommene Inhalte als solche kenntlich gemacht.

3. Die Arbeit oder Teile davon habe ich bislang nicht an einer Hochschule des In- oder Auslands als Bestandteil einer Prüfungs- oder Qualifikationsleistung vorgelegt.*

4. Die Richtigkeit der vorstehenden Erklärungen bestätige ich.

5. Die Bedeutung der eidesstattlichen Versicherung und die strafrechtlichen Folgen einer unrichtigen oder unvollständigen eidesstattlichen Versicherung sind mir bekannt. Ich versichere an Eides statt, dass ich nach bestem Wissen die reine Wahrheit erkläre und nichts verschwiegen habe.

Ort und Datum

Heidelberg, 02/07/2019

Unterschrift



**Wenn dies nicht zutrifft, machen Sie folgende Angaben:*

3. Die Arbeit oder Teile davon habe ich wie folgt an einer Hochschule des In-oder Auslands als Bestandteil einer Prüfungs-oder Qualifikationsleistung vorgelegt:

Titel der Arbeit: Dr. Sc. hum.

Hochschule und Jahr: University Hospital Heidelberg, 2019

Art der Prüfungs- oder Qualifikationsleistung: Dr. Sc. hum.